Quaternary fluvial environments in NE Morocco inferred from geochronological and sedimentological investigations

Inaugural-Dissertation

zur

Erlangung des Doktorgrades

der Mathematisch-Naturwissenschaftlichen Fakultät

der Universität zu Köln

Köln, 2018

vorgelegt von

Melanie Bartz

aus Dormagen

Berichterstatter/Gutachter: Prof. Dr. Helmut Brückner

Prof. Dr. Olaf Bubenzer

Tag der mündlichen Prüfung: 04.07.2017

Abstract

The investigation of fluvial archives in NE Morocco is of high interest for unravelling palaeoenvironmental changes linked to Quaternary climate fluctuations, long-term tectonic activity and/or human influence. The prehistoric site of Ifri n'Ammar is situated in NE Morocco and represents a key location in unravelling the history of anatomically modern humans (AMH) in northern Africa as it reveals Middle and Late Palaeolithic occupation phases since ~170 ka. Therefore, this study uses two fluvial systems of different nature – the ephemeral stream Wadi Selloum and the perennial Moulouya River – in order to reconstruct the varying environmental conditions for the last ~170 ka, the time when AMH started to disperse into the region.

Both fluvial systems provide valuable insights into the geomorphic evolution of the study area. It has been shown that the two fluvial systems responded to different environmental triggers: the small catchment of the Wadi Selloum is highly affected by the sensitive ecosystem of the Mediterranean region. The ephemeral stream is characterised by a discontinuous and heterogeneous sediment record caused by short-term climatic shifts and human influence. In contrast, tectonic activity appears to be the main driver for the evolution of the lower Moulouya terraces, rather than climate cyclicity during the Quaternary.

Establishing chronostratigraphies of river sedimentary sequences always remains challenging. However, based on different luminescence dating techniques (OSL, pIRIR, TL), electron spin resonance (ESR) dating using the multiple centres approach (Al and Ti centres of quartz), and palaeomagnetic analyses, geochronological frameworks for the two fluvial archives located in the direct vicinity of Ifri n'Ammar could successfully be established. First numerical ages in this area yield burial ages of the lower Moulouya terraces and the Wadi Selloum deposits dating back to Early Pleistocene and Late Pleistocene/Holocene times, respectively.

In addition to the use of absolute and relative dating techniques, laboratory (sedimentology, geochemistry, mineralogy) and microscopic (micromorphology) analyses have been carried out in order to identify periods of enhanced flooding in both fluvial systems on the one hand, and periods of pedogenesis on the other. The Wadi Selloum gives information about morphodnamic phases in the time of AMH settling: periods of enhanced aggradation occurred around ~100 ka, ~75 ka, ~55 ka, after the LGM, and during the Holocene, whilst sedimentation ended after ~1.3 ka. Pedogenesis may be used as environmental indicator for more humid climate conditions during MIS 3 (palaeo-Calcisol), the early Holocene (Calcisol) and the late Holocene (Fluvisol).

Although palaeoenvironmental implications should be taken with caution due to the discontinuity of the ephemeral stream system, it appears that more humid and warmer climate conditions favoured human settling in this area. This study thus provides first insights into the palaeoenvironmental changes around the rock shelter of Ifri n'Ammar during the last glacial-interglacial cycle.

Kurzzusammenfassung

Die Untersuchung von fluvialen Archiven ist in NO Marokko von großem Interesse für die Aufklärung von Paläoumweltveränderungen, die meist mit klimatischen Schwankungen, langfristiger tektonischer Aktivität und/oder menschlichem Einfluss im Quartär verbunden sind. Die prähistorische Höhle Ifri n'Ammar stellt in dieser Region eine Schlüsselstelle dar. Durch Mittel- und Spätpaläolithische Funde offenbart die archäologische Stätte Informationen über die Geschichte des Anatomisch Modernen Menschen (AMH) in den letzten ~170 ka. Aus diesem Grund werden in dieser Studie zwei fluviale Systeme unterschiedlicher Natur - der ephemere Wadi Selloum und der perennierende Fluss Moulouya – untersucht, um die wechselnden Umweltbedingungen für die letzten ~170 ka zu rekonstruieren, als AMH begannen die Region zu besiedeln.

Beide fluvialen Systeme liefern wertvolle Erkenntnisse über die geomorphologische Entwicklung des Untersuchungsgebietes. Es wurde gezeigt, dass sie jeweils auf unterschiedliche Umweltauslöser reagieren: Das eher kleine Einzugsgebiet des Wadi Selloum ist stark von dem sensiblen Ökosystem des Mittelmeerraumes betroffen. Dies führt zu einem diskontinuierlichen und heterogenen Sediment-Archiv, was vor allem auf kurzzeitige klimatische Veränderungen und menschlichen Einfluss zurückzuführen ist. Im Gegensatz dazu scheint der Hauptantrieb für die Entwicklung der unteren Moulouya-Terrassen die tektonische Aktivität zu sein, während Klimaschwankungen im Laufe des Quartärs eine weit geringere Rolle spielten.

Das Erstellen von Chronostratigraphien ist vor allem bei Fluss-Sediment-Sequenzen herausfordernd. Auf Basis unterschiedlicher Lumineszenz-Datierungstechniken (OSL, pIRIR, TL), Elektronenspinresonanz-Datierung (ESR) unter der Benutzung der Multizentren-Anwendung (Al- und Ti-Zentren in Quarz) und paläomagnetischen Analysen konnte ein geochronologischer Rahmen in beiden Fluvialarchiven erstellt werden. Die ersten absoluten Datierungen in dieser Region liefern Ablagerungsalter der unteren Moulouya-Terrassen im Frühpleistozän, während die Wadi Selloum Ablagerungen ins Spätpleistozän/Holozän zurück datieren.

Neben der Anwendung von absoluten und relativen Datierungsverfahren wurden Labor- (Sedimentologie, Geochemie, Mineralogie) und mikroskopische (Mikromorphologie) Analysen durchgeführt, um in beiden fluvialen Systemen Perioden mit einerseits erhöhtem Abfluss und andererseits Bodenbildungsphasen zu identifizieren. Der Wadi Selloum gibt Auskunft über morphodynamische Phasen in der Zeit der AMH-Besiedlung: Perioden der verstärkten Aggradation traten um ~100 ka, ~75 ka, ~55 ka, nach dem Letzten Glazialen Maximum (LGM) und während des Holozäns auf, während die Sedimentation nach ~1.3 ka endete. Pedogenese zeichnet sich als Umweltindikator für feuchtere Klimabedingungen während des MIS 3 (Paläo-Calcisol), des frühen Holozäns (Calcisol) und des späten Holozäns (Fluvisol) aus.

Obwohl durch die Diskontinuität des ephemeren Fluvialsystems die Interpretation von Paläolandschaften kritisch gesehen werden sollte, so scheint es, dass feuchte und wärmere Klimaverhältnisse die menschliche Besiedlung in dieser Region begünstigten. Aufgrund erster Umweltimplikationen in dieser Region gibt diese Studie erste Einblicke in Paläoumweltveränderungen in der direkten Umgebung von Ifri n'Ammar während des letzten Glazial-Interglazial Zyklus.

Acknowledgements

This PhD thesis gives me the opportunity to express my gratefulness to a lot of people who helped and supported me during the last years.

Firstly, I would like to thank my supervisor Prof. Dr. Helmut Brückner for initiating this project and providing me the opportunity to work within the framework of the CRC 806. In particular, he helped me to widen my research from various perspectives. I am very thankful for his motivation and support to pursue my own ideas during the time of my PhD research. His guidance helped me in all the time of research and writing of this thesis. I feel very grateful working in his team, since being a student assistant during my Bachelor studies.

Beside my supervisor, I would like to express my gratitude to my advisor Dr. Gilles Rixhon. I am most grateful for his help during in total four months of field work in Morocco. Also in Cologne, his motivation and encourage helped me to look at this research in different ways and to open my mind for new approaches. I would like to thank him especially for taking a lot of time for fruitful discussions. His support was essential for having success during my PhD research.

My sincere thanks also goes to Prof. Dr. Olaf Bubenzer who agreed to co-supervise this thesis and also gave me new intellectual approaches for completing my thesis. Moreover, I would like to thank Prof. Dr. Martin Melles and Dr. Dominik Brill for being a part of the commission during my PhD defense.

The support by the “Institut National des Sciences de l’Archéologie et du Patrimoine du Maroc” (INSAP) and by the “Commission for Archaeology of Non-European Cultures” (KAAK) of the German Archaeological Institute (DAI) is gratefully acknowledged. I would like to express my special thanks to Dr. Josef Eiwanger (KAAK). Without his permanent and warmly support during field work in Afsou, this research would not have been possible. I also thank Abdeslam Mikdad (INSAP), who kindly welcomed us to Morocco.

Furthermore, I thank Prof. Dr. Gerd-Christian Weniger for his help during field work, his nicely organised meetings at the Neanderthal museum and the constructive discussions on the archaeology and environment of North Africa. In the same way, I would like to thank Dr. Jörg Linstädter, Alessandro Potì and Sonja Tomasso, who created a nice atmosphere during our times in Morocco.

I would like to thank Dr. Nicole Klasen for her support in the experimental luminescence work conducted in this project, constructive discussions and helpful comments. Also, Dr. Martin Kehl is thanked for supervising me in micromorphological approaches.

At this point, I would like to take the opportunity to thank the whole working group of Prof. Dr. Helmut Brückner for fruitful discussions and making me feel valued - as scientist and person. In particular, I thank Dr. Dominik Brill and Dr. Matthias May, who helped me a lot with encouraging words. I would like to take opportunity to thank Juliane Scheder and Hannes Laermanns for being my friends since years and creating a friendly atmosphere in the office. I liked talking with them about different topics, working in the laboratory and interpreting our research data on many occasions. Furthermore, I thank further members and friends from the Institute of Geography, e.g., Helge Aasen, Kristof Dorau, Corinna Földi, Franziska Sohns, Nina Szemkus and Nora Tilly for a very nice laboratory and institute life.

During the last years I had the opportunity to work abroad in order to gain further knowledge in geochronology. Special thanks is dedicated to Prof. Dr. Rainer Grün and Dr. Mathieu Duval (Griffith University, Brisbane/Australia) who provided me an opportunity to join the research team at the CENIEH in Burgos/Spain. Dr. Mathieu Duval gave me access to the ESR laboratory and facilities and without his precious support it would not have been possible to complete this research. I also want to thank Dr. Gloria Lopéz, Dr. Davinia Moreno and the other members at the CENIEH for making my time in Burgos memorable. Moreover, Prof. Dr. Nigel Spooner and Dr. Lee Arnold are especially thanked for the opportunity to work in the centre of Physical Sciences at the University of Adelaide/Australia, I liked being there very much.

I would like to thank Dr. Martin Seeliger and Dr. Meriam El Ouahabi for supporting the fieldwork. In this way, I would like to express my thanks to all the students who attended the student internships with enthusiastic support.

Dr. Gilles Rixhon, Dr. Dominik Brill, Dr. Jörg Linstädter, Maike Norpoth, Juliane Scheder, Hannes Laermanns, and Christoph Burow are thanked for proofreading and language polishing of this thesis.

I thank the German Research Foundation for funding this research (DFG; Grant-No.: SFB 806/2). The “Graduate School of Geosciences (GSGS)” and the “Albertus-Magnus Graduate Centre (AMGC)” are kindly acknowledged for providing travel grants in order to attend national and international conferences as well as visit research centres abroad.

Finally, I would like to thank my family, in particular my mother and my grandmother, for supporting me spiritually throughout writing this thesis and in my life in general. Last but not least, I want to express my sincere thanks to Marcel Kranz for his patience, motivation and great understanding during the last months.

Table of Contents

List of Figures

List of Tables

Chapter 1

1 Introduction

1.1 The Collaborative Research Centre 806

The Collaborative Research Centre (CRC) 806 “*Our Way To Europe. Culture-Environment Interaction and Human Mobility in the Late Quaternary*“ (http://www.sfb806.uni-koeln.de/) is funded by the German Research Foundation (Deutsche Forschungsgemeinschaft; DFG SFB 806) and is composed of geoscientists and archaeologists from the universities of Cologne, Bonn and the RWTH Aachen. The aim of the CRC is the investigation of the trans-continental and intercontinental dispersal behaviour of anatomically modern humans (AMH) from Africa to Western Eurasia.

The origin and dispersal of AMH have been a fundamental question in human evolutionary studies (e.g., Howell, 1999; Stringer, 2002; Groucutt et al., 2015). Mitochondrial DNA (mtDNA) analyses relates to the ancestor of the modern human in Africa (Cann et al., 1987). Furthermore, the earliest fossils of *Homo sapiens sapiens* have been found in Eastern Africa, and relatively old fossils have been reported in southern Africa and the Near East. Therefore, the origin of *Homo sapiens sapiens* is expected in Africa, wherefrom the AMH left the African continent and migrated into Eurasia (Foley and Lahr, 1992; Finlayson, 2005; Reed and Tishkoff, 2006). Recently, the two Out-of-Africa-models (Out-of-Africa-I-model of the early kind of *Homo erectus* demonstrating a first phase of migration around 1.8 Ma; Out-of-Africa-II-model, which reveals the migratory movement of the AMH around 190 ka) are still under debate, since the dispersal process appears to have been affected by behavioural variability (e.g., Petraglia et al., 2010; Groucutt et al., 2015). Also the dispersal direction out of Africa is generally discussed. Whilst the “Eastern Corridor”, from Northeast-Africa to Europe is considered to be an important route taken by AMH (Richter et al., 2012), a western path across the Straits of Gibraltar might have also been an alternative (Straus, 2001; Linstädter et al., 2012a).

The CRC investigates the eastern and western way of dispersal from East Africa to Europe. Whilst the first phase of the CRC 806 (2009-2013) focused on the primary expansion of AMH after 190 ka, induced by climatic, environmental and cultural fluctuations, the ongoing second phase (2013-2017) mostly concentrates on secondary expansions and retreat into areas which had already been inhabited. The CRC 806 thus aims at understanding the environmental driving forces of these developments and their possible interactions with the cultural system.

This thesis is embedded in the subproject C2 of the second phase of the CRC 806, entitled "*Early Holocene Contacts between Africa and Europe and their Palaeoenvironmental Context*", which deals with human contacts between Africa and Europe in the Western Mediterranean region. During the first phase of the CRC 806, C2 focused on the Holocene Epipalaeolithic-Neolithic transition (Linstädter et al., 2012a), whilst the second phase deals with an extended time range into the Late Pleistocene. Continuity alongside discontinuity concerning intercontinental contacts between both sides of the Straits of Gibraltar are known (Linstädter et al., 2012a). Thus, the question whether AMH took the western path to spread into the Iberian Peninsula remains open.

A key site on the African side of the Straits of Gibraltar is the rock shelter of Ifri n'Ammar, located in NE Morocco (Nami and Moser, 2010), where the first occupation phase of AMH started as early as ~170 ka (Richter et al., 2010). The main research topic of this thesis focuses on the reconstruction of past landscape and palaeoclimatic changes in order to investigate the relationship between human occupation phases – which are known to have been discontinuous – and natural conditions. The most promising climate and landscape records in the study area are provided by fluvial archives (e.g., Zielhofer et al., 2010). Therefore, two fluvial systems of different nature – the ephemeral stream Wadi Selloum and the perennial Moulouya River – are studied (offsite archives) and linked with the settling phases of Ifri n'Ammar (onsite archive).

1.2 Fluvial environments in the Western Mediterranean region – state of the art

Since the middle of the 20th century, Quaternary fluvial formations in the Mediterranean region have been investigated. During the first decades, only a few studies focused on regional Pleistocene fluvial records to infer palaeoenvironmental changes (e.g., Vita-Finzi, 1969, 1976; Harvey and Wells, 1987).

Establishing chronostratigraphies of river sedimentary sequences always remains challenging (Macklin et al., 2002; Rixhon et al., 2017a). Whilst radiocarbon dating has been widely used in Mediterranean fluvial environments in order to unravel palaeoenvironmental features and the long-term river evolution (e.g., Vita-Finzi, 1976; Harvey and Wells, 1987; Macklin et al., 1995; Thorndycraft and Benito, 2006; El Amrani et al., 2008; Wolf and Faust, 2015), its application only spans the last 30-50 ka and requires the preservation of organic material within the sediment sequences (Rixhon et al., 2017a). During the last 20 years, several technical developments have enhanced the use of further geochronological tools in fluvial environments (Rixhon et al., 2017a). Optically stimulated luminescence (OSL) is able to directly date the timing of sedimentation (Duller, 2008); thus, it is also possible to determine Late and Middle Pleistocene river erosion and aggradation phases in the Western Mediterranean region (e.g., Fuller et al., 1998; Rose and Meng, 1999). Electron spin resonance (ESR; e.g., Duval et al., 2015) and terrestrial cosmogenic nuclide dating (e.g., Antón et al., 2012) clearly improved studies of Pleistocene alluvial geochronologies. For instance, ESR dating allowed the reconstruction of different aggradation and incision phases in fluvial systems of the Early Pleistocene on the Iberian Peninsula (e.g., Duval et al., 2015; Sancho et al., 2016).

Understanding fluvial responses to external controls represents a major task when dealing with past landscape changes at different timescales. In the Mediterranean region, climate was firstly considered as the most significant driver for fluvial development leading to a pronounced “Older and Younger” alluviation model (Vita-Finzi, 1969, 1976), which has often been argued to be more complex (e.g., Wagstaff, 1981; van Andel et al., 1986). Later on, the interaction between climatic forcing and human activity was considered as additional driving factor of changing fluvial processes, such as enhanced soil erosion in the alluvial plain (e.g., Brückner, 1986; van Andel et al., 1990; Faust et al., 2004; Hooke, 2006; Wolf et al., 2014). Sea-level changes can also affect the lowermost reach of a river due to glacio-eustatic or tectonic processes (e.g., Day et al., 1995; Krijgsman et al., 1999; Santisteban and Schulte, 2007). At last, fluvial response to tectonic activity can highlight long-term Quaternary crustal deformations (e.g., Maher and Harvey, 2008; Barcos et al., 2014; Poujol et al., 2014).

Whilst Macklin et al. (2002) have reported climate-driven changes in catchment hydrology and vegetation cover since the MIS 6 in Spain, studies dealing with fluvial archives predating the MIS 2 are rare in Mediterranean Morocco. Using the terrace sequence of the Kert River, Barathon et al. (2000) and El Amrani et al. (2008) aimed at reconstructing palaeoclimatic and palaeoenvironmental changes together with human-environment interactions from the final stage of the Late Pleistocene onwards. Holocene overbank fines were investigated in the lowermost reach of the Moulouya River focusing on the human- and climate-induced fluvial response (e.g., Ibouhouten et al., 2010; Zielhofer et al., 2008, 2010) or the result of eustatic variations (Pissart and Boumeaza, 2010). Only a few studies dealt with tectonically driven responses of fluvial systems in northern Morocco during mid- and late Holocene times (Zarki et al., 2004; Poujol et al., 2014).

1.3 Objectives of the present study

In NE Morocco, fluvial geo-archives have been used for reconstructing Holocene environmental changes (e.g., El Amrani et al., 2008; Ibouhouten et al., 2010; Zielhofer et al., 2008, 2010). However, the pre-Holocene evolution of the fluvial systems in this region is as yet poorly investigated. Due to the focus of the subproject C2 within the CRC 806, this study aims at using fluvial archives in NE Morocco to reconstruct the varying environmental conditions for the last ~170 ka, the time when AMH started to disperse into the region.

Hypothesis 1 – Both small and large fluvial systems provide valuable insights into the geomorphic evolution of the study area

Objective a: Investigating ephemeral stream deposits of Wadi Selloum

The high sensitivity of the Mediterranean region with regard to environmental parameters (e.g., climate, hydrology, vegetation; cf., Brückner, 1994) often leads to short-term high-energetic events in small scale fluvial systems. Therefore, ephemeral stream systems in semi-arid environments are known to be discontinuous in water and sediment discharge as well as deposition (Bull, 1997). However, as the fluvial system draining the apron of Ifri n'Ammar, the most important AMH site of the region (Nami and Moser, 2010), Wadi Selloum's fluvial record shall be used for understanding the geomorphological processes (e.g., Bertrams et al., 2012).

Objective b: Studying fluvial terrace systems along the lower Moulouya River

Fluvial terrace systems provide valuable insights into palaeoclimatic fluctuations (e.g., Bridgland and Westaway, 2008), rates of crustal deformation (e.g., Demoulin et al., 2017) and/or evidence of early human activity (e.g., Mishra et al., 2007). The Holocene environmental history of the lower Moulouya River has previously been studied with a focus on environmental changes resulting from climatic variations and related eustatic sea-level changes, as well as human and/or tectonic activity (Pissart and Boumeaza, 2010; Zielhofer 2008, 2010; Zarki et al., 2004). In contrast, Pleistocene terrace sediments were either completely neglected (Ibouhouten et al., 2010; Zielhofer et al., 2008, 2010) or erroneously interpreted as the Pliocene substratum (Pissart and Boumeaza, 2010). The study of the Moulouya River deposits in the lower reach shall provide further knowledge about environmental impulses (e.g., tectonics, climate) that give information about the geomorphic evolution during the Pleistocene.

Hypothesis 2 – Deposits of ephemeral streams and perennial rivers serve as suitable geo-archives for reconstructing past landscape changes

Objective c: Dating fluvial deposits of different natures

So far, only radiocarbon dating has been applied to Late Pleistocene and Holocene river deposits in NE Morocco (e.g., El Amrani et al., 2008; Zielhofer et al., 2008, 2010). Other absolute dating techniques were unfortunately disregarded for establishing geochronological frameworks of fluvial sediments. In order to get information about past alluvial environments, it is a crucial point to accurately date fluvial sedimentation in this study. For this, luminescence and electron spin resonance (ESR) dating shall be used to date sediment archives as old as several hundreds of thousands of years. Since luminescence signals (OSL or IRSL) are characterised by lower saturation levels compared to those of ESR, the latter dating technique serves as a valuable tool to date the older fluvial sediments; it should, however, be cross-checked with another method, e.g., palaeomagnetic dating (e.g., Sancho et al., 2016).

Objective d: Differentiating between phases of fluvial morphodynamic activity and stability

Morphodynamic activity phases may be expressed in frequent flooding periods due to increased rainfall, whilst stable land surfaces, evident in palaeosols within sediment sequences, are indicators of morphodynamic stability phases. Understanding the morphodynamic evolution gives insights into past landscape changes. In the given case, this will focus on the last ~170 ka, which were characterised by discontinuous occupation phases in Ifri n'Ammar (Nami and Moser, 2010). Thus, this study shall identify periods of enhanced flooding in both fluvial systems on the one hand, and periods of pedogenesis on the other.

Objective e: Unravelling long-term tectonic activity in the convergence zone of NE Morocco

The Moulouya River drains an area characterised by active crustal deformation during the Late Cenozoic due to the ongoing N-S convergence between the African and Eurasian plates (Barcos et al., 2014). Therefore, providing a detailed description of the distribution of the river terraces in the lowermost reach of the Moulouya River – including the identification of changes in the valley morphology and the establishment of a relative stratigraphy of Late Cenozoic landforms in the sedimentation basin of the lower Moulouya – shall give information about the fluvial response to tectonic activity. In order to understand the long-term river evolution and the nature of crustal deformations (e.g., Demir et al., 2012; Demoulin et al., 2017), field survey, geomorphological mapping and clast lithological analysis have to be performed.

Objective f: Linking the Wadi Selloum and the lower Moulouya River

The Wadi Selloum is a first-order tributary of the Moulouya River. The chronostratigraphical record of the Wadi Selloum shall be linked to the one of the lower Moulouya River. Similarities and differences shall be presented as well.

Hypothesis 3 – Palaeoenvironmental information can be linked to the occupation phases of settlement history of Ifri n'Ammar

Objective g: Determining palaeoenvironmental archives that provide information about the human impact

Fluvial runoff and sedimentation rates at the catchment-scale may be strongly influenced by human impact. Hence, driving mechanism concerning climate and/or environmental changes, which also enhance or reduce the fluvial activity, may be determined in fluvial archives (e.g., Faust et al., 2004). Due to the fact that access to freshwater is the most important precondition for human occupation, the occupants of Ifri n'Ammar may have influenced the environment of the two major water resources in their area, the Wadi Selloum and the Moulouya River.

Objective h: Correlation between human occupation phases and palaeoenvironmental changes

Fluvial records of the Wadi Selloum and the lower Moulouya River are the only geo-archives in the direct vicinity of the prehistoric rock shelter of Ifri n'Ammar. The activity and stability phases which they represent may help to decipher the human occupation phases of Ifri n'Ammar during the last ~170 ka. Thus, the occupation phases of the onsite archive (Ifri n'Ammar) shall be linked with palaeoenvironmental changes of the studied offsite archives (Wadi Selloum, lower Moulouya River).

1.4 Research design and applied methodology

The palaeogeographical research conducted in this PhD thesis investigates the fluvial geomorphological evolution in NE Morocco in order to reconstruct the landscape of Pleistocene times and find potential reasons for the occupation phases of the AMH in this region. The analysis of fluvial landscapes follows the research design of Stokes et al. (2012) (fig. 1.1).

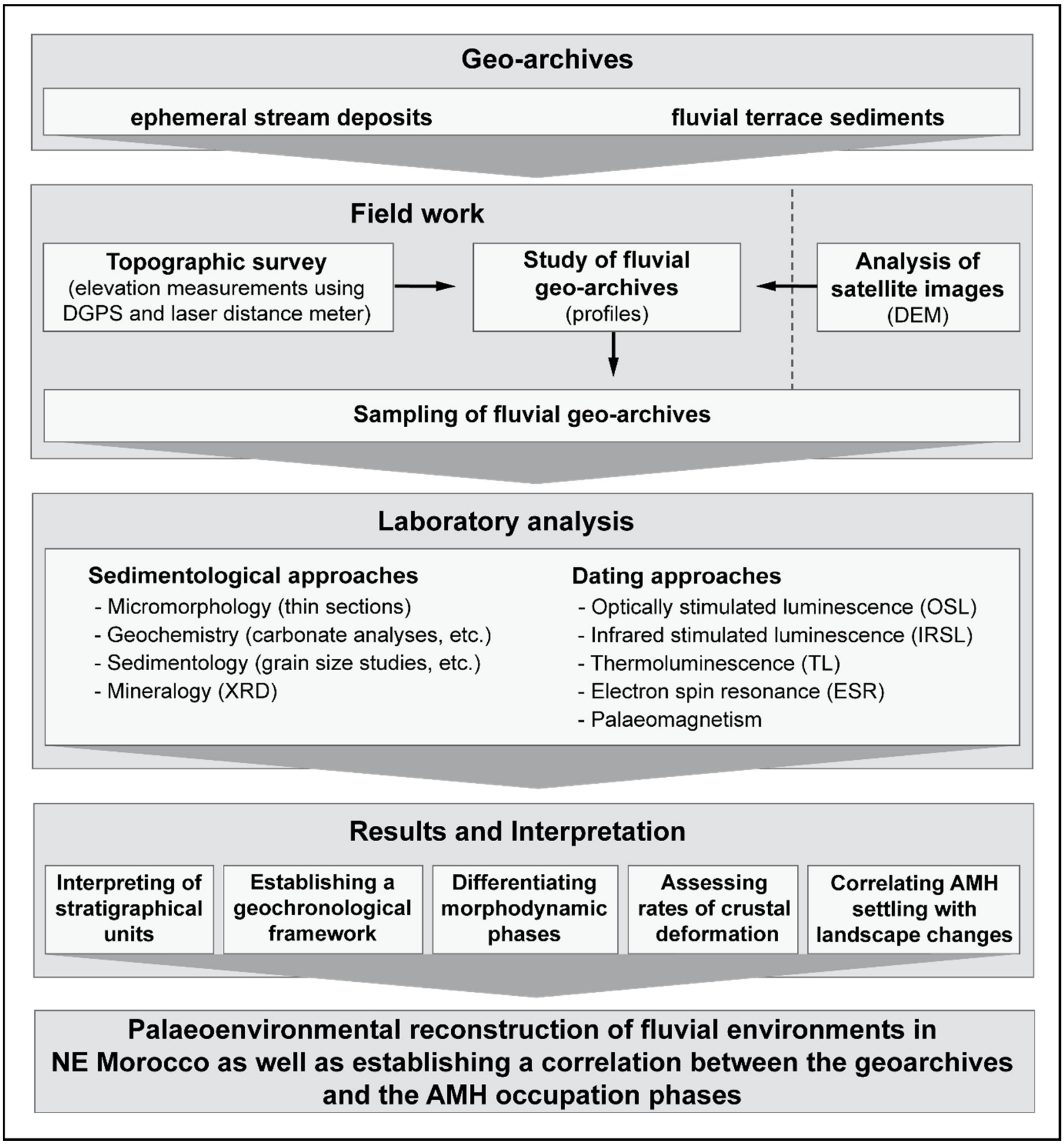

Fig. 1.1: The research design of the study (own design 2017).

1.4.1 Field work

Prior to the start of this project, preliminary field surveys, including sampling, were carried out in 2012 and 2013. During the second phase of the CRC 806, three main field campaigns were conducted in 2014, 2015 and 2016. Differential global positioning system (DGPS; Topcon HiPer Pro) and laser distance meter (TruPulse 200 Rangefinder) were used to obtain high-resolution information of the fluvial landscape topography and to generate a relative stratigraphy of fluvial landforms. Alongside profile descriptions, geomorphological mapping supplemented by the analysis of satellite images was carried out.

Preliminary sedimentological studies were directly performed in the field, including assessment of grain size, colour (Munsell Soil Color Chart), texture, and carbonate content according to AG Boden (2005). Sediment and micromorphological samples were collected in the Wadi Selloum profiles for further laboratory analyses. In the larger system of the Moulouya, clast lithological analysis was performed to unravel the source areas of coarse-grained fluvial material. In addition to the sampling for luminescence and/or ESR dating at Wadi Selloum and Moulouya River sites, palaeomagnetic samples were collected to achieve a relative age cross-check for deposits of the lower Moulouya.

1.4.2 Sedimentology, micromorphology and geochemistry

In order to unravel the sedimentary nature and post-depositional processes in the fluvial environment, sediment and soil properties were analysed in the Laboratory for Physical Geography (University of Cologne). The grain size distribution (Folk and Ward, 1957; Blott and Pye, 2001) was measured to determine transport processes of the fluvial sediments (e.g., Zielhofer et al., 2008; Bertrams et al., 2012). In the fluvial context, thin section analysis (cf., Beckmann, 1997; Stoops, 2003) has proven to be a useful tool for reconstructing pedogenic features (e.g., Faust et al., 2004; Badía et al., 2009; von Suchodoletz et al., 2015); therefore, it was applied to the ephemeral stream profiles of Wadi Selloum. Organic and inorganic carbon contents give information about soil forming processes and surface layers (e.g., Bertrams et al., 2014). By using different geochemical and mineralogical analyses (e.g., loss on ignition, Scheibler method, XRD), morphodynamic phases were investigated.

1.4.3 Geochronology

Amongst the array of Quaternary numerical dating methods for establishing chronologies of fluvial deposits (Rixhon et al., 2017a), optically stimulated luminescence (OSL), thermoluminescence (TL) and electron spin resonance (ESR) dating methods were applied in the framework of this study. In addition, palaeomagnetism was used to get relative age information about fluvial deposition of the lower Moulouya River.

1.4.3.1 Trapped charge dating

Luminescence and ESR dating methods belong to the group of trapped charge dating methods (Aitken, 1985; Grün, 2001; Duller, 2008). Minerals such as quartz or K-feldspar act as dosimeter and absorb the natural radiation dose over geological time scales (Rixhon et al., 2017a). Natural radiation, originating from the decay of radioactive uranium (U), thorium (Th) and potassium (K) isotopes, delocalises electrons within the crystal lattice, which are later trapped in defects in the crystal system (Aitken, 1985; Duller, 2008). Usually, a smaller proportion of the environmental radiation is the contribution of cosmic rays (Prescott and Hutton, 1988).

Similar to luminescence, ESR dating of sedimentary quartz is based on the study of light-sensitive signals whose intensity is reset (bleached) under sunlight exposure during sediment transportation (Voinchet et al., 2015; Rixhon et al., 2017a). Thus, trapped charge dating can be used to estimate the burial time of sediments. As a result of the isolation of sediments from sunlight after deposition, the time elapsed since the last transport cycle can be determined by assessing both the luminescence and ESR signal accumulated in a sediment sample (palaeodose) and the flux of ionising radiation to which it has been exposed since burial (dose rate) (Huntley et al., 1985; Aitken, 1992). The sediment age is calculated by dividing the palaeodose by the dose rate (Aitken, 1985; Preusser et al., 2008).

However, several intrinsic methodological issues may cause erroneous dose and hence age estimation: (i) depositional processes may limit the degree of sediment bleaching, i.e., partial or incomplete bleaching (Olley et al., 1999; Wallinga, 2002; Voinchet et al., 2015). This is especially true for fluvial systems since solar resetting may be limited by the attenuation of light through the water column due to enhanced suspension load, increased water depth or transport distance in a given fluvial system (Rittenour, 2008); (ii) post-depositional interactions in the sediments such as bioturbation or pedoturbation can lead to the mixing of differently bleached grains (Bateman et al., 2003); (iii) the appearance of grain to grain heterogeneities due to different luminescence properties or micro-dosimetric effects (cf. Murray and Roberts, 1997; Nathan et al., 2003).

Luminescence dating

In luminescence dating, ionising radiation causes the excitation of electrons within an atom in the crystal lattice. Electrons are pushed in a higher energetic state, leaving holes. They become trapped in crystal defects and stored for a period of time. The crystal is stimulated by exposure to light (or heat in case of TL) and evicts electrons from traps. Hence, electrons recombine with luminescence recombination centres and thereby emitting light photons; this is measured as the luminescence signal (Aitken, 1985). Several relevant reviews related to the technical details of luminescence dating of fluvial deposits have been published (e.g., Wallinga, 2002; Rittenour, 2008; Rixhon et al., 2017a). Nevertheless, OSL is limited due to the low saturation level of the OSL signal in quartz, resulting in an upper dating limit in Late Pleistocene times depending on sample specific luminescence characteristics and environmental dose rates (Wintle and Murray, 2006). In order to circumvent OSL saturation issues and to extend the upper age range of optical dating, IRSL of K-feldspar serves as a valuable alternative in dating older Pleistocene deposits exhibiting higher dose saturation levels (up to Middle Pleistocene times) than conventional OSL methods (Jain, 2014). IRSL ages may suffer from age underestimation due to anomalous fading, a process by which the mineral loses its signal over time (Wintle, 1973; Huntley and Lamothe, 2001). However, elevated temperature post-infrared infrared stimulated luminescence (pIRIR) measures feldspar signals, which are less or even unaffected by anomalous fading. Luminescence dating (OSL of quartz, pIRIR of K-feldspar and TL of a pottery shard) was carried out at the Cologne Luminescence Laboratory (CLL; University of Cologne).

Electron spin resonance dating

In ESR dating, the mineral can develop a paramagnetic behaviour under the effect of radioactive irradiation. Paired electrons are ionised in the mineral leading to unpaired and free electrons, which can be trapped in a lattice defect and form a paramagnetic centre. In the presence of an external magnetic field, the electron's magnetic moment aligns itself to the field in two discrete orientations. For a given magnetic field strength and by absorbing a photon with a certain frequency the electron can change its orientation, thus producing a measurable energy absorption spectrum (cf., Ikeya, 1993; Duval, 2016). Further technical details can be found, e.g., in Grün, 1989. ESR dating of aluminium (Al) or titanium (Ti) centres in optically bleached quartz allows dating Early to Middle Pleistocene fluvial sediments (e.g., Bahain et al., 2007; Voinchet et al., 2010; Moreno et al., 2012; Duval and Guilarte, 2015). The reliability of the ESR dating method is improved by the multiple centres (MC) approach (Toyoda et al., 2000), where both the Al and the Ti centres in quartz are measured. This method takes advantage of the different centre characteristics (i.e., bleaching kinetics, saturation level, ESR signal intensity) and checks whether both centres would provide consistent ESR results. In the fluvial context, Duval et al. (2015) have demonstrated the usefulness of the MC approach for dating Early Pleistocene terraces. In the framework of this thesis, ESR dating of quartz (Yokoyama et al., 1985) was carried out at the Centro

Nacional de Investigación sobre la Evolución Humana (CENIEH, Burgos), supervised by Dr. Mathieu Duval.

1.4.3.2 Palaeomagnetism

Generally, palaeomagnetic research aims at understanding magnetic properties of rocks and sediments, as well as past configurations of the geomagnetic field in order to get geochronological information about the depositional context from the Precambrian to the Quaternary (Butler, 1992; Tauxe et al., 2016). Further details about the physical background and principles of palaeomagnetism can be found in Butler (1992) and Tauxe et al. (2016). River sediments may acquire magnetic remanence upon deposition which thus provide chronostratigraphic information for terrace sequences (e.g., Jacobson et al., 1988; Li et al., 1997; Sancho et al., 2016). Therefore, palaeomagnetism was applied to obtain relative age information for the fluvial terrace systems of the lower Moulouya. Palaeomagnetic analyses were carried out at the CENIEH (Burgos), accomplished by Prof. Dr. Josep M. Parés and Claudia Álvarez Posada.

1.4.4 Outline of the study

After this introductive Chapter, including a presentation of the project, methodology and study area, this PhD thesis is subdivided into two main sections: part I deals with the ephemeral stream deposits of the Wadi Selloum (Chapters 2 and 3), whilst part II focuses on the fluvial terraces of the lower Moulouya (Chapters 4 and 5). A major aim was to establish a chronostratigraphical framework and to reconstruct the palaeoenvironmental variations for both river systems.

Chapter 2 describes the challenge in dating ephemeral stream deposits in semi-arid environments using OSL. The new age results allow for a critical discussion about specific difficulties, such as partial bleaching (e.g., Olley et al., 1999; Klasen et al., 2013) and the low saturation level of quartz (Wintle and Murray, 2006). For the first time, OSL ages – and numerical ages – are presented for the ephemeral stream deposits in the direct vicinity of the rock shelter Ifri n’Ammar. For an inter-method comparison, one pottery shard was dated using TL. These results are published in *Quaternary Geochronology* (Bartz et al., 2015).

Chapter 3 focuses on the palaeoenvironmental reconstruction of the landscape near Ifri n’Ammar. OSL and pIRIR dating was applied to establish chronostratigraphies of additional sediment profiles of the Wadi Selloum. In addition to luminescence dating, tools of micromorphology, sedimentology, geochemistry and mineralogy were applied to identify phases of morphodynamic stability characterised by pedogenesis. The investigation of the fluvial archives of Wadi Selloum render valuable insights into palaeoenvironmental changes during the last ~100 ka. These results are published in *Catena* (Bartz et al., 2017).

Chapter 4 deals with the first description of Pleistocene fluvial terrace systems in the lowermost reach of the Moulouya River. The Moulouya flows across a newly identified fault zone resulting from the collision between the African and Eurasian plates. Contrasting fluvial environments were observed on both sides of the thrust: whereas long-lasting aggradation occurred in the footwall reach, a well-expressed terrace staircase developed in the hanging wall reach. These results are published in *Journal of African Earth Sciences* (Rixhon, Bartz et al., 2017).

Chapter 5 focuses on establishing a geochronological framework of the terrace systems of the lower Moulouya using ESR, luminescence and palaeomagnetic analyses of siliciclastic deposits. This study gives first insights into rates of incision and crustal deformation along the main fault zone mentioned in Chapter 4. The results of this research were submitted to *Quaternary Science Reviews* (Bartz et al.).

Chapter 6 discusses the diverse results with respect to the working hypotheses listed in Chapter 1.3. Finally, Chapter 7 provides a conclusion and outlook of this cumulative PhD thesis.

1.5 The study area

1.5.1 Geodynamical setting of NE Morocco

Morocco is located at a triple junction between a continental plate (Africa), an oceanic plate (Atlantic Ocean) and an active convergent plate zone (the Alpine belt system) (Michard et al., 2008). This results in a mountainous topography extending from Archean to Cenozoic times. Furthermore, diverse tectonic systems from sedimentary basins to metamorphic fold belts are evident (Michard et al., 2008). The Rif Belt (Betic-Rif-Tell orogen) of North Africa is a key segment of the larger Mediterranean Alpine belts. It forms the westernmost part of the Maghrebide belt, which spreads along the North African coast and shapes the southern rim of the Gibraltar Arc. The northern limb of it corresponds to the Betic Cordillera (Lonergan and White, 1997; Piqué et al., 2007; Chalouan et al., 2008). The Atlas system is formed by the High and Middle Atlas Mountains (fig. 1.2). While the E-ENE striking High Atlas trends from the Atlantic Coast over Algeria to the Saharan-Atlas, the NE trending Middle Atlas

Mountains separates from the High Atlas to the Beni Snassen Massif (Frizon de Lamotte et al., 2008; Barcos et al., 2014).

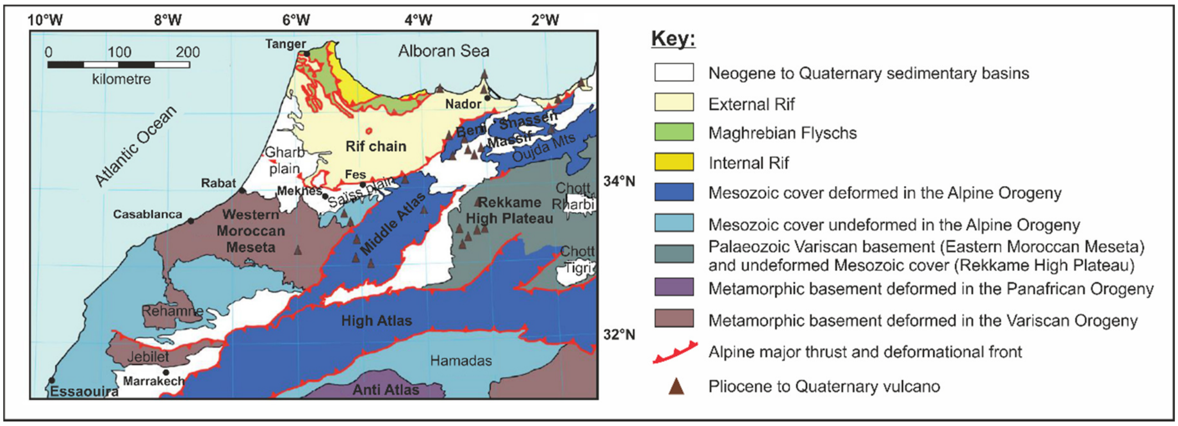

Fig. 1.2: Geological map and tectonic sketch of the Alpine mountain ranges in northwestern Africa (modified after Barcos et al., 2014).

The NW-SE convergence between Africa and Iberia in the Straits of Gibraltar has induced large deformations in the northern part of Morocco since the Miocene onwards. Crustal deformation in the Western Mediterranean is most likely the result of shortening of the Betic-Rif mountain ranges and extension of the Sea of Alboran (Fadil et al., 2006). Kinematic analyses of fault systems in the Rif and Tell Atlas indicated shortening directions associated to a clockwise block rotation of 15 to 25° (from NNE to NNW) and shortening rates of 1-2.3 mm/a (Meghraoui et al., 1996; Meghraoui and Pondrelli, 2012). The Rif mountain range showed NE-SW folding during the Quaternary distinguished by left-lateral, strike-slip faults and fold-and-thrust structures (Meghraoui and Pondrelli, 2012). For instance, horizontal and vertical slip rates of ~0.9 and ~0.5 mm/a, respectively, have been determined along the Trougout fault system in the northeastern Rif region (Poujol et al., 2014). Trend-topography surface analysis highlighted an E-W trending lithospheric dome in the eastern Rif and in the Beni Snassen massif (Barcos et al., 2014). Based on morphometric indicators, the latter is also characterised at its northern margin by N-S shortening resulting in active deformations (Barcos et al., 2014). Deformations in Middle Quaternary terraces of catchments located eastward (Kert river) and westward (Oujda region) of the Moulouya River were highlighted by Ait Brahim et al. (2002). At last, Holocene deposits in the lower reach of the Moulouya River were affected by local uplift (Zarki et al., 2004) and complex deformation features (fig. 1.3).

Fig. 1.3: Deformation of fluvial deposits are evident (white lines) in Holocene overbank fines located at the southern, i.e. right, river bank of the lower Moulouya River near the village Douar Ouled Belkhir. Own observations (view towards north, person for scale; photograph: G. Rixhon 2015).

1.5.2 Geographical and geological characteristics of the Moulouya catchment

The recent climate in NE Morocco is of the semi-arid Mediterranean type, characterised by hot and dry summers (mean summer temperatures around 25 °C) and cool and moist winters (mean winter temperatures around 13 °C) (Driouech et al., 2009). The average annual precipitation is estimated with 1400 million m^3 in the entire Moulouya River catchment area (Snoussi et al., 2002; fig. 1.4). The annual pluviometric index ranges from 150-200 mm/a in the lowlands to 600 mm/a in the Atlas Mountains (Kaemmerer and Revel, 1991; Ngadi, 1995; Snoussi et al., 2002).

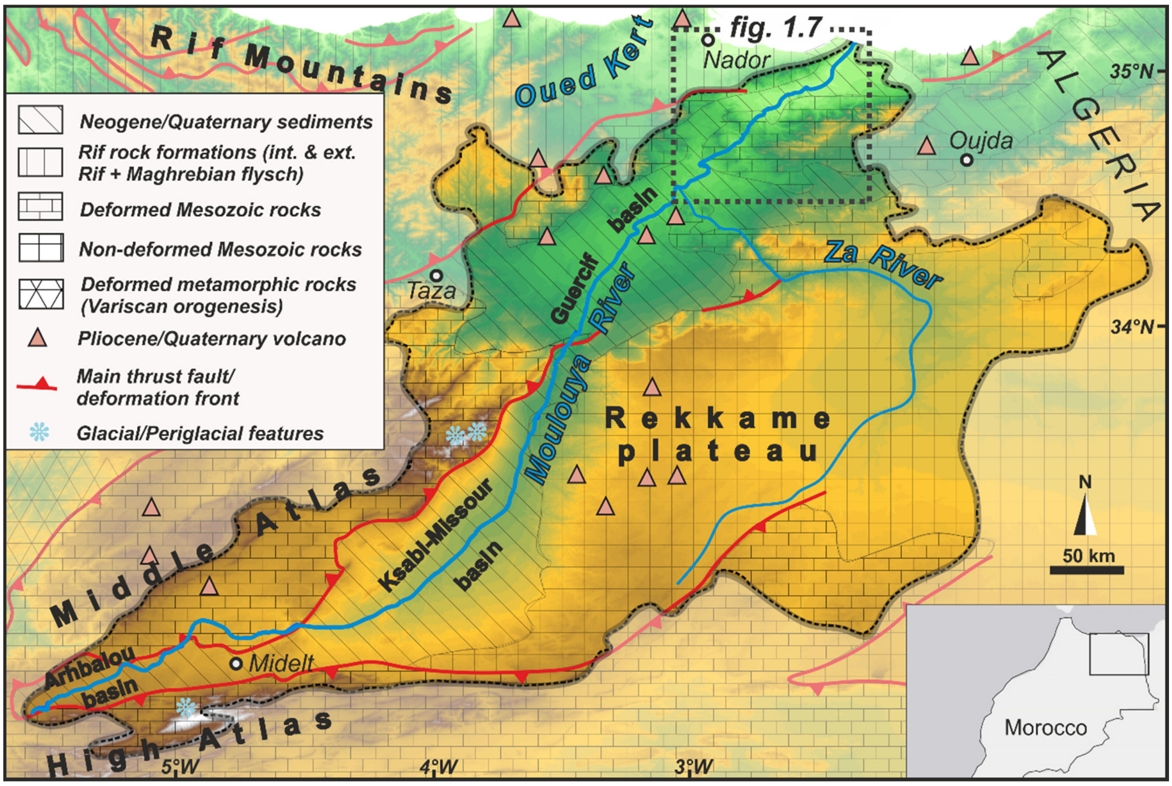

Fig. 1.4: Relief map of the Moulouya catchment (delimited by dashed black lines) including the main geological structures (cf., Barcos et al., 2014) and glacial/periglacial features (cf., Raynal et al., 1953; Awad, 1963; Hughes et al., 2011). The dashed rectangle refers to the zoom in of the study area (see fig. 1.7).

The Moulouya River (fig. 1.4) represents the largest fluvial system in NE Morocco and is characterised by a catchment area of ~74.000 km^2 (Pastor et al., 2015). From its headwaters at the junction of the High and Middle Atlas (at ~2000 m a.s.l.; above sea level) to its outlet into the Alboran Sea, the ˜600 km-long main trunk flows in a SW-NE direction (Pastor et al., 2015). It successively drains the Arhbalou, Ksabi-Missour, Guercif and Zebra-Triffa-Ouled Mansour Neogene sedimentary basins (fig. 1.4). The s-shaped Moulouya River has a hypsometric integral value of 0.313 and shows, especially in the lower reaches, changes in its river gradient (Barcos et al., 2014). A disequilibrium state presented by deformations of drainage network and the presence of large knickpoints have been detected for the Moulouya catchment (Barcos et al., 2014; Pastor et al., 2015), which can be subdivided into three main reaches: the upper, middle and lower one (Barcos et al., 2014).

1.5.2.1 The upper reaches

The Atlas Mountains are characterised by two main uplifting processes: thickening of the crust and thinning of the mantle lithosphere as a result of buoyant thermal anomaly during the Cenozoic (Babault et al., 2008). The upper reaches, encompassing the southern to southeastern foot slopes of the Middle Atlas and the northernmost flanks of the High Atlas, which are composed of Palaeozoic substratum affected by the Hercynian orogeny. Here, granites are overlain by Mesozoic evaporites and clastics as well as marine carbonates and shales (Jébrak et al., 1998; Arboleya et al., 2004; Bouabdli et al., 2005; Pastor et al., 2015). Nowadays, the northern High Atlas Mountains drained by the Moulouya and its tributaries are not glaciated, although the highest massifs and peaks bear witness of former glacial and periglacial activity (Awad, 1963). For instance, the north-facing slopes of the W-E striking Jbel Ayachi anticlinal ridge, which is located at the northernmost rim of the High Atlas Mountains and culminates at 3751 m a.s.l. (see the blue star in fig. 1.4), exhibits well-developed cirques filled with hummocky moraines and U-shaped valleys, whose flanks are extensively covered by large talus slopes (fig. 1.5). Unfortunately, a chronological framework for these features in this area is still lacking (Hughes et al., 2011).

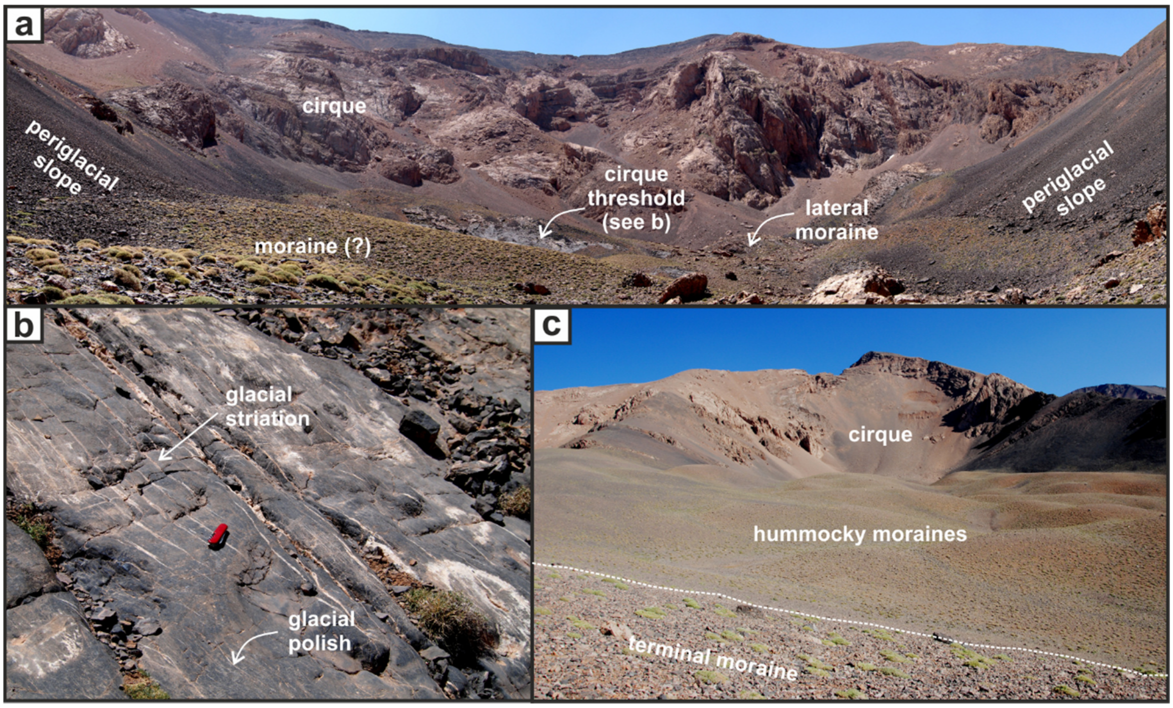

Fig. 1.5: Glacial landforms in the northern High Atlas Mountains at Jbel Ayachi (own observations 2014; Photographs: M. Bartz and G. Rixhon). a) Evidence of glacial and periglacial features are apparent at an elevation of ~3000 m a.s.l. (view towards southwest). b) Zoom in of the cirque threshold showing glacial striations and polish on the surface of the bedrock. c) Cirque formation at an elevation of ~2900 m a.s.l. with moraines in the apron (view towards southwest).

1.5.2.2 The middle reaches

The Moulouya drains the southeastern flanks of the Middle Atlas Mountains and the western margin of the Moroccan High Plateaus. The latter mostly consists of Late Cretaceous marine red clays and sandstones (Piqué et al., 2001). The Middle Atlas forms a thrust belt characterised by moderate crustal shortening (Arboleya et al., 2004), where the southeastern rim is composed of Jurassic rocks that overthrust Tertiary and Quaternary fanglomerates (Pastor et al., 2015).

In the Ksabi basin, Quaternary terrace staircases and stacked terraces co-exist (Raynal, 1961; Lefèvre, 1989; Kaemmerer and Revel, 1991). The Missour basin displays Quaternary fluvial terraces with associated incision rates of ~0.3 mm/a along the foreland folds (Pastor et al., 2015).

Glacial and periglacial features have also been observed in the middle reaches of the Moulouya River (see the two blue stars in fig. 1.4). The highest peaks of the Middle Atlas Mountains, namely the Jbel Bou Iblane (3340 m a.s.l.) and Jbel Bou Naceur (3310 m a.s.l.), exhibit evidence of stone polygons, solifluction, debris flow levees and rock glaciers (Raynal et al., 1953; Hughes et al., 2004, 2011; fig. 1.6). According to Awad (1963), the former equilibrium-line altitude (ELA) is estimated to have been at ~2800 m a.s.l. during the main phase of a glaciation. Terminal and lateral moraines as well as rock glaciers at the Jbel Bou Iblane and Jbel Bou Naceur, respectively, extend down to ~2100-2500 m a.s.l. (Raynal et al., 1953; Awad, 1963). Those former glacial and periglacial features in the Middle Atlas have not yet been dated.

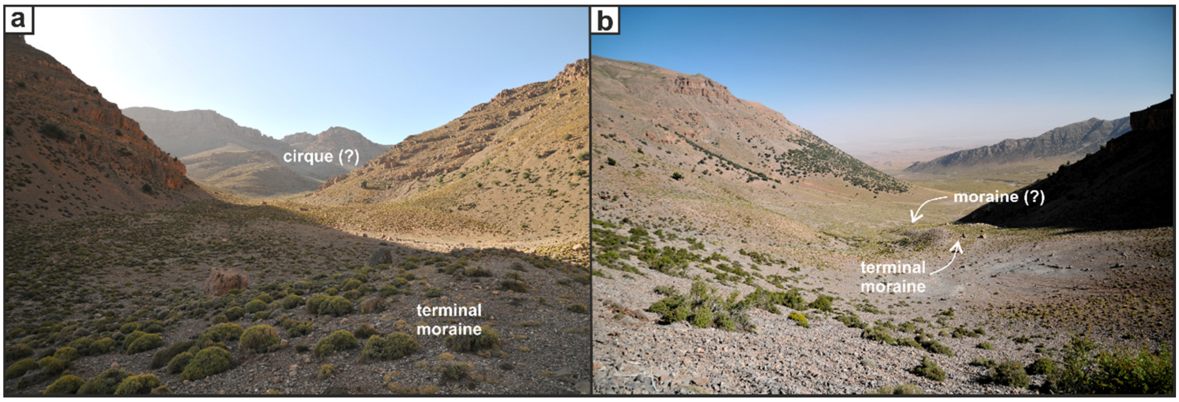

Fig. 1.6: Glacial features in the southern Middle Atlas Mountains at Jbel Bou Naceur (own observations 2013/2014; photographs: H. Brückner). a) view towards northeast/upslope; b) view towards southwest/downslope.

1.5.2.3 The lower reaches

The lowermost sedimentary basin, composed of the Zebra-Triffa plain and the Ouled Mansour plateau, is mostly filled with Neogene marine deposits (Ruellan, 1971; Boughriba et al., 2006). The synclinal depression is bordered by the anticlinal ridges of the Beni Snassen to the south (northernmost prolongation of the Middle Atlas Mountains) and the Kebdana to the north (easternmost part of the Rif Mountains). Both consist mainly of Mesozoic carbonate rocks, sandstone and slate formations (Ruellan, 1971; Khattach et al., 2004).

The ephemeral stream Wadi Selloum (~290 km²), a northern tributary of the Moulouya River (fig. 1.7; Barcos et al., 2014), drains the direct vicinity of the rock shelter of Ifri n'Ammar (34°47'03.68'' N 3°05'32.42'' W, elevation: 470 m a.s.l.; Nami and Moser, 2010). This area is exclusively composed of Mesozoic limestone and dolomite (Benjelloun et al., 1971).

Fig. 1.7: Study area of the lower Moulouya River in NE Morocco. The red rectangles refer to the two study sites, namely the ephemeral stream Wadi Selloum (left hand side) and the Moulouya fluvial terraces (right hand side). The white squares represent archaeological sites of the area (according to Nami and Moser, 2010; Linstädter et al., 2012a, 2012b, in press).

Glacial relict features have not yet been reported in the lower Moulouya catchment (Osmaston and Harrison, 2005); this is most likely due to the fact that the eastern Rif Mountains and the western Beni Snassen Massif lie beneath the former regional ELA (Hughes et al., 2011). While evidence of periglacial features have been observed at the Jbel Tidirhine (2456 m a.s.l.) in the middle Rif Mountains (Mensching, 1960), they are missing in the lower Moulouya catchment.

1.5.3 Archaeological background

1.5.3.1 North African prehistory

Many Palaeolithic and Epipalaeolithic sites have been excavated in North Morocco, covering time scales of the last 250 ka and representing the three main techno-complexes (Linstädter et al., 2012a): (i) Middle Palaeolithic, (ii) Upper Palaeolithic, and (iii) Epipalaeolithic. Prior to a brief overview of the different cultural systems in Pleistocene and Holocene times, it should be noted that since the C2 project focuses on relations between Europe and Northern Africa, the terminology used in this thesis is the one common in European archaeology. Therefore, the terms of Early, Middle and Late Palaeolithic are used, instead of Early, Middle and Late Stone Age which are more common on the African side (e.g., McBrearty and Brooks, 2000; Dörschner et al., 2016).

(i) The onset of the Middle Palaeolithic is assumed to be between 300 and 250 ka (Garcea, 2004). It corresponds to a crucial time period with regard to the dispersal of the AMH. This techno-complex is characterised by the absence of hand axes and the appearance of Levallois artefacts (Linstädter et al., 2012a).

(ii) The Upper Palaeolithic is mainly characterised by the Iberomaurusian hunter-gatherer culture; it most probably started during the last glacial maximum (LGM) ~20 ka BP (Linstädter, 2013). Significant changes happened at 16 ka BP in the Maghreb region, highlighted by thick accumulations of shell fragments referred to as “*Escargotière*”. These middens of snail shells are widespread in the circum-Mediterranean region, which was at that point characterised by collecting subsistence economies where land snails constituted an important aspect of diet (Lubell et al., 1976; Nami and Moser, 2010; Zielhofer, 2007; Linstädter, 2012a).

(iii) The Holocene Epipalaeolithic follows the Palaeolithic. Its final stage, characterised by an initial impact of early food producing groups, is also called “Epipaléolithique de transition” (Camps, 1974) or “Épipalaeolithique indifferencié” (Nami, 2008). In the current state of knowledge, the onset of Early Neolithic food production in NE Morocco dates back to 7.6 ka cal BP, therefore representing its earliest occurrence in North Africa (Linstädter et al., in press). In NE Morocco, several open-air sites (well-preserved in alluvial deposits of the Moulouya, e.g., Mtlili, Taoungat; fig. 1.7) as well as rock shelters (e.g., Ifri Oudadane, Hassi Ouenzga, Ifri n'Etsedda; fig. 1.7) provided Epipalaeolithic and Neolithic deposits (Linstädter et al., 2012a, in press).

The transition from the Late Neolithic to the not well represented Metal Ages dates back to ~4.1 ka cal BP (Linstädter et al., 2012b). Few open-air sites (e.g., Bouchih 1; fig. 1.7) have archaeological findings in overbank fines of the lower Moulouya River (Linstädter et al., 2012c).

With the beginning of the Islamic colonisation, archaeological remains were found in a greater extent, dating back to the time span 1.23±0.03 – 0.86±0.05 ka cal BP (fig. 1.7; Safsaf 3, 4, 5-4, 6 and Bouchih 2; Linstädter et al., 2012c). In contrast, remains of later colonisation periods – e.g., the French colonial era – are rather rare in NE Morocco.

1.5.3.2 The rock shelter of Ifri n'Ammar

Since 1995, a prehistoric research project has been carried out by a cooperation of the *Institut National des Sciences de l'Archéologie et du Patrimoine* (LN.5.A.P, Rabat) and the *Kommission für Archäologie Außereuropäischer Kulturen des Deutschen Archäologischen Instituts* (KAAK, Bonn).

The key settlement site of Ifri n'Ammar (fig. 1.8) is characterised by a detailed Middle Palaeolithic (Mousterian and Aterian) to Upper Palaeolithic (Iberomaurusian) stratigraphy (Nami and Moser, 2010). Two successions of Middle Palaeolithic layers, namely a lower sequence "*occupation inférieure"* and an upper sequence "*occupation supérieure"*, have as yet been unearthed. The horizons are separated by calcrete layers, void of any archaeological remains (Mikdad et al., 2000; Nami and Moser, 2010). Richter et al. (2010) dated several artefacts of burnt chert of the Middle Palaeolithic succession with TL dating techniques: the lower and upper sequences rendered TL ages between 171±12 – 145±9 ka and 130±8 – 83±6 ka, respectively. In addition to the use of TL dating, radiocarbon dating was applied to date the *occupation supérieure* beneath the Iberomaurusian stratigraphy; this resulted in ^{14}C-ages of 51.5±1.5 ka BP and 39.8±1.2 ka BP in the upper part (Moser, 2003; Linstädter et al., 2012a). Obviously, the radiocarbon ages demonstrate contradictions in comparison with the TL dating results (weighted mean TL age: 83±6 ka; Richter et al., 2010), which may simply be due to insolulable charcoal samples or even more probable in the upper dating limit of the radiocarbon dating technique (Richter et al., 2010; Rixhon et al., 2017a). The *occupation inférieure* complex is characterised by Middle Palaeolithic assemblages, including stemmed pieces (representing the so-called *Aterian* culture) (Nami and Moser, 2010). The same holds true for the assemblage above the calcrete layers (Nami and Moser, 2010).

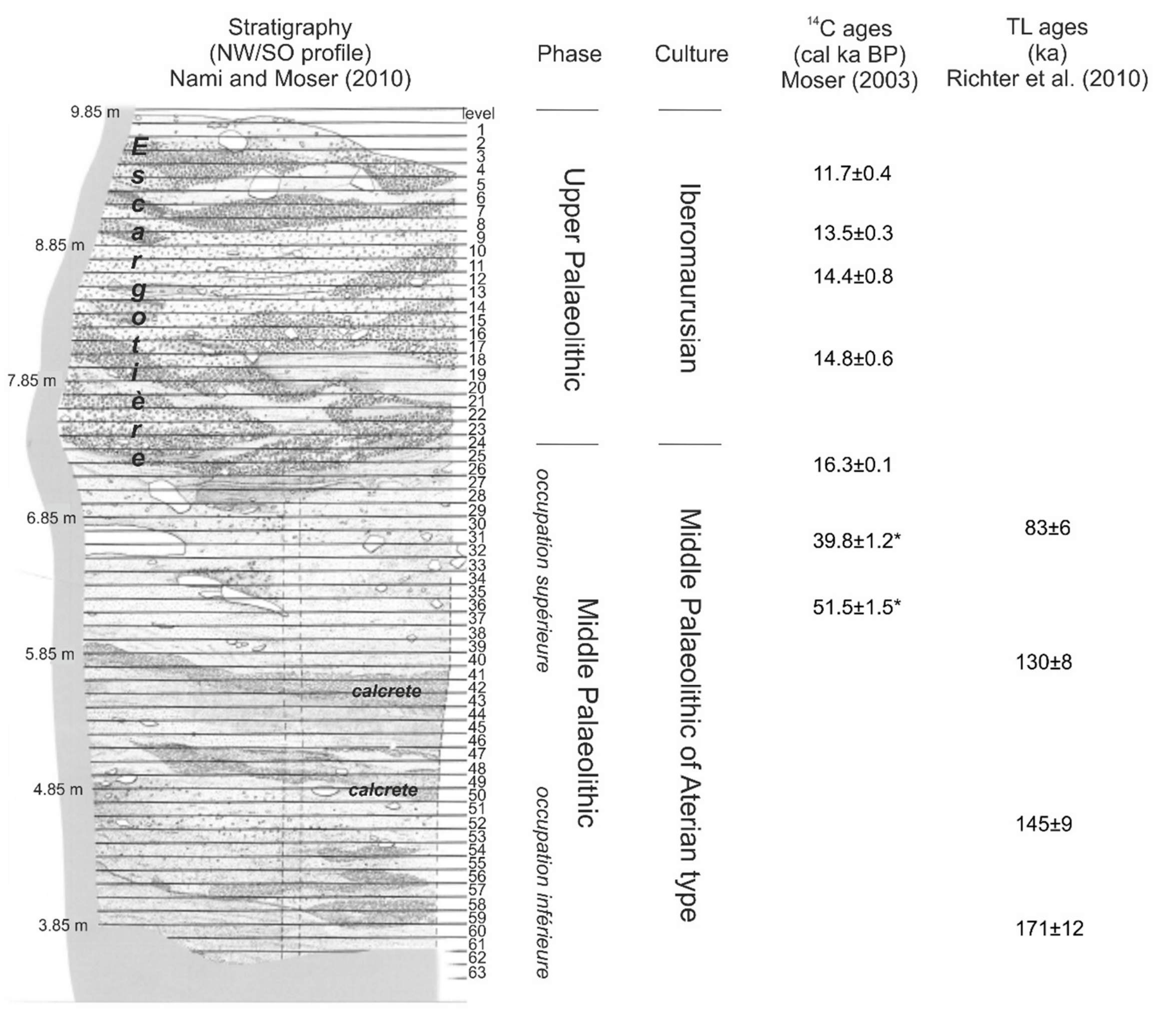

Fig. 1.8: Archaeological stratigraphy of the prehistoric rock shelter of Ifri n'Ammar showing chronologic information (further details about the data set can be found in Moser, 2003; Richter et al., 2010; Linstädter et al., 2012a). Thermoluminescence (TL) ages are presented at a 1σ-confidence interval, ^{14}C ages are shown with 2σ. Radiocarbon ages in the upper Middle Palaeolithic sequence (with asterisk) are uncalibrated (modified after Nami and Moser, 2010).

The upper part of the archaeological sequence (fig. 1.8) is represented by the Upper Palaeolithic Iberomaurusian culture. The transition layer between the Middle and the Upper Palaeolithic, a deep-reddish horizon, is called "*couche rouge*" (Moser, 2003). The subsequent stage (Late Iberomaurusian) shows gastropod-rich layers, the so-called *Escargotières*, ^{14}C-dated between 13.9±0.08 ka BP (16.8 – 16.5 ka cal BP) and 10.0±0.08 ka BP (11.3 – 12.1 ka cal BP) (Linstädter et al., 2012a; Moser, 2003). The lithic assemblage of the Ifri n'Ammar Iberomaurusian is dominated by backed bladelets. The spectrum of raw materials in the rock shelter is characterised by a diversity of chert varieties, chalcedon, limestone, quartz and sandstone due to raw material sources in the vicinity of this archaeological site (Nami and Moser, 2010). The Iberomaurusian deposit of Ifri n'Ammar correlates with the Iberomaurusian sequence of the neighbouring site Ifri el Baroud (Moser, 2003). Several findings of perforated gastropods and molluscs are interpreted as jewellery objects (Moser, 2003); they must, however, be distinguished from the small holes and slots in the tests which were manipulated by humans for better extracting the snail meat for consumption (Hutterer et al., 2014).

So far, the onsite archaeological sequence ends with the Upper Palaeolithic (Nami and Moser, 2010). As artefacts in disturbed top layers and surface finds suggest, Epipalaeolithic and Neolithic deposits might have existed in Ifri n'Ammar. However, proper deposits have not been preserved (pers. comm. J. Eiwanger, 2014).

Chapter 2

2 Luminescence dating of ephemeral stream deposits around the Palaeolithic site of Ifri n’Ammar (Morocco)

Melanie Bartz [a], Nicole Klasen [a], Anja Zander [a], Dominik Brill [a], Gilles Rixhon [a],
Martin Seeliger [a], Josef Eiwanger [b], Gerd-Christian Weniger [c], Abdeslam Mikdad [d],
Helmut Brückner [a]

[a] Institute of Geography, University of Cologne, Albertus-Magnus-Platz, 50923 Cologne, Germany
[b] Commission for Archaeology of Non-European Cultures (KAAK), Dürenstr. 35-37, 53173 Bonn, Germany
[c] Neanderthal Museum, Talstraße 300, 40822 Mettmann, Germany
[d] Institut National des Sciences de l'Archéologie et du Patrimoine (INSAP), 1, rue Ghandi, Rabat, Morocco

Abstract

The prehistoric site of Ifri n'Ammar is situated in northeastern Morocco, in the northern prolongation of the Middle Atlas Mountains. It is a key location in unravelling the history of anatomically modern humans (AMH) in northern Africa as it reveals Middle and Late Palaeolithic occupation phases since ~170 ka. Whilst the archaeological sequence within the rock shelter has been well studied, the timing of landscape dynamics around Ifri n'Ammar is still poorly understood. This study therefore aims to establish a detailed chronology of the Wadi Selloum profile at the apron of the shelter, based on optically stimulated luminescence (OSL) dating of ephemeral stream deposits. Coarse-grain quartz was used for single-grain and multiple-grain dating procedures to investigate the luminescence properties of these deposits and to get more accurate age information concerning the phases of human occupation. Continuous wave OSL (CW-OSL) revealed a dominant fast component for all quartz samples. The dose distribution of the uppermost samples showed overdispersion values >25% and significant positive skewness. We identified partial bleaching as the main source of scatter in the equivalent dose (De) distribution. The lowermost sample appeared to be close to signal saturation. The shapes of the dose response curve varied widely between aliquots and coarse quartz grains exhibited therefore very different dose saturation behaviours among aliquots. With fully saturated dose response curves (DRCs), meaningful D0 values were assumed for De estimation. The eight OSL samples yielded stratigraphically consistent ages ranging from 1.3 ± 0.2 ka to 76 ± 5 ka, thus reaching the Middle Palaeolithic period. Moreover, a pottery shard dated to 7.4 ± 0.6 ka (Early Neolithic period) by thermoluminescence (TL), perfectly matched the Holocene OSL samples extracted at the same depth of the profile. In summary, our results point to fluvial aggradation during OIS 5.1, the late glacial period, and the Holocene.

Keywords

OSL, TL, Wadi, Morocco, Dose saturation level

Published in *Quaternary Geochronology* 30 (2015), 460-465.
https://doi.org/10.1016/j.quageo.2015.02.012

Quaternary Geochronology 30 (2015) 460–465

Contents lists available at ScienceDirect

Quaternary Geochronology

journal homepage: www.elsevier.com/locate/quageo

Luminescence dating of ephemeral stream deposits around the Palaeolithic site of Ifri n'Ammar (Morocco)

Melanie Bartz [a, *], Nicole Klasen [a], Anja Zander [a], Dominik Brill [a], Gilles Rixhon [a], Martin Seeliger [a], Josef Eiwanger [b], Gerd-Christian Weniger [c], Abdeslam Mikdad [d], Helmut Brückner [a, *]

[a] *Institute of Geography, University of Cologne, Albertus-Magnus-Platz, 50923 Cologne, Germany*
[b] *Commission for Archaeology of Non-European Cultures (KAAK), Dürenstr. 35-37, 53173 Bonn, Germany*
[c] *Neanderthal Museum, Talstraße 300, 40822 Mettmann, Germany*
[d] *Institut National des Sciences de l'Archéologie et du Patrimoine (INSAP), 1, Rue Ghandi, Rabat, Morocco*

ARTICLE INFO

Article history:
Received 4 November 2014
Received in revised form
6 February 2015
Accepted 16 February 2015
Available online 17 February 2015

Keywords:
OSL
TL
Wadi
Morocco
Dose saturation level

ABSTRACT

The prehistoric site of Ifri n'Ammar is situated in northeastern Morocco, in the northern prolongation of the Middle Atlas Mountains. It is a key location in unravelling the history of anatomically modern humans (AMH) in northern Africa as it reveals Middle and Late Palaeolithic occupation phases since ~170 ka. Whilst the archaeological sequence within the rock shelter has been well studied, the timing of landscape dynamics around Ifri n'Ammar is still poorly understood. This study therefore aims to establish a detailed chronology of the Wadi Selloum profile at the apron of the shelter, based on optically stimulated luminescence (OSL) dating of ephemeral stream deposits. Coarse-grain quartz was used for single-grain and multiple-grain dating procedures to investigate the luminescence properties of these deposits and to get more accurate age information concerning the phases of human occupation. Continuous wave OSL (CW-OSL) revealed a dominant fast component for all quartz samples. The dose distribution of the uppermost samples showed overdispersion values >25% and significant positive skewness. We identified partial bleaching as the main source of scatter in the equivalent dose (D_e) distribution. The lowermost sample appeared to be close to signal saturation. The shapes of the dose response curve varied widely between aliquots and coarse quartz grains exhibited therefore very different dose saturation behaviours among aliquots. With fully saturated dose response curves (DRCs), meaningful D_0 values were assumed for D_e estimation.

The eight OSL samples yielded stratigraphically consistent ages ranging from 1.3 ± 0.2 ka to 76 ± 5 ka, thus reaching the Middle Palaeolithic period. Moreover, a pottery shard dated to 7.4 ± 0.6 ka (Early Neolithic period) by thermoluminescence (TL), perfectly matched the Holocene OSL samples extracted at the same depth of the profile. In summary, our results point to fluvial aggradation during OIS 5.1, the late glacial period, and the Holocene.

1. Introduction

The impact of environmental changes on the emergence and dispersal of anatomically modern humans (AMH) is particularly important in North Africa, since the Straits of Gibraltar might have served as western migration route from Africa to Europe (Linstädter et al., 2012). The prehistoric rock shelter of Ifri n'Ammar in NE Morocco (Fig. 1a) reveals discontinuous Middle and Late Palaeolithic occupation phases since ~170 ka (Moser, 2003; Nami and Moser, 2010; Richter et al., 2010), thereby constituting one of the oldest AMH settlement sites in this part of the continent. Contrasting with the archaeological background, the Pleistocene and Holocene palaeoenvironmental conditions in this area are as yet poorly reconstructed.

Given that the ephemeral stream deposits of the Wadi Selloum represent the only available archive in the direct vicinity of the rock shelter, this study aimed at evaluating the suitability of such

---

* Corresponding authors.
E-mail addresses: M.Bartz@uni-koeln.de (M. Bartz), h.brueckner@uni-koeln.de (H. Brückner).

http://dx.doi.org/10.1016/j.quageo.2015.02.012
1871-1014/© 2015 Elsevier B.V. All rights reserved.

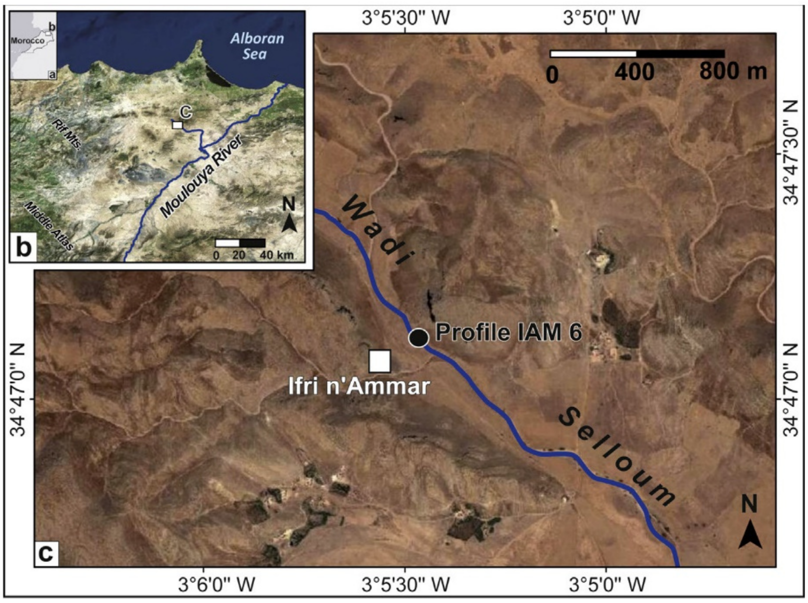

Fig. 1. a and b: Study area in north-eastern Morocco; c: Upper catchment area of the Wadi Selloum with location of the river bank profile IAM 6 situated at the apron of the prehistoric site of Ifri n'Ammar (black circle and white square, respectively) (based on Esri 2014).

sediments to establish a robust chronology on off-site archives. We applied optically stimulated luminescence (OSL) dating, a technique that has been widely used for dating fluvial sediments (e.g. Wallinga, 2002; Rittenour, 2008). However, especially when working on fluvial systems characterised by episodic flow regimes such as ephemeral streams (Abdalla et al., 2014), complex luminescence characteristics must often be taken into account. Whilst Bubenzer et al. (2007) yielded consistent OSL dating results for fluvio-lacustrine sediments of Wadi Asfura (Egypt) by using small aliquots to account for partial bleaching, Klasen et al. (2013) could not determine the particular contribution of partial bleaching, heterogeneous beta microdosimetry and weak OSL signals to the D_e scatter within sediments from Wadi Sabra (Jordan). A second challenge for dating Pleistocene fluvial sediments is the comparably low saturation level of the quartz fast component (Wintle and Murray, 2006). McLaren et al. (2004) applied optical dating to Wadi Faynan (Jordan) sediments and showed minimum ages of some samples due to quartz saturation. The saturation level of quartz was investigated by Timar-Gabor et al. (2012) and Timar-Gabor and Wintle (2013), who demonstrated the significance of fully saturated dose response curves (DRCs) to determine the quartz saturation level D_0.

Our study is based on eight fluvial samples from a profile at the apron of Ifri n'Ammar, focussing on (i) the investigation of potential sources of scatter within the D_e distributions; (ii) approaches to assess the saturation level of the oldest quartz sample; and (iii) the suitability of the Wadi Selloum deposits as potential archive for reconstructing local palaeoenvironmental changes.

2. Study area, archaeological background and sampling strategy

The prehistoric site of Ifri n'Ammar (34°47′03.68″ N 3°05′32.42″ W, elevation: 470 m above sea level) is located in the northern prolongation of the Middle Atlas Mountains in NE Morocco (Fig. 1a, b). The archaeological layers of the rock shelter reveal discontinuous phases of modern human settlements during the last ~170 ka. The lower part of a Middle Palaeolithic sequence is dated from 171 ± 12 ka to 83 ± 6 ka by TL dating of heated flint (Richter et al., 2010). The uppermost part of the Middle Palaeolithic sequence has been radiocarbon dated between 51.5 ± 1.3 ka BP and 38.9 ± 2.0 ka BP while a Late Palaeolithic sequence related to the Iberomaurusian culture is radiocarbon dated between 13.9 ± 0.08 ka BP and 10.0 ± 0.08 ka BP (Moser, 2003; Linstädter et al., 2012).

The semi-arid climate of the region is reflected by the hydrological regime, dominated by episodic flash floods, which are characterised by rapid flow velocities and high sediment discharges (Abdalla et al., 2014). The ~35 km-long Wadi Selloum, a western tributary of the Moulouya River (Fig. 1b), drains the foothills of the Ifri n'Ammar rock shelter in a south-eastern flow direction (Fig. 1c). The coarse fraction of these ephemeral stream deposits is exclusively composed of limestone and dolomite originating from the Mesozoic formations (Atlas rock series) outcropping in the catchment (Abdellaziz Benjelloun et al., 1971), whereas the presence of quartz in the fine-grained fraction is most probably the result of wind transport from the Moulouya basin (Jébrak et al., 1998).

In this study, we investigated a 4.9 m-high profile displaying ephemeral stream deposits (IAM 6), which is located ~150 m to the north-east of the rock shelter (Fig. 1c). The profile is characterised by the alternation of coarse- and fine-grained sediments and was thus subdivided into four units (Fig. 2). Unit 1 (4.90–4.10 m below surface, b.s.) and unit 4 (1.84–0 m b.s.) are both composed of homogeneous silty fine sand. In contrast, unit 2 (4.10–2.18 m b.s.) is characterised by heterogeneous coarse-grained accumulations and exhibits a fining-upward tendency. The gravel-dominated unit 3 (2.18–1.84 m b.s.) shows sharp boundaries to the lower and upper units. Altogether eight OSL samples were collected from IAM 6: C-L3395 from unit 1, C-L3393 from unit 2, and C-L3392 to C-L3396 as well as C-L3544 and C-L3545 from unit 4 (Fig. 2). Additionally, a pottery shard extracted from unit 4 was used for age control on the basis of TL dating (Fig. 2). To evaluate the bleaching characteristics of the ephemeral stream deposits, a modern sample from the active Wadi Selloum bed was collected.

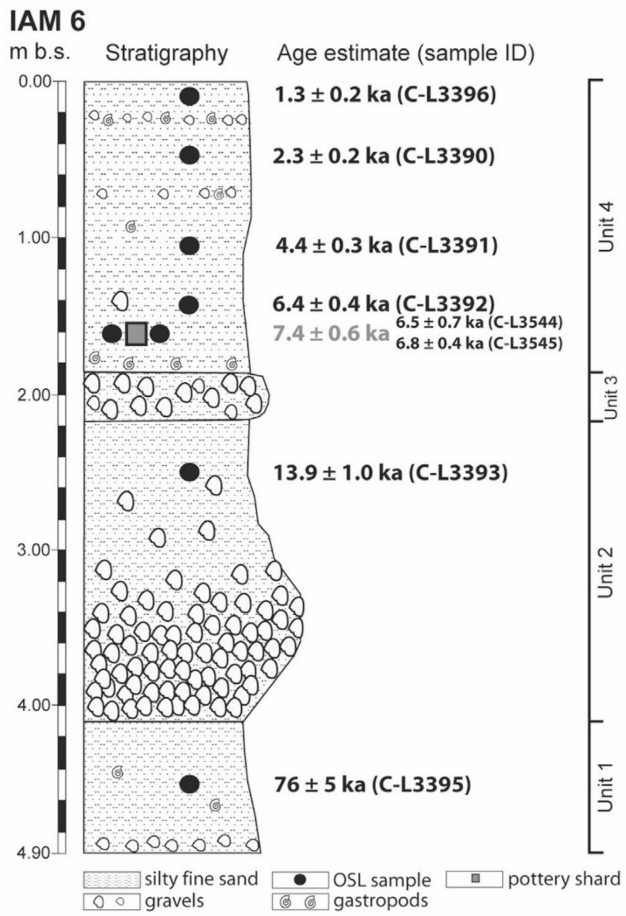

Fig. 2. Stratigraphy of profile IAM 6 divided in four sedimentary units (1–4, from base to top), with depths, age estimates and ID's of the eight OSL samples and of the TL-dated pottery shard.

3. Methods

3.1. Sample preparation and measurement equipment

Quartz grains (100–150 μm) for OSL were separated using solutions of sodium polytungstate ($\rho_1 = 2.62$ g/cm^3, $\rho_2 = 2.68$ g/cm^3) after leaching with H_2O_2, HCl and $Na_4P_2O_7$. Afterwards, the quartz grains were etched with hydrofluoric acid (40% for 40 min) plus a final HCl (10% for 1 h) wash. TL sample preparation was carried out on the polymineralic 4–11 μm grain-size fraction following the procedure described in Stoneham (1991). High-resolution γ-spectrometry using a high-purity germanium detector was carried out for dose rate determination, using the conversion factors of Adamiec and Aitken (1998) and alpha and beta attenuation factors of Bell (1980) and Mejdahl (1979). The contribution of cosmic dose rate was assessed following the approach of Prescott and Hutton (1988, 1994). To account for attenuation of ionising radiation by pore water, in-situ water contents of 4–12% were used. The α-efficiency for the TL sample was determined using a ^{241}Am source delivering an effective α-dose rate of ~10 Gy/min, after annealing signals at 480 °C for 60 s. The internal beta dose rate for the pottery shard was determined by means of beta counting on fine grained material, whereas the internal alpha dose rate was not measured.

Automated Risø TL/OSL DA 15 readers equipped with ^{90}Sr/^{90}Y beta sources were used for both (i) OSL and (ii) TL measurements: (i) Quartz multiple-grain signals were stimulated for 40 s using blue LEDs (470 ± 20 nm) and detected through a Hoya U340 glass filter (7.5 mm), whereas quartz single grains were stimulated with a green laser (532 nm) for 2 s; (ii) for TL measurements a combination of Schott BG39 2 mm and Corning 7–59 4 mm filters with a max. peak transmission at ~380 nm.

3.2. OSL and TL measurement procedures

The single-aliquot-regenerative-dose (SAR) approach of Murray and Wintle (2003) was applied for D_e determination of the quartz samples and measured aliquots had to fulfil the following SAR rejection criteria: (i) test dose error $\leq$ 10%; (ii) recuperation <5% of the sensitivity-corrected natural OSL signal; (iii) recycling ratio between 0.9 and 1.1 (for single grains from 0.8 to 1.2); (iv) IR depletion ratio between 0.9 and 1.1 and (v) $D_e < 2^*D_0$.

The signal used for D_e assessment is based on the initial part of the decay curve (0–0.8 s) after subtraction of a late background (36–40 s). Additional early background subtraction with intervals of 0–0.5 s (signal) and 0.5–1.8 s (background) to maximise the influence of the fast component (Ballarini et al., 2007; Cunningham and Wallinga, 2010) was applied to all samples. Laboratory doses of up to 1000 Gy were applied to two aliquots of sample C-L3395 to reach the absolute saturation level which is required for a reliable determination of D_0 (Timar-Gabor et al., 2012; Timar-Gabor and Wintle, 2013). For D_e determination, 80–100 multiple-grain aliquots (1 mm) and 2640 single grains (for sample C-L3396) were measured.

Preheat-plateau tests and dose recovery tests with increasing temperatures between 180 and 280 °C (held for 10 s) in combination with a cut heat 20 °C below preheat temperature were performed for all samples to determine an appropriate preheat temperature (2 mm, 10 aliquots per temperature step). Dose recovery tests were conducted using blue-LED stimulation at 25 °C for 100 s for signal resetting. To investigate the OSL signal components, fitting of continuous wave (CW-OSL) OSL curves was applied. CW-OSL measurements were carried out on three aliquots per sample with a continuous light intensity of 32 mW/cm^2 for 40 s at 125 °C. The CW-OSL curves were fitted using the software package R (Kreutzer et al., 2012). For TL dating (Zimmermann, 1971) of the pottery shard, a multiple-aliquot additive dose-protocol (MAAD) was used. Signals were stimulated by heating to 480 °C at a rate of 5 °C/s after a preheat at 220 °C for 120 s. For alpha efficiency determination, six aliquots were annealed at 480 °C for 60 s and received an α-dose of 66.4 Gy before the MAAD-TL protocol was applied.

4. Results

4.1. Luminescence properties

Based on preheat-plateau tests, appropriate preheat temperatures between 200 and 240 °C were selected for further SAR procedures (Tab. S1). The laboratory doses were recovered with measured/given dose ratios of 0.91–1.05, with overdispersion values <5% (Tab. S1). Transfer of charge to optically sensitive traps due to preheating prior to optical stimulation was negligible, and IR depletion tests (Duller, 2003) showed no influence of feldspar contamination. Oriented on the trap parameters and mean photo-ionisation cross-sections given by Jain et al. (2003) and Singarayer and Bailey (2003), the CW-OSL curves revealed a dominant fast component contributing ~85% to the total OSL signal (Fig. 3). Only sample C-L3395 yielded a weaker fast component, contributing only ~65% to the total signal, though early background subtraction was used for further D_e estimation of sample C-L3395.

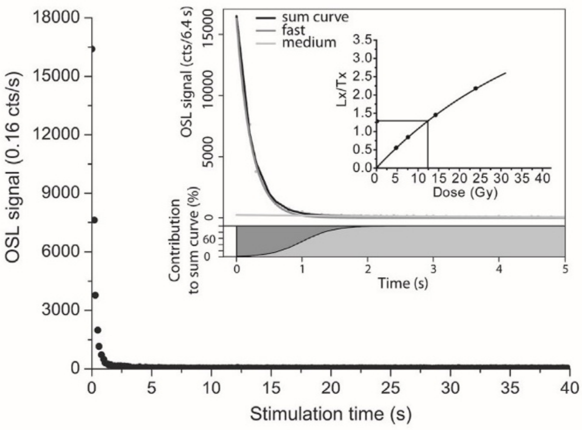

Fig. 3. OSL signal intensity of sample C-L3392. Continuous wave-OSL (CW-OSL, insert) was applied on three 1 mm aliquots and yielded a dominant fast component. The dose response curve (insert) was best fitted by a single saturation exponential function of a natural 1 mm aliquot.

The dose response curves (DRCs) of the samples were best fitted by a single saturation exponential function. The quartz grains for sample C-L3395 exhibited different dose saturation levels (D_0) for OSL signals among aliquots with variations from 68 Gy to 164 Gy (n = 63; average = 92 Gy). Based on this, c. 40% of the measured aliquots lay above 2*D_0 (Fig. 4a). Testing the dependency of the D_0 value on fully saturated DRCs of two natural aliquots (Timar-Gabor et al., 2012; Timar-Gabor and Wintle, 2013), revealed D_0 values of 80 Gy and 90 Gy (Fig. 4b).

Single-grain measurements of sample C-L3396 have shown that only 3% (79 grains) of the quartz grains give OSL signals >80 cts., including ~23% (18 grains) with sensitivity-corrected OSL signals that do not intersect the dose response curve (class 3 grains of Yoshida et al., 2000). In total, only 50 of the 2640 measured grains passed the SAR criteria.

Radionuclide data for all samples are presented in Tab. S2. No radioactive disequilibrium was found in any sample, including the surrounding material of the pottery shard. An alpha-efficiency of 0.13 ± 0.02 was determined for the polymineral fine grain material of the shard.

4.2. Equivalent dose distributions and age model results

The D_e distributions (Tab. S3) varied significantly in type and form: (i) C-L3396 and C-L3390 displayed asymmetric dose distributions with significant positive skewness and overdispersion values >25%. In case of sample C-L3396 (Fig. 5a), multiple-grain and single-grain measurements yielded overdispersion values >60% and positive skewness. The overdispersion of the modern sample was >80% (1 Gy–46 Gy, central dose = 10.9 ± 1.6 Gy; Fig. 5b); (ii) samples C-L3391 to C-L3395 exhibited little scatter. Consequently, the minimum age model (MAM, Galbraith et al., 1999) was used for D_e calculation of samples with high overdispersion and positive skewness, and the central age model (CAM, Galbraith et al., 1999) was applied for samples with a Gaussian-like D_e distribution. According to Arnold and Roberts (2009), an overdispersion value of 20% should be expected for single-grain distributions of well-bleached samples; this value was assessed for D_e calculations with the MAM estimations (Tab. S3). The four uppermost samples C-L3396 to C-L3392, yielded Holocene ages from 1.3 ± 0.2 ka to 6.4 ± 0.4 ka. The OSL ages of samples C-L3544 and C-L3545 (6.5 ± 0.7 ka and 6.8 ± 0.4 ka) overlap with the TL age of the pottery shard (7.4 ± 0.6 ka). The two lowermost samples C-L3393 and C-L3395 yielded ages of 13.9 ± 1.0 ka and 76 ± 5 ka.

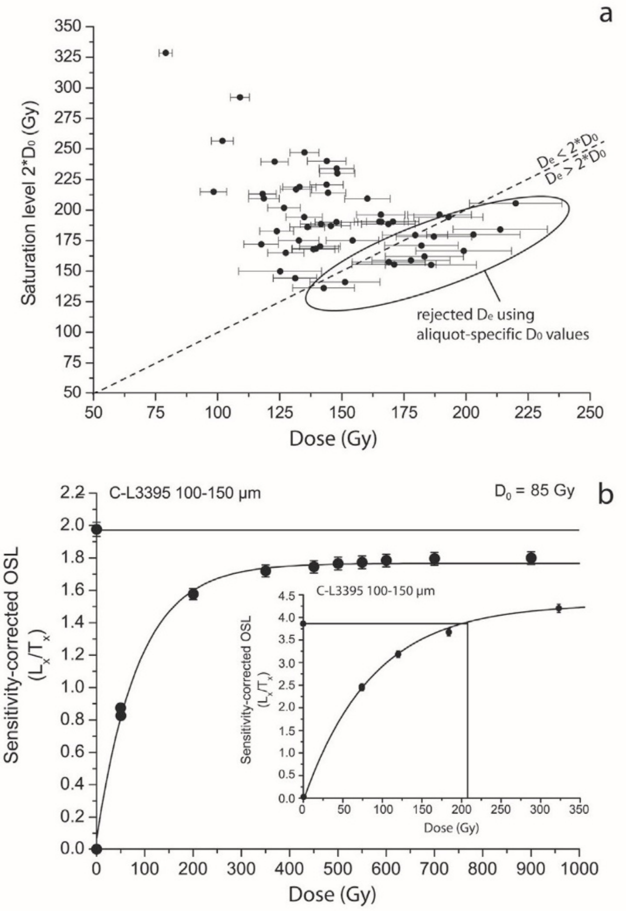

Fig. 4. a: Signal saturation behaviour of sample C-L3395 showing aliquot-specific D_0 and D_e values; b: Dose response curves (DRCs) of sample C-L3395 constructed up to 1000 Gy (two aliquots) and 320 Gy (insert). The curves were fitted by a single saturation exponential function using early background subtraction for D_e determination.

5. Discussion

5.1. Suitability of OSL properties for dating ephemeral stream deposits

5.1.1. Source of scatter in D_e distributions

The two uppermost samples C-L3396 and C-L3390 revealed significant scatter within their D_e distributions (Fig. 5a). Since the distribution of the dose recovery results yielded no influence of significant internal sources of scatter (Tab. S1), external sources of scatter must be taken into account. For fluvial samples, in particular partial bleaching may result in an apparent overestimation of the true burial dose (e.g. Olley et al., 1998). The interpretation of scatter as the result of partial bleaching in case of the uppermost samples C-L3396 and C-L3390 is backed by statistical parameters such as positive skewness and high overdispersion (Arnold et al., 2007). This statement is supported by 23% of class 3 grains (Yoshida et al., 2000) in the single-grain data set of sample C-L3396. Class 3 grains will give rise to measured palaeodoses and, thus, may cause overestimation of the burial age if multiple-grain aliquots are used (Yoshida et al., 2000). In addition, the comparison of multiple-grain and single-grain D_e values calculated with the MAM and the CAM

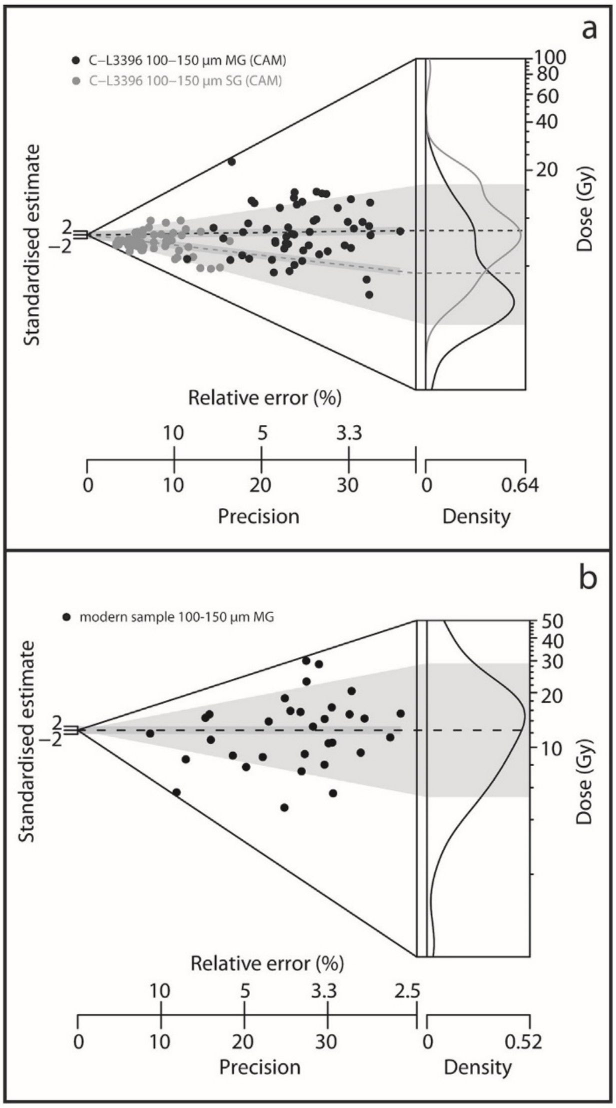

Fig. 5. Equivalent dose (D_e) distributions of a) sample C-L3396 and b) modern sample displayed as a combination of a radial plot and a kernel density estimate (KDE) plot (Galbraith and Green, 1990) generated as abanico plot (R luminescence package Kreutzer et al., 2012); the linking of both plots provides the ability to establish a visual correlation between error characteristics (radial plot) and dose frequency (KDE, on the z-axis of the radial plot). Individual D_e values of 1 mm multiple-grain (MG, black circles) aliquots and single grains (SG, grey circles) are illustrated. The dashed lines illustrate the central age D_e (CAM).

showed significantly higher D_e values for multiple-grain aliquots. Therefore, we regarded the MAM to be the appropriate age model to calculate the equivalent dose.

Considering the residual doses of the modern analogue as high as 46 Gy (Fig. 5b), partial bleaching is not necessarily trivial for all samples, but influenced especially the younger samples, because partial bleaching is insignificant compared to the large doses that the samples have received since burial (Jain et al., 2004; Murray et al., 2012). This is verified by the Gaussian-like D_e distribution of the other OSL samples, pointing to complete bleaching prior to deposition.

5.1.2. *The saturation level of coarse-grain quartz*

The saturation characteristics of natural sample C-L3395 were investigated. According to Wintle and Murray (2006), equivalent doses higher than 2^*D_0 are affected by large uncertainties and should be interpreted carefully. However, to guarantee a meaningful rejection of D_e values from the distribution, D_0 has to be assessed properly. For standard D_e measurements, regenerative doses up to 320 Gy were used and yielded significant inter-aliquot variations in dose saturation behaviour (Fig. 4a) due to differences in the OSL decay curves and DRCs as observed by Jacobs et al. (2008). However, according to Timar-Gabor et al. (2012) and Timar-Gabor and Wintle (2013), appropriate D_0 values are only achieved on the basis of sufficiently high regenerative doses that guarantee fully saturated DRCs (Fig. 4b). For sample C-L3395, signal saturation was reached at ~500 Gy and revealed D_0 values of ~85 Gy (two aliquots, Fig. 4b) which is not significantly different compared to the average D_0 value of ~92 Gy from aliquot-specific standard D_e measurements. Aliquot-specific D_0 values cannot be used reliably because of the high variation in non-saturated DRCs and hence changing saturation levels. Therefore we used an average D_0 value of 85 Gy as rejection criterion. However, a lot of subsamples had to be rejected as their D_e values were higher than 2^*D_0 (Fig. 4a). Accordingly, the central D_e of 135 Gy and the estimated age of 76 ± 5 ka of sample C-L3395 probably tend to underestimate the real burial age.

5.2. *Wadi Selloum as palaeoenvironmental archive — first implications*

OSL ages obtained on the ephemeral stream deposits are consistent with the stratigraphy (Fig. 2), whereas gaps in the chronology may be probably related to enhanced erosion phases during flash flood activity. Fine-grained deposits of the lowermost unit 1 were dated to at least 76 ± 5 ka (C-L3395) and thus point to deposition occurring during OIS 5.1. The following hiatus of ~60 ka may be correlated to the ~1.9 m-thick, clast-supported layer at the base of unit 2, although the latter could not be dated. Its deposition may be associated either with a single large event or with a period of increased flash flood activity during the last glacial cycle. The 13.9 ± 1.0 ka age of sample C-L3393 indicates deposition of the upper part of unit 2 during the late glacial period and also brackets the formation of the coarse-grained unit 3 during the Late Pleistocene/Early Holocene time span (Fig. 2). The sharp boundary at the base of unit 3 points to an erosional discordance that may be related to one (or several) flash flood event(s). The uppermost 2 m of the homogeneous, fine-grained unit 4 were deposited between 6.4 ± 0.4 ka and 1.3 ± 0.2 ka (C-L3392 to C-L3396). In addition, the concordance between the TL-dated pottery shard (7.4 ± 0.6 ka) and the OSL ages of the fluvial sediments extracted at the same depth further supports the reliability of the OSL chronology (Fig. 2).

Covering the period of at least the last 75 ka, the upper deposits of the Wadi Selloum seem representing a suitable off-site archive to establish chronological correlations with the Middle and Upper Palaeolithic sequences of Ifri n'Ammar (Moser, 2003; Richter et al., 2010; Linstädter et al., 2012). As the base of unit 1 and its contact to the underlying Mesozoic limestone bedrock lies below the current bed of the Wadi Selloum, the existing chronology may even be extended to reach older Pleistocene sediments. Furthermore, the discontinuous sedimentation record of erosion and accumulation phases illustrates fluctuating palaeoenvironmental conditions in this region of NE Morocco.

6. **Conclusion**

Partial bleaching and signal saturation represent the main challenges for OSL-dating the Late Pleistocene quartz samples from the ephemeral stream deposits of Wadi Selloum. Single-grain measurements in combination with the minimum age model (MAM) were successfully applied to cope with partial bleaching affecting the youngest sediments. Careful investigation of the oldest sample, which almost reached saturation, showed that a meaningful D_e can be estimated if the D_0 values are properly assessed. Nevertheless, the burial age of this sample may be underestimated due to the rejection of doses higher than the saturation level. Our consistent OSL age sequence obtained on the Wadi Selloum deposits and successfully checked with a TL-dated pottery shard embedded in the profile provides the first chronological framework from off-site archives located in the direct vicinity of Ifri n'Ammar. Though affected by long time hiatuses, these sediments record (at least) the last 75 ka and may therefore be used to establish chronological correlations with the Middle and Upper Palaeolithic sequences of the rock shelter. In the near future, supplementary sedimentological and geochemical analyses, along with further luminescence age estimates from other profiles, will be carried out on these ephemeral stream sediments. Altogether, these new data should ideally allow us to identify palaeoenvironmental conditions favourable (or not) to human occupation in Ifri n'Ammar.

Acknowledgements

This project is affiliated to the CRC 806 “Our way to Europe”, which is generously funded by the German Research Foundation (DFG) (CRC 806). The support by the “Institut National des Sciences de l'Archéologie et du Patrimoine du Maroc” (INSAP) and by the “Commission for Archaeology of Non-European Cultures” (KAAK) of the German Archaeological Institute (DAI) is gratefully acknowledged. We thank the anonymous reviewer for the constructive comments that helped to improve the paper.

Appendix A. Supplementary data

Supplementary data related to this article can be found at http://dx.doi.org/10.1016/j.quageo.2015.02.012.

References

Abdalla, F., El Shamy, I., Bamousa, A.O., Mansour, A., Mohamed, A., Tahoon, M., 2014. Flash floods and groundwater recharge potentials in arid land alluvial basins, Southern Red Sea Coast, Egypt. Int. J. Geosci. 5, 971–982.

Abdellaziz Benjelloun, S.E., Douieb, M., Saadi, M., Ennadifi, Y., 1971. Carte Géol. du Maroc. 167 (1), 100000 (Tistoutine).

Adamiec, G., Aitken, M., 1998. Dose rate conversion factors: update. Anc. TL 16, 37–50.

Arnold, L.J., Bailey, R.M., Tucker, G.E., 2007. Statistical treatment of fluvial dose distributions from southern Colorado arroyo deposits. Quat. Geochronol. 2, 162–167.

Arnold, L.J., Roberts, R.G., 2009. Stochastic modelling of multi-grain equivalent dose (D_e) distributions; implications for OSL dating of sediment mixtures. Quat. Geochronol. 4, 204–230.

Ballarini, M., Wallinga, J., Wintle, A.G., Bos, A.J.J., 2007. A modified SAR protocol for optical dating of individual grains from young quartz samples. Radiat. Meas. 42, 360–369.

Bell, W.T., 1980. Alpha dose attenuation in quartz grains for thermoluminescence dating. Anc. TL 12, 4–8.

Bubenzer, O., Hilgers, A., Riemer, H., 2007. Luminescence dating and archaeology of Holocene fluvio-lacustrine sediments of Abu Tartur, Eastern Sahara. Quat. Geochronol. 2, 317–321.

Cunningham, A.C., Wallinga, J., 2010. Selection of integration time intervals for quartz OSL decay curves. Quat. Geochronol. 5 (6), 657–666.

Duller, G.A.T., 2003. Distinguishing quartz and feldspar in single grain luminescence measurements. Radiat. Meas. 37, 161–165.

Esri, 2014. DigitalGlobe, Earthstar Geographics, CNES/Airbus DS, GeoEye, USDA FSA, USGS, Getmapping, Aerogrid, IGN, IGP, Swisstopo, and the GIS User Communit.

Galbraith, R.F., Green, P.F., 1990. Estimating the component ages in a finite mixture. Nucl. Tracks Radiat. Meas. 17 (3), 197–206.

Galbraith, R.F., Roberts, R.G., Laslett, G.M., Yoshida, H., Olley, J.M., 1999. Optical dating of single and multiple grains of quartz from Jinmium rock shelter, northern Australia: part I, experimental design and statistical models. Archaeometry 41 (2), 339–364.

Jacobs, Z., Wintle, A.G., Roberts, R.G., Duller, G.A.T., 2008. Equivalent dose distributions from single grains of quartz at Sibudu, South Africa: context, causes and consequences for optical dating of archaeological deposits. J. Archaeol. Sci. 35, 1808–1820.

Jain, M., Murray, A.S., Bøtter-Jensen, L., 2003. Characterisation of blue-light stimulated luminescence components in different quartz samples implications for dose measurement. Radiat. Meas. 37, 441–449.

Jain, M., Murray, A.S., Bøtter-Jensen, L., 2004. Optically stimulated luminescence dating: how significant is incomplete light exposure in fluvial environments? Quaternaire 15 (1–2), 143–157.

Jébrak, M., Marcoux, É., Nasloubi, M., Zaharaoui, M., 1998. From sandstone- to carbonate-hosted stratabound deposits: an isotope study of galena in the Upper-Moulouya District (Morocco). Miner. Depos. 33, 406–415.

Klasen, N., Hilgers, A., Schmidt, C., Bertrams, M., Schyle, D., Lehmkuhl, F., Richter, J., Radtke, U., 2013. Optical dating of sediments in Wadi Sabra (SW Jordan). Quat. Geochronol. 18, 9–16.

Kreutzer, S., Schmidt, C., Fuchs, M.C., Dietze, M., Fischer, M., Fuchs, M., 2012. Introducing an R package for luminescence dating analysis. Anc. TL 30 (1), 1–8.

Linstädter, J., Eiwanger, J., Mikdad, A., Weniger, G.-C., 2012. Human occupation of Northwest Africa: a review of Middle Palaeolithic to Epipalaeolithic sites in Morocco. Quat. Int. 274, 158–174.

McLaren, S.J., Gilbertson, D.D., Grattan, J.P., Hunt, C.O., Duller, G.A.T., Barker, G.A., 2004. Quaternary palaeogeomorphologic evolution of the Wadi Faynan area, southern Jordan. Palaeogeogr. Palaeoclimatol. Palaeoecol. 205, 131–154.

Mejdahl, V., 1979. Thermoluminescence dating: beta-dose attenuation in quartz grains. Archaeometry 21, 61–72.

Moser, J., 2003. L'Ibéromaurusien. AVA-Forschungen Band 8. La Grotte d'Ifri n'Ammar, Tome 1. Linden Soft.

Murray, A.S., Wintle, A.G., 2003. The single aliquot regenerative dose protocol: potential for improvements in reliability. Radiat. Meas. 37, 377–381.

Murray, A.S., Thomsen, K.S., Masuda, N., Buylaert, J.P., Jain, M., 2012. Identifying well-bleached quartz using the different bleaching rates of quartz and feldspar luminescence signals. Radiat. Meas. 47, 688–695.

Nami, M., Moser, J., 2010. La grotte d'Ifri n'Ammar. Le Paléolithique moyen. Forschungen zur Archäologie Außereuropäischer Kulturen, 9. Reichert Verlag, Wiesbaden.

Olley, J., Caitcheon, G., Murray, A., 1998. The distribution of apparent dose as determined by optically stimulated luminescence in small aliquots of fluvial quartz: implications for dating young sediments. Quat. Sci. Rev. 17 (11), 1033–1040.

Prescott, J.R., Hutton, J.T., 1988. Cosmic ray and gamma ray dosimetry for TL and ESR. Nucl. Tracks Radiat. Meas. 14 (1/2), 223–227.

Prescott, J.R., Hutton, J.T., 1994. Cosmic ray contributions to dose rates for luminescence and ESR dating: large depths and long-term time variations. Radiat. Meas. 23 (2/3), 497–500.

Richter, D., Moser, J., Nami, M., Eiwanger, J., Mikdad, A., 2010. New chronometric data from Ifri n'Ammar (Morocco) and the chronostratigraphy of the Middle Palaeolithic in the Western Maghreb. J. Hum. Evol. 59 (6), 672–679.

Rittenour, T.M., 2008. Luminescence dating of fluvial deposits: applications to geomorphic, palaeoseismic and archaeological research. Boreas 37, 613–635.

Singarayer, J.S., Bailey, R.M., 2003. Further investigations of the quartz optically stimulated luminescence components using linear modulation. Radiat. Meas. 37, 451–458.

Stoneham, D., 1991. Authenticity testing. In: Göksu, H.Y., et al. (Eds.), Scientific Dating Methods, pp. 175–192.

Timar-Gabor, A., Vasiliniuc, S., Vandenberghe, D.A.G., Cosma, C., Wintle, A.G., 2012. Investigations into the reliability of SAR-OSL equivalent doses obtained for quartz samples displaying dose response curves with more than one component. Radiat. Meas. 47, 740–745.

Timar-Gabor, A., Wintle, A.G., 2013. On natural and laboratory generated dose response curves for quartz of different grain sizes from Romanian loess. Quat. Geochronol. 18, 34–40.

Wallinga, J., 2002. Optically stimulated luminescence dating of fluvial deposits: a review. Boreas 31, 303–322.

Wintle, A.G., Murray, A., 2006. A review of quartz optically stimulated luminescence characteristics and their relevance in single-aliquot regeneration dating protocols. Radiat. Meas. 41, 369–391.

Yoshida, H., Roberts, R.G., Olley, J.M., Laslett, G.M., Galbraith, R.F., 2000. Extending the age range of optical dating using single ‘supergrains’ of quartz. Radiat. Meas. 32, 439–446.

Zimmermann, D.W., 1971. Thermoluminescent dating using fine grains from pottery. Archaeometry 13, 29–52.

Supplementary material – Bartz et al. (2015) Quaternary Geochronology 30, 460-465

Table S1: Results of the dose recovery tests dependent on preheat temperatures for all OSL samples (100–150 µm): n_a = amount of accepted aliquots; n_m = measured aliquots; OD = overdispersion.

sample ID	grain size (µm)	n_a/n_m	preheat (°C)	given dose (Gy)	measured dose (Gy)	measured/given dose ratio	OD (%)
C-L3396	100-150	9/9	200	9.3	9.8 ± 0.2	1.05	4.7 ± 0.4
C-L3390	100-150	8/11	240	5.7	5.5 ± 0.1	0.97	2.1 ± 0.3
C-L3391	100-150	3/3	240	9.3	9.0 ± 0.2	0.97	0
C-L3392	100-150	9/10	240	13.0	12.4 ± 0.2	0.95	2.3 ± 0.2
C-L3393	100-150	8/11	220	14.2	13.7 ± 0.3	0.96	4.6 ± 0.4
C-L3395	100-150	10/14	240	157	154.4 ± 14	0.98	0
C-L3544	100-150	2/3	220	11.4	11.1 ± 0.1	0.97	0
C-L3545	100-150	2/3	240	12.8	11.7 ± 0.2	0.91	0
modern sample	100-150	4/4	220	8.6	8.5 ± 0.3	0.99	3.8 ± 0.6

Table S2: Dose rate data set for OSL samples. Summary of specific activities and concentrations of uranium (U), thorium (Th) and potassium (K) determined by high-resolution γ-ray spectrometry. From the measured concentrations dose rates were achieved using the conversion factors of Adamiec and Aitken (1998) and alpha and beta attenuation factors of Bell (1980) and Mejdahl (1979). In addition, the cosmic dose rate attenuation after Prescott and Hutton, 1988; Prescott and Hutton, 1994 was used.

sample ID	grain size (µm)	depth (m b.s.)	H_2O (%)	radionuclide concentration			dose rate (Gy/ka)			
				U (ppm)	Th (ppm)	K (%)	β- dose rate	γ- dose rate	cosmic dose rate	total dose rate
C-L3396	100-150	0.15	4 ± 1	1.22 ± 0.09	4.16 ± 0.30	0.92 ± 0.05	0.88 ± 0.04	0.54 ± 0.02	0.26 ± 0.03	1.68 ± 0.10
C-L3390	100-150	0.45	9 ± 3	1.77 ± 0.12	6.39 ± 0.46	1.38 ± 0.08	1.24 ± 0.07	0.76 ± 0.04	0.22 ± 0.02	2.22 ± 0.13
C-L3391	100-150	1.05	11 ± 4	1.63 ± 0.08	5.73 ± 0.33	1.28 ± 0.05	1.12 ± 0.06	0.68 ± 0.03	0.19 ± 0.02	1.99 ± 0.16
C-L3392	100-150	1.50	6 ± 2	1.49 ± 0.10	5.62 ± 0.41	1.22 ± 0.07	1.12 ± 0.06	0.69 ± 0.03	0.17 ± 0.01	1.98 ± 0.10
C-L3393	100-150	2.42	5 ± 1	0.90 ± 0.06	2.83 ± 0.21	0.61 ± 0.04	0.59 ± 0.03	0.37 ± 0.02	0.16 ± 0.02	1.11 ± 0.08
C-L3395	100-150	4.50	12 ± 4	1.39 ± 0.10	5.88 ± 0.43	1.18 ± 0.07	1.02 ± 0.07	0.64 ± 0.04	0.11 ± 0.01	1.76 ± 0.12
C-L3544	100-150	1.65	4 ± 1	1.41 ± 0.21	4.94 ± 0.36	1.05 ± 0.06	1.01 ± 0.05	0.62 ± 0.03	0.17 ± 0.02	1.80 ± 0.09
C-L3545	100-150	1.65	4 ± 1	1.38 ± 0.10	4.67 ± 0.34	1.01 ± 0.06	0.97 ± 0.05	0.60 ± 0.02	0.17 ± 0.02	1.73 ± 0.08
modern sample	100-150	0.10	4 ± 1	0.65 ± 0.05	1.60 ± 0.13	0.32 ± 0.02	0.34 ± 0.02	0.22 ± 0.01	0.26 ± 0.03	0.82 ± 0.06

Table S3: Dose distribution characteristics, equivalent dose determinations and age calculations of OSL samples: n_a = amount of accepted aliquots (grains); n_m = measured aliquots (grains); skew c = skewness; kurt k = kurtosis; $2\sigma_c$ and $2\sigma_k$ = 2× standard error of skewness and kurtosis; RSD = relative standard deviation; OD = overdispersion; CAM = central age model; MAM = minimum age model; n/a = not applicable.

sample ID	**aliquot diameter (mm)**	**grain size (µm)**	**n_a/n_m**	**dose distribution characteristics**						**D_e values (Gy)**		**age (ka)**	
				skew c	**$2\sigma_c$**	**kurt k**	**$2\sigma_k$**	**RSD (%)**	**OD (%)**	**CAM**	**MAM**	**CAM**	**MAM**
C-L3396	1	100-150	54/86	3.43	0.67	34.20	1.34	109.1	64.0 ± 5.0	8.32 ± 0.72	$3.49^{+0.80}_{-0.66}$	5.0 ± 0.5	$2.1^{+0.49}_{-0.41}$
C-L3396	SG	100-150	(50/2640)	1.74	0.69	3.70	1.39	80.8	67.5 ± 5.8	4.36 ± 0.43	$2.23^{+0.16}_{-0.44}$	2.6 ± 0.3	$1.3^{+0.11}_{-0.25}$
C-L3390	1	100-150	48/101	2.30	0.71	8.30	1.42	37.2	26.3 ± 1.4	5.45 ± 0.21	$5.16^{+0.35}_{-0.38}$	2.5 ± 0.2	$2.3^{+0.20}_{-0.21}$
C-L3391	1	100-150	68/89	0.44	0.59	6.20	1.19	20.9	15.7 ± 0.6	8.73 ± 0.47	n/a	4.4 ± 0.3	n/a
C-L3392	1	100-150	54/112	0.95	0.67	11.60	1.33	20.7	13.7 ± 0.5	12.67 ± 0.68	n/a	6.4 ± 0.4	n/a
C-L3393	1	100-150	69/93	1.28	0.59	10.5	1.18	24.3	17.7 ± 0.7	15.42 ± 0.84	n/a	13.9 ± 1.0	n/a
C-L3395	1	100-150	38/110	-0.06	0.79	8.8	1.59	22.9	15.9 ± 0.8	135.35 ± 3.71	n/a	76.0 ± 4.9	n/a
C-L3544	1	100-150	55/95	0.21	0.66	11.0	1.32	19.6	13.4 ± 0.5	11.80 ± 0.22	n/a	6.5 ± 0.7	n/a
C-L3545	1	100-150	70/108	0.55	0.59	7.8	1.17	19.8	14.3 ± 0.5	11.83 ± 0.21	n/a	6.8 ± 0.4	n/a
modern sample	1	100-150	32/100	1.57	0.87	2.4	1.73	75.0	80.7 ± 9.1	n/a	n/a	n/a	n/a

Chapter 3

3 Unravelling fluvial deposition and pedogenesis in ephemeral stream deposits in the vicinity of the prehistoric rock shelter of Ifri n'Ammar (NE Morocco) during the last 100 ka

Melanie Bartz [a], Gilles Rixhon [a], Martin Kehl [a], Meriam El Ouahabi [b], Nicole Klasen [a], Dominik Brill [a], Gerd-Christian Weniger [c], Abdeslam Mikdad [d], Helmut Brückner [a]

[a] Institute of Geography, University of Cologne, Albertus-Magnus-Platz, 50923 Cologne, Germany

[b] U. R. Argiles, Géochimie et Environnements sédimentaires, Department of Geology, University of Liège, Place du 20 Août 7, 4000 Liège, Belgium

[c] Neanderthal Museum, Talstraße 300, 40822 Mettmann, Germany

[d] Institut National des Sciences de l'Archéologie et du Patrimoine (INSAP), 1, rue Ghandi, Rabat, Morocco

Abstract

Our study focuses on the ephemeral stream deposits of Wadi Selloum to identify phases of morphodynamic stability (pedogenesis) and activity (flooding) in the direct vicinity of the rock shelter of Ifri n'Ammar (NE Morocco). As one of the oldest settlement sites of anatomically modern humans (AMH) in North Africa, Ifri n'Ammar documents periodical occupations since ~170 ka. Since the discontinuous settlement record may reflect climate forcing with subsequent landscape changes, we aim at reconstructing the palaeoenvironmental variability recorded in the ephemeral stream deposits. In addition to the use of micromorphological, sedimentological, geochemical and mineralogical methods, the geochronological framework of ephemeral stream deposits was established by the application of different luminescence dating techniques. The deposition ages between 102±8 ka and 1.3±0.2 ka span different morphodynamically stable and active phases. Periods of enhanced aggradation occurred around ~100 ka, ~75 ka, ~55 ka, after the LGM, and during the Holocene, whilst sedimentation ended after ~1.3 ka. The Wadi Selloum might be characterised by enhanced flooding during humid phases. Pedogenesis may be used as environmental indicator for more humid climate conditions during MIS 3 (palaeo-Calcisol), the early Holocene (Calcisol) and the late Holocene (Fluvisol). This study thus provides first insights into the palaeoenvironmental changes around the rock shelter of Ifri n'Ammar during the last glacial-interglacial cycle.

Keywords

Morocco, Environmental change, Luminescence dating, Micromorphology, Soil formation, Human occupation

Published in *Catena* 152 (2017), 115-134.

https://doi.org/10.1016/j.catena.2016.12.007

Catena 152 (2017) 115–134

Contents lists available at ScienceDirect

Catena

journal homepage: www.elsevier.com/locate/catena

Unravelling fluvial deposition and pedogenesis in ephemeral stream deposits in the vicinity of the prehistoric rock shelter of Ifri n'Ammar (NE Morocco) during the last 100 ka

Melanie Bartz [a,*], Gilles Rixhon [a], Martin Kehl [a], Meriam El Ouahabi [b], Nicole Klasen [a], Dominik Brill [a], Gerd-Christian Weniger [c], Abdeslam Mikdad [d], Helmut Brückner [a,*]

[a] Institute of Geography, University of Cologne, Albertus-Magnus-Platz, 50923 Cologne, Germany
[b] U. R. Argiles, Géochimie et Environnements sédimentaires, Department of Geology, University of Liège, Place du 20 Août 7, 4000 Liège, Belgium
[c] Neanderthal Museum, Talstraße 300, 40822 Mettmann, Germany
[d] Institut National des Sciences de l'Archéologie et du Patrimoine (INSAP), 1, rue Ghandi, Rabat, Morocco

ARTICLE INFO

Article history:
Received 25 February 2016
Received in revised form 8 November 2016
Accepted 8 December 2016
Available online 17 January 2017

Keywords:
Morocco
Environmental change
Luminescence dating
Micromorphology
Soil formation
Human occupation

ABSTRACT

Our study focuses on the ephemeral stream deposits of Wadi Selloum to identify phases of morphodynamic stability (pedogenesis) and activity (flooding) in the direct vicinity of the rock shelter of Ifri n'Ammar (NE Morocco). As one of the oldest settlement sites of anatomically modern humans (AMH) in North Africa, Ifri n'Ammar documents periodical occupations since ~170 ka. Since the discontinuous settlement record may reflect climate forcing with subsequent landscape changes, we aim at reconstructing the palaeoenvironmental variability recorded in the ephemeral stream deposits. In addition to the use of micromorphological, sedimentological, geochemical and mineralogical methods, the geochronological framework of ephemeral stream deposits was established by the application of different luminescence dating techniques.

The deposition ages between 102 ± 8 ka and 1.3 ± 0.2 ka span different morphodynamically stable and active phases. Periods of enhanced aggradation occurred around ~100 ka, ~75 ka, ~55 ka, after the LGM, and during the Holocene, whilst sedimentation ended after ~1.3 ka. The Wadi Selloum might be characterised by enhanced flooding during humid phases. Pedogenesis may be used as environmental indicator for more humid climate conditions during MIS 3 (palaeo-Calcisol), the early Holocene (Calcisol) and the late Holocene (Fluvisol). This study thus provides first insights into the palaeoenvironmental changes around the rock shelter of Ifri n'Ammar during the last glacial-interglacial cycle.

1. Introduction

Located in NE Morocco, the rock shelter of Ifri n'Ammar represents a key settlement site for anatomically modern humans (AMH) in North Africa. It exhibits discontinuous occupation phases since ~170 ka and therefore records one of the oldest evidence of AMH presence in this region (Nami and Moser, 2010; Richter et al., 2010). It has been shown that climate forcing has affected human settlements in Northern Morocco since the Last Glacial Maximum (LGM; e.g. Barton et al., 2005; Courty and Vallverdu, 2001; Linstädter et al., 2012; Lubell, 2001; Zielhofer and Linstädter, 2006). Numerous investigations on fluvial archives also unravelled palaeoenvironmental conditions during the Late Glacial and the Holocene in the Western Mediterranean (e.g. Barathon et al., 2000; Benito et al., 2015; El Amrani et al., 2008; Ibouhouten et al., 2010; Pissart and Boumeaza, 2010; Wolf and Faust, 2015; Zielhofer et al., 2008, 2010). In contrast, very little information was obtained on geo-archives predating the LGM in NE Morocco (Rixhon et al., 2017).

Against this background, we have investigated the ephemeral stream deposits of the Wadi Selloum at the footslope of the archaeological site of Ifri n'Ammar as this environment exhibits fluvial archives (at least) as old as the marine isotope stage (MIS) 4 (Bartz et al., 2015). However, ephemeral stream deposits are challenging geo-archives for reconstructing landscape changes, since these fluvial systems are highly discontinuous (Bull, 1997). Indeed, it is difficult to distinguish between phases of morphodynamic activity, including both fluvial downcutting and aggradation (e.g. Patton and Schumm, 1981), and morphodynamic stability, mostly indicated by pedogenesis (e.g. Fedoroff and Courty, 2013). This is mostly because climatic and anthropogenic influences as well as autogenous changes may cause spatially variable incision or filling episodes within these fluvial systems (Bull, 1997; Faust et al., 2004; Wolf et al., 2014).

---

* Corresponding authors.

E-mail addresses: m.bartz@uni-koeln.de (M. Bartz), h.brueckner@uni-koeln.de (H. Brückner).

http://dx.doi.org/10.1016/j.catena.2016.12.007
0341-8162/© 2016 Elsevier B.V. All rights reserved.

Detailed sedimentological and geochemical analyses may help to differentiate phases of variable morphodynamics. Fluvial sediments of perennial river systems, such as the Medjerda River in Tunisia, contain clear features of pedogenesis as indicated by thin section studies (Faust et al., 2004), and intercalated layers deposited by severe flood events inferred from geochemical sediment composition (Zielhofer et al., 2004). In Morocco, Holocene terraces of the Kert River (Barathon et al., 2000; El Amrani et al., 2008) show features of different soil forming phases determined from pedological and sedimentological criteria (Zielhofer et al., 2008). Similar patterns have been observed in deposits of the Moulouya River (Ibouhouten et al., 2010; Zielhofer et al., 2010). Although catchments of ephemeral stream systems are usually much smaller, similar studies can be undertaken. Grain-size analyses of sediments from Wadi Sabra (Jordan) provide evidence of fluvial and fluvio-aeolian sedimentation during MIS 3 and MIS 2, whilst periods of soil formation could be identified by analyses of carbonates and organic matter (Bertrams et al., 2012).

Establishing chronologies for ephemeral stream sediments is likewise challenging. Gastropod shells found in our ephemeral stream profiles could be theoretically sampled for radiocarbon dating, but this material is prone to reworking issues in ephemeral fluvial systems (Rixhon et al., in press). Whilst optically stimulated luminescence (OSL) dating has been successfully applied in such settings (e.g. Bartz et al., 2015; Bubenzer et al., 2007; Klasen et al., 2013), the applicability of OSL dating of quartz is usually limited to ~200 ka due to the low saturation level of the quartz fast component (Wintle and Murray, 2006). For older sediments, infrared stimulated luminescence (IRSL) dating of feldspars may represent a valuable alternative, although IRSL ages may suffer from anomalous fading, leading to a loss of signal over time and possible age underestimation (e.g. Huntley and Lamothe, 2001; Wintle, 1973). In this respect, post-infrared infrared stimulated luminescence dating at an elevated temperature of 290 °C (pIRIR_{290}; Thiel et al., 2011) offers feldspar signals which are less affected or unaffected by anomalous fading (Thomsen et al., 2008).

This study thus aims at (i) identifying pedogenetic processes and flooding activity in Wadi Selloum's ephemeral stream deposits as indicators for morphodynamic stability and activity, respectively, using micromorphological, sedimentological, geochemical and mineralogical proxies; (ii) establishing a chronology for the depositional units by a combination of different luminescence dating approaches; and (iii) discussing the Wadi Selloum record in the Late Quaternary palaeoenvironmental context of the Western Mediterranean region and possible correlations of the inferred environmental changes with the phases of occupation in the Ifri n'Ammar rock shelter.

2. Study area

2.1. Climatic and geomorphological setting

The ~290 km^2 wide catchment of the Wadi Selloum, a western tributary of the lower Moulouya river, drains the northernmost prolongation of the Middle Atlas Mountains in NE Morocco (Benjelloun et al., 1971) (Fig. 1a, b). The present climate is semi-arid with annual precipitation ranging between 200 and 600 mm (Snoussi et al., 2002). Most of the rainfall is concentrated during episodic and high-intensity events (Snoussi et al., 2002). The precipitation pattern is reflected by the hydrological regime, dominated by episodic flash floods with rapid flow velocity and high sediment discharge (Abdalla et al., 2014). Rain-fed agriculture and extensive grazing of sheep and goats are common, thus causing recent human-induced soil erosion.

The studied area of the Wadi Selloum encompasses ~20 km^2 of the upper catchment (Fig. 1b, c), exclusively composed of Mesozoic limestone and dolomite (Benjelloun et al., 1971). The ephemeral stream system drains the foothills of the rock shelter of Ifri n'Ammar in a south-eastern flow direction, and is fed by two tributaries (Fig. 2a). The ephemeral stream sediments observed in the (sub-)vertical bank profiles generally consist of alternations of coarse-grained (gravel) and fine-grained (silt- and clay-rich) deposits. Whilst the latter is essentially transported as suspension load, the former mostly represents bed load material and is indicative of channel deposits. Given the discontinuity of ephemeral stream systems (Bull, 1997), we observed spatial heterogeneity in the wadi banks. The width of the valley floor is highly variable: it amounts to only ~150 m between the rock shelter and Rock Selloum (Fig. 2a), but rapidly increases downstream, where channel widening is also observed. Several rock fall events occurred along the limestone cliff of Rock Selloum; the deposits of the two largest of them (rf I and rf II) extend to the valley floor directly upstream of Ifri n'Ammar (Fig. 2a). Geomorphological analysis of Quaternary terrace systems of the lowermost Moulouya reach along with a morphometric analysis of the whole Moulouya catchment, including a focus on the Wadi Selloum catchment, highlights a long-term disequilibrium of both the main trunk and the tributary (Barcos et al., 2014; Rixhon et al., 2017). This might be reflected by two 3–4 m-high knickpoints (kp I and kp II; Fig. 2b) disrupting the present-day ephemeral stream

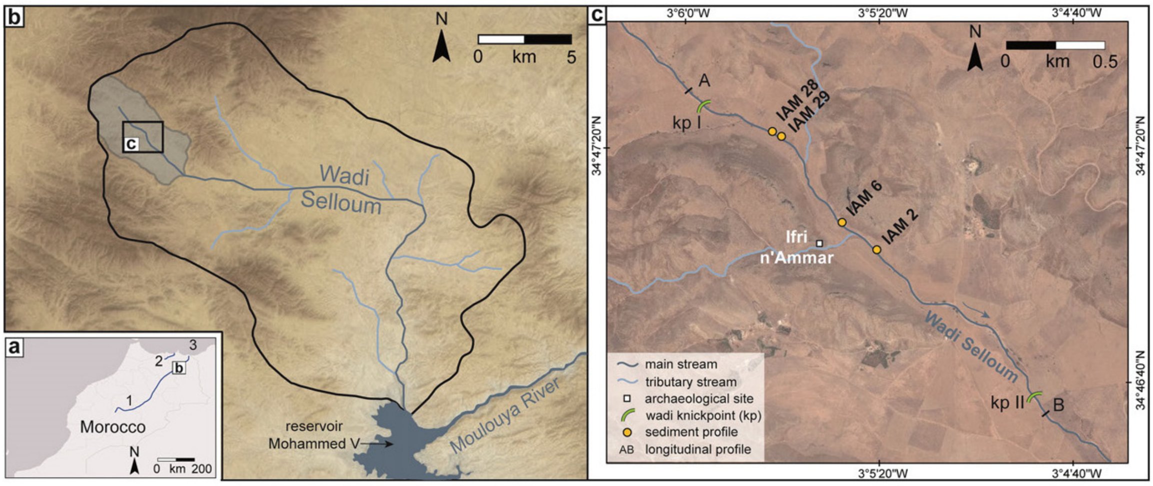

Fig. 1. a: The study area in NE Morocco; 1 – Moulouya River, 2 – Kert River, 3 – Alboran Sea. b: Catchment area of the Wadi Selloum (~290 km^2), a tributary of the lower Moulouya river (based on ASTER Global DEM; USGS, 2015); the studied upper catchment is indicated in grey. c: The upper catchment of the Wadi Selloum in the direct vicinity of the rock shelter Ifri n'Ammar (based on Esri, 2014), presenting the locations of the profiles (IAM 2, IAM 6, IAM 28 and IAM 29) and the knickpoints (kp I and kp II). The bed topography was measured between A and B by DGPS.

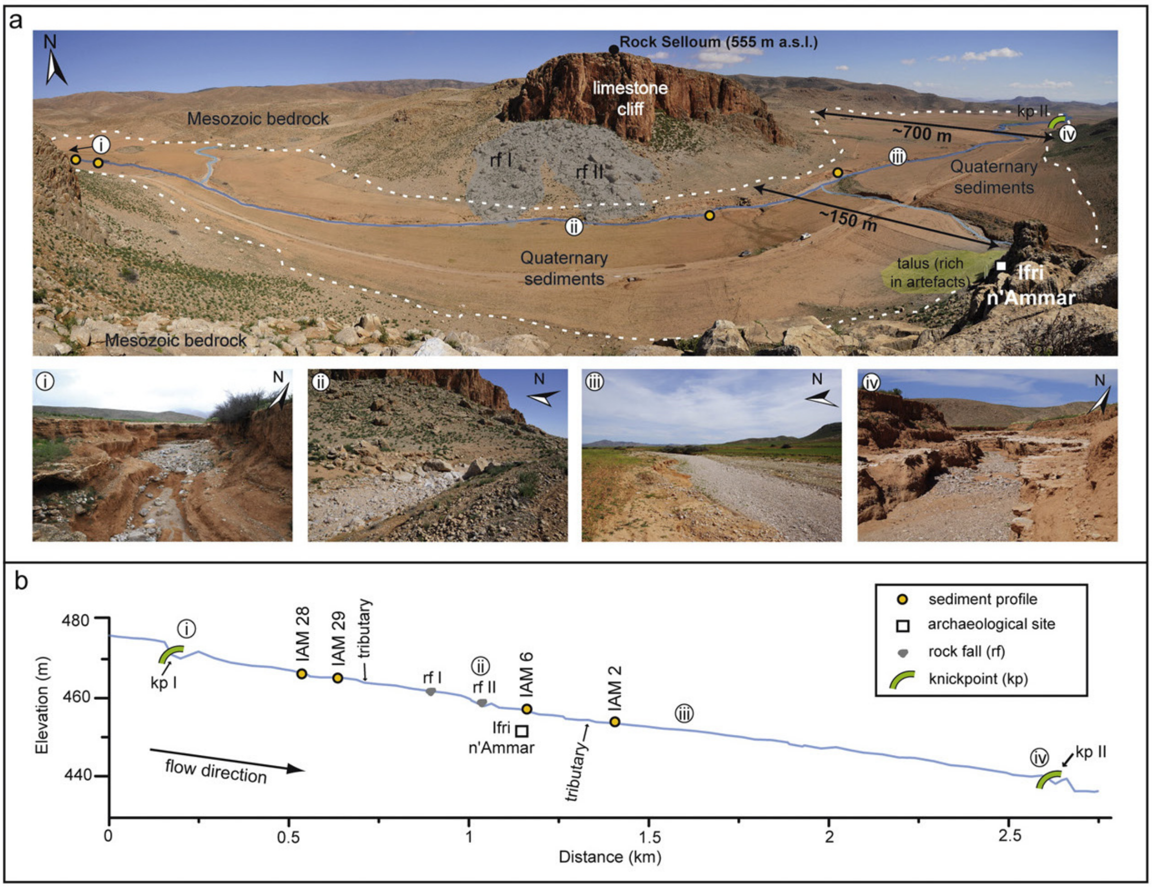

Fig. 2. a: Overview of the Wadi Selloum valley in the vicinity of Ifri n'Ammar; the main geomorphological features are indicated. i – An alternation of coarse-grained gravel and fine-grained overbank deposits at the location of knickpoint (kp) I. The top of kp I is characterised by a dm-thick calcrete. ii – Rock fall (rf) deposits in the main trunk of Wadi Selloum. iii – Downstream of Ifri n'Ammar, the valley bottom of Wadi Selloum widens to ~700 m due to an increase in the accommodation space. iv – Knickpoint (kp) II is characterised by ~2 m-thick profiles with calcretes at the base of the modern stream bed. b: Longitudinal profile of the studied Wadi Selloum section with locations of the photographs i-iv, the investigated profiles, the two knickpoints (kp I and kp II), the two rock falls (rf I an rf II) and the rock shelter of Ifri n'Ammar. The bed topography was measured by DGPS.

channel, although their locations seem closely related to decimetre-thick calcrete crusts within the episodically active stream bed (Fig. 2a).

2.2. Archaeological background

The archaeological layers of the Ifri n'Ammar rock shelter reveal discontinuous phases of AMH settlements during the last ~170 ka. The lower part shows a Middle Palaeolithic sequence (Mikdad et al., 2004; Nami and Moser, 2010), which is dated to time spans between 171 ± 12 ka and 145 ± 9 ka, as well as between 130 ± 8 ka and 83 ± 6 ka (thermoluminescence, TL, ages of heated flint; Richter et al., 2010). The uppermost part of the Middle Palaeolithic sequence has been ^{14}C-dated to a time span between 51.5 ± 1.3 ka BP and 38.9 ± 2.0 ka BP (Linstädter et al., 2012; Mikdad et al., 2002; Moser, 2003). The upper part of the archaeological sequence covers the Upper Palaeolithic related to the Iberomaurusian culture, which is ^{14}C-dated between 13.9 ± 0.08 ka BP (16.8–16.5 ka cal BP) and 10.0 ± 0.08 ka BP (11.7 ± 0.4 ka cal BP) (Linstädter et al., 2012; Moser, 2003).

3. Materials and methods

3.1. Fieldwork and sampling strategy

The current stream bed topography of the main trunk (Fig. 2b) was measured by differential GPS (Topcon DGPS). Ephemeral stream deposits were investigated and documented (FAO, 2006) in four different profiles; the latter are located downstream of (IAM 2), next to (IAM 6) and upstream of (IAM 28 and IAM 29) the archaeological site (Fig. 1c). Within the current stream bed the contact with the carbonate bedrock was not reached in any of the profiles.

From profile IAM 2 (Fig. 3), five luminescence samples were collected at depths of 0.90 (C-L3830), 1.90 (C-L3388), 2.85 (C-L3385), 3.85 (C-L3383) and 4.80 (C-L3389) m below surface (b.s.). Eight micromorphological samples (thin section, TS) were taken at depths of 1.97, 2.32, 2.52, 2.92, 3.22, 3.57, 3.92 and 4.22 m b.s. (TS 2.1–2.8). The profile IAM 2 was sampled in 10 cm intervals down to 4.80 m b.s. Two luminescence samples from profile IAM 6 (Fig. 4), previously dated by OSL (C-L3393 and C-L3395; Bartz et al., 2015), were measured with the pIRIR$_{290}$ dating technique for an inter-method comparison. In addition, two samples for micromorphological studies were taken at 1.05 and 4.50 m b.s. (TS 6.1–6.2). The profile IAM 6 was also sampled in 10 cm intervals down to 4.90 m b.s., except between 2.90 and 4.20 m b.s. where a strongly cemented layer hampered any sampling. From IAM 29 (Fig. 5), two luminescence samples were collected at depths of 0.90 and 1.97 m b.s. (C-L3828 and C-L3829), and samples for micromorphological analyses at 1.50 and 1.97 m b.s. (TS 29.1–29.2). Sediments from the IAM 29 profile were also sampled at 10 cm intervals from the surface to 2.50 m b.s.; we assume that this profile is analogous to the IAM 28 profile (Fig. 5). Four additional samples for micromorphological analyses were collected in the upper part of the IAM 28 profile (Fig. 6), at depths of 0.40, 0.70, 1.05 and 1.60 m b.s. (TS 28.1–28.4).

3.2. Sedimentological, geochemical and micromorphological analyses

Sediment samples were air-dried and sieved to separate the matrix fraction <2 mm for further analyses. The grain-size distribution was measured three times in 116 classes with a laser particle sizer (Beckman Coulter LS13320) after removal of organic matter with H_2O_2 (10%). After pre-treatment the samples were dispersed overnight within an overhead shaker using 2 ml 0.05 M sodium pyrophosphate ($Na_4O_7P_2$) to avoid coagulation. The GRADISTAT software version 4.0 (Blott and Pye, 2001) was applied for calculation of grain-size parameters after Folk and Ward (1957). The loss on ignition (LOI) was determined by oven-drying (Carbolite ELF 11/14) the samples at 105 °C for 12 h and by ignition in an annealing furnace at 550 °C for 4 h (LOI_{550}; Heiri et al., 2001). The LOI_{550} was used as an indicator for pedogenic accumulation of organic matter, although its accuracy is limited due to possible dehydration of clay or metal oxides, loss of volatile salts or loss of inorganic carbon in minerals (Heiri et al., 2001; Mook and Hoskin, 1982; Sutherland, 1998). Analysis of the mineralogical phases was performed by X-ray diffraction (XRD, Bruker D8-Advance diffractometer with CuKα radiations) on powdered bulk sediment (Moore and Reynolds, 1997). The relative abundance of minerals (including carbonates) was estimated from the height of the main peak with the DIFFRACplus EVA software (Boski et al., 1998; Cook et al., 1975). Thin section preparation followed the procedure of Beckmann (1997). The observations were performed with a polarising transmitted-light microscope and description followed the guidelines of Stoops (2003). The colours of dried sediments and soil material were determined with the Munsell Soil Color Chart. Soil identification followed the "World Reference Base for Soil Resources" (IUSS Working Group WRB, 2014).

3.3. Application of luminescence dating techniques to ephemeral stream deposits

Sample preparation for dose measurements included treatment with H_2O_2 (10%), HCl (10%) and sodium oxalate to remove carbonates, organics and clay remains. Whilst density separation with sodium polytungstate was used to isolate coarse-grained (100–150 μm) quartz (ρ_1 = 2.62–2.68 g cm^{-3}) and feldspars (ρ_2 ≤2.58 g cm^{-3}), the polymineral fine-grained fraction (4–11 μm) was extracted using a centrifuge. The quartz minerals were etched with HF (40%) for 40 min plus a final HCl (10%) wash.

All measurements were carried out in the Cologne Luminescence Laboratory (CLL) on automated Risø TL/OSL DA 20 readers equipped with $^{90}Sr/^{90}Y$ beta sources for irradiation, delivering dose rates of ~0.08 Gy s^{-1}. Quartz multiple-grain signal emissions (1 mm and 2 mm aliquots) were detected using blue light emitting diodes (470 ± 20 nm) and a Hoya U 340 glass filter (7.5 mm), whereas quartz single grains were stimulated for 2 s with a green Nd:YVO_4 diode-pumped laser (532 nm) (Bøtter-Jensen et al., 2000). Equivalent dose (D_e) determination followed the single-aliquot regenerative-dose (SAR) protocol of Murray and Wintle (2000, 2003), using the initial part of the decay curve (0–0.8 s) after subtraction of a late background (36–40 s) for quartz multiple-grain aliquots. For single-grain measurements, the OSL signal was derived from the first 0.054 s of stimulation minus a background of the last 0.4 s. A preheat-plateau test with increasing temperatures between 180 and 280 °C (held for 10 s), in combination with a cut heat 20 °C below the preheat temperature, was performed for sample C-L3828 to determine the appropriate thermal pre-treatment (7 multiple-grain aliquots per temperature step). Dose recovery tests (given dose = 80 Gy), in combination with different preheat temperatures, were conducted using 100 s blue-LED stimulation at room temperature (~25 °C) for signal resetting. To investigate the OSL signal components, fitting of continuous wave (CW)-OSL curves was applied. CW-OSL measurements were carried out on three aliquots of sample C-L3828 and fitted using the software package R-Luminescence (Kreutzer et al., 2012).

IR stimulation (880 ± 80 nm) and signal detection through an interference filter (410 nm) were used for measuring the coarse-grained feldspar samples and the fine-grained polymineral sample. The first 2.4 s of stimulation minus a background of the last 40 s were used. The pIRIR signal was measured at 290 °C ($pIRIR_{290}$; Thiel et al., 2011) for 200 s after a preheat of 320 °C (hold for 60 s). At the end of each cycle, a 325 °C IR bleaching was used. The prior IR stimulation temperature was chosen by performing prior IR stimulation temperature tests on three coarse-grained feldspar samples (C-L3395, C-L3829, C-L3830) and on the fine-grained polymineral sample C-L3389 to investigate the dependency of D_e on prior IR stimulation (Buylaert et al., 2012). Although results of Thiel et al. (2011) and Buylaert et al. (2012) suggest that the $pIRIR_{290}$ seems to be unaffected by anomalous fading, sample C-L3395 was checked for anomalous fading using the procedure of Auclair et al. (2003). A bleaching test with optical treatment in the solar simulator (Hönle SOL2) between 0.5 and 24 h was carried out for sample C-L3389 to test the bleaching characteristics of the $pIRIR_{290}$-protocol. Furthermore, dose recovery (given doses commensurate with D_e of each sample) and residuals after 24 h signal resetting in the solar simulator were determined for all samples.

The measured aliquots had to fulfil the following SAR rejection criteria for both quartz and $pIRIR_{290}$ samples: (i) test dose error ≤10%; (ii) recuperation <5% of the sensitivity-corrected natural signal; (iii) recycling ratio between 0.9 and 1.1 (for single grains between 0.85 and 1.15); (iv) $D_e < 2 * D_0$; and (v) IR depletion ratio ≤10% (Duller, 2003). The central age model (CAM; Galbraith et al., 1999) was used for D_e calculation.

High-resolution γ-spectrometry using a high-purity germanium detector was carried out for dose rate determination. DRAC v1.1 (Durcan et al., 2015) was applied for dose rate and age calculation using the conversion factors of Guérin et al. (2011), and alpha and beta attenuation factors of Bell (1980) and Guérin et al. (2012); the latter was specifically chosen for either quartz or feldspar grains. The contribution of cosmic dose rates was assessed following the approach of Prescott and Hutton (1994). To account for attenuation of ionising radiation by pore water, field water contents (mass of water relative to the dried sample) of 4–20% were considered with an uncertainty of ~30%. For coarse-grained feldspar, an α-efficiency of 0.11 ± 0.03 (Balescu and Lamothe, 1993) was used, whilst an α-efficiency of 0.07 ± 0.02 (Preusser et al., 2005) was assumed for polymineral fine grains. An internal potassium content of 12.5 ± 0.5% (Huntley and Baril, 1997) was assumed for feldspars.

4. Results

4.1. Profile descriptions

In the following, the investigated profiles are described from their positions downstream to upstream of the rock shelter of Ifri n'Ammar. Depths of all units or their boundaries are given below surface (b.s.).

4.1.1. Profile IAM 2

The bipartite, ~5 m-high profile IAM 2 (Fig. 3) is located ~230 m to the east of Ifri n'Ammar (Fig. 1c). Reddish yellow (7.5YR 6/6) silts form unit 1 (5.00–4.00 m). They include sparse charcoal remains, terrestrial gastropods (e.g. *Otala* cf. *lactea*) and carbonate precipitations. Reddish yellow (7.5YR 6/6) sandy silts, embedding

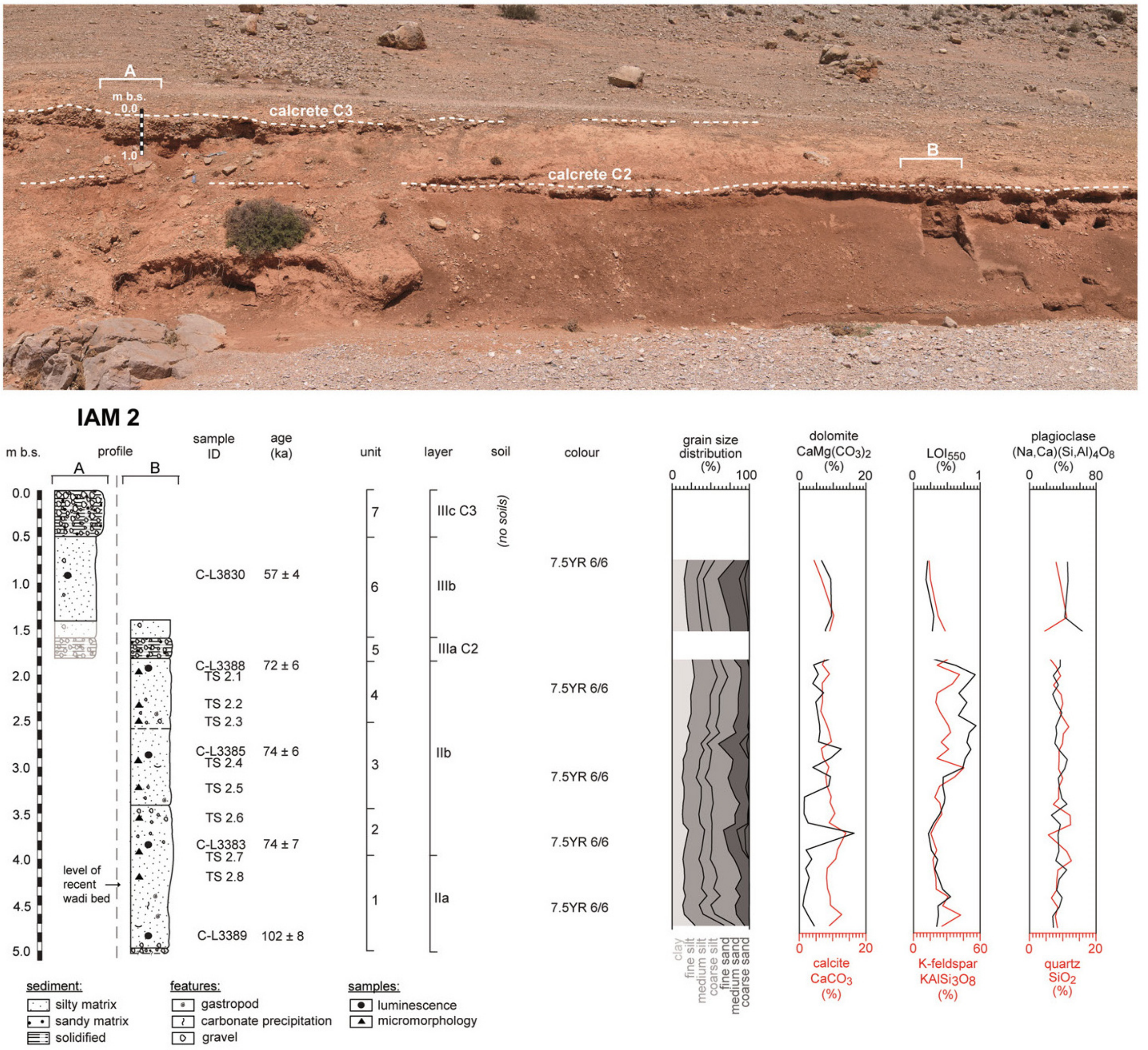

Fig. 3. Stratigraphical record of profile IAM 2 including sedimentological and geochemical results. Samples for luminescence dating and micromorphology are indicated with depths, ages and sample IDs. Sediment units of each profile as well as layers for profile correlation in the catchment are presented together with pedogenic features. The two calcretes C2 and C3 (white dashed lines) can be used to correlate parts A and B of the bipartite profile IAM 2.

sparse, subangular, up to 2 cm-large gravel, form unit 2 (4.00–3.40 m). Reddish yellow (7.5YR 6/6) sediments with a coarsening-upward tendency, from fine sandy silts to silty fine sands, form unit 3 (3.40–2.50 m), including a few specimens of *Otala* cf. *lactea* and charcoal remains. The overlying stratum at 2.50–1.80 m (unit 4) shows a silty matrix with a reddish yellow (7.5YR 6/6) sediment colour. The base of unit 5 is marked by an erosional unconformity at 1.80 m. This unit (1.80–1.60 m) is formed by solidified gravels of up to 10 cm in size (C2). Marked by a sharp basal boundary, the homogeneous unit 6 (1.60–0.50 m) is formed by reddish yellow (7.5YR 6/6) sandy silts, embedding sparse, subangular, up to 3 cm-large gravel. The top 0.60 m-thick solidified layer (unit 7; C3) is composed of up to ~20 cm-large gravel.

4.1.2. Profile IAM 6

The ~4.90 m-high profile IAM 6 (Fig. 4) is located ~150 m to the northeast of Ifri n'Ammar (Fig. 1c). We refer to the stratigraphic description of Bartz et al. (2015) for this profile. Reddish yellow (7.5YR 6/6) sandy silt form the lowermost unit 1 (4.90–4.10 m). The base of the composite unit 2 is marked by an erosional unconformity at 4.10 m. Gravels in a sandy matrix are cemented in the lower part of unit 2 (4.10–3.65 m), forming a calcrete layer (C2); they are less solidified in the middle part (3.65–3.00 m). The upper part of unit 2 (3.00–2.30 m) is formed by reddish yellow (7.5YR 6/6) silty sands. The overlying unit 3 (2.30–2.10 m) is characterised by gravel in a sandy matrix. The uppermost unit 4 of the profile (2.10–0 m) is characterised by a fining-upward

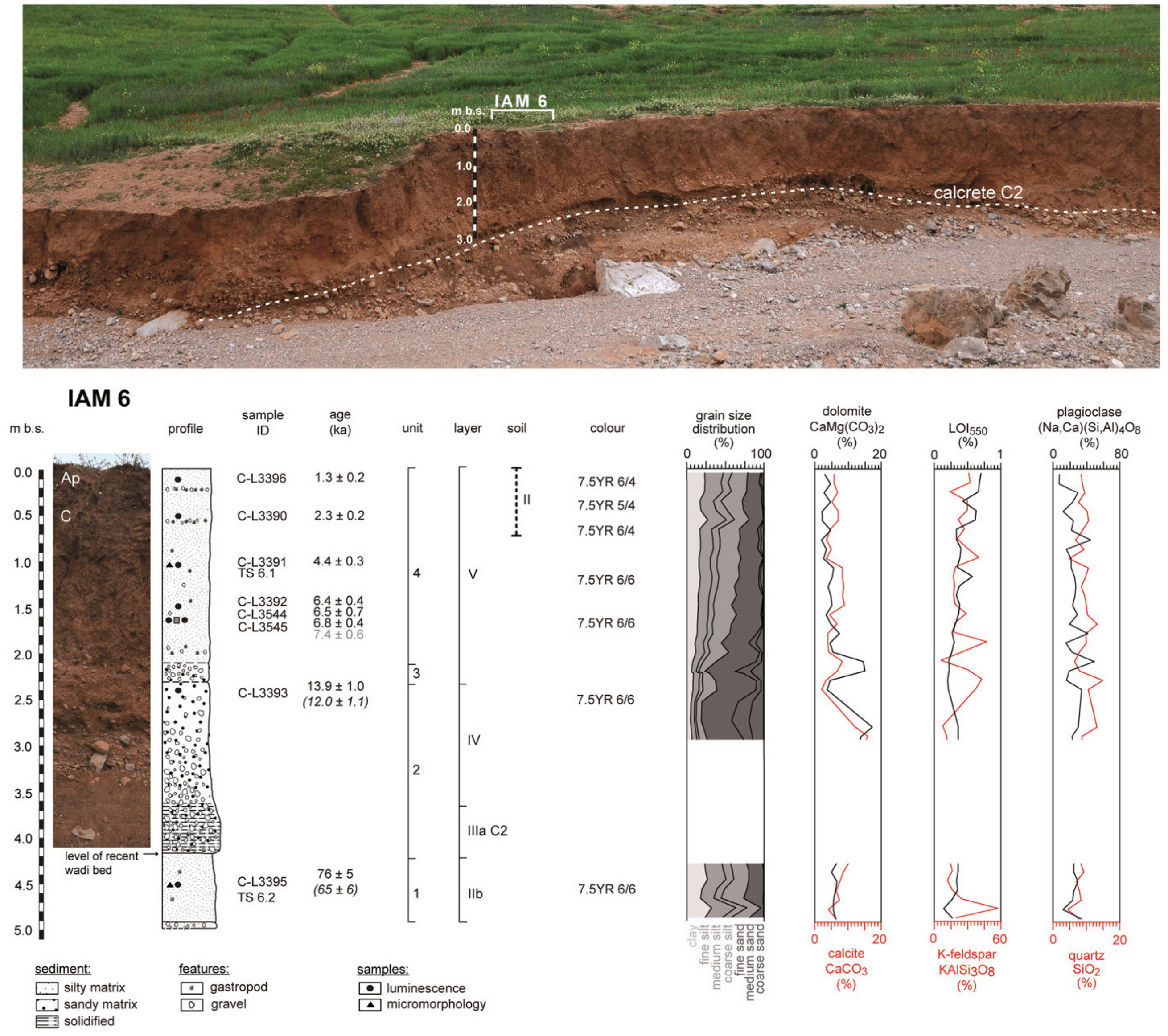

Fig. 4. Stratigraphical record of profile IAM 6 (modified from Bartz et al., 2015) including sedimentological and geochemical results. Samples for luminescence dating and micromorphology are indicated with depths, ages (pIRIR$_{290}$ ages in brackets for an inter-method comparison) and sample IDs. Sediment units of each profile as well as layers for profile correlation in the catchment are presented together with pedogenic features. The white dashed line in the upper photograph indicates the top of the calcrete C2.

sequence from silty fine sands to fine sandy silts. It is interspersed by layers of well-preserved terrestrial gastropods (e.g. *Otala* cf. *lactea*, *Rumina decollata*) and pieces of charcoal at 0.60 and 0.20 m. A change in the sediment colour to light brown (7.5YR 6/4) is observed from 0.40 m up to the top.

4.1.3. Profile IAM 29

The ~3.20 m-high profile IAM 29 (Fig. 5) is located ~600 m to the northwest of Ifri n'Ammar (Fig. 1c). The 0.60 m-thick basal unit 1 (3.20–2.60 m) is composed of up to 10 cm-large, subangular carbonate gravel and stones (C1), cemented by a calcareous sandy matrix. The overlying unit 2 (2.60–1.70 m) is dominated by reddish yellow (7.5YR 6/6) sandy silts, intercalated by a gravel-dominated layer (2.35–2.20 m) composed of 5 cm-large subangular components. The unit 3 (1.70–1.30 m) is characterised by reddish (7.5YR 7/4), clay-rich silts, with up to 2 cm-large carbonate nodules. The overlying unit 4 (1.30–1.15 m) is composed of up to 10 cm-large subangular gravel, embedded in clay-rich silts. The uppermost unit 5 (1.15–0 m) is a coarsening-upward sequence from clay-rich silts to fine sandy silts. The sediment colour changed from reddish yellow (7.5YR 7/6) to yellowish brown (10YR 5/4). The uppermost layer of the profile (0.60–0 m) includes organic material (e.g. roots), terrestrial gastropods (e.g. *Otala* cf. *lactea*) as well as carbonate and dolomite fragments.

4.1.4. Profile IAM 28

The ~3.20 m-high profile IAM 28 (Fig. 6) is situated ~40 m upstream of profile IAM 29 (Fig. 1c). Since both profiles present similar sediment characteristics, the unit classification of IAM 29 is adopted for this profile. Basal gravels (C1) form unit 1 (3.20–2.60 m). Light

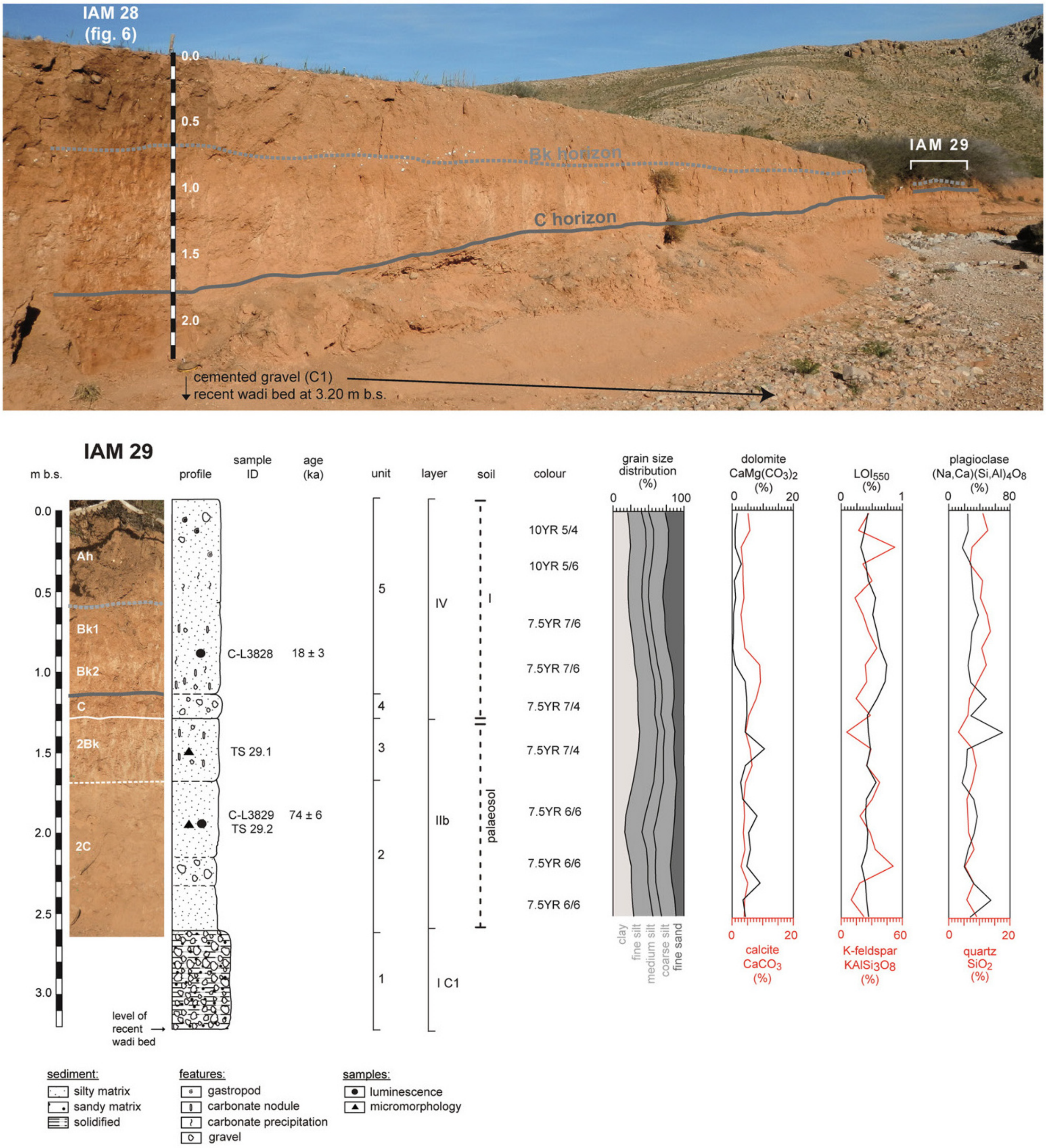

Fig. 5. Upper part: profiles IAM 28 and IAM 29 viewed from the ephemeral stream bed. They can be correlated by the Bk horizon (light grey dashed line) and the C horizon (dark grey solid line). Lower part: stratigraphical record of profile IAM 29 including sedimentological and geochemical results. Samples for luminescence dating and micromorphology are indicated with depths, ages and sample IDs. Sediment units of each profile as well as layers for profile correlation in the catchment are presented together with pedogenic features. See Fig. 6 for the detailed description of profile IAM 28.

brownish (7.5YR 6/4) silts compose unit 2 (2.60–2.15 m). The overlying yellowish/reddish (7.5YR 7/4 to 7/6), clayey/silty unit 3 (2.15–1.95 m) is characterised by well-developed subangular blocky peds and up to 2 cm-large carbonate nodules. Unit 4 (1.95–1.80 m) is composed of subangular gravel (~10 cm in size). The uppermost unit 5 (1.80–0 m) shows colour changes from reddish yellow (7.5YR 7/6) to yellowish brown (10YR 5/4). A compact clay-rich silt was observed from 1.80 to 0.60 m; it also exhibits carbonate

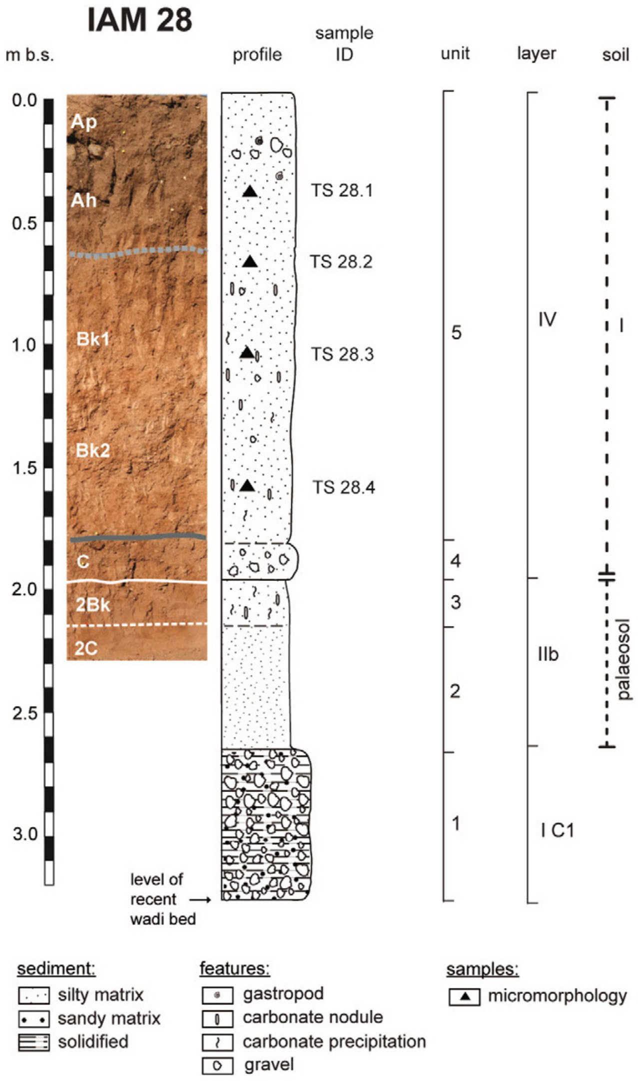

Fig. 6. Stratigraphical record of profile IAM 28. Micromorphological samples are indicated with depths and sample IDs. Sediment units of each profile as well as layers for profile correlation in the catchment are presented together with pedogenic features. Profile IAM 28 is correlated with profile IAM 29 (see Fig. 5).

precipitations and up to 1 cm-large nodules. The latter only occur up to 0.95 m, whereas carbonate precipitation was observed up to ~0.40 m. Furthermore, the sediment structure is characterised by slightly developed blocky peds from 0.95 to 0.60 m. The uppermost layer of the profile (0.60–0 m) includes occasional roots, subangular gravel (~3 cm in diameter) and terrestrial gastropods (e.g. *Otala* cf. *lactea*).

4.2. Sediment properties and soil micromorphology

The results of micromorphological analyses are presented in Tables 1 and 2. According to similar characteristics and recurring patterns observed in the 16 thin sections (TS), they may be classified into three distinct groups. Group 1 has characteristic A horizon features, group B relates to B horizons, and group 3 points to sediments weakly altered by pedogenesis (C horizons).

4.2.1. A horizon features

Group 1 encompasses TS 28.1, 28.2 and 6.1 (Fig. 7). The silty and sandy fractions are dominated by angular to subangular quartz, K-feldspar and plagioclase grains (Fig. 7d). The coarser fabric units occur unsorted in a dense matrix, which results in a single (TS 28.1) to double (TS 6.1 and TS 28.2) spaced porphyric c/f-related distribution. Whilst TS 28.1 shows a partly undifferentiated b-fabric, the TS display a calcitic crystallitic b-fabric due to dispersed micrite in the groundmass. Primary carbonates, mostly corresponding to fragments of gastropod shells and carbonate rocks, are only present in small amounts which is in agreement with rather small values of both dolomite and calcite. The TS are characterised by moderately developed pedality and ped separation (Fig. 7a–c). The microstructure is spongy, crumb and granular, which can be related to infillings in burrows and to bioturbated parts of the TS. Less than 1 mm small pieces of charcoal are evident. Most of the crumbs are mammilated excrements. Some circular or ellipsoidal burrows with perfectly smooth walls consisting of compacted fine-grained material are evident. Pedofeatures are rare; only a few Fe and Mn nodules occur in the groundmass. Only TS 28.2 is characterised by low abundance of secondary carbonate coatings along voids in the lower parts of the section (Fig. 7e). Very rarely, dusty clay coatings with poorly oriented clay along mineral grains were observed. The darkening of the topsoil in comparison to the subsoil is related to an enrichment of organic material (Ah horizon), although the organic content of the A horizons are rather low with values of $LOI_{550} < 1\%$. An Ap horizon describes the topsoil which is influenced by tillage, but otherwise with similar characteristics as the Ah horizon.

4.2.2. B horizon features

Group 2 encompasses TS 28.3, 28.4 and 29.1 (Fig. 8). The c/f-related distribution is single- (TS 28.4) to double- (TS 28.4 and 29.1) spaced porphyric, dominated by silt- to sand-size quartz and feldspar grains. In these B horizons, precipitation of secondary carbonates is the most prominent feature, however, abundant grains of primary carbonate (shell and rock fragments) are found as well. The richness in calcareous components is reflected in high amounts of calcite and dolomite. In addition, the B horizons are characterised by the development of a subangular-blocky microstructure, which, in the case of TS 28.4 is weakly developed. The aggregation is conspicuous due to the development of well-separated subangular blocky peds (Fig. 8a–c), especially in TS 29.1 where aggregates are separated by planes (Fig. 8c). The degree of pedality is moderate (TS 28.3 and 29.1) to weak (TS 28.4). TS 28.4 shows unaccommodated peds, whilst in TS 28.3 and 29.1 peds are partially accommodated. As voids, mainly planes are visible beside chambers and channels. All TS show a crystallitic b-fabric, due to finely-dispersed calcite grains. Various pedofeatures occur: infillings of secondary carbonate (Fig. 8d, e), calcite coatings (Fig. 8g–i), and Fe and Mn nodules (Fig. 8e). Intercalations are visible in TS 28.4 (Fig. 8f). Oriented clay is only documented in form of thin coatings around quartz and feldspar grains. Calcite depletion pedofeatures were not found. Rarely biogenic pedofeatures are visible in form of mammilated excrements and passage features. The subsoil horizons Bk1 and Bk2, respectively, are characterised by different degrees of carbonate precipitation.

4.2.3. C horizon features

Group 3 encompasses TS 2.1–2.8, 6.2 and 29.2 (Fig. 9). Mineral grains are distinguished by a subangular to angular shape in a single- to double-spaced porphyric c/f-related distribution of the groundmass. Beside quartz, K-feldspar and plagioclase minerals, all TS contain primary carbonates, mainly corresponding to calcite and dolomite grains and shell remains. Charcoal residues rarely occur in the groundmass. Rounded aggregates are randomly formed in the sediment and are composed of finer material than the micromass

Table 1
Micromorphological results of thin section (TS) analyses focusing on structure and groundmass features as well as residues of biogenic origin. The observations were performed with a polarising transmitted light microscope. The descriptions follow the guidelines of Stoops (2003): – = none; (▪) = rarely; ▪ = few; ▪▪ = moderate; ▪▪▪ = dominant.

Sample ID	TS group	Soil horizon	Structure									Groundmass			
			Aggregation			Voids					Microstructure	c/f-rel. distr.	b-Fabric	Residues of biologic origin	
			Ped separation	Degree of developed pedality	Accommodation	Packing voids	Chambers	Channels	Planes	Vughs				Charcoal	Gastropod shell
TS 2.1	3	C	Weakly separated	Weakly developed	Unaccommodated	▪	▪▪	▪▪	▪	▪▪	Chamber-channel, locally subangular blocky or granular	Double-spaced porphyric	Crystallitic	(▪)	▪
TS 2.2	3	C	–	–	–	▪	▪▪▪	▪▪	–	▪▪	Chamber and granular	Single-spaced porphyric	Crystallitic	–	▪
TS 2.3	3	C	–	–	–	▪	▪▪	▪▪	–	▪	Chamber-channel and granular	Single-spaced porphyric	Crystallitic	(▪)	(▪)
TS 2.4	3	C	–	–	–	▪	▪▪	▪▪	▪	▪▪	Chamber-channel and granular	Single-spaced porphyric	Crystallitic	(▪)	(▪)
TS 2.5	3	C	–	–	–	▪	▪▪	▪▪▪	–	▪	Chamber-channel and granular	Double-spaced porphyric	Crystallitic	(▪)	(▪)
TS 2.6	3	C	–	–	–	▪	▪▪	▪▪	–	▪	Chamber-channel and granular	Single-spaced porphyric	Crystallitic	–	▪
TS 2.7	3	C	–	–	–	▪	▪▪	▪▪	–	▪▪	Chamber-channel and granular	Double-spaced porphyric	Crystallitic	(▪)	(▪)
TS 2.8	3	C	Weakly separated	Weakly developed	Unaccommodated	▪	▪▪▪	▪▪▪	–	▪▪	Chamber-channel, locally subangular blocky and granular	Double-spaced porphyric	Crystallitic	(▪)	▪
TS 6.1	1	A	Moderately separated	Moderately developed	Unaccommodated	▪▪	▪▪	▪▪	–	▪▪	Spongy, subangular blocky and granular	Double-spaced porphyric	Crystallitic	(▪)	▪
TS 6.2	3	C	–	–	–	▪	▪▪	▪▪	▪	▪▪	Chamber-channel, locally granular	Single-spaced porphyric	Crystallitic	–	(▪)
TS 28.1	1	Ap	Moderately separated	Moderately developed	Unaccommodated	▪▪	▪▪▪	▪▪▪	–	▪	Spongy, chamber-channel and granular	Single-spaced porphyric	Crystallitic, partly undifferentiated	(▪)	▪
TS 28.2	1	A/B	Moderately separated	Moderately developed	Unaccommodated	▪▪	▪▪	▪▪	▪	▪	Chamber-channel, subangular blocky and granular	Double-spaced porphyric	Crystallitic	(▪)	▪
TS 28.3	2	Bk1	Moderately separated	Moderately developed	Partially accommodated	–	▪	▪	▪▪▪	▪	Subangular blocky, partly massive	Double-spaced porphyric	Crystallitic	–	(▪)
TS 28.4	2	Bk2	Weakly separated	Weakly developed	Unaccommodated	▪	▪▪	▪▪	▪▪	▪	Massive, partly subangular blocky or granular	Single-spaced porphyric	Crystallitic	–	▪
TS 29.1	2	2Bk	Moderately separated	Moderately developed	Partially accommodated	▪▪	▪▪	▪▪	▪▪▪	▪▪	Subangular blocky, partly massive	Double-spaced porphyric	Crystallitic	–	▪
TS 29.2	3	2C	–	–	–	▪	▪▪▪	▪▪▪	▪	▪▪	Chamber-channel, partly single-grain	Single-spaced porphyric	Crystallitic	–	(▪)

Table 2
Micromorphological results of thin section (TS) analyses focusing on pedofeatures. The observation was performed with a polarising transmitted light microscope. The descriptions follow the guidelines of Stoops (2003): – = none; (▪) = rarely; ▪ = few; ▪▪ = moderate; ▪▪▪ = dominant.

Sample ID	TS group	Soil horizon	Calcitic pedofeatures				Fe/Mn pedofeatures		Biogenic pedofeatures			Others
			Hypocoatings	Coatings	Infillings	Nodules	Nodules	Coatings	Mammilated or spherical excrements	Sediment cocoons	Passage features	Intercalations
TS 2.1	3	C	▪	▪	▪	▪	▪▪	–	▪	(▪)	(▪)	–
TS 2.2	3	C	–	–	▪	–	▪	–	▪	(▪)	▪	–
TS 2.3	3	C	–	–	▪	–	▪	–	(▪)	▪▪	(▪)	–
TS 2.4	3	C	–	–	–	–	▪	–	▪	▪	(▪)	–
TS 2.5	3	C	–	–	–	–	▪	–	▪▪	–	(▪)	–
TS 2.6	3	C	–	–	–	–	▪	–	▪	▪	(▪)	–
TS 2.7	3	C	–	–	–	–	▪	▪	(▪)	(▪)	–	–
TS 2.8	3	C	–	–	–	–	▪	–	▪	–	▪	–
TS 6.1	1	A	–	–	–	–	▪	–	▪▪	▪	(▪)	–
TS 6.2	3	C	–	–	–	–	▪	–	–	▪	(▪)	–
TS 28.1	1	Ap	–	–	–	–	▪	–	▪▪▪	(▪)	▪	–
TS 28.2	1	A/B	–	(▪)	–	–	▪	–	▪▪▪	▪	(▪)	–
TS 28.3	2	Bk1	–	▪	▪▪	▪▪	▪▪	–	(▪)	–	(▪)	–
TS 28.4	2	Bk2	–	▪	▪▪	▪▪	▪▪	–	–	–	▪	▪
TS 29.1	2	2Bk	▪▪	▪	▪▪▪	▪▪	▪▪	–	(▪)	–	–	–
TS 29.2	3	2C	▪	–	–	–	▪▪	–	▪▪	▪▪	▪▪	–

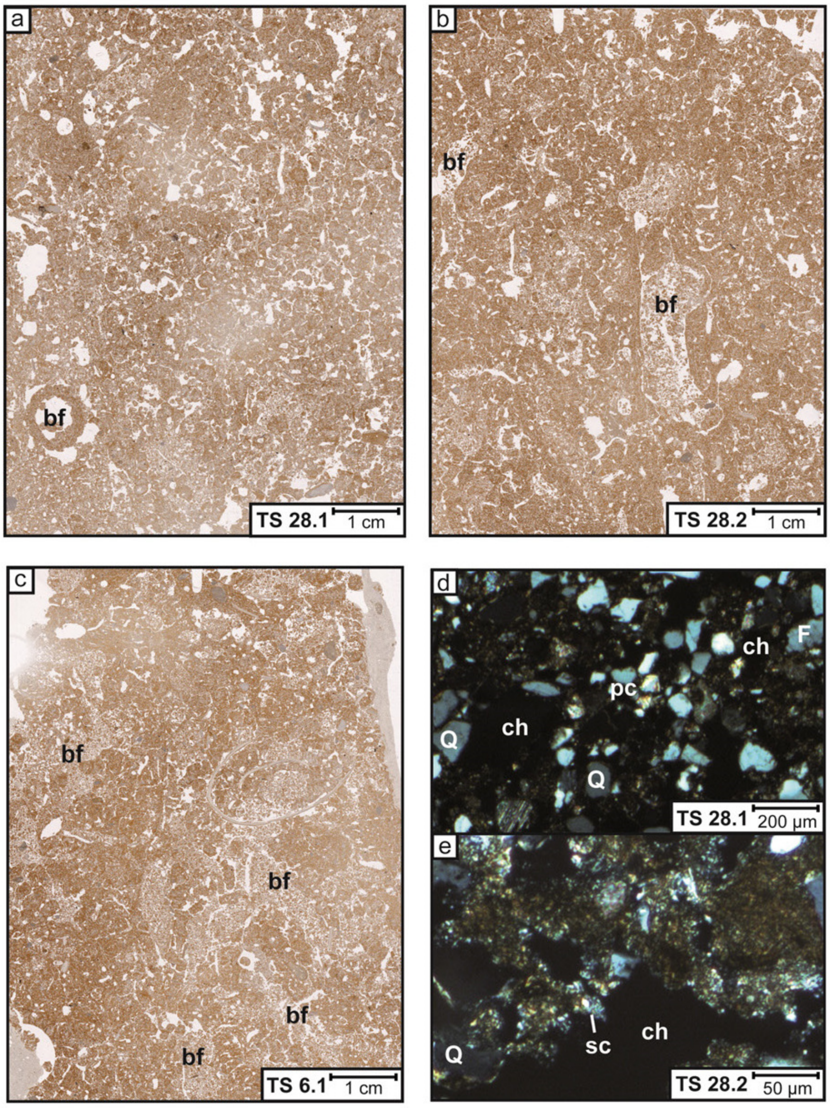

Fig. 7. Thin sections (TS) 28.1, 28.2 and 6.1 associated to TS group 1 (A horizon features). a–c: Flatbed scans characterised by bioturbation features (bf) and the presence of biogenic aggregates. d: Mainly quartz (Q) and feldspar (F) are visible beside rarely distributed primary carbonates (pc, here in form of rock fragments) under crossed-polarised light (XPL). e: Quartz minerals occur unsorted in a dense fine matrix with a crystallitic b-fabric (XPL). Note the slight degree of secondary carbonate (sc) precipitation along voids, e.g. chambers (ch).

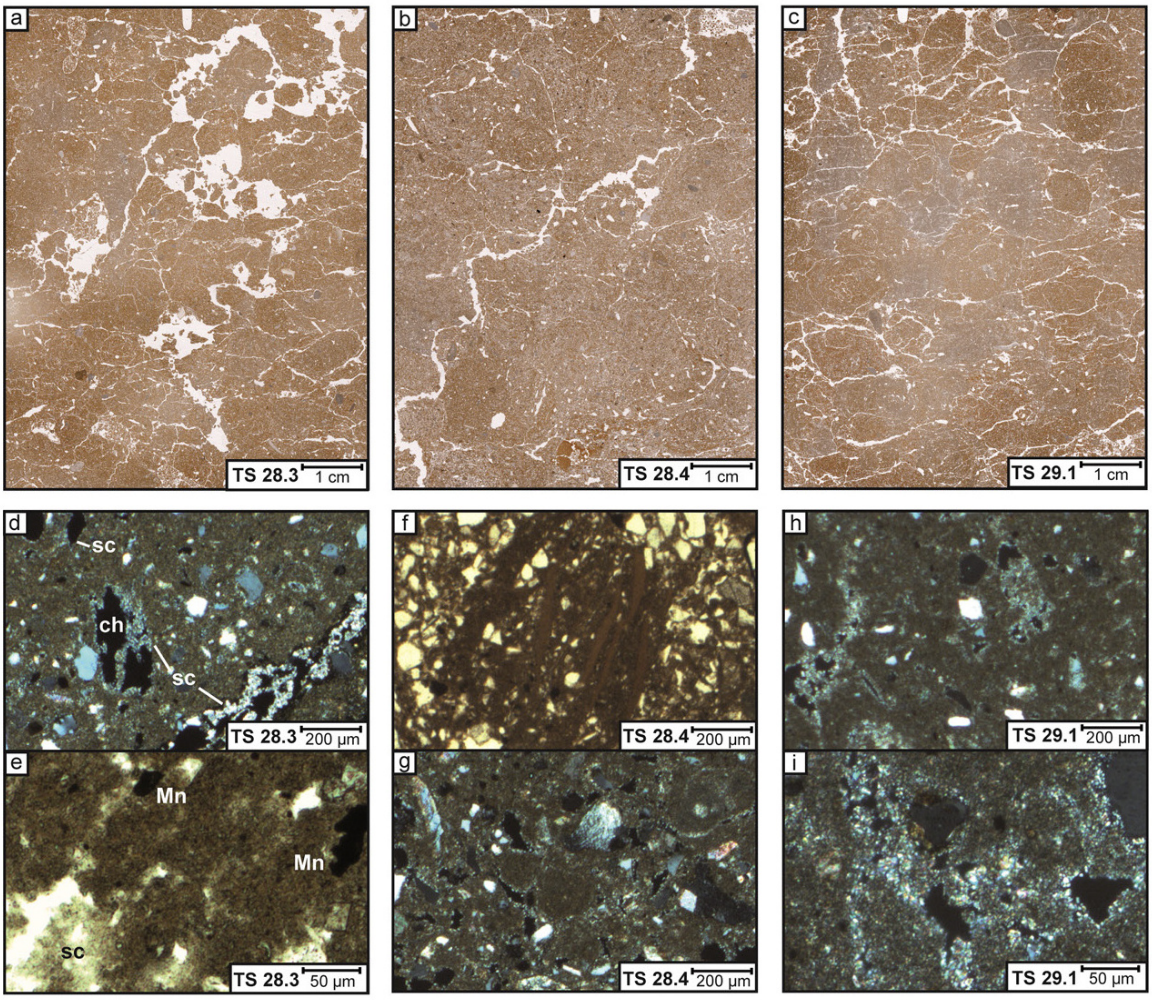

Fig. 8. TS 28.3, 28.4 and 29.1, associated to TS group 2 (B horizon features). a-c: flatbed scans, indicating aggregation in form of subangular blocky peds. d: Secondary carbonate (sc) precipitation in form of infillings and calcite coatings along chambers (ch) in a dense matrix under crossed-polarised light (XPL). e: Secondary carbonate (sc) precipitation in chambers as infillings as well as Mn nodules under plain-polarised light (PPL). f: Intercalation of fine sediment in a coarser matrix characterised by silt- to sand-sized rock fragments (PPL). g, h, i: Precipitation of secondary carbonate along voids (XPL).

(Fig. 9h, i, k, n). The microstructure is a mixture of channel, chamber and granular types. A crystallitic b-fabric is mainly expressed. Accommodation is insignificant and, occasionally, pedality is weakly developed. Voids occur frequently as chambers and channels, partly as vughs and packing voids. Pedofeatures are rare and mainly consist of Fe and Mn nodules. Sparse hypocoatings are found in TS 2.1, 6.2 and 29.2 (Fig. 9g, l, m, o). Precipitation of secondary carbonates is visible in form of infillings to a slight degree in TS 2.1 (Fig. 9f), 2.3 and 2.4. The fluvial nature of the sediment is evident by locally preserved microlayers, showing a fining-upward sequence (Fig. 9j). Biogenic pedofeatures in form of mammilated excrements, sediment cocoons and passage features occur rarely. LOI_{550} values are rather low (<1%).

4.3. Soil identification

Three soils have been identified in the Wadi Selloum deposits: profiles IAM 28 and IAM 29 (Figs. 5, 6) comprise one buried soil in form of a 2Bk-2C sequence (palaeosol) in units 2 and 3, and a second soil characterised by an Ah-Bk1-Bk2-C sequence (soil I) in units 4 and 5. Here, the two Bk horizons provide information about age-related carbonate precipitation. The 2Bk horizon of the palaeosol is characterised by high and intensive precipitation of secondary carbonate and strong pedality (TS group 2, Fig. 8). Soil I belongs to the Calcisol group displaying processes of dissolution of primary carbonates in the A horizons (TS group 1, Fig. 7) and precipitation of secondary carbonates in the B horizons (TS group 2, Fig. 8). As based on the similarity of soil properties with the modern Bk horizon at profiles IAM 28 and IAM 29, the palaeosol may thus represent a subsoil horizon of a former Calcisol. Profile IAM 6 (Fig. 4) reveals pedofeatures characteristic for A horizons (TS group 1, Fig. 7) which are found at ~1 m depth (Fig. 4), reflecting intense bioturbation near a former land surface. Here, a third soil is formed characterised by an Ap-C sequence (soil II) and classified as a weakly developed Fluvisol. Below the A horizon, a clear differentiation in soil horizons is not evident, probably because aggradation of young sediments hampered formation of a Calcisol.

4.4. Geochronological framework

4.4.1. Luminescence properties and D_e determination

Only sample C-L3828 (profile IAM 29) revealed a quartz signal below saturation level. For this sample, a preheat temperature of

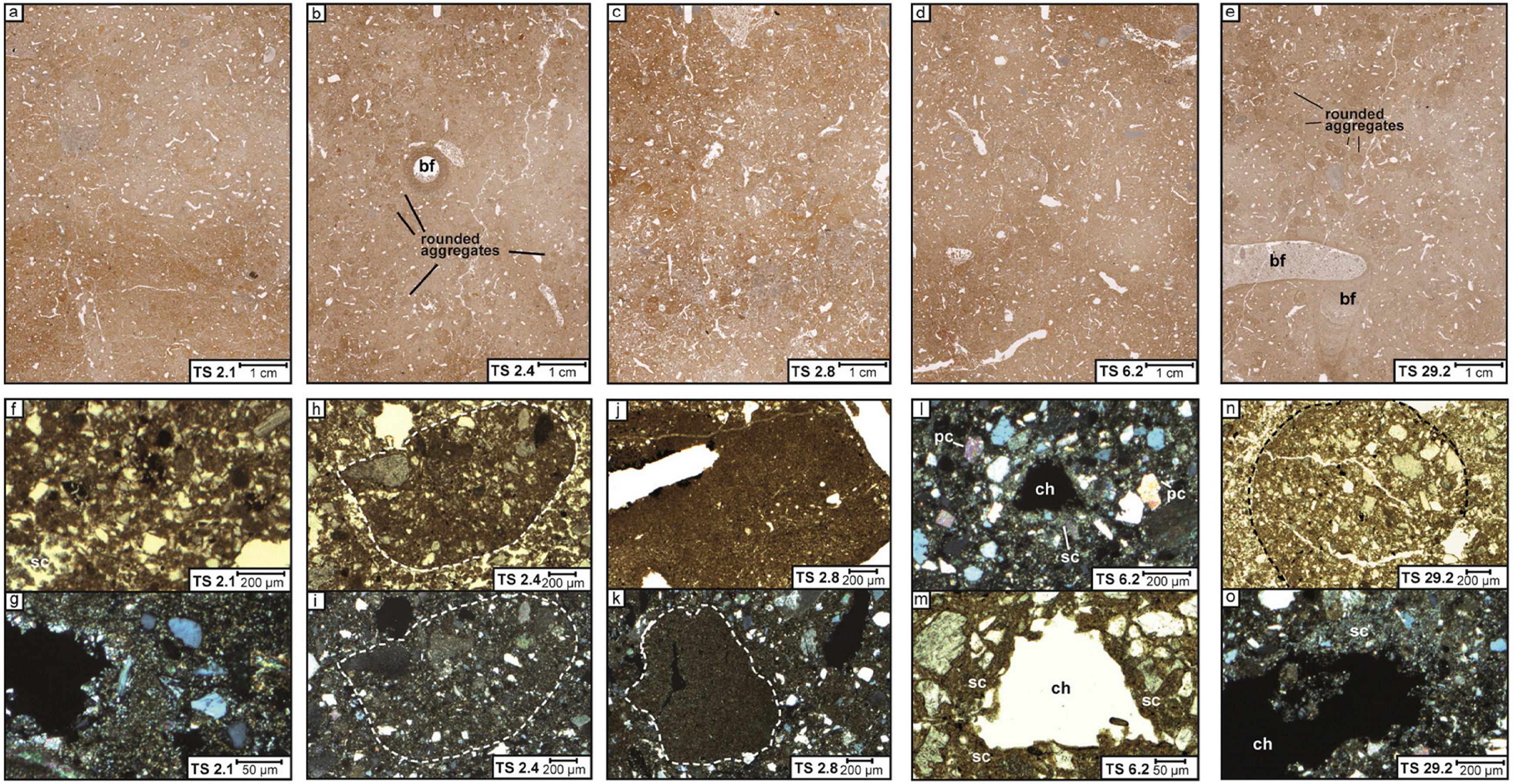

Fig. 9. TS 2.1, 2.4, 2.8, 6.2 and 29.2 associated to TS group 3 (C horizon features). a–e: Flatbed scans showing a high degree of bioturbation in form of chambers and channels, as well as bioturbation features (bf). f: Precipitation of secondary carbonates (sc) along voids under plain-polarised light (PPL). g: Precipitation of secondary carbonates (sc) along voids under crossed-polarised light (XPL). h: (PPL) and i: (XPL) Rounded aggregates are evident, filled by fine-grained material beside rock fragments (borders are marked with white dashed lines). j: Microlayers showing a fining-upward sequence and indicating original fluvial sedimentation (PPL). k: Rounded aggregate filled by fine-grained material (XPL). l: (XPL) and m: (PPL) Hypocoating of secondary carbonate (sc) along one chamber (ch). Coarse-grained rock fragments of primary carbonates (pc) are evident in the matrix. n: Rounded aggregate filled by a mixture of fine- and coarse-grained material originating from the matrix (PPL). o: Slight degree of secondary carbonate (sc) precipitation (XPL). Note that the chamber is not marked by carbonate precipitation.

200 °C was best suited to recover the given dose (0.98 ± 0.05, Fig. 10a), a dominant fast component was presented by CW-OSL component fitting. For the 64 measured multiple-grain aliquots a total of 6 aliquots (~10%) were rejected due to saturation. For single-grain measurements, ~20% of all grains provided bright signals (out of 1400 measured grains) including 106 grains (~38%) with signals above the saturation limit. For D_e determination, 45 multiple-grain aliquots and 40 single grains passed the SAR acceptance criteria. Whilst the multiple-grain data yielded overdispersion >40% (Fig. 10b), the single-grain dose distribution was characterised by even larger scatter (overdispersion >80%; Fig. 10b). The multiple-grain and single-grain dose distributions are approximately symmetrical. Suggesting that sample C-L3828 is affected by post-depositional processes (based on micromorphological analyses; Bk horizon, profile IAM 29), rather than partial bleaching, we used the CAM to calculate a D_e value of 33.7 ± 4.7 Gy and 74.7 ± 6.1 Gy for the single-grain and multiple-grain data set, respectively. The finite mixture model (Galbraith, 2005) was inappropriate for D_e determination due to missing dose populations.

Due to saturation of the quartz signal in most samples, potassium feldspars were also investigated. Sensitivity changes could be corrected adequately, and recuperation was <2% of the sensitivity-corrected natural signal. The prior IR stimulation temperature tests yielded a plateau between 50 and 175 °C for all samples (Fig. 10c). Since intensities of the pIRIR_{290} signal decreased with increasing prior IR temperature and yielded weak signals (Fig. 10d), a prior IR stimulation temperature of 50 °C followed by IR stimulation at 290 °C was used for all feldspar and polymineral samples. Dose recovery ratios between 0.94 ± 0.02 and 1.05 ± 0.03 revealed satisfactory reproducibility (Fig. 10e). Residual doses between ~1 and ~5 Gy (Fig. 10e) and the results of the bleaching experiment of sample C-L3389 (Fig. 10f) indicated adequate resetting of the pIRIR_{290} signal in our samples. Due to rather small residual doses and insignificantly altered D_e, subsequent subtraction from dose recovery and natural doses was redundant. For D_e determination, 13 to 40 aliquots were accepted in case of the feldspar samples, whilst 8 aliquots of the fine-grained polymineral sample C-L3389 passed the SAR criteria. The main reason for rejection was the weak pIRIR_{290} signal. The D_e distributions (Table 3) were characterised by overdispersion values <20%; we applied the CAM for D_e determination for all feldspar and polymineral samples. Fading rates (g-values) of pIRIR_{290} signals (sample C-L3395) varied significantly between aliquots, with values from 0.3 to 1.2%/decade and an average of 0.8 ± 0.4%/decade.

The associated dosimetry data are presented in Table 4. Gamma spectrometric measurements did not yield radioactive disequilibria in the uranium decay chain.

4.4.2. *Chronostratigraphy of Wadi Selloums ephemeral stream deposits*

All luminescence age estimates are in stratigraphically correct order within each profile. OSL and pIRIR_{290} data are in agreement with age estimates of 13.9 ± 1.0 ka and 12.0 ± 1.1 ka (sample C-L3393), as well as 76 ± 5 ka and 65 ± 6 ka (sample C-L3395), respectively (Fig. 4). Luminescence dating yielded ages dating back to MIS 5c: The five samples from profile IAM 2 yielded pIRIR_{290} ages ranging between 102 ± 8 ka (C-L3389) and 57 ± 4 ka (C-L3830) from base to top (Fig. 3). The lower sample from profile IAM 29 (Fig. 5) yielded an age of 74 ± 6 ka (pIRIR_{290}; C-L3829), whilst single-grain and multiple-grain dating of the upper sample (OSL; C-L3828) yielded ages of 18 ± 3 ka and 41 ± 4 ka, respectively.

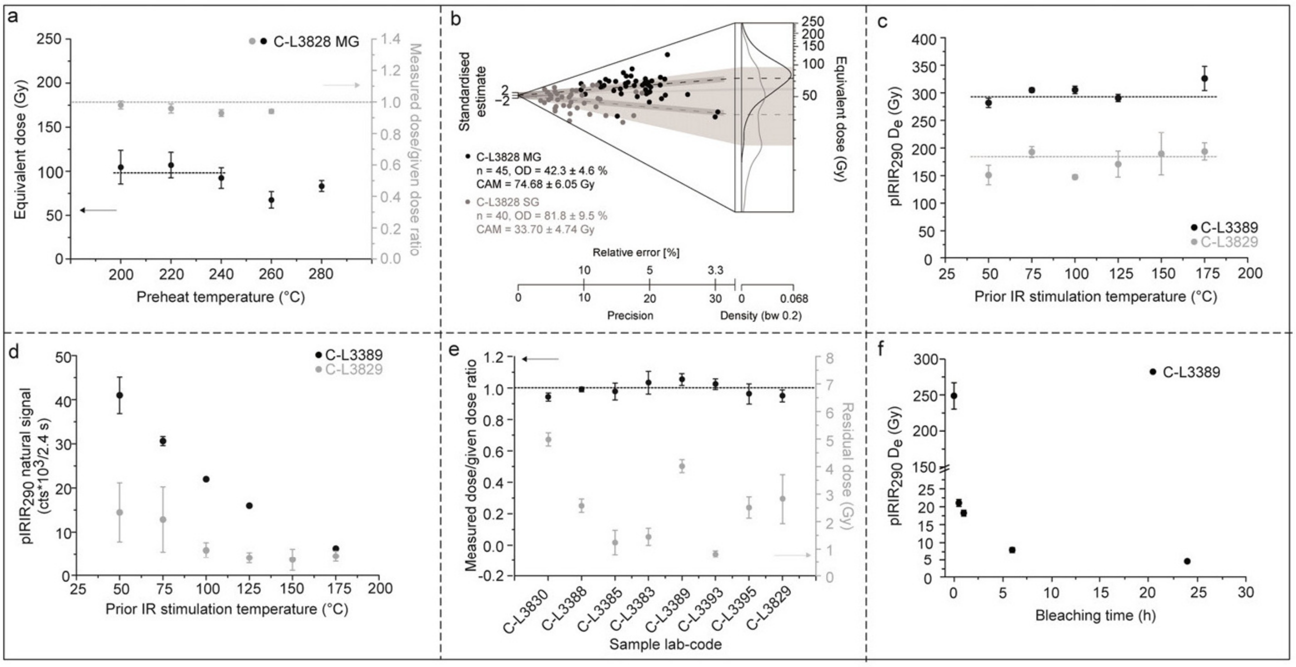

Fig. 10. Luminescence dating results. a: Preheat-plateau (black circles) and dose recovery (grey circles) test results of quartz sample C-L3828 (multiple-grain aliquots). b: Multiple-grain (MG; black circles) and single-grain (SG; grey circles) equivalent dose (D_e) distributions of sample C-L3828 displayed as a combination of a radial plot and a kernel density estimate (KDE) plot (Galbraith and Green, 1990), generated as abanico plot (Dietze et al., 2016). n = number of grains; OD = overdispersion; CAM = central age model (Galbraith et al., 1999). c: Dependence of D_e on prior IR stimulation temperature of sample C-L3389 (fine-grained polymineral) and sample C-L3829 (coarse-grained feldspar); three aliquots were measured. d: Natural pIRIR_{290} signal as a function of the first stimulation temperature (three multiple-grain aliquots, 1 mm). e: Dose recovery results (black circles) and residual doses (grey circles) of all feldspar and polymineral samples; four aliquots were used for both dose recovery and residual dose tests after bleaching in the solar simulator for 24 h. f: Bleaching experiment for sample C-L3389 (fine-grained polymineral; three aliquots for each time).

Table 3
Dose distribution characteristics, equivalent dose (D_e) determinations and age calculations of OSL and pIRIR$_{290}$ samples: SG = single grain; n_a = amount of accepted aliquots (grains); n_m = measured aliquots (grains); OD = overdispersion; CAM = central age model (Galbraith et al., 1999); MAM = minimum age model (Galbraith et al., 1999); n/a = not applicable; * = Bartz et al. (2015).

Profile	Sample ID	Lab. code	Mineral	Grain size (µm)	Aliquot diameter (mm)	n_a/n_m	OD (%)	D_e values (Gy)		Age estimates (ka)	
								CAM	MAM	CAM	MAM
IAM 2	IAM 2-J	C-L3830	Feldspar	100–150	2	21/43	13.7 ± 0.9	139.06 ± 8.21	n/a	56.5 ± 4.4	n/a
	IAM 2-H	C-L3388	Feldspar	100–150	1	13/24	16.5 ± 1.4	166.13 ± 11.49	n/a	72.3 ± 6.4	n/a
	IAM 2-D	C-L3385	Feldspar	100–150	1	14/24	16.2 ± 1.4	169.49 ± 11.46	n/a	73.7 ± 6.4	n/a
	IAM 2-B	C-L3383	Feldspar	100–150	1	20/41	19.2 ± 1.5	177.31 ± 11.91	n/a	74.0 ± 6.5	n/a
	IAM 2-I	C-L3389	Polymineral	4–11	9.8	8/8	2.9 ± 0.3	253.73 ± 13.36	n/a	101.5 ± 8.0	n/a
IAM 6	IAM 6-0	C-L3396	Quartz*	100–150	SG	(50/2640)	67.5 ± 5.8	4.36 ± 0.43	2.23 + 0.16 -0.44	2.6 ± 0.3	1.3 ± 0.2
	IAM 6-1	C-L3390	Quartz*	100–150	1	48/101	26.3 ± 1.4	5.45 ± 0.21	5.16 + 0.35 -0.38	2.5 ± 0.2	2.3 ± 0.2
	IAM 6-2	C-L3391	Quartz*	100–150	1	68/89	15.7 ± 0.6	8.73 ± 0.47	n/a	4.4 ± 0.3	n/a
	IAM 6-3	C-L3392	Quartz*	100–150	1	54/112	13.7 ± 0.5	12.67 ± 0.68	n/a	6.4 ± 0.4	n/a
	IAM 6-4	C-L3393	Quartz*	100–150	1	69/93	17.7 ± 0.7	15.42 ± 0.84	n/a	13.9 ± 1.0	n/a
	IAM 6-4	C-L3393	Feldspar	100–150	1	14/39	7.6 ± 0.5	19.96 ± 1.11	n/a	12.0 ± 1.1	n/a
	IAM 6-5	C-L3395	Quartz*	100–150	1	38/110	15.9 ± 0.8	135.35 ± 3.71	n/a	76.0 ± 4.9	n/a
	IAM 6-5	C-L3395	Feldspar	100–150	1	40/45	15.1 ± 0.7	155.47 ± 8.68	n/a	64.6 ± 5.8	n/a
	IAM 6B1	C-L3544	Quartz*	100–150	1	55/95	13.4 ± 0.5	11.80 ± 0.22	n/a	6.5 ± 0.7	n/a
	IAM 6B2	C-L3545	Quartz*	100–150	1	70/108	14.3 ± 0.5	11.83 ± 0.21	n/a	6.8 ± 0.4	n/a
IAM 29	IAM 29-1	C-L3828	Quartz	100–150	1	45/64	42.3 ± 4.6	74.68 ± 6.05	n/a	41.1 ± 3.7	n/a
	IAM 29-1	C-L3828	Quartz	100–150	SG	(40/1400)	81.8 ± 9.5	33.70 ± 4.74	n/a	18.2 ± 2.7	n/a
	IAM 29-2	C-L3829	Feldspar	100–150	2	34/45	16.0 ± 0.8	174.22 ± 10.07	n/a	73.7 ± 5.6	n/a
Wadi bed	Modern sample	C-L3542	Quartz*	100–150	1	32/100	80.7 ± 9.1	n/a	n/a	n/a	n/a

5. Discussion

5.1. How reliable are the luminescence ages of the ephemeral stream deposits?

The pIRIR$_{290}$ and OSL ages for samples C-L3393 and C-L3395 (Table 3; IAM 6) are in agreement within their 1σ-errors, but show slightly younger feldspar ages implying that our feldspar samples might be affected by anomalous fading. Kars et al. (2014) and Komatsu and Tsukamoto (2015) have mentioned that fading correction in pIRIR$_{290}$ is not redundant. Li and Li (2012) reported D_e underestimation in pIRIR$_{290}$ for samples with high natural doses and recommended an increased temperature up to 200 °C for the prior IR stimulation temperature, which is impossible for the samples of our study due to weak feldspar luminescence signals (Fig. 10d). However, prior IR stimulation temperature tests revealed no influence of anomalous fading. Thus, the prior IR stimulation temperature of 50 °C is able to effectively recombine all electrons stored in traps close enough to recombination centres to have a probability of tunnelling (Buylaert et al., 2012). This is in agreement with our results of the fading experiment which yields an average g-value of 0.8 ± 0.4%/decade. It is, however, rather a laboratory artefact than anomalous fading in nature (Buylaert et al., 2012; Thiel et al., 2011). Thus, we used fading uncorrected feldspar ages for further interpretations. An issue for our feldspars may be the internal dose rate. According to Huntley and Baril (1997), the average internal K content of orthoclase feldspars, based on multiple-grain measurements, is 12.5 ± 0.5%, which was also assumed for K-feldspars in

Table 4
Dose rate data set for quartz and feldspar samples. Summary of radionuclide concentrations of uranium (U), thorium (Th) and potassium (K) determined by high-resolution γ-spectrometry. The DRAC v1.1 (Durcan et al., 2015) was applied for dose rate calculation using the conversion factors of Guérin et al. (2011), and alpha and beta attenuation factors of Bell (1980) and Guérin et al. (2012) (quartz- and feldspar-specific). The contribution of the cosmic dose rate was assessed following the approach of Prescott and Hutton (1994). * = Bartz et al. (2015).

Profile	Sample ID	Lab. code	Mineral	Grain size (µm)	Depth (m b.s.)	Water content (%)	Radionuclide concentration			Dose rate (Gy/ka)	
							U (ppm)	Th (ppm)	K (%)	Cosmic dose rate	Total dose rate
IAM 2	IAM 2-J	C-L3830	Feldspar	100–150	0.90	15 ± 5	1.69 ± 0.09	6.05 ± 0.36	1.11 ± 0.01	0.19 ± 0.02	2.46 ± 0.12
	IAM 2-H	C-L3388	Feldspar	100–150	1.90	15 ± 5	1.50 ± 0.10	5.57 ± 0.41	1.05 ± 0.06	0.16 ± 0.02	2.29 ± 0.13
	IAM 2-D	C-L3385	Feldspar	100–150	2.85	15 ± 5	1.57 ± 0.08	5.60 ± 0.33	1.06 ± 0.04	0.14 ± 0.01	2.30 ± 0.12
	IAM 2-B	C-L3383	Feldspar	100–150	3.85	20 ± 6	1.69 ± 0.12	6.39 ± 0.46	1.20 ± 0.07	0.12 ± 0.01	2.39 ± 0.14
	IAM 2-I	C-L3389	Polymineral	4–11	4.80	20 ± 6	1.78 ± 0.12	6.70 ± 0.48	1.30 ± 0.07	0.10 ± 0.01	2.50 ± 0.15
IAM 6	IAM 6-0	C-L3396	Quartz*	100–150	0.15	4 ± 1	1.22 ± 0.09	4.16 ± 0.30	0.92 ± 0.05	0.26 ± 0.03	1.68 ± 0.10
	IAM 6-1	C-L3390	Quartz*	100–150	0.45	9 ± 3	1.77 ± 0.12	6.39 ± 0.46	1.38 ± 0.08	0.22 ± 0.02	2.22 ± 0.13
	IAM 6-2	C-L3391	Quartz*	100–150	1.05	11 ± 4	1.63 ± 0.08	5.73 ± 0.33	1.28 ± 0.05	0.19 ± 0.02	1.99 ± 0.16
	IAM 6-3	C-L3392	Quartz*	100–150	1.50	6 ± 2	1.49 ± 0.10	5.62 ± 0.41	1.22 ± 0.07	0.17 ± 0.02	1.98 ± 0.10
	IAM 6-4	C-L3393	Quartz*	100–150	2.42	5 ± 1	0.90 ± 0.06	2.83 ± 0.21	0.61 ± 0.04	0.15 ± 0.02	1.11 ± 0.08
	IAM 6-4	C-L3393	Feldspar	100–150	2.42	5 ± 1	0.90 ± 0.06	2.83 ± 0.21	0.61 ± 0.04	0.15 ± 0.02	1.66 ± 0.10
	IAM 6-5	C-L3395	Quartz*	100–150	4.50	12 ± 4	1.39 ± 0.10	5.88 ± 0.43	1.18 ± 0.07	0.11 ± 0.01	1.76 ± 0.12
	IAM 6-5	C-L3395	Feldspar	100–150	4.50	12 ± 4	1.39 ± 0.10	5.88 ± 0.43	1.18 ± 0.07	0.11 ± 0.01	2.41 ± 0.13
	IAM 6B1	C-L3544	Quartz*	100–150	1.65	4 ± 1	1.41 ± 0.21	4.94 ± 0.36	1.05 ± 0.06	0.17 ± 0.02	1.80 ± 0.09
	IAM 6B2	C-L3545	Quartz*	100–150	1.65	4 ± 1	1.38 ± 0.10	4.67 ± 0.34	1.01 ± 0.06	0.17 ± 0.02	1.73 ± 0.08
IAM 29	IAM 29-1	C-L3828	Quartz	100–150	0.90	10 ± 3	1.33 ± 0.07	5.41 ± 0.33	1.12 ± 0.01	0.20 ± 0.02	1.83 ± 0.05
	IAM 29-2	C-L3829	Feldspar	100–150	1.97	12 ± 4	1.60 ± 0.09	5.77 ± 0.35	1.02 ± 0.01	0.16 ± 0.02	2.36 ± 0.12
Wadi bed	Modern sample	C-L3542	Quartz*	100–150	0.10	4 ± 1	0.65 ± 0.05	1.60 ± 0.13	0.32 ± 0.02	0.26 ± 0.03	0.82 ± 0.06

the Wadi Selloum catchment. Based on single-grain feldspar measurements, Reimann et al. (2012) have shown a dependence between the luminescence intensity and the internal K content. Hence, only the brightest grains have an average K content of 12.5%, whilst the dimmer grains may contain less K (Reimann et al., 2012). A lot of feldspar multiple-grain aliquots were rejected due to weak luminescence signals. Following Reimann et al. (2012) this may hint to overestimated dose rates due to generally dim feldspar grains within the multiple-grain aliquots. However, measurements of individual potassium concentrations are not available for our samples, therefore using an assumed potassium concentration of 12.5 ± 0.5% seems to be the best way to calculate the dose rate.

Insufficient bleaching prior to final deposition is a common bias resulting in age overestimation of fluvial deposits (e.g. Wallinga, 2002). First investigations on modern quartz samples collected in the Wadi Selloum catchment showed that partial bleaching influenced samples with residual doses as high as 46 Gy (Bartz et al., 2015). This is not necessarily redundant for older samples, but with a mean residual dose of ~11 Gy it should influence especially the younger samples (Bartz et al., 2015; Jain et al., 2004; Murray et al., 2012). Overall agreement of quartz and feldspar ages indicates that both luminescence signals are able to date the true burial age of the ephemeral stream deposits. Since the time required for complete resetting of the pIRIR$_{290}$ signal is much longer than that of the OSL signal, this convergence is only possible when both luminescence signals are well bleached before deposition (Murray et al., 2012; Thomsen et al., 2016).

Post-depositional processes were observed in our micromorphological studies (TS group 2; Fig. 8) which confirm biological activity (e.g. passage features) that leads to sediment mixing. These post-depositional processes and processes during deposition (i.e. partial resetting of the luminescence signal) should be carefully considered for luminescence samples with large scatter in the D_e distribution (Bateman et al., 2003; Murray et al., 2012). Sample C-L3828, collected in a Bk horizon (Fig. 5), shows significant scatter in the quartz D_e distribution when using both small aliquots (1 mm) and single grains (Fig. 10b). We interpret that the large D_e scatter derives mainly from post-depositional processes in the sediment layer. Therefore, the minimum age model (Galbraith et al., 1999) is not suitable for D_e determination, since bioturbated samples might be contributed by low and high D_e values, in contrast to partially bleached samples (Bartz et al., 2015; Bateman et al., 2007). When comparing our single-grain CAM dose to that of the multiple-grain CAM dose, then the single-grain dose systematically underestimates the multiple-grain dose, which is similar to investigations of Thomsen et al. (2016). In the single-grain data set, ~38% of all grains yielded OSL signals in saturation, which might be the result of transported grains from lower sediment horizons. On the one hand, the use of multiple-grain aliquots might not be appropriate, since single grains with high doses contribute to the cumulative light sum of multiple-grain aliquots which would be rejected on the single-grain base. In this case the true burial age might be overestimated when using multiple-grain aliquots. On the other hand, it is still questionable whether the single-grain dose is underestimated due to many rejected saturated grains. Bearing in mind that an age cross-check does not exist for sample C-L3828, we carefully interpret that the CAM dose might give us a burial age of 18 ± 3 ka on the single-grain base (Table 3), but should rather be considered as minimum age. It should also be taken with caution that the sampling location of sample C-L3828 (profile IAM 29; unit 5; Fig. 5) is affected by carbonate movements over time. Precipitation of secondary carbonates in the Bk horizon influences the external dose rate which is thus not constant since burial due to carbonate replacements of water and air in the sediment pores (Nathan and Mauz, 2008).

Luminescence dating of ephemeral stream sediments still remains challenging due to complex luminescence characteristics. Although independent age control was not available to cross-check our luminescence results in the Wadi Selloum, thorough laboratory experiments and inter-method comparisons between OSL and pIRIR$_{290}$ allow for establishing a reliable chronology of the Wadi Selloum deposits.

5.2. Pedogenetic features in ephemeral stream deposits of Wadi Selloum

Soil forming processes are observed in the Wadi Selloum deposits and may serve as environmental marker to detect landscape changes (Eppes et al., 2008). The accumulation or translocation of secondary carbonates are obvious in the three identified soils in our study. Channel or chamber microstructures reflect biological activity in the form of root growth and soil mesofauna. Mammilated or spherical and often elongated mineral excrements of high packing density and slightly reddish-brown colour resemble earthworm casts of *Lumbricidae* (Stoops, 2003). Aldeias et al. (2014) observed similar excrements in Last Glacial deposits of the Contrebandiers Cave (Western coast of Morocco), and related them to earthworms. Earthworm calcite was not detected in thin sections of our study. Therefore, it is still unclear, which type of soil-dwelling mesofauna produced these excrements. It is likely that the circular to ellipsoid burrows, showing well-formed walls and defined as sediment cocoons, were built by solitary wasp, as also suggested by Aldeias et al. (2014) for similar burrows at Contrebandiers Cave. Moreover, weakly expressed redoximorphic features such as Fe and Mn nodules are further indicators of pedogenesis. Formation of these features is mediated by microbial reduction of Fe and Mn in the presence of organic matter under reducing conditions and precipitation as oxides in the presence of oxygen, for instance under the influence of water table fluctuations (Lindbo et al., 2010).

During the late Holocene a weak Fluvisol (soil II) developed in profile IAM 6, whilst earlier pedogenesis is evident from the well-preserved Calcisol (soil I) in profiles IAM 28 and IAM 29 that developed during the mid- and early Holocene. The palaeosol in profiles IAM 28 and IAM 29 shares common features with the Calcisol (Bk horizon), but developed during the Late Pleistocene. Similarly, Badía et al. (2015) have shown that in semiarid NE Spain young soils of the Late Holocene are Calcaric Fluvisols and older soils developed since the Holocene-Pleistocene boundary are Haplic Calcisols. Nevertheless, changes of pedogenic properties over time cannot be regularly age-related due to the variability of the climate along the Late Pleistocene (Badía et al., 2009). The older Calcisol (palaeosol) post-dates 74 ± 6 ka (pIRIR$_{290}$; C-L3829) and indicates the oldest recorded soil in the Wadi Selloum deposits. The palaeosol sequence was only captured in two profiles, illustrating the high variability in degradation and aggradation processes of such ephemeral stream systems (Bull, 1997). Yet, information about pedogenesis during MIS 3 are not documented in terrestrial archives from NE Morocco. Eppes et al. (2008) have suggested that pedogenic carbonate precipitates during drier climates and is susceptible to dissolution during wetter periods in Italy. In Southern Spain, García-García et al. (2016) have shown Calcisol development between >44 and 34 ka due to more humid climate conditions.

5.3. Morphodynamic phases during the last 100 ka

Based on sediment characteristics and luminescence ages, chronostratigraphies for the four profiles are proposed (Fig. 11), and observed similarities between profiles are referred to as layers in the following.

5.3.1. Layer I – oldest channel deposits

Given its age (>74 ± 6 ka) and its high degree of solidification, we suggest that the lowermost gravel layer I (C1) of profiles IAM 28 and IAM 29 might represent the oldest channel deposits of Wadi Selloum

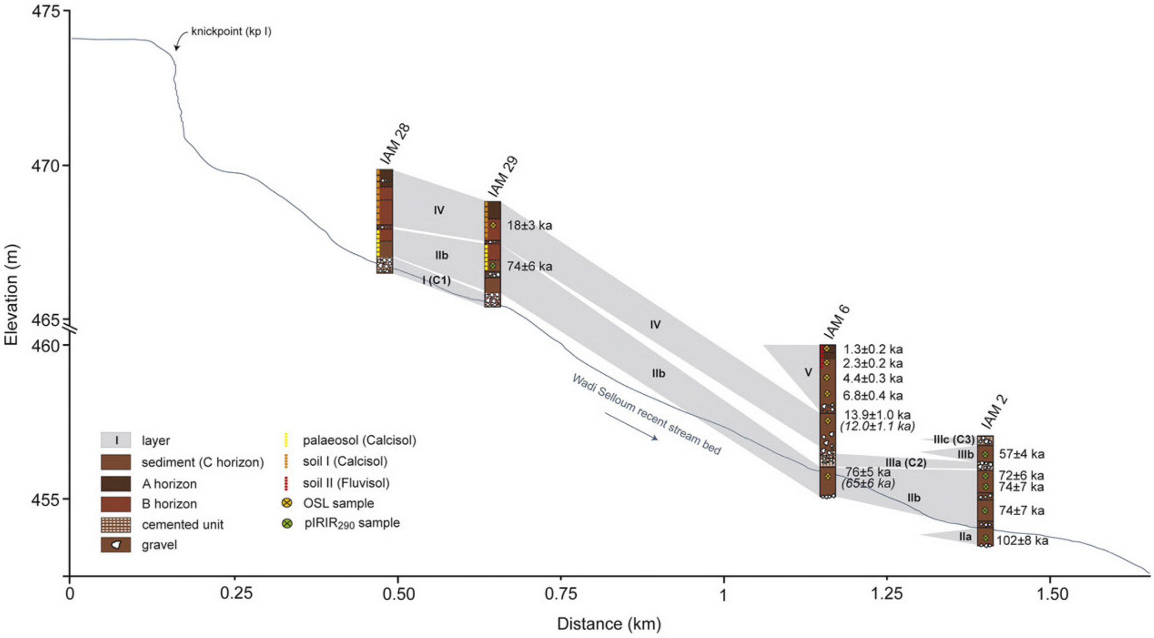

Fig. 11. Correlation of sedimentary layers of the studied profiles IAM 2, IAM 6, IAM 28 and IAM 29. In profile IAM 6 two samples were dated by OSL and pIRIR$_{290}$ for an inter-method comparison; the pIRIR$_{290}$ ages are presented in brackets.

(Figs. 5, 6). Similar observations were reported from a wadi system in Jordan, where variable degrees of carbonate cementation affected younger and older channel deposits (i.e. channel calcretes; McLaren, 2004). The absence of layer I in profile IAM 2 (dated to 102 ± 8 ka at its base) underlines the longitudinal discontinuity of ephemeral stream deposits (Bull, 1997). Such systems are characterised by significant channel changes over time, particularly related to the occurrence of high-energy flash floods (Patton and Schumm, 1981; Poesen and Hooke, 1997), as demonstrated by intense morphological changes during six decades in ephemeral stream channels of eastern Spain (Segura-Beltrán and Sanchis-Ibor, 2013).

5.3.2. Layer II – ephemeral stream deposits around 100 ka and 75 ka

The fine-grained sediments (layer II) can be subdivided in layers IIa and IIb with luminescence ages of ~100 (MIS 5c) and ~75 ka (MIS 5a), respectively. Whilst layer IIa is only observed in profile IAM 2 (Fig. 3), the silty/clay-rich layer IIb is evident in all profiles and seems thus pointing to enhanced aggradation during MIS 5a. It is characterised by a large amount of local material (carbonate, dolomite) and a minor component of allochthonous aeolian sediments (quartz, K-feldspar, plagioclase). It is not straightforward to correlate these massive, unstratified ~2.50 m-thick deposits in profile IAM 2 with one or several flooding event(s) around 75 ka. Contrary to coarse-grained gravels, fine-grained sediments (silts/clays) might also have been transported by hillslope processes and not deposited as overbank sediments (Bull, 1997; Patton and Schumm, 1981). Increasing stabilisation of the land surface by vegetation, confirmed by the development of the palaeosol (Calcisol), may have led to enhanced sedimentation of finer sediments (Sandercock et al., 2007).

5.3.3. Layer III – palaeochannel features and overbank aggradation around 55 ka

In profile IAM 2, the cemented layers IIIa (C2) and IIIc (C3) show similar characteristics to channel calcretes described in the Tabernas Basin in SE Spain (Nash and Smith, 2003). The active stream bed of Wadi Selloum at knickpoints kp I and kp II revealed dm-thick $CaCO_3$-cemented layers at the base of gravel deposits (Fig. 2a, b). The development of these calcretes seems closely related to along-channel subsurface waters, extremely rich in carbonate, originating from the local Mesozoic rocks (Benjelloun et al., 1971). The assumption of geomorphologically stable surfaces and enhanced pedogenetic processes with subsequent calcrete development for C2 and C3 seems unrealistic because these rather thin calcretes show no evidence of hardpan formation (Candy et al., 2003). We therefore assume that layers C2 and C3 correspond to palaeochannels, located higher in the stratigraphic sequence than the present stream bed: +2.50 m (C2) and +4.0 m (C3), with respective aggradation periods of ~72 ka/~55 ka and <55 ka. Apparently, only sediments from the beginning of MIS 3 could be identified in profile IAM 2, whilst other investigated profiles do not show characteristics of MIS 3 deposits.

5.3.4. Layer IV – aggradation around 15 ka

After a phase of morphodynamic stability attested by the palaeosol (Calcisol; layer II; profiles IAM 28 and IAM 29), the layer IV is visible in profiles IAM 6, IAM 28 and IAM 29 (Fig. 11), reflecting enhanced aggradation which took place at least between 18 ± 3 ka and 13.9 ± 1.0 ka (Bartz et al., 2015). It is characterised by coarse silt to fine sand particles and high contents of allochthonous minerals (quartz, K-feldspar and plagioclase), which may suggest that aeolian input increased during MIS 2. Profile IAM 6 presents an erosional disconformity of coarser sediments (unit 3; Fig. 4), indicating enhanced hillslope deposition, characterised by unsorted angular deposits, after ~14 ka.

5.3.5. Layer V – Holocene aggradation, landscape stability and recent incision

Only represented in profile IAM 6, the Holocene sequence between 6.8 ± 0.4 ka and 1.3 ± 0.2 ka (layer V, Figs. 4, 11) seems to display relative stability of the landscape and subsequent sediment trapping (Sandercock et al., 2007). The weakly developed Fluvisol (soil II) in the upper part of profile IAM 6 reflects the development of a stable land surface during the late Holocene, at least since ~1.3 ka. Afterwards, fluvial incision seems to be the dominant process in the catchment. Nowadays, the landscape is only covered by sparse vegetation due to intensive anthropogenic land use, which, in turn, induces soil degradation and erosion. This might have been the main reason for enhanced incision during recent times.

5.4. Correlation with the archaeological sequence of Ifri n'Ammar and Late Quaternary palaeoenvironmental records of the Western Mediterranean region

The chronostratigraphies of the ephemeral stream deposits and of the archaeological sequence of Ifri n'Ammar are both discontinuous and span the time periods comprised between 102 ± 8 to 1.3 ± 0.2 ka (Table 3) and 171 ± 12 ka to 11.7 ± 0.4 cal ka BP (Nami and Moser, 2010; Richter et al., 2010), respectively. Fig. 12 summarises the correlation between morphodynamic phases of Wadi Selloum, the archaeological data of Ifri n'Ammar (Linstädter et al., 2012; Nami and Moser, 2010) as well as palaeoclimate records retrieved off the coast of West Africa as well as in the Alboran Sea and the Aegean Sea (Ehrmann et al., 2013; Pérez-Folgado et al., 2004; Tjallingii et al., 2008).

5.4.1. MIS 5

The deposition of layer II correlates with MIS 5c (IIa) and MIS 5a (IIb). Given the uncertainty affecting both the TL ages of the archaeological sequence and our luminescence ages, layer II only matches the Middle Palaeolithic period around 83 ± 6 ka in Ifri n'Ammar (Nami and Moser, 2010; Richter et al., 2010). MIS 5c and MIS 5a are marked by warmer conditions in the Alboran Sea (Pérez-Folgado et al., 2004). Additionally, two distinct African Humid Periods (AHP) are attested during MIS 5c (>105–95 ka; Ehrmann et al., 2013) and MIS 5a (83.5–72 ka; Ehrmann et al., 2013) characterised by a more humid climate and enhanced precipitation (Ehrmann et al., 2013). Such warm and humid conditions can be seen as favourable for human occupation, somehow verified by extensive findings of Middle Palaeolithic artefacts in Ifri n'Ammar (Nami and Moser, 2010). Likewise, MIS 5 appears to be an intense period of AMH settling in coastal areas of Morocco (e.g. Campmas et al., 2015).

5.4.2. MIS 4–MIS 3

From the four investigated profiles, only one luminescence age points to MIS 4–MIS 3 (profile IAM 2). In parallel to this time period during which little aggradation is observed in our ephemeral stream system, few information is available for the final stage of the Middle Palaeolithic and the early Upper Palaeolithic in Ifri n'Ammar. This

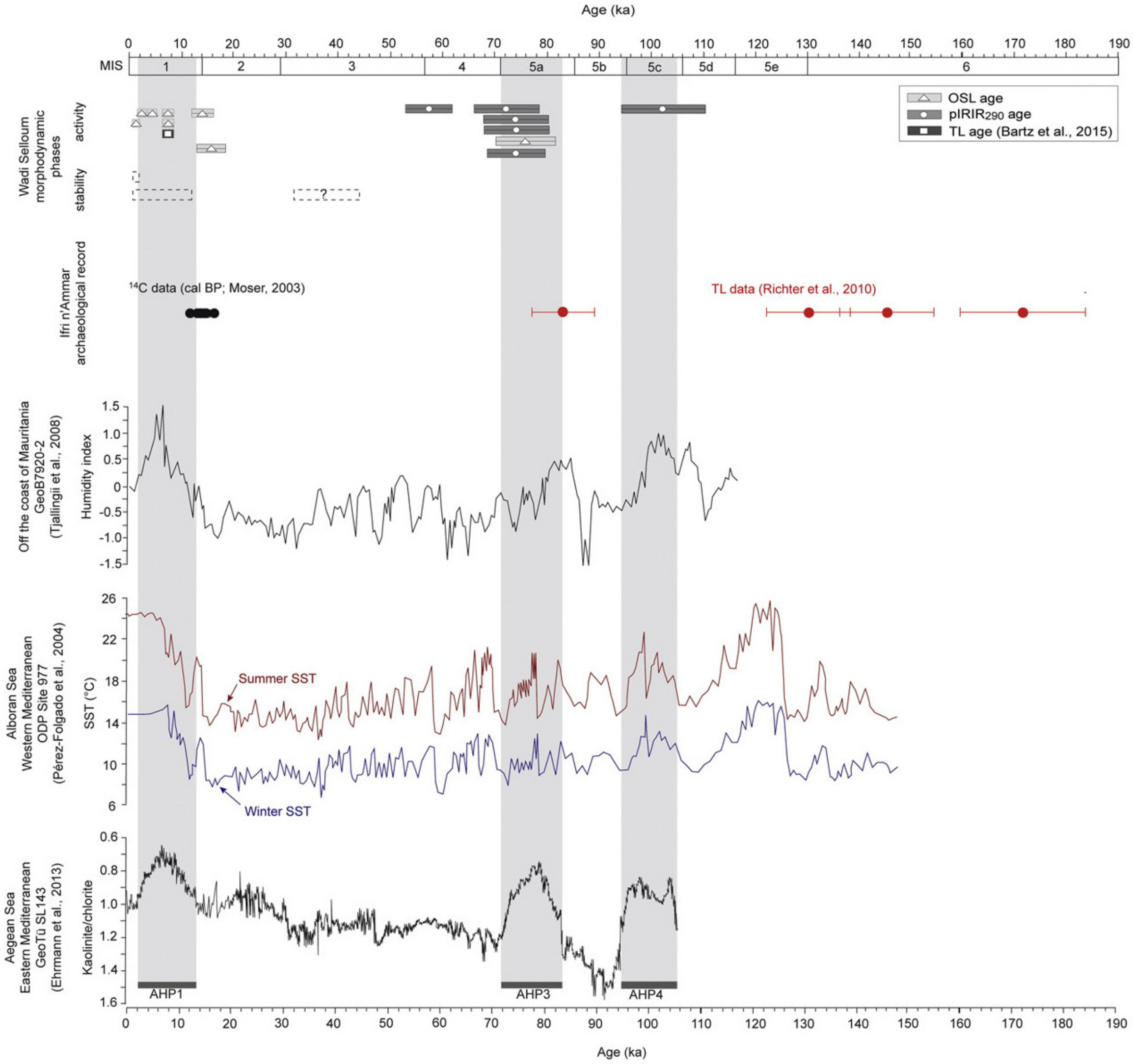

Fig. 12. Correlation between morphodynamic phases of Wadi Selloum, archaeological data of Ifri n'Ammar (Moser, 2003; Richter et al., 2010), as well as palaeoclimate records from the Mediterranean region (Ehrmann et al., 2013; Pérez-Folgado et al., 2004; Tjallingii et al., 2008). MIS = marine isotope stage; AHP = African humid period.

might indicate that human occupation in this region declined between ~50 ka and the end of Heinrich Event (HE) 2 around 24 ka (Linstädter et al., 2012). Tjallingii et al. (2008) have described MIS 4 as an arid period. Also, a higher supply of aeolian material in the Mediterranean from the North African deserts indicates drier conditions (Ehrmann et al., 2013). Additionally, the coldest sea surface temperatures occurred during MIS 4, especially around 60 ka (Pérez-Folgado et al., 2004). MIS 3 is characterised by climatic variations linked to North Atlantic HE and Dansgaard-Oeschger (D/O) cycles reflected by several proxy records of marine sediments from the Alboran Sea (Moreno et al., 2002; Moreno, 2012). Tjallingii et al. (2008) have mentioned abrupt millennial-scale alternations of arid and humid events during MIS 3. Other fluvial records from the Iberian Peninsula have shown that river sediments of MIS 4 and MIS 3 are usually not observed (Santisteban and Schulte, 2007). Due to the development of the palaeosol post-dating 74 ± 6 ka (Fig. 5), increased stabilisation of the land surface together with enhanced vegetation growth may be assumed, probably during MIS 3, when more humid conditions prevailed.

5.4.3. MIS 2

The aggradation time span of layer IV (at least 18 ± 3 ka to 13.9 ± 1.0 ka) fairly well matches the period of the Iberomaurusian culture in north-western Africa (Linstädter et al., 2012), particularly well represented in the archaeological sequence of Ifri n'Ammar (Moser, 2003; Nami and Moser, 2010). In the latter, this culture was characterised by mollusc consumption during the Bølling-Allerød interstadial period (Zielhofer, 2007). Based on fluvial archives of the lower Kert River (Fig. 1a), which include deposits from the Bølling-Allerød and the Younger Dryas (Barathon et al., 2000), El Amrani et al. (2008) inferred a cool and humid (partly arid) climate after 30 ka BP, mainly characterised by sediment aggradation. A highly consistent picture of river activity is evidenced across the Mediterranean basin during MIS 2 (Macklin et al., 2002). This is in agreement with other fluvial basins in the Mediterranean (Santisteban and Schulte, 2007).

5.4.4. Holocene

The middle to late Holocene aggradation recorded in layer V (6.8 ± 0.4 ka to 1.3 ± 0.2 ka, Fig. 11) is concomitant with the Neolithic period, which is not represented in the archaeological sequence. However, numerous Neolithic traces are observed in the entrance talus of the cave, and confirmed by a TL-dated pottery shard (7.4 ± 0.6 ka) extracted from the profile IAM 6 (Bartz et al., 2015). The onset of the Neolithic period in this region was related to the Mediterranean climate optimum around 7.5 ka (Zielhofer and Linstädter, 2006). However, the more humid Neolithic period seems to have been interrupted by a more arid event around 6–5 cal ka BP (Fletcher and Zielhofer, 2013). The perennial Kert River reflects high aggradation rates in mid- to late Holocene times (El Amrani et al., 2008). This is in agreement with Zielhofer et al. (2010), who reported flood activity in the Lower Moulouya River particularly during an arid event between 3.2 and 2.7 cal ka BP. This short climatic event is also reflected in the alluvial sequences of the Medjerda River in Tunisia (Faust et al., 2004).

Channel-parallel layering of terrestrial gastropods (e.g. *Otala* cf. *lactea*) and charcoal remains around 2.3 ± 0.2 ka (Fig. 4) might point to a palaeo-surface. It was, however, not long enough stable for a pronounced soil formation, as evidenced by the sparsity of pedofeatures visible in TS 6.1 and preserved stratification of the Fluvisol (layer V of profile IAM 6; Fig. 4). Therefore, we assume that Wadi Selloum was affected by short-term environmental changes during the late Holocene. Flood variability during that time range is also reported for the rivers Moulouya and Kert (Benito et al., 2015; El Amrani et al., 2008; Ibouhouten et al., 2010; Zielhofer et al., 2010). From marine palaeoclimate records (Fig. 12), an African Humid Period was observed between 14 and 2 ka (Ehrmann et al., 2013). These records would suggest fluvial activity during more humid climate conditions in Wadi Selloum. After ~1.3 ka, the sedimentation appears to have ended in Wadi Selloum. Similar observations were reported from the terrace sequences of the Kert River (El Amrani et al., 2008) and the Moulouya River (Zielhofer et al., 2010).

Since AMH have settled in the vicinity of Ifri n'Ammar for many millennia, human impact on fluvial morphodynamics of Wadi Selloum, though difficult to quantify, may have played a significant role. In particular, the transition of hunter-gatherer communities to agricultural activity resulted in an intensified agricultural land-use that may have triggered soil erosion (Linstädter et al., 2012), which, in turn, activated geomorphologic erosional processes. In southern Morocco, the beginning of the Islamic period around 1.3 ka BP led to expanded pastoralism, deforestation and agriculture, which changed the vegetation structure (McGregor et al., 2009). Schulte (2003) reported that human impact on river dynamics in the Vera and Penedes basins in Spain may have been crucial with respect to magnitude of surface runoff and sedimentation.

6. Summary and conclusion

The discontinuity of ephemeral stream systems underlines the difficulties for interpreting morphodynamic phases in Wadi Selloum. The application of luminescence dating techniques (OSL, pIRIR$_{290}$, TL; see also Bartz et al., 2015) has established for the first time a geochronological framework for ephemeral stream deposits in NE Morocco. Thus, a well-dated ephemeral stream archive is presented, which supports the reconstruction of wadi morphodynamics. The depositional ages for the Wadi Selloum sediment sections show aggradation during MIS 5c and MIS 5a, as well as from after the LGM to the Bølling-Allerød period, and the Holocene. Morphodynamic activity of Wadi Selloum may be linked to humid periods (African Humid Periods: >105–95, 83.5–72 and 14–2 ka; Ehrmann et al., 2013), but should be taken with caution due to the high discontinuity of the studied archive and the uncertainties of the luminescence ages. Pedogenesis may be used as significant environmental marker, indicating more humid climate conditions in form of secondary carbonate precipitation during MIS 3 (Calcisol; palaeosol), since early Holocene times (Calcisol; soil I) and the late Holocene (Fluvisol; soil II).

Nevertheless, the reconstruction of the palaeo-landscape is still challenging due to the high erosional power of the complex ephemeral stream system. A single high-energy flash flood event can cause a significant gap in the sediment archive, which then leads to a discontinuous record. Due to the complexity of the given ephemeral stream system, it is difficult to establish a linkage between the occupation phases of the rock shelter of Ifri n'Ammar on the one hand, and environmental changes on the other hand.

Our data correspond to the time of the Middle Palaeolithic and the Iberomaurusian culture and provide first insights into palaeoenvironmental changes around Ifri n'Ammar. The question whether humans occupied Ifri n'Ammar during warm/wet or cold/dry climate conditions remains open; however, our data may suggest that humans occupied Ifri n'Ammar during wetter and warmer climatic conditions.

Acknowledgements

This project is part of the CRC 806 "Our Way to Europe", which is funded by the *German Research Foundation* (*DFG*) (ref. no. SFB 806/2). The support by the *Institut National des Sciences de l'Archéologie et du Patrimoine du Maroc* (*INSAP*) and by the *Commission for Archaeology of Non-European Cultures* (*KAAK*) of the *German Archaeological Institute* (*DAI*), in particular Josef Eiwanger, is gratefully acknowledged. We thank Rainer Hutterer, Bonn, for his help in the determination of terrestrial gastropods, and Nina Szemkus, Cologne, for her commitment to this project. Three anonymous reviewers are acknowledged for their constructive comments that helped to improve the manuscript.

References

Abdalla, F., El Shamy, I., Bamousa, A.O., Mansour, A., Mohamed, A., Tahoon, M., 2014. Flash floods and groundwater recharge potentials in arid land alluvial basins, southern Red Sea coast, Egypt. Int. J. Geosci. 5, 971–982.

Aldeias, V., Goldberg, P., Dibble, H.L., El-Hajraoui, M., 2014. Deciphering site formation processes through soil micromorphology at Contrebandiers Cave, Morocco. J. Hum. Evol. 69, 8–30.

Auclair, M., Lamothe, M., Huot, S., 2003. Measurement of anomalous fading for feldspar IRSL using SAR. Radiat. Meas. 37, 487–492.

Badía, D., Martí, C., Palacio, E., Sancho, C., Poch, R.P., 2009. Soil evolution over the Quaternary period in a semiarid climate (Segre river terraces, northeast Spain). Catena 77, 165–174.

Badía, D., Martí, C., Casanova, J., Gillot, T., Cuchi, J.A., Palacio, J., Andrês, R., 2015. A Quaternary soil chronosequence study on the terraces of the Alcanadre River (semiarid Ebro basin, NE Spain). Geoderma 241–242, 158–167.

Balescu, S., Lamothe, M., 1993. Thermoluminescence dating of the Holsteinian marine formation of Herzeele, northern France. J. Quat. Sci. 8 (2), 117–124.

Barathon, J.-J., El Abassi, H., Lechevalier, C., Malek, F., Jolly-Saad, M.-C., 2000. Mise au point sur les formations holocênes dans le Rif oriental (Maroc)/A chronology of Holocene deposits in the eastern Rif Mountains (Morocco). Géomorphologie 6 (4), 221–238.

Barcos, L., Jabaloy, A., Azdimousa, A., Asebriy, L., Gómez-Ortis, D., Rodríguez-Peces, M.J., Tejero, R., Pérez-Peña, J.V., 2014. Study of relief changes related to active doming in the eastern Moroccan Rif (Morocco) using geomorphological indices. J. Afr. Earth Sci. 100, 493–509.

Barton, R.N.E., Bouzouggar, A., Collcutt, S.N., Gale, R., Higham, T.F.G., Humphrey, L.T., Parfitt, S., Rhodes, E., Stringer, C.B., Malek, F., 2005. The late upper palaeolithic occupation of the Moroccan northwest Maghreb during the last glacial maximum. Afr. Archaeol. Rev. 22 (2), 77–100.

Bartz, M., Klasen, N., Zander, A., Brill, D., Rixhon, G., Seeliger, M., Eiwanger, J., Weniger, G.-C., Mikdad, A., Brückner, H., 2015. Luminescence dating of ephemeral stream deposits around the palaeolithic site of Ifri n'Ammar (Morocco). Quat. Geochronol. 30, 460–465.

Bateman, M.D., Frederick, C.D., Jaiswal, M.K., Singhvi, A.K., 2003. Investigations into the potential effects of pedoturbation on luminescence dating. Quat. Sci. Rev. 22, 1169–1176.

Bateman, M.D., Boulter, C.H., Carr, A.S., Frederick, C.D., Peter, D., Wilder, M., 2007. Detecting post-depositional sediment disturbance in sandy deposits using optical luminescence. Quat. Geochronol. 2, 57–64.

Beckmann, T., 1997. Präparation bodenkundlicher Dünnschliffe für mikromorphologische Untersuchungen. Hohenheimer Bodenkundliche Hefte. 40, pp. 89–103.

Bell, W.T., 1980. Alpha dose attenuation in quartz grains for thermoluminescence dating. Ancient TL 12, 4–8.

Benito, G., Macklin, M.G., Zielhofer, C., Jones, A.F., Machado, M.J., 2015. Holocene flooding and climate change in the Mediterranean. Catena 130, 13–33.

Benjelloun, S.E., Douïeb, M., Saadi, M., Ennadifi, Y., 1971. Carte Géologique du Maroc. 167, 1:100000, Tistoutine.

Bertrams, M., Protze, J., Löhrer, R., Schyle, D., Richter, J., Hilgers, A., Klasen, N., Schmidt, C., Lehmkuhl, F., 2012. Multiple environmental change at the time of the modern human passage through the Middle East – first results from geoarchaeological investigations on upper Pleistocene sediments in the Wadi Sabra (Jordan). Quat. Int. 274, 55–72.

Blott, S.J., Pye, K., 2001. GRADISTAT: a grain size distribution and statistics package for the analysis of unconsolidated sediments. Earth Surf. Process. Landf. 26, 1237–1248.

Boski, T., Pessoa, J., Pedro, P., Thorez, J., Dias, J.M.A., Hall, I.R., 1998. Factors governing abundance of hydrolysable amino acids in the sediments from the NW European continental margin (47–50°N). Prog. Oceanogr. 42, 145–164.

Bøtter-Jensen, L., Bulur, E., Duller, G.A.T., Murray, A.S., 2000. Advances in luminescence instrument systems. Radiat. Meas. 32, 523–528.

Bubenzer, O., Hilgers, A., Riemer, H., 2007. Luminescence dating and archaeology of Holocene fluvio-lacustrine sediments of Abu Tartur, eastern Sahara. Quat. Geochronol. 2, 317–321.

Bull, W.B., 1997. Discontinuous ephemeral streams. Geomorphology 19, 227–276.

Buylaert, J.-P., Jain, M., Murray, A.S., Thomsen, K.J., Thiel, C., Sohbati, R., 2012. A robust feldspar luminescence dating method for middle to late Pleistocene sediments. Boreas 41, 435–451.

Campmas, E., Michel, P., Costamagno, S., Amani, F., Stoetzel, E., Nespoulet, R., El Hajraoui, M.A., 2015. Were upper Pleistocene human/non-human predator occupations at the Témara caves (El Harhoura 2 and El Mnasra, Morocco) influenced by climate change? J. Hum. Evol. 78, 122–143.

Candy, I., Black, S., Sellwood, B.W., Rowan, J.S., 2003. Calcrete profile development in Quaternary alluvial sequences, southeast Spain: implications for using calcretes as a basis for landform chronologies. Earth Surf. Process. Landf. 28, 169–185.

Cook, H.E., Johnson, P.D., Matti, J.C., Zemmels, I., 1975. Methods of sample preparation and X-ray diffraction analysis in x-ray mineralogy laboratory. In: Kaneps, A.G., et al. (Eds.), Init. Rep. DSDP XXVIII. Printing Office, Washington, DC, pp. 997–1007.

Courty, M.-A., Vallverdu, J., 2001. The microstratigraphic record of abrupt climate changes in cave sediments of the western Mediterranean. Geoarchaeology 16 (5), 467–500.

Dietze, M., Kreutzer, S., Burow, C., Fuchs, M.C., Fischer, M., Schmidt, C., 2016. The abanico plot: visualising chronometric data with individual standard errors. Quat. Geochronol. 31, 12–18.

Duller, G.A.T., 2003. Distinguishing quartz and feldspar in single grain luminescence measurements. Radiat. Meas. 37, 161–165.

Durcan, J.A., King, G.E., Duller, G.A.T., 2015. DRAC: dose rate and age calculator for trapped charge dating. Quat. Geochronol. 28, 54–61.

Ehrmann, W., Seidel, M., Schmiedl, G., 2013. Dynamics of late Quaternary North African humid periods documented in the clay mineral record of central Aegean Sea sediments. Glob. Planet. Chang. 107, 186–195.

El Amrani, M., Macaire, J.-J., Zarki, H., Bréhéret, J.-G., Fontugne, M., 2008. Contrasted morphosedimentary activity of the lower Kert River (northeastern Morocco) during the late Pleistocene and the Holocene. Possible impact of bioclimatic variations and human action. Compt. Rendus Geosci. 340, 533–542.

Eppes, M.C., Bierma, R., Vinson, D., Pazzaglia, F., 2008. A soil chronosequence study of the Reno valley, Italy: insights into the relative role of climate versus anthropogenic forcing on hillslope processes during the mid-Holocene. Geoderma 147, 97–107.

Esri, 2014. DigitalGlobe, Earthstar Geographics, CNES/Airbus DS, GeoEye, USDA FSA, USGS, Getmapping, Aerogrid, IGN, IGP, Swisstopo, and the GIS User Community.

FAO; Food and Agriculture Organization of the United Nations, 2006n. Guidelines for Soil Description. fourth ed. Rome.

Faust, D., Zielhofer, C., Baena Escudero, R., Diaz del Olmo, F., 2004. High-resolution fluvial record of late Holocene geomorphic change in northern Tunisia: climatic or human impact? Quat. Sci. Rev. 23, 1757–1775.

Fedoroff, N., Courty, M.-A., 2013. Revisiting the genesis of red Mediterranean soils. Turk. J. Earth Sci. 22, 359–375.

Fletcher, W.J., Zielhofer, C., 2013. Fragility of western Mediterranean landscapes during Holocene rapid climate changes. Catena 103, 16–29.

Folk, R.L., Ward, W.C., 1957. Brazos River bar: a study in the significance of grain size parameters. J. Sediment. Petrol. 27, 3–26.

Galbraith, R.F., 2005. Statistics for Fission Track Analysis. Chapman & Hall/CRC, Boca Raton.

Galbraith, R.F., Green, P.F., 1990. Estimating the component ages in a finite mixture. Nucl. Tracks Radiat. Meas. 17 (3), 197–206.

Galbraith, R.F., Roberts, R.G., Laslett, G.M., Yoshida, H., Olley, J.M., 1999. Optical dating of single and multiple grains of quartz from Jinmium rock shelter, northern Australia: part I, experimental design and statistical models. Archaeometry 41 (2), 339–364.

García-García, F., Calero, J., Pérez-Valera, F., 2016. Morphological, pedological, and sedimentary evolution on the fringe of the southwestern European drylands during the late Pleistocene and Holocene: evidence of climate and land use changes. Catena 143, 128–139.

Guérin, G., Mercier, N., Adamiec, G., 2011. Dose-rate conversion factors: update. Ancient TL 29, 5–8.

Guérin, G., Mercier, N., Nathan, R., Adamiec, G., Lefrais, Y., 2012. On the use of the infinite matrix assumption and associated concepts: a critical review. Radiat. Meas. 47, 778–785.

Heiri, O., Lotter, A.F., Lemcke, G., 2001. Loss on ignition as a method for estimating organic and carbonate content in sediments: reproducibility and comparability of results. J. Paleolimnol. 25, 101–110.

Huntley, D.J., Baril, M.R., 1997. The K content of the K-feldspars being measured in optical dating or in thermoluminescence dating. Ancient TL 15 (1), 11–13.

Huntley, D.J., Lamothe, M., 2001. Ubiquity of anomalous fading in K-feldspars and the measurement and correction for it in optical dating. Can. J. Earth Sci. 38, 1093–1106.

Ibouhouten, H., Zielhofer, C., Mahjoubi, R., Kamel, S., Linstädter, J., Mikdad, A., Bussmann, J., Werner, P., Härtling, J.W., Fenech, K., 2010. Archives alluviales holocêne et occupation humaine en Basse Moulouya (Maroc nord-oriental). Géomorphologie 16, 41–56.

IUSS Working Group WRB, 2014. World reference base for soil resources 2014. International Soil Classification System for Naming Soils and Creating Legends for Soil Maps. World Soil Resources Reports No. 106. FAO, Rome.

Jain, M., Murray, A.S., Bøtter-Jensen, L., 2004. Optically stimulated luminescence dating: how significant is incomplete light exposure in fluvial environments? Quaternaire 15 (1–2), 143–157.

Kars, R.H., Reimann, T., Ankjærgaard, C., Wallinga, J., 2014. Bleaching of the post-IR IRSL signal: new insights for feldspar luminescence dating. Boreas 43, 780–791.

Klasen, N., Hilgers, A., Schmidt, C., Bertrams, M., Schyle, D., Lehmkuhl, F., Richter, J., Radtke, U., 2013. Optical dating of sediments in Wadi Sabra (SW Jordan). Quat. Geochronol. 18, 9–16.

Komatsu, T., Tsukamoto, S., 2015. Late Glacial lake-level changes in the Lake Karakul basin (a closed glacierized-basin), eastern Pamirs, Tajikistan. Quat. Res. 83, 137–149.

Kreutzer, S., Schmidt, C., Fuchs, M.C., Dietze, M., Fischer, M., Fuchs, M., 2012. Introducing an R package for luminescence dating analysis. Ancient TL 30 (1), 1–8.

Li, B., Li, S.-H., 2012. A reply to the comments by Thomsen et al. on "Luminescence dating of K-feldspar from sediments: a protocol without anomalous fading correction". Quat. Geochronol. 8, 49–51.

Lindbo, D.L., Stolt, M.H., Vepraskas, M.J., 2010. Redoximorphic features. In: Stoops, G., Marcelino, V., Mees, F. (Eds.), Interpretation of Micromorphological Features of Soils and Regoliths. Elsevier, Amsterdam, pp. 129–147.

Linstädter, J., Eiwanger, J., Mikdad, A., Weniger, G.-C., 2012. Human occupation of Northwest Africa: a review of middle Palaeolithic to Epipalaeolithic sites in Morocco. Quat. Int. 274, 158–174.

Lubell, 2001. Late Pleistocene-early Holocene Maghreb. In: Peregrine, P.N., Ember, M. (Eds.), The Encyclopedia of Prehistory. 1, pp. 129–149 (Africa, Plenum, New York).

Macklin, M.G., Fuller, I.C., Lewin, J., Maas, G.S., Passmore, D.G., Rose, J., Woodward, J.C., Black, S., Hamlin, R.H.B., Rowan, J.S., 2002. Correlation of fluvial sequences in the Mediterranean basin over the last 200 ka and their relationship to climate change. Quat. Sci. Rev. 21, 1633–1641.

McGregor, H.V., Dupont, L., Stuut, J.-B.W., Kuhlmann, H., 2009. Vegetation change, goats, and religion: a 2000-year history of land use in southern Morocco. Quat. Sci. Rev. 28 (15–16), 1434–1448.

McLaren, 2004. Characteristics, evolution, and distribution of Quaternary channel calcretes, southern Jordan. Earth Surf. Process. Landf. 29, 1487–1507.

Mikdad, A., Moser, J., Ben-Ncer, A., 2002. Recherche préhistoriques dans le gisement d'Ifri n'Ammar au Rif Oriental (Maroc). Premiers résultats. Beiträge zur Allgemeinen und Vergleichenden Archäologie 22, 1–20.

Mikdad, A., Moser, J., Nami, M., Eiwanger, J., 2004. La stratigraphie du site Ifri n'Ammar (Rif Oriental, Maroc): premiers résultats sur les dépôts du Paléolithique moyen. Beiträge zur Allgemeinen und Vergleichenden Archäologie 24, 125–137.

Mook, D.H., Hoskin, C.M., 1982. Organic determinations by ignition: caution advised. Estuar. Coast. Shelf Sci. 15 (6), 697–699.

Moore, D.M., Reynolds, R.C., 1997. X-ray Diffraction and the Identification and Analysis of Clay Minerals. Oxford University Press, Oxford.

Moreno, A., 2012. A multiproxy paleoclimate reconstruction over the last 250 kyr from marine sediments: the northwest African margin and the western Mediterranean sea. In: Hublin, J.-J., McPherron, S.P. (Eds.), Modern Origins. A North African Perspective, Vertebrate Paleobiology and Paleoanthropology. Springer Science and Business Media, Heidelberg, New York, London.

Moreno, A., Cacho, I., Canals, M., Prins, M.A., Sánchez-Goñi, M.F., Grimalt, J.O., Weltje, G.J., 2002. Saharan dust transport and high-latitude glacial climatic variability: the Alboran Sea record. Quat. Res. 58, 318–328.

Moser, J., 2003. La Grotte d'Ifri n'Ammar, Tome 1, L'Ibéromaurusien. AVA-Forschungen Band 8. Linden Soft.

Murray, A.S., Wintle, A.G., 2000. Luminescence dating of quartz using an improved single-aliquot regenerative-dose protocol. Radiat. Meas. 32, 57–73.

Murray, A.S., Wintle, A.G., 2003. The single aliquot regenerative dose protocol: potential for improvements in reliability. Radiat. Meas. 37, 377–381.

Murray, A.S., Thomsen, K.J., Masuda, F., Buylaert, J.P., Jain, M., 2012. Identifying well-bleached quartz using the different bleaching rates of quartz and feldspar luminescence signals. Radiat. Meas. 47, 688–695.

Nami, M., Moser, J., 2010. La grotte d'Ifri n'Ammar. Le Paléolithique moyen. Forschungen zur Archäologie Außereuropäischer Kulturen vol. 9. Reichert Verlag, Wiesbaden.

Nash, D.J., Smith, R.F., 2003. Properties and development of channel calcretes in a mountain catchment, Tabernas basin, southeast Spain. Geomorphology 50, 227–250.

Nathan, R.P., Mauz, B., 2008. On the dose-rate estimate of carbonate-rich sediments for trapped charge dating. Radiat. Meas. 43, 14–25.

Patton, P.C., Schumm, S.A., 1981. Ephemeral-stream processes: implications for studies of Quaternary valley fills. Quat. Res. 15, 24–43.

Pérez-Folgado, M., Sierro, F.J., Flores, J.A., Grimalt, J.O., Zahn, R., 2004. Palaeoclimatic variations in foraminifer assemblages from the Alboran Sea (western Mediterranean) during the last 150 ka in ODP site 977. Mar. Geol. 212, 113–131.

Pissart, A., Boumeaza, T., 2010. Âge et origine de la terrasse limoneuse de la basse Moulouya (Maroc nord-oriental). Bulletin de la Société Géographique de Liège 54, 85–96.

Poesen, J.W.A., Hooke, J.M., 1997. Erosion, flooding and channel management in Mediterranean environments of southern Europe. Prog. Phys. Geogr. 21 (2), 157–199.

Prescott, J.R., Hutton, J.T., 1994. Cosmic ray contributions to dose rates for luminescence and ESR dating: large depths and long-term time variations. Radiat. Meas. 23, 497–500.

Preusser, F., Andersen, B.G., Denton, G.H., Schlüchter, C., 2005. Luminescence chronology of late Pleistocene glacial deposits in north Westland, New Zealand. Quat. Sci. Rev. 24, 2207–2227.

Reimann, T., Thomsen, K.J., Jain, M., Murray, A.S., Frechen, M., 2012. Single-grain dating of young sediments using the pIRIR signal from feldspar. Quat. Geochronol. 11, 28–41.

Richter, D., Moser, J., Nami, M., Eiwanger, J., Mikdad, A., 2010. New chronometric data from Ifri n'Ammar (Morocco) and the chronostratigraphy of the middle Palaeolithic in the western Maghreb. J. Hum. Evol. 59 (6), 672–679.

Rixhon, G., Briant, R.M., Cordier, S., Duval, M., Jones, A., Scholz, D., Revealing the pace of river landscape evolution during the Quaternary: recent developments in numerical dating methods, Quat. Sci. Rev., http://dx.doi.org/10.1016/j.quascirev.2016.08.016 (in press).

Rixhon, G., Bartz, M., El Ouahabi, M., Szemkus, N., Brückner, H., 2017. Contrasting terrace systems of the lower Moulouya river as indicator of crustal deformation in NE Morocco. J. Afr. Earth. Sci. 126, 45–57.

Sandercock, P.J., Hooke, J.M., Mant, J.M., 2007. Vegetation in dryland river channels and its interaction with fluvial processes. Prog. Phys. Geogr. 31 (2), 107–129.

Santisteban, J.I., Schulte, L., 2007. Fluvial networks of the Iberian peninsula: a chronological framework. Quat. Sci. Rev. 26, 2738–2757.

Schulte, L., 2003. River response and terrace agradation in the Mediterranean Iberian peninsula during historical times. In: Thorndycraft, V.R., Benito, G., Barriendos, M., Llasat, C. (Eds.), Palaeofloods, Historical Floods and Climatic Variability: Applications in Flood Risk Assessment (Proceedings of the PHEFRA Workshop, Barcelona, 16th–19th October, 2002).

Segura-Beltrán, F., Sanchis-Ibor, C., 2013. Assessment of channel changes in a Mediterranean ephemeral stream since the early twentieth century. The Rambla de Cervera, eastern Spain. Geomorphology 201, 199–214.

Snoussi, M., Haida, S., Imassi, S., 2002. Effects of the construction of dams on the water and sediment fluxes of the Moulouya and the Sebou rivers, Morocco. Reg. Environ. Chang. 3, 5–12.

Stoops, 2003. Guidelines for Analysis and Description of Soil and Regolith Thin Sections. Soil Science Society of America, Inc., Madison, Wisconsin.

Sutherland, 1998. Loss-on-ignition estimates of organic matter and relationships to organic carbon in fluvial bed sediments. Hydrobiologia 389, 153–167.

Thiel, C., Buylaert, J.P., Murray, A.S., Tsukamoto, S., 2011. On the applicability of post-IR IRSL dating to Japanese loess. Geochronometria 38, 369–378.

Thomsen, K.J., Murray, A.S., Jain, M., Bøtter-Jensen, L., 2008. Laboratory fading rates of various luminescence signals from feldspar-rich sediment extracts. Radiat. Meas. 43, 1474–1486.

Thomsen, K.J., Murray, A.S., Buylaert, J.P., Jain, M., Hansen, J.H., Aubry, T., 2016. Testing single-grain quartz OSL methods using sediment samples with independent age control from the Bordes-Fitte rockshelter (Roches d'Abilly site, central France). Quat. Geochronol. 31, 77–96.

Tjallingii, R., Claussen, M., Stuut, J.-B.W., Fohlmeister, J., Jahn, A., Bickert, T., Lamy, F., Röhl, U., 2008. Coherent high- and low-latitude control of the northwest African hydrological balance. Nat. Geosci. 1, 670–675.

USGS, 2015. NASA EOSDIS Land Processes Distributed Active Archive Center (LP DAAC). USGS/Earth Resources Observation and Science (EROS) Center, Sioux Falls, South Dakota.

Wallinga, J., 2002. Optically stimulated luminescence dating of fluvial deposits: a review. Boreas 31, 303–322.

Wintle, A., 1973. Anomalous fading of thermoluminescence in mineral samples. Nature 245, 143–144.

Wintle, A.G., Murray, A., 2006. A review of quartz optically stimulated luminescence characteristics and their relevance in single-aliquot regeneration dating protocols. Radiat. Meas. 41, 369–391.

Wolf, D., Faust, D., 2015. Western Mediterranean environmental changes: evidences from fluvial archives. Quat. Sci. Rev. 122, 30–50.

Wolf, D., Seim, A., Faust, D., 2014. Fluvial system response to external forcing and human impact – late Pleistocene and Holocene fluvial dynamics of the lower Guadalete River in western Andalucía (Spain). Boreas 43, 422–429.

Zielhofer, C., 2007. Climate change and landscape-ecological effects in the western Mediterranean – future, present and learning from the past. Eur. Reg. 15 (2), 110–118.

Zielhofer, C., Linstädter, J., 2006. Short-term mid-Holocene climatic deterioration in the west Mediterranean region: climatic impact on Neolithic settlement pattern? Z. Geomorphol. N.F. 142, 1–17.

Zielhofer, C., Faust, D., Baena Escudero, R., Diaz del Olmo, F., Kadereit, A., Moldenhauer, K.-M., Porras, A., 2004. Centennial-scale late-Pleistocene to mid-Holocene synthetic profile of the Medjerda Valley, northern Tunisia. The Holocene 14 (6), 851–861.

Zielhofer, C., Faust, D., Linstädter, J., 2008. Late Pleistocene and Holocene alluvial archives in the southwestern Mediterranean: changes in fluvial dynamics and past human response. Quat. Int. 181, 39–54.

Zielhofer, C., Bussmann, J., Ibouhouten, H., Fenech, K., 2010. Flood frequencies reveal Holocene rapid climate changes (lower Moulouya River, northeastern Morocco). J. Quat. Sci. 25 (5), 700–714.

Chapter 4

4 Contrasting terrace systems of the lower Moulouya River as indicator of crustal deformation in NE Morocco

Gilles Rixhon [a], Melanie Bartz [a], Meriam El Ouahabi [b], Nina Szemkus [a], Helmut Brückner [a]

[a] Institute of Geography, University of Cologne, Albertus-Magnus-Platz, 50923 Cologne, Germany

[b] U. R. Argiles, Géochimie et Environnements sédimentaires, Department of Geology, University of Liège, Place du 20 Août 7, 4000 Liège, Belgium

Abstract

The Moulouya River has the largest catchment in Morocco and drains an area characterised by active crustal deformation during the Late Cenozoic due to the N-S convergence between the African and Eurasian plates. As yet, its Pleistocene terrace sequence remains poorly documented. Our study focuses on the lowermost reach of the river in north-eastern Morocco, which drains the Zebra-Triffa sedimentary basin directly upstream of the estuary. New field observations, measurements and sedimentological data reveal contrasting fluvial environments on each side of a newly identified, W-E striking thrust zone disrupting the sedimentary basin. On the one hand, long-lasting fluvial aggradation, materialised by 37 m-thick stacked terraces, has occurred in the footwall of the thrust. On the other hand, the hanging wall is characterised by a well-preserved terrace staircase, with three Pleistocene terrace levels. Whilst the identification of this thrust zone question some previous interpretations about the local (hydro-) geology, it is consistent with the statement that most of the Plio-Quaternary deformation in the eastern Rif Mountains has concentrated in this region of Morocco. Our new data and interpretations also agree with morphometric indicators showing that the whole Moulouya catchment is at disequilibrium state (i.e. several knickzones in its longitudinal profile). We also suggest that the knickzone in the Beni Snassen gorge, located directly upstream of the Zebra-Triffa sedimentary basin, could (partly) result from a transient fluvial reaction to Late Cenozoic thrusting activity and correlated uplift in the hanging wall.

Keywords

Fluvial terraces, River sediments, Late Cenozoic, Thrust zone, Moulouya River, North-eastern Morocco

Published in *Journal of African Earth Sciences* 126 (2017), 45-57.

https://doi.org/10.1016/j.jafrearsci.2016.11.005

Journal of African Earth Sciences 126 (2017) 45–57

Contents lists available at ScienceDirect

Journal of African Earth Sciences

journal homepage: www.elsevier.com/locate/jafrearsci

Contrasting terrace systems of the lower Moulouya river as indicator of crustal deformation in NE Morocco

Gilles Rixhon [a], [*], Melanie Bartz [a], Meriam El Ouahabi [b], Nina Szemkus [a], Helmut Brückner [a]

[a] *Institute for Geography, University of Cologne, Zülpicher Straße 45, 50674 Cologne, Germany*
[b] *Department of Geology, University of Liège, Allée du six Août 14, 4000 Liège, Belgium*

ARTICLE INFO

Article history:
Received 23 December 2015
Received in revised form
4 November 2016
Accepted 7 November 2016
Available online 9 November 2016

Keywords:
Fluvial terraces
River sediments
Late Cenozoic
Thrust zone
Moulouya river
North-eastern Morocco

ABSTRACT

The Moulouya river has the largest catchment in Morocco and drains an area characterized by active crustal deformation during the Late Cenozoic due to the N–S convergence between the African and Eurasian plates. As yet, its Pleistocene terrace sequence remains poorly documented. Our study focuses on the lowermost reach of the river in north-eastern Morocco, which drains the Zebra-Triffa sedimentary basin directly upstream of the estuary. New field observations, measurements and sedimentological data reveal contrasting fluvial environments on each side of a newly identified, W–E striking thrust zone disrupting the sedimentary basin. On the one hand, long-lasting fluvial aggradation, materialized by 37 m-thick stacked terraces, has occurred in the footwall of the thrust. On the other hand, the hanging wall is characterized by a well-preserved terrace staircase, with three Pleistocene terrace levels. Whilst the identification of this thrust zone question some previous interpretations about the local (hydro-) geology, it is consistent with the statement that most of the Plio-Quaternary deformation in the eastern Rif mountains has concentrated in this region of Morocco. Our new data and interpretations also agree with morphometric indicators showing that the whole Moulouya catchment is at desequilibrium state (i.e. several knickzones in its longitudinal profile), showing several knickzones in its longitudinal profile, is at disequilibrium state. We also suggest that the knickzone in the Beni Snassen gorge, located directly upstream of the Zebra-Triffa sedimentary basin, could (partly) result from a transient fluvial reaction to Late Cenozoic thrusting activity and correlated uplift in the hanging wall.

1. Introduction

Located in the convergence zone between the African and Eurasian plates, the northern part of Morocco represents an area of active crustal deformation during the Late Cenozoic (e.g. Meghraoui et al., 1996). The 1994–2004 Al Hoceima earthquake sequence is evidence of the active seismicity of this region (e.g. Akoglu et al., 2006). Whilst seismicity was investigated by diverse methods, for instance radar interferometry (Akoglu et al., 2006), the reconstruction of Late Cenozoic and modern rates of crustal deformation is mainly based on GPS measurements (Fadil et al., 2006; Vernant et al., 2010), morphotectonics (i.e. displacement of geomorphological markers: Poujol et al., 2014; Pastor et al., 2015), and morphometric indicators (Barcos et al., 2014).

Morphometric indicators show that most of the fluvial systems draining the north-eastern part of Morocco are in disequilibrium (Barcos et al., 2014). This is especially true for the ~74,000 km^2 large Moulouya catchment, the second largest fluvial system of North Africa debouching into the Mediterranean Sea after the Nile. As a result of ongoing N–S compressive shortening in north-eastern Morocco, Barcos et al. (2014) also postulate that the main W–E striking deformational front between the Rif belt and the Atlas mountains stretches across the lowermost 65 km-long valley reach of the Moulouya river, the so-called Zebra-Triffa sedimentary basin. Even though river terrace sequences generally represent useful indicators to detect crustal deformation (e.g. Demir et al., 2012), the fluvial sedimentary record of the Moulouya remains poorly documented. Excepted a few studies about Late Cenozoic deposits in its middle reach (Raynal, 1961; Lefèvre, 1984, 1989), a reliable reconstruction of the Quaternary terraces along the entire river course is still lacking. As for the lowermost valley reach, where most of the recent

---

[*] Corresponding author.
E-mail address: grixhon@uni-koeln.de (G. Rixhon).

http://dx.doi.org/10.1016/j.jafrearsci.2016.11.005
1464-343X/

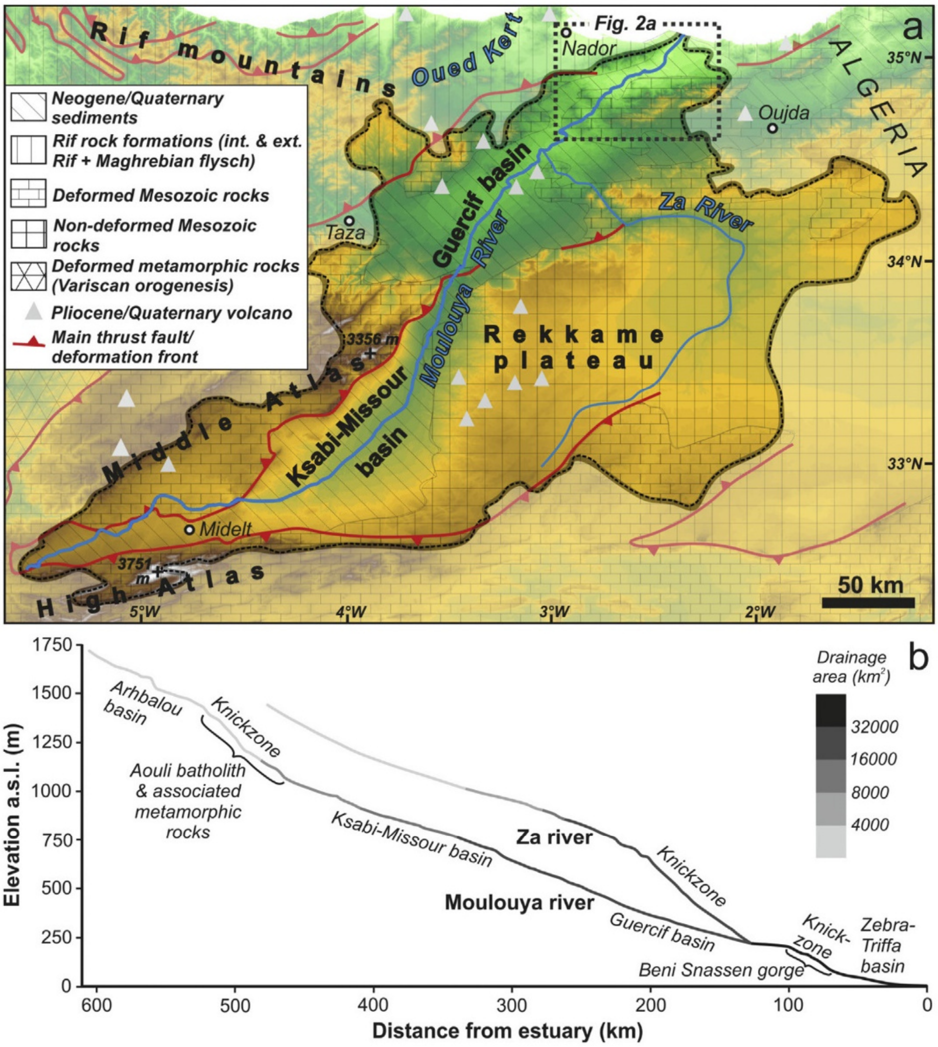

Fig. 1. (A) Relief map of the Moulouya catchment (delimited by black dashed line), with the main regional geological structures of northern Morocco (according to Barcos et al., 2014). The dashed rectangle refers to the zoom in of the lower Moulouya (Fig. 2A). (B) Longitudinal profiles of the Moulouya river and its main tributary, the Za river, with location of the main sedimentary basins and knickzones. Modified after Pastor et al. (2015).

geomorphological and stratigraphical research took place, all studies exclusively focused on the Holocene sedimentary record to infer climatic and human-induced changes (Ibouhouten et al., 2010; Zielhofer et al., 2008, 2010), eustatic variations (Pissart and Boumeaza, 2010) or tectonic deformation (Zarki et al., 2004). However, the distribution of these (almost) continuous Holocene overbank fine-grained sediments along this reach was either not mapped (Ibouhouten et al., 2010; Zielhofer et al., 2008, 2010) or at a very poor resolution (Pissart and Boumeaza, 2010). Even more problematic is the fact that Pleistocene terrace sediments in the previous studies were either completely disregarded (Ibouhouten et al., 2010; Zielhofer et al., 2008, 2010) or erroneously interpreted as Pliocene marine conglomerates (Pissart and Boumeaza, 2010).

Therefore, this study first aims at (i) providing a comprehensive image of the river terraces' distribution, including changes in the valley morphology, and (ii) establishing a relative stratigraphy of Late Cenozoic landforms in the lowermost Moulouya reach. To achieve these goals, we conducted a field survey based on profile description and geomorphological mapping using a differential global positioning system (DGPS) and a laser distance meter. In two selected profiles, clast lithological analysis and measurements of carbonate contents were carried out to investigate the sedimentary environment and the post-depositional evolution of the river deposits. Field survey was supplemented by the analysis of satellite images. Finally, the reconstruction of the Quaternary fluvial environments in the lower Moulouya reach was used to better understand the position of the deformational front in this sedimentary basin and the resulting fault pattern.

2. Study area

2.1. Geodynamic background of north-eastern Morocco

In the northern part of Morocco, there is a general consensus to consider N–S compressive shortening as the main geodynamic process from the Miocene to the Quaternary. Ait Brahim et al. (2002) showed that Messinian sedimentary sequences are affected by N–S to N140° E compression in the eastern Rif belt and that Middle Pleistocene terrace sequences in the region of Oujda and of the Oued Kert, located eastward and westward of the Moulouya, respectively, were deformed (Fig. 1A). Based on kinematic analyses of Pliocene and Quaternary fault systems in the Rif mountains, a N–S to NW–SE main compressional stress direction, associated with shortening rates of 1–2.3 mm/yr, was suggested (Meghraoui et al., 1996). Recently, trend-topography surface analysis highlighted an E–W trending lithospheric dome in the eastern Rif and in the Beni Snassen massif (Barcos et al., 2014). Morphometric indicators also revealed active deformations accommodating a N-S shortening at the northern margin of the Beni Snassen massif (Barcos et al., 2014). At last, recent geodetic observations evidenced a southward motion of the Rif mountains (~3 mm/a) relative to the interior of the African plate (Fadil et al., 2006; Vernant et al., 2010).

2.2. The Moulouya catchment

2.2.1. General hydro-geomorphogical setting

Originating in the southern part of the Middle Atlas, the >600 km-long, SW–NE oriented Moulouya river represents the second largest fluvial system of North Africa draining into the Mediterranean Sea (Fig. 1A). With a catchment area of ~74,000 km^2 (Pastor et al., 2015), its river network drains the northernmost part of the High Atlas to the south, the High plateaus to the east, the eastern half of the Middle Atlas to the west and the south-eastern margin of the Rif mountains to the north (Fig. 1A). The main trunk flows across several intramontane basins filled with Neogene sediments. From source to mouth, they are the Arhbalou, Ksabi-Missour, Guercif and Zebra-Triffa-Ouled Mansour basins, the last one being located directly upstream of the river estuary (Fig. 1A and B). Morphometric indicators along with deformations of the drainage network and the presence of large knickzones in the Moulouya catchment point to a disequilibrium state (Fig. 1B; Barcos et al., 2014; Pastor et al., 2015). The catchment shows an S-shaped hypsometric curve and has a hypsometric value of 0.313, while the normalized stream-length gradient index (SLk) points to high anomalies along the entire river course (Barcos et al., 2014).

The Moulouya catchment is characterized by a semi-arid to arid Mediterranean climate. Average precipitations range from 150 to 600 mm between the basin lowlands and the Atlas Mountains (Kaemmerer and Revel, 1991). Highest fluctuations of the water discharge occur from October to January; they are generally related to heavy rainfall events, usually very concentrated in time (Snoussi et al., 2002). This results in very high peak discharges: e.g. ~5200 m^3/s for the 1963 flood event (i.e. >200 times greater than the mean annual discharge; Snoussi et al., 2002; Zielhofer et al., 2008).

2.2.2. The middle reaches (Ksabi-Missour basin)

In the High and Middle Atlas regions, two main processes resulted in rock uplift: thrusting due to tectonic shortening, active since the Paleogene, and long-wavelength surface uplift due to mantle-driven buoyancy since the Late Cenozoic (Babault et al., 2008). In the Ksabi basin (Fig. 1A), the existence of a Quaternary terrace staircase, encompassing up to eight distinct levels, and stacked terraces were recognized (Raynal, 1961; Lefèvre, 1989; Kaemmerer and Revel, 1991). The landscape is characterized by a tight inter-fingering between alluvial deposits of the Moulouya and footslope sedimentation landforms (alluvial cones, glacis), the latter usually capping the river sediments (Lefèvre, 1989). Further to the north in the Missour basin (Fig. 1A), recent ^{10}Be dating of fluvial landforms, i.e. terrace fans from a tributary of the Moulouya draining the eastern flank of the Middle Atlas, allowed inferring incision rates of ~0.3 mm/a, implying that mantle-driven uplift amounted to ~0.1–0.2 mm/a during the Middle Pleistocene (Pastor et al., 2015).

2.2.3. The lowermost reach: the Zebra-Triffa-Ouled Mansour sedimentary basin

Downstream of the 30 km-long gorge cut into the Beni Snassen massif (see below) until the estuary, the ~65 km-long reach of the Moulouya successively drains the so-called Zebra plain, Triffa plain and Ouled Mansour plateau (Fig. 2A). For clarity, the geologic basin formed by these three geographic areas will be named lowermost sedimentary basin in the following text. It is a large WSW–ENE striking synclinal depression mostly filled with Neogene marine deposits (Ruellan, 1971; Boughriba et al., 2006). As a component of the larger-scale Melilla basin, it emerged around 3.6 Ma (Rouchy et al., 2003). This synclinal structure is bordered by two complex, generally WSW–ENE striking anticlinal ridges: the Beni Snassen and the Kebdana mountains to the south and the north, respectively (Fig. 2A). Both massifs are primarily formed by diverse Mesozoic carbonate rocks, including limestone, dolomite, dolomitic limestone, calcareous marl and sandstone, and marl (Ruellan, 1971). They are secondarily composed of sandstone and slate formations of the Palaeozoic flysh series (Ruellan, 1971; Khattach et al., 2004).

Located to the north of the Triffa plain (Fig. 2A), the up to 10 km-wide and up to 130 m-high Ouled Mansour plateau is mostly formed of Mio-Pliocene marls and partly solidified sands (Ruellan, 1971). Despite many recent geological or geophysical studies, mostly dealing with the hydrogeology of the lowermost part of the Moulouya catchment (e.g. Khattach et al., 2004; Boughriba et al., 2006; Chennouf et al., 2007a,b; Fetouani et al., 2008; Sardinha et al., 2012), the geological structure of the Ouled Mansour plateau remains confusing. This is especially true for the >20 km-long, continuous lineament at its southern edge (Fig. 2A). Whilst the latter was traditionally mapped as a flexural feature (e.g. Ruellan, 1971; Boughriba et al., 2006; Fetouani et al., 2008), Khattach et al. (2004) and Chennouf et al. (2007a) interpreted the Ouled Mansour plateau as a Miocene horst, thereby implying the presence of normal faults at its borders. In this respect, several WSW–ENE striking fault lines stretching across the Triffa-Ouled Mansour area are represented on the neotectonic map of Morocco (Faure-Muret and Morel, 1994). However, their exact position remains somewhat imprecise given the 1: 1,000,000 scale of the map, and the nature of fault motion remains unknown. A SW–NE striking deformational front between the Rif belt and the Atlas mountains through the lowermost sedimentary basin of the Moulouya was assumed on the structural map of Morocco (Saadi, 1982). This main deformational front is also postulated by Barcos et al. (2014) but has a W–E orientation and a different extension. Note finally that these last authors reported active faulting, both normal and reverse, affecting Quaternary river deposits at the northern rim of the Beni Snassen massif (i.e the lowermost Moulouya catchment, Fig. 2A) but without any precision about the location and the extension of these faults.

In the lowermost reach of the Moulouya, the up to 15 m-thick recent flood deposits are formed of unconsolidated clayey/silty/sandy laminae spanning the whole Holocene period (Zielhofer et al., 2008, 2010; Ibouhouten et al., 2010; Pissart and Boumeaza, 2010). For clarity, these sediments, which are not in the focus of this study, will be referred to as Holocene overbank fines in the following. Up to three distinct erosional terraces were carved into these overbank fines during a stepwise Holocene river incision according to Pissart and Boumeaza (2010). The detailed chronostratigraphic study of this sedimentary record, along with palaeoecological proxies, allowed inferring its strong coupling with Holocene rapid climate changes (Zielhofer et al., 2008, 2010; Ibouhouten et al., 2010), although this was formerly contested by Zarki et al. (2004). At last, abundant archaeological material along with fire places found in these sediments reveal temporary human settlements along the lower Moulouya (Fig. 2B; Ibouhouten et al., 2010; Linstädter et al., 2012), with a peak of human presence during the Epipalaeolithic (~7.8–10.1 ka cal BP) and the Neolithic (~5.5–7.4 ka cal BP).

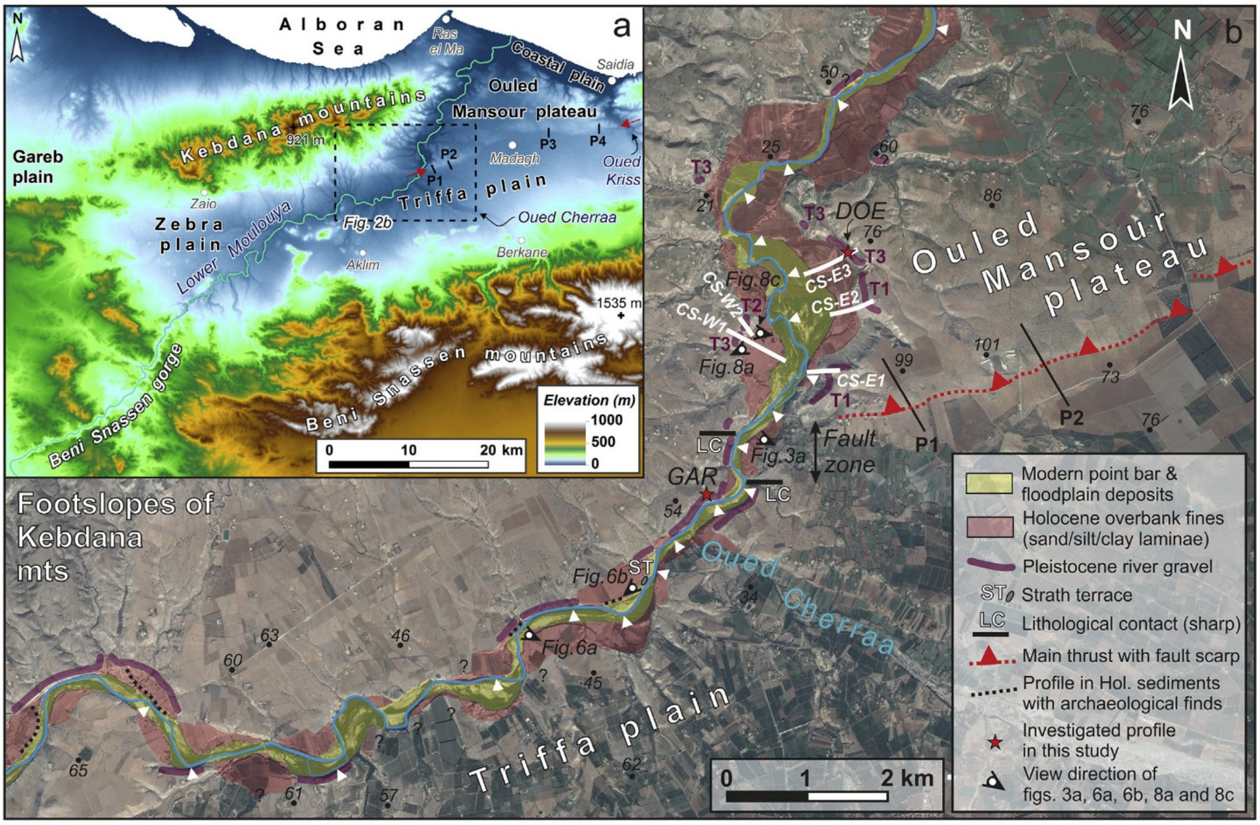

Fig. 2. (A) SRTM-based DEM of the lower Moulouya catchment, showing the Beni Snassen gorge and the ~65 km-long river reach draining the lowermost sedimentary basin (Zebra plain-Triffa plain-Ouled Mansour plateau). The red arrows refer to the continuous fault scarp at the southern edge of the Ouled Mansour plateau and P1 to P4 locate the cross sections represented in Fig. 4. The dashed rectangle refers to our study area. (B) The 20 km-long studied valley reach of the lower Moulouya with main morphological and geological features as well as profiles described in the text (satellite image: Google Earth, CNES/Astrium, 02.08.2014). White triangles refer to the locations where valley and floodplain width measurements were performed (see Fig. 5A). DGPS cross sections (CS) are represented by bold white lines and were performed both on the eastern (E1-3) and western (W1-2) valley sides (see Fig. 9). Small black circles with numbers are absolute elevations according to topographic points mentioned on Moroccan 1:50,000 topographic maps. T1, T2 and T3 refer to the Pleistocene terrace levels characteristic of the hanging wall reach (see text and Figs. 8, 9, 11). Uncertain extension of fluvial units is symbolised by question marks. Details about the profiles in Holocene sediments with archaeological finds can be found in Zielhofer et al. (2008, 2010) and Linstädter et al. (2012). (For interpretation of the references to colour in this figure legend, the reader is referred to the web version of this article.)

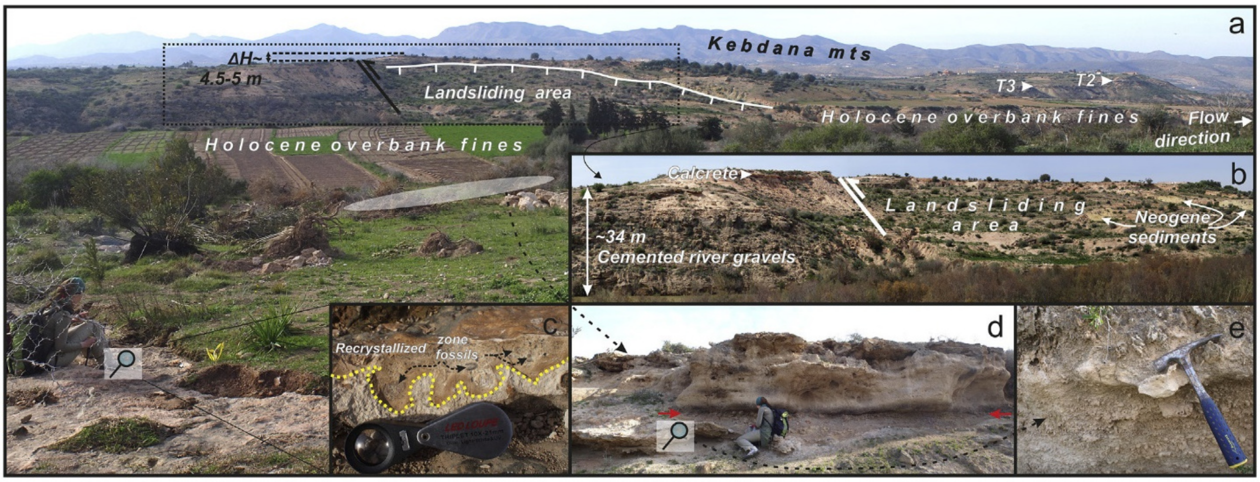

Fig. 3. (A) Panorama view of the western valley side in the fault zone, characterized by an up to 330 m-long landsliding area (scarp delimited by white line), stretching to the current channel. Note also the sharp 4.5–5 m-high vertical offset (ΔH) at the western tip of this area, where the presumed thrust zone (black line with arrow) occurs. T2 and T3 refer to two distinct terrace levels observed in the terrace staircase downstream (see 4.3.1.). (B) Detailed view of the western valley side, exhibiting a lithological transition, along flow direction, between 34 m-thick river gravels sealed by a calcrete and Neogene marine deposits, locally observable in the landsliding area. (C) Neogene marine deposits: contact between unaltered carbonates (light greyish zone) and recrystallized carbonates with fossils at the ground surface of the eastern valley side. (D) Fossil-rich outcrop in the upper part of the eastern valley wall. Note the blackish zone (red arrows), attesting for recrystallization of the shelly carbonate layers. (E) Close-up of the marine fossils (shell fragments mostly). (All photos: G. Rixhon). (For interpretation of the references to colour in this figure legend, the reader is referred to the web version of this article.)

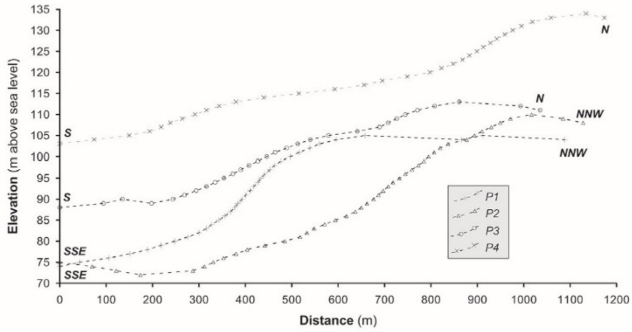

Fig. 4. Topographic cross sections at the southern edge of the Ouled Mansour plateau (location on Fig. 2A).

3. Material and methods

This study tests the hypothesis of Barcos et al. (2014) of a main deformational front related to ongoing N–S compression disrupting the lowermost sedimentary basin of the Moulouya: the presence of a thrust zone at the transition between the Triffa plain to the south and the Ouled Mansour plateau to the north is thus postulated. For clarity in the following text, the river reach draining the Triffa plain is assimilated to the footwall and the one draining the Ouled Mansour plateau to the hanging wall. A detailed discussion about the thrust zone is provided in section 5.3.

Field survey included geomorphological mapping and the description and sampling of two profiles along the ~20 km-long studied river reach draining the north-western part of the footwall (Triffa plain) and the south-western part of the hanging wall (Ouled Mansour plateau, Fig. 2B). Geomorphological mapping was firstly based on DGPS (Topcon HiPer Pro) and laser distance meter (TruPulse 200 Rangefinder) measurements. Both were used to estimate the relative elevations of the main fluvial morphological landforms above the modern floodplain. Moreover, five valley cross sections in the hanging wall reach were obtained from DGPS elevation data (see location in Fig. 2B). The latter were corrected using the elevation of topographic points mentioned on Moroccan 1:50,000 topographic maps (Berkane, les Triffa and Zaio) and were processed with the GPS-Track-Analyse.NET software. DGPS and laser distance meter measurements reach an altimetric accuracy of ~2 cm and <0.3–0.5 m, respectively. To complement field mapping, Astrium satellite images provided by Google Earth were used: their resolution is appropriate for reconstructing the regional occurrence of major geomorphological units. They allowed inferring (i) the widths of both the present-day floodplain and the valley filled with Holocene overbank fines at twenty selected spots (see location in Fig. 2B), and (ii) the height of the fault scarp at the southern edge of the Ouled Mansour plateau along four cross sections (see location in Figs. 2A and B).

Two river profiles were thoroughly studied: the GAR and DOE profiles (Fig. 2B). They were selected because they are representative of the contrasting valley reaches draining the footwall and the hanging wall, respectively (see 4.2. and 4.3.). The ~37 m-high GAR profile is located on the western bank of the Moulouya (34°58′15.2″ N; 2°27′35.7″ O) and was measured by laser distance meter. The ~23 m-high DOE profile is located ~3.6 km downstream of the previous one, on the eastern bank of the Moulouya (34°59′59.2″ N; 2°26′27.3″ O) and was measured by laser distance meter and DGPS. Clast lithological analysis was applied to both profiles: two sets were collected in the lower and upper parts of the GAR profile and one in the DOE profile (see 4.2.2. and 4.3.2., respectively). For each set, more than 150 pebbles were directly extracted and sieved. Given the mean individual clast size in both profiles, analysis is performed in the (very) coarse gravel fraction (−4 to −6 grain size classes on the φ scale, i.e. 1.6–6.4 mm). Clast lithological analysis performed in fluvial terraces is useful to unravel the source areas of coarse alluvial material transported by large rivers (e.g. Rixhon and Demoulin, 2010; Demir et al., 2012). Contrasting proportions observed in the clasts' nature may also reflect major catchment-wide changes in sediment supply (Maddy et al., 1991). At last, a quantitative evaluation of the carbonate content in the fine-grained matrix of the GAR profile was performed using the Scheibler apparatus, where 0.5 g of sediments was moistened and reacted with 10% HCl (Beck et al., 1993). Horizons of densely-cemented secondary carbonates frequently occur in ancient fluvial sediments of the Moulouya (Ruellan, 1971; Kaemmerer and Revel, 1991); this is typical for river terrace deposits of semi-arid Mediterranean environments (e.g. Candy and Black, 2009).

4. Geomorphological mapping and profile description

4.1. *Lithological and morphological duality of the valley*

Remarkable lithological variations associated with specific morphological features characterize the valley walls along the <1 km-long fault zone, located directly before the river cuts into the Ouled Mansour plateau (Figs. 2B and 3A). All observations detailed below are reported along flow direction: the footwall (Triffa plain) and the hanging wall (Ouled Mansour plateau) are the upstream and downstream reaches, respectively.

First, sharp lithological contacts are observed along the fault zone: the footwall reach is composed of fluvial gravels capped by fine-grained deposits, whereas the valley sides of the hanging wall reach are formed by marine sediments exhibiting different facies (Fig. 3A and B; see also sections 4.2 and 4.3). On the western valley side, the latter are composed of yellowish sands and greyish marls; they locally crop out in a 330 m-long and 190 m-wide landsliding area, located directly downstream of the lithological contact and stretching to the current channel (Fig. 3B). Note that these locally cemented sands and marls constitute most of both valley walls in the hanging wall further downstream. On the eastern valley side, light greyish fine-grained carbonate sediments containing abundant marine fossils (shell fragments mostly) form the hanging wall directly downstream of the lithological contact (Fig. 3C–E). Note that the latter is located >500 m southward of the lithological contact on the opposite valley side (Fig. 2B). Recrystallization processes associated with deep brownish/reddish colourations occur in these fossil-bearing sediments, both at depth and at the surface (Fig. 3C and D).

Second, clear vertical offsets disrupt the topography in the fault zone. While the vertical offset is 4–5 m-high on the western valley side (Fig. 3A), the fault scarp is very prominent on the opposite side and reaches heights up to 30–35 m eastward of the valley (Fig. 4). The scarp is (almost) continuously observable in the topography from the Moulouya valley (west) up to the valley of the Oued Kriss at the Algerian border (east) along more than 20 km (Fig. 2A). Note that its direction changes from WSW–ENE to W–E north of the locality of Madagh (Fig. 2A).

Third, larger-scale contrasts in the valley morphology and channel dynamics are readily recognizable in the several km-long reaches located up- and downstream of the fault zone. The valley geometry along with the elevation difference between the modern floodplain and the top of the valley walls is particularly contrasting: nearly symmetrical, 30-40 m-high valley walls evolve into asymmetrical ones, up to 50 and 90 m-high on the western and eastern river banks, respectively, directly downstream of the fault zone (Fig. 2B). The mean lateral development of the modern floodplain significantly increases from ~215 m to ~360 m between the footwall

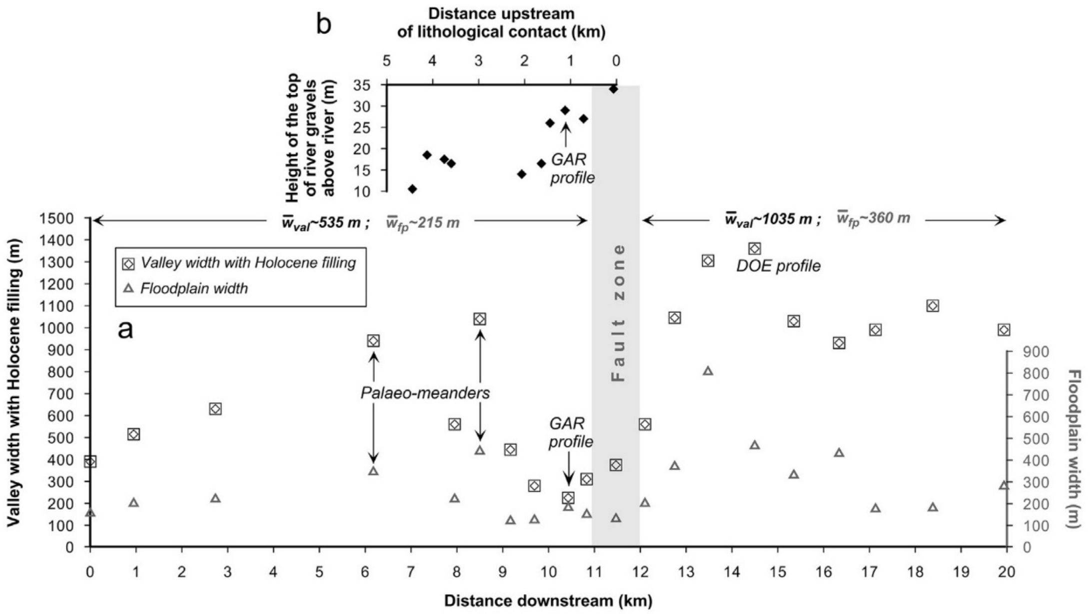

Fig. 5. (A) Evolution of the floodplain width and the valley width filled with Holocene flood deposits in the up- and downstream reaches of the fault zone (grey area), with location of the DOE and GAR profiles. Note the contrasting mean values between both valley reaches. (B) Elevation of the top of the cemented river gravel upstream of the lithological contact observed on the western valley side. This graph clearly reveals a diminishing trend in the upstream direction, decreasing from more than 30 m in the fault zone to about 10 m ca. 4 km upstream of it.

and the hanging wall (Fig. 5A). Whereas it is restricted to values below 180 m in the 2 km-long reach directly upstream of the fault zone, maximal values exceeding 800 m are observed only 1.5 km downstream of the fault zone. The mean valley width filled with Holocene overbank fines in the footwall is also twice as narrow as that of the hanging wall (~535 and ~1035 m, respectively, Fig. 5A). In particular, the valley width reaches minimal values of ~300 m in the 2 km-long reach directly upstream of the fault zone, whereas it rapidly exceeds 1000 m in the next kilometre downstream (Fig. 5A). At last, recent channel dynamics observed on satellite images (from 2003 to 2013) in the hanging wall is characterized both by incipient free meandering in the broad floodplain and active point bar development and migration.

4.2. The footwall reach (Triffa plain)

4.2.1. General characteristics

Along the 10 km-long reach upstream of the fault zone, no Neogene marine sediment can be observed anywhere at the base of the valley walls. Here, the latter are formed by several m-thick cemented river gravels, capped by fine-grained sediments exhibiting several dm-thick calcretes at the top. These gravel bodies build

Fig. 6. (A) Panorama view of the outer bank of a meander located ~4 km upstream of the fault zone. Note the sharp contact (red arrow) between the underlying cemented Pleistocene river gravels and the overlying Holocene overbank fines, in which settlement sites of the Epipalaeolithic, Early Neolithic and Bronze age, attested by five ^{14}C dates (red circles), were found in archaeological excavations (Linstädter et al., 2012). (B) View of the strath terrace carved into cemented river gravels and sands, located ~2 km upstream of the fault zone. Also overlain by Holocene overbank fines, its top (white dashed line) is perched 3–4 m above the modern river channel. (C) Detailed view of the abrasion flutes and potholes observed on the strath surface. (All photos: G. Rixhon). (For interpretation of the references to colour in this figure legend, the reader is referred to the web version of this article.)

sub-vertical valley sides at several locations (see section 4.2.2). They frequently include cemented sand lenses, locally exhibiting cross-bedding. Holocene overbank fines are rarely present simultaneously on both river banks; they are discontinuous and frequently occur in the inner banks of meanders (Fig. 2B). Elevation measurements of the top of the river gravels above the current channel, where clearly identifiable, decrease from ~34 m in the fault zone to about 10 m ca. 4 km upstream of it (Fig. 5B). Recent overbank fines may locally overlie the cemented river gravels at locations where the observable gravel thickness does not exceed 10 m (Fig. 6A). ^{14}C dating of former human settlement places embedded in these fine sediments attest a Holocene depositional age (Linstädter et al., 2012). A bench-like surface, located ~2 km upstream of the fault zone on the western valley side, is also observed. It is carved into cemented river gravels and sand lenses, displaying abrasion flutes and potholes (Fig. 6B and C). Partly covered by recent overbank fines, the top of this strath terrace is located 3–4 m above the current channel (Fig. 6B).

4.2.2. The GAR profile

The GAR profile is located on the western bank of the Moulouya, directly upstream of the fault zone (Fig. 2B). In this valley section, the narrow modern floodplain and the Holocene overbank fines (i.e. together less than 225 m-wide) are only observed on the eastern valley side whereas fluvial lateral erosion formed undercut slopes on the western valley side. The ~37 m-thick sedimentary succession of the profile exhibits a repetitive pattern of two similar fining-upward sequences: river gravel at the bottom (units 1 and 4), sand layers in the middle (units 2 and 5) and silty/clayey sediments at the top (units 3 and 6) in each sequence (Fig. 7A). The first sequence is at least ~23 m-thick (base not visible because of the water table) and the second is ~14 m-thick (Fig. 7A). Units 1 and 4, forming the lower and upper river gravel bodies, respectively, are ~15 and ~6 m-thick (depths of ~37-22 m and ~14-8 m). They are both clast-supported, poorly to moderately sorted and strongly cemented. Individual clast size usually amounts to several centimetres, rarely exceeding 20 cm. Both contain several m-long and dm-thick sand lenses, also cemented, that regularly display cross-bedding structures. $CaCO_3$ contents from the cemented fine-grained matrix amount to 53–70% in these units (Fig. 7B). Clast lithological analysis performed in each unit, however, reveals contrasting results (Fig. 7C). A dominance of carbonate rocks over rocks primarily built by silicate minerals is clearly observed in unit 1 (93 vs. 7%). This ratio between both rock types is much more balanced in unit 4: 52 vs. 48%. In unit 1, more than 50% of the analysed pebbles are microgranular limestone, sometimes with calcite veins, whilst other carbonates are macrogranular limestone/calcareous sandstone (21.2%), dolomite (11.3%), belong to other categories or are indeterminable, e.g. due to strong weathering (10%). Rocks built by silicate minerals, i.e. chert, sandstone, quartzite, slate and acidic volcanic rocks, are sparse. In unit 4, the same kinds of carbonate rocks are found but in lesser proportions: microgranular and macrogranular limestones amount to 34.2 and 7.5%, respectively, while dolomite only represents 7.0%. Rocks built by silicate minerals are much diverse but are primarily dominated by both high- and low-degree metamorphic rocks, amongst which quartzite, including quartz pebbles originating from neo-formed quartz veins (22.5%), and slate or phyllite (10.7%). Plutonic rocks, encompassing granitic, dioritic and sheet intrusion rocks, and basalt represent 5.9 and 3.2%, respectively. Chert pebbles amount to 3.2%; sandstone, grauwacke and breccia pebbles were also observed.

Units 2 and 5, forming the lower and upper cemented sand layers, respectively, are at least 3 m and several dm-thick (depths of ~22–19 m and ~8–7.5 m). They display, just like the sand lenses embedded in the gravel bodies, tafoni weathering features. $CaCO_3$ content amounts to 46–54% in these units (Fig. 7B). The (at least)

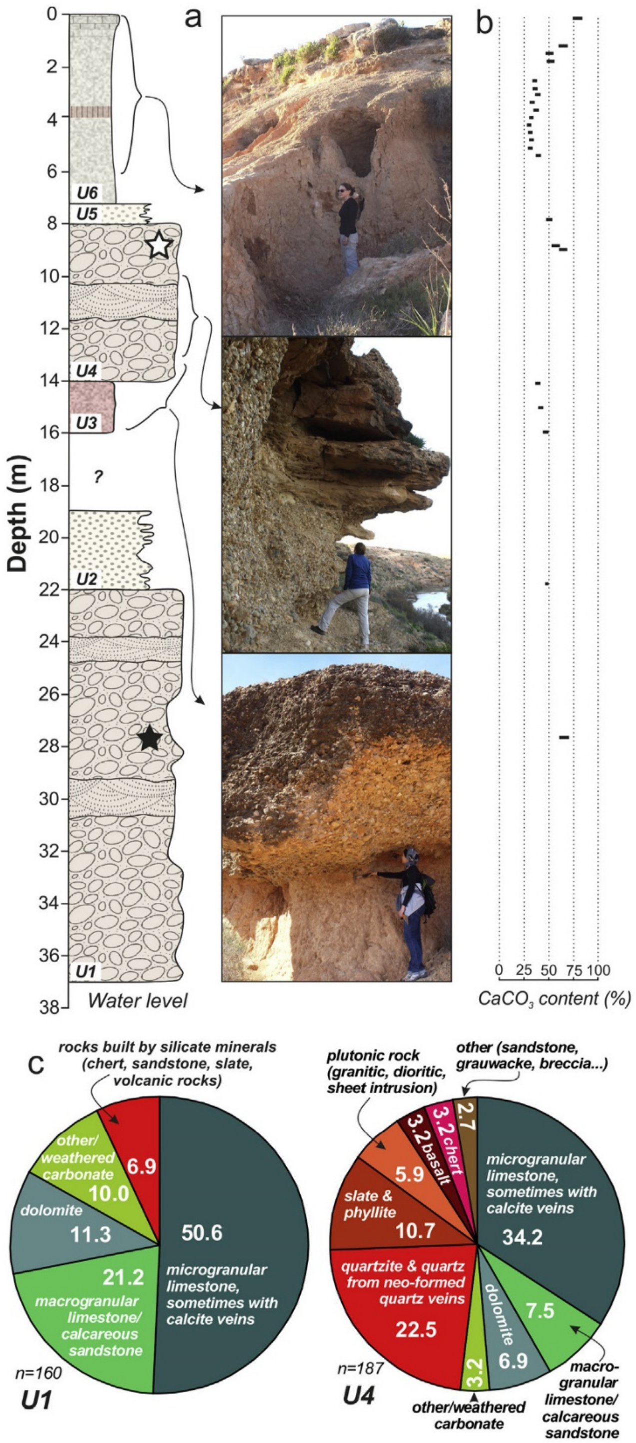

Fig. 7. (A) Stratigraphic log of the 37 m-thick GAR profile, illustrated by detailed photos, exhibiting a recurrent pattern of two similar fining-upward sequences: two stacked river terraces, each one built-up by a cemented river gravel body at the base and alluvium (floodplain loam) on top. U1 to U6 refer to the six sedimentary units (see 4.2.2.). The black and white stars represent the sampling locations for clast lithological analysis in the lower (U1) and upper (U4) gravel body, respectively. Top photo: overbank fines of U6; middle photo: cemented gravel body of U4, embedding a several dm-thick sand lens; bottom photo: sharp contact between the reddish silty/clayey sediments of U3 and the gravel body of U4 (the person points to the erosional disconformity). (All photos: G. Rixhon). (B) Carbonate content in the fine-grained matrix. (C) Contrasting results of clast lithological analyses (numbers in percent).

2 m-thick cemented silty/clayey sediments forming unit 3 at depths comprised between ~16 and ~14 m are homogeneous and show a deep, uniform brownish/reddish colouration along with $CaCO_3$ contents ranging from 36 to 49% (Fig. 7B). While the lower contact of these sediments could not be identified, the upper contact with the overlying gravel body is sharp and erosive (Fig. 7A). The upper, light brownish, ~7–7.5 m-thick silty/clayey sediments forming unit 6 are homogeneous, although a several dm-thick layer characterized by a stronger reddish colouration is observable at mid-height. They also show a gradual upward induration, reflected by the $CaCO_3$ contents evolving from ~30% at the base to >75% at the top (Fig. 7B). The whole sequence is indeed sealed by a several dm-thick, very strongly cemented horizon.

4.3. The hanging wall reach (Ouled Mansour plateau)

4.3.1. General characteristics

In the several km-long reach downstream of the fault zone, thorough field survey together with DGPS measurements allowed to identify three distinct contacts between Neogene marine deposits and fluvial terrace sediments (Figs. 8 and 9), and to document their relative elevation above the modern floodplain. From the highest to the lowest, these contacts are found at relative elevations of 67 ± 1, 35 ± 1 and 25 ± 1 m (Figs. 8 and 9), with associated absolute elevations of 77 ± 1, 45 ± 1 and 35 ± 1 m above sea level. According to this, the corresponding terrace levels are named T1, T2 and T3, respectively (Figs. 8 and 9). They are characterized by an identical sedimentary pattern. Several m-thick, massive gravel bodies, strongly cemented due to the induration of the matrix material, are overlain by several m-thick fine-grained sediments, all sealed by a several dm-thick, locally dismantled calcrete (Fig. 8A and B). Frequent cemented sand lenses, locally exhibiting cross-bedding, are embedded in the gravel bodies. These cemented terrace sediments can be traced over several hundreds of meters in most instances; the corresponding terrace levels consequently build morphological units in the landscape (Fig. 8A). They are unequally distributed: T1 is only observable on the eastern valley side, T2 only on the western valley side and T3 on both of them (Fig. 2B). The nature of the underlying Neogene sediments also varies: locally cemented sands underneath T1 and T2, and marls underneath T3. Sand layers underlying T2 are strongly tilted to the west (Fig. 8C). Holocene overbank fines almost continuously occur on both river banks. Similarly to the older terrace levels, DGPS measurements reveal three main morphological units in the Holocene overbank fines with the following relative elevations above the current floodplain: 14 ± 2, 6 ± 1 and 3 ± 1 m (Fig. 9). On the eastern valley side, a ~1.5 km-long palaeo-channel is cut into the Holocene 6 ± 1 m-high terrace (Fig. 9).

4.3.2. The DOE profile

It is located on the eastern bank of the Moulouya, more than one kilometre downstream of the fault zone (Fig. 2B). The base of the fluvial sediments unconformably lies on Neogene marls at a relative elevation of 25 ± 1 m (Fig. 10A) and allows for a correlation of these fluvial sediments to the T3 terrace. The contact could not be observed at the base of the DOE profile due to the presence of slope failure deposits, but it was clearly identified several hundred metres to the west of the profile. The overall ~22.5–23 m-thick profile is characterized by a fining-upward sequence (Fig. 10A): river gravel at the bottom (unit 1), sand body in the middle (unit 2) and silt/clay sediments at the top (unit 3). The up to 8–9 m-thick unit 1 corresponds to a massive, generally poorly-sorted and nearly completely cemented gravel body (depths from 23 to 15-14 m). A subdivision of unit 1 into three subunits with gradational contacts can be undertaken (Fig. 10B). The lowermost subunit is almost void of any organization and is characterized by the highest proportion of boulders, reaching up to 60 cm in size. The middle subunit shows large grain size variations from boulders (but less numerous than in the previous subunit) to sand, stratified in lenses. Clast orientation may locally be observed and several metre-long sand lenses sometimes exhibit cross-bedding structures (Fig. 10C). The uppermost subunit is clearly clast-supported due to the scarcity of the fine-grained matrix; in general it shows a better sorting of the pebble fraction. Lithological clast analysis reveals a clear predominance of carbonate rocks over rocks primarily built by silicate minerals (90.3 vs. 9.7%, respectively, Fig. 10D). As with the lower gravel body of the GAR profile, the same kinds of carbonate rocks are found, almost in identical proportions: microgranular limestone, sometimes including calcite veins, macrogranular limestone/calcareous sandstone and dolomite represent 51.9, 17.5 and 14.3%, respectively. The only significant difference concerns the composition of silicate rocks; only quartz (5.2%) and chert (4.5%) pebbles are found.

The sandy unit 2 cuts the underlying unit in a channel-like structure, implying thicknesses varying between ~4 and ~5 m (depths from 15–14 to 9.5–9 m, Fig. 10A). Where strongly cemented, it displays tafoni weathering features (Fig. 10B). It also includes channel structures filled with pebbles, one of them being several tens of metres-long but only a few decimetres-thick. The 9 to 9.5 m-thick unit 3 is formed of a homogeneous, light brownish silty/clayey stratum. In the upper part, it is characterized by a strong reddish colouration over a thickness of several metres (Fig. 10B). Although no carbonate content was measured in this profile, this unit also seems to exhibit a gradual upward cementation. Same as in the GAR profile, the whole sequence is sealed by a several dm-thick, very strongly cemented horizon.

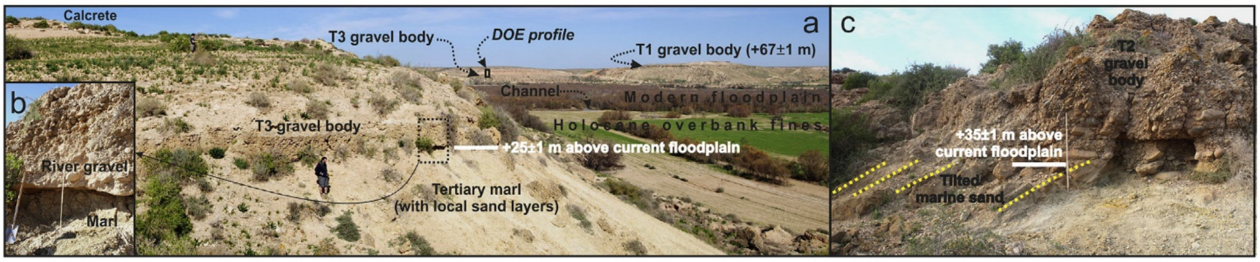

Fig. 8. (A) Panoramic view from the western valley side of the hanging wall reach and its terrace staircase incised into the Ouled Mansour plateau. In the foreground, sharp contact, i.e. erosional disconformity, between Neogene marl deposits and cemented river gravels of the terrace level T3, sealed by a calcrete (persons for scale). In the background, note the clear elevation difference between T3 and T1. The black rectangle refers to the DOE profile detailed in Fig. 10. Close-up of the erosional disconformity, stick is 1 m-long. (C) Sharp contact between Neogene sand deposits, partially lithified, and cemented river gravels of the terrace level T2 (stick is 1 m-long). Note the westward dipping (yellow dashed lines) of the sand layers. (Photos: M. Bartz and G. Rixhon). (For interpretation of the references to colour in this figure legend, the reader is referred to the web version of this article.)

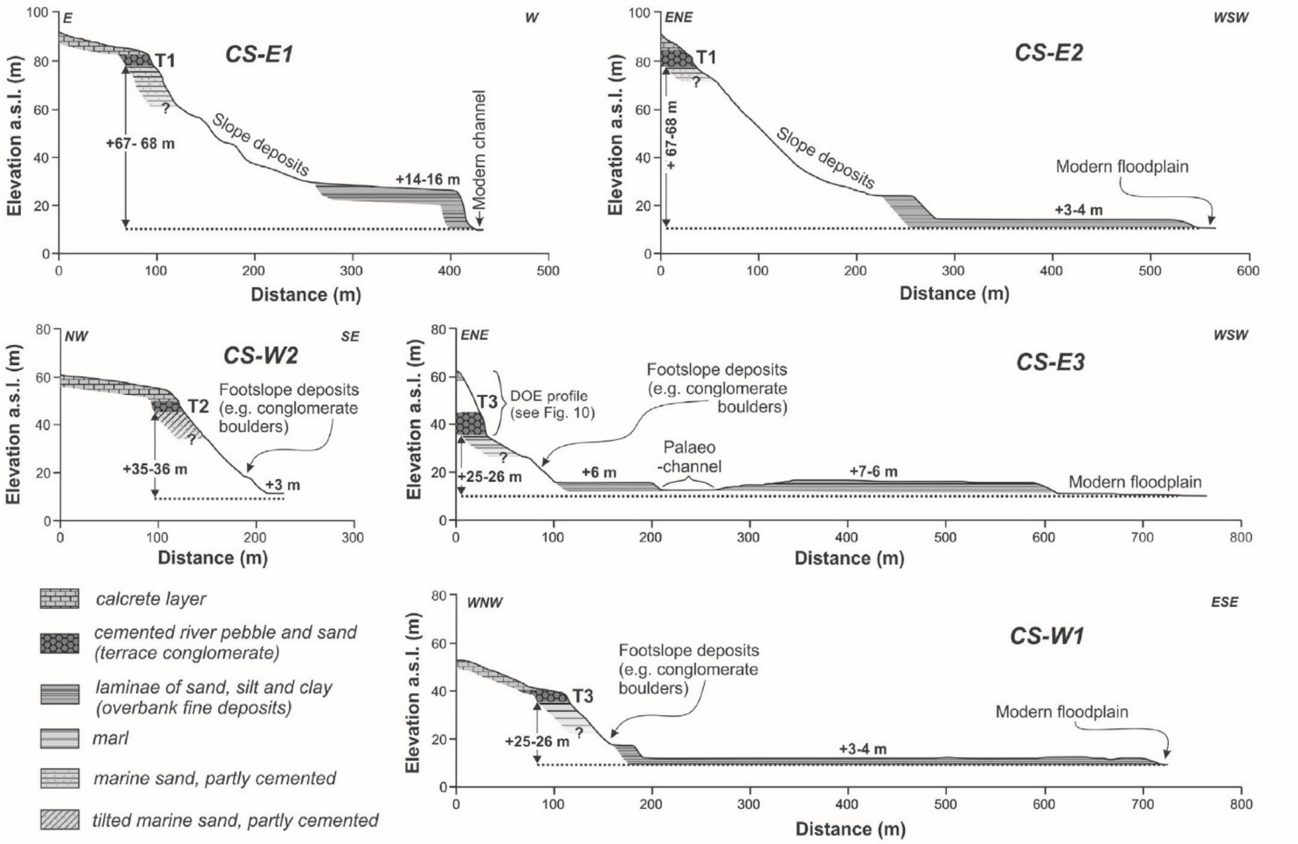

Fig. 9. Topographic cross sections based on DGPS measurements in the terrace staircase of the hanging wall reach (see Fig. 2B for location). Contacts between Neogene marine deposits and cemented river gravels at three distinct relative elevations above the current floodplain define three Pleistocene terrace levels, referred to as T1 to T3 from the highest to the lowest. Note also three other morphological units in the Holocene overbank fines (see 4.3.1.).

5. Data interpretation and discussion

The main thrust zone identified in this study (see section 5.3) has obviously affected the long-term evolution of the lower Moulouya. As attested by our field observations and data, fault activity lead to very much contrasting fluvial reactions up- and downstream of the thrust zone: fluvial aggradation primarily occurred in the footwall block (Triffa plain), whereas development of a terrace flight related to gradual river incision occurred in the uplifted hanging wall (Ouled Mansour plateau). Similar contrasting fluvial environments are indeed commonly observed where river systems cut across active thrust zones (e.g. Cording et al., 2014; Monegato and Poli, 2015), notably involving considerable deformations of terrace profiles (Thompson et al., 2002; Amos et al., 2007).

5.1. *Stacked terraces and calcrete development in the footwall reach*

The ~37 m-thick, fluvial sedimentary succession of the GAR profile points to long-lasting aggradation in the footwall reach. It also probably reveals a composite fill terrace (e.g. Pazzaglia, 2013), with a second terrace body (~14 m-thick) stacked over the first main one (at least ~23 m-thick). Arguments for this interpretation are (i) the recurring pattern of two similar fining-upward sequences, i.e. from gravel at the bottom to silt/clay at the top; (ii) the deep reddish colouration of the intermediate fines, indicating paleosol development in the middle of the sequence; (iii) the sharp erosive contact between intermediate fines (unit 3) and the upper gravel body (unit 4).

In the same profile, the different petrographic assemblages of both gravel bodies must also be discussed (Fig. 7C). The prevailing amount of carbonate rocks in the lower terrace body (>90%) probably reflects a local origin of the transported material, with predominant inputs from the Beni Snassen and/or the Kebdana mountains. Both massifs are primarily composed of diverse kinds of Mesozoic carbonates rocks (see 2.3.1.; Hollard, 1985). By contrast, the upper terrace body is characterized by a balanced proportion between carbonates rocks on the one hand and varied metamorphic (quartz/quartzite, slate, phyllite) and plutonic (granite, diorite, dyke-related) rocks as well as basalt on the other hand. With the exception of the small-sized batholith in the Beni Snassen massif, the second kind of rocks is practically absent in the lower Moulouya catchment. This points to a more complex mixing of the river bedload, reflecting both local input and longitudinal input from further upstream. In this respect, the largest outcrop of crystalline rocks is located in the upper Moulouya, directly upstream of the Ksabi basin (Fig. 1B; Hollard, 1985; Margoum et al., 2015). The main trunk, along a >50 km-long reach, and several tributaries have incised into both plutonic rocks (granite, granodiorite, diorite), belonging to the Paleozoic Aouli batholith, and associated contact metamorphic rocks (quartzite, micaceous schist). Triassic basalt occurs in this area as well and in the lowermost part of the Za catchment (Hollard, 1985; Margoum et al., 2015), the main eastern tributary of the Moulouya (Fig. 1A). Granitic rocks also crop out in this second area but to a much lesser extent than in the upper Moulouya and metamorphic rocks are almost absent there (Hollard, 1985). Since the latter represent more

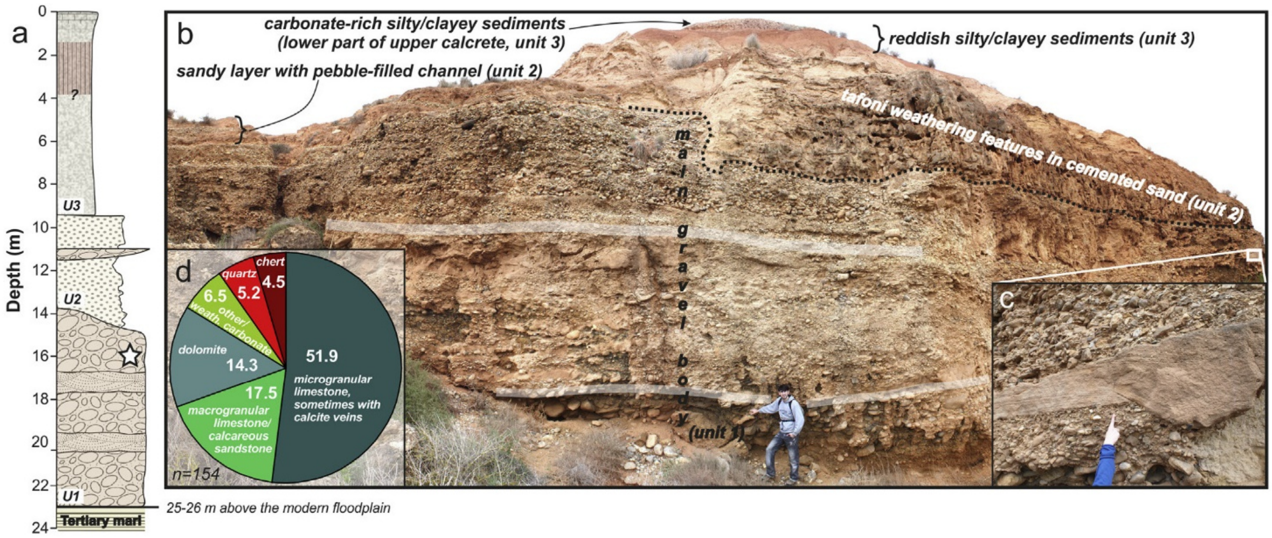

Fig. 10. (A) Stratigraphic log of the 22–23 m-thick DOE profile, exhibiting a fining-upward sequence with three distinct units (U1 to U3). The white star refers to the sampling location for clast lithological analysis. (B) Panoramic view of the profile, showing the main gravel body (U1) and the overlying sandy (U2) and silty/clayey (U3) sediments. The dashed black line delimits the boundary between U1 and U2. The white stripes refer to the transition zones between the different sub-units of U1 (see 4.3.2.). The white rectangle refers to Fig. 10C. (C) Detailed view of a sand lens embedded in U1 and exhibiting cross-bedding. (D) Result of clast lithological analysis (numbers in percent). (All photos: G. Rixhon).

than 30% of the clasts analysed in unit 4 of the GAR profile (Fig. 7C), we assume that material eroded from the upper Moulouya area was significantly deposited in the upper terrace body. We thus suggest that such a petrographic variation in the transported bedload might reflect an important catchment-wide change in sediment supply (Maddy et al., 1991): deeper basement rocks have been probably unroofed and denudated in this erosional area and transported up to the lower Moulouya sedimentary basin located several hundreds of kilometres downstream. This change in sediment supply might have been related to the transition of the Ksabi-Missour basin from an endorheic to an exhoreic drainage system as a result of its capture by a former Moulouya river (Pastor et al., 2015). It remains however unknown when this piracy event occurred after the last depositional episode in this basin during the Early Pliocene (Pastor et al., 2015). We finally argue that the observed petrographic change is an additional argument for long-lasting, perhaps discontinuous, aggradation in the footwall reach, leading to the formation of a composite fill terrace, i.e. the deposition of these crystalline rocks occurred after the formation of the lower terrace body.

We also observe a bipartite distribution of carbonate contents in the matrix of the GAR profile: it displays relatively high values from unit 1 to unit 5 and a decrease at the base of unit 6 followed by a significant upward increase (Fig. 7B). We suggest that different processes were involved in secondary carbonate precipitation and calcrete formation. Sealing the sediment sequence, the very upper part probably corresponds to a densely-cemented hardpan horizon (Kaemmerer and Revel, 1991; Candy and Black, 2009). Very frequently encountered in semi-arid Mediterranean environments, it is typical of *per descendum* calcrete profiles and is associated to pedogenic processes (Ruellan, 1971; Kaemmerer and Revel, 1991; Candy and Black, 2009). In contrast, the rather homogeneous cementation in the lower part of the sequence is probably the result of processes resumed under the generic term of groundwater calcrete (Kaemmerer and Revel, 1991; Candy and Black, 2009). More specifically, it might correspond either to a channel calcrete (Nash and Smith, 2003) or more likely to a valley calcrete (Nash and McLaren, 2003); the latter is typically several m-thick and develops within broad drainage courses, cementing alluvium of valley flanks. We assume that the same general bipartite interpretation can be drawn for fluvial sediments of the lower Moulouya where a similar cementation pattern is observed (e.g. in the DOE profile). In the Ksabi basin (Fig. 1A), the same conclusion was reached by Kaemmerer and Revel (1991), who also identified a bipartite induration pattern in old terrace sediments of the Moulouya. However, further investigations, including micromorphology (Nash and McLaren, 2003), are required to better specify calcium carbonate accumulation and calcrete formation in our study area.

5.2. *Pleistocene terrace staircase and related incision episodes in the hanging wall reach*

The Moulouya developed a well-preserved terrace flight with three distinct terrace levels in the hanging wall reach: they are named T1 to T3, from the highest to the lowest (Figs. 8, 9). Their strongly cemented gravel deposits, due to massive secondary $CaCO_3$ precipitation (see 4.2.2.), contrast with the loose gravel and the unconsolidated clayey/silty/sandy laminae forming the current channel and the Holocene overbank fines, respectively. T1, T2 and T3 are thus interpreted as Pleistocene terrace deposits. A similar conclusion was reached by Ruellan (1971): latest Pleistocene and Holocene deposits in the Zebra and Triffa plains bear (almost) no traces of any carbonate redistribution, whereas older Pleistocene deposits are all cemented by carbonate precipitation. Sedimentary successions from the three Pleistocene terrace levels, though only clearly exposed for T3, seem also to display fining-upward sequences, just like in the aggradation area of the footwall reach. These observations converge with the terrace stratigraphy in the Ksabi basin (Fig. 1A). A similar sedimentary pattern was recognized in all of the 10-15 m-thick alluvial formations there (Lefèvre, 1989); it consists of (i) an erosional contact at the base; (ii) a bipartite conglomerate, i.e. heterometric, boulder-rich and unstratified in the lower part evolving into metre-sized oblique and cross-bedded layering to the top; (iii) solidified sands with oblique bedding; and (iv) laminated silty layers capping the sequence (where still present). This sequence is remarkably similar to the one exhibited in the DOE profile (Fig. 10). We therefore assume that there is a recurrent fining-upward sequence in Pleistocene terrace deposits along the whole Moulouya course. We agree with Lefèvre's (1989) correlation between the deposition of the coarse sediment layers and river systems of high competence, characterized by former torrential flow regimes. This is particularly well exemplified by the lowermost subunit in the DOE profile, with no sedimentary organization and the highest proportion of boulders up to 60 cm in size (Fig. 10B). Such a depositional environment is usually encountered in semi-arid streams significantly affected by flash floods and characterized by high sediment supplies (Thorndycraft and Benito, 2006).

Incised into the underlying Neogene marine sediments, the terrace staircase in the hanging wall thereby records three main Pleistocene downcutting episodes after the formation of T1 (Fig. 11). From the top to the base, they amount to slightly more than 30 m, ~10 m and >25 m, based on the vertical spacing between the bases of successive terrace levels, and in the third case, between T3 and the unrecognized base of the current floodplain. According to Pazzaglia (2013), given the alluvium thickness of each Pleistocene terrace level (see Fig. 9), they are all likely to represent fill terraces (Fig. 11), exhibiting clear erosive contacts at their respective bases (Fig. 8).

Interpreting the three morphological units in the Holocene overbank fines, observable on both sides of the fault zone, is more delicate. They may correspond either to a main ~15-16 m-thick aggradational terrace subsequently cut by two degradational terraces at relative elevations of 6 ± 1 and 3 ± 1 m (Fig. 11), or to three distinct aggradational terraces. In the main aggradational terrace, the ^{14}C age distribution in the different profiles investigated by Zielhofer et al. (2008, 2010, see Fig. 2b) repeatedly and consistently displays younger deposition ages from the base to the top: the most recent age of ~1.4 ka is found at a relative elevation of ~14 m. This age distribution and the strath terrace carved in older fluvial deposits at a relative elevation of 3 ± 1 m (Fig. 6B) both argue for the first interpretation. A similar conclusion was reached by Pissart and Boumeaza (2010).

5.3. *Identification of a main thrust zone in north-eastern Morocco*

5.3.1. *Implications at the basin scale*

Previous studies interpreted either the southern edge of the Ouled Mansour plateau as a major flexure (Ruellan, 1971; Boughriba et al., 2006; Fetouani et al., 2008) or the whole structure as a Miocene horst, implying the presence of normal faults at its borders (Khattach et al., 2004; Chennouf et al., 2007a). On the one hand, we reject the hypothesis of a flexure in the very upper part of the Earth's crust in the light of our new observations and data, i.e. sharp and anomalous lithological contacts, recrystallization processes and diverse morphological variations including contrasting fluvial environments within a very short distance. On the other hand, faulting is much more adequate to explain our observations. This agrees well with recent studies using gravimetric and aeromagnetic data: the location of the >20 km-long continuous fault scarp indeed fairly well matches W–E to WSW–ENE striking lineaments independently detected in this area (Khattach et al., 2006; Chennouf et al., 2007b; El Gout et al., 2010). However, the hypothesis of a horst structure must be questioned against the geodynamic background of north-eastern Morocco (Khattach et al., 2004; Chennouf et al., 2007a). Normal faults accommodate extensional stress in the Earth's crust (e.g. Twiss and Moores, 2007) and this contradicts the widely recognized N–S compressive shortening having occurred since the Late Neogene in this region (Meghraoui et al., 1996; Ait Brahim et al., 2002; Fadil et al., 2006; Vernant et al., 2010; Barcos et al., 2014). Moreover, gravimetric-induced observations (Khattach et al., 2006; Chennouf et al., 2007b; El Gout et al., 2010) highlight a NNW dip of the WSW–ENE striking fault segment matching the ~10 km-long fault scarp between the Moulouya valley to the west and the locality of Madagh to the east (Fig. 2A). Although fault motion is not indicated, the fault geometry and the higher topographic position of the Ouled Mansour plateau imply that the latter was the upthrown hanging wall block. In the light of these new considerations, we interpret this structure as a thrust zone disrupting the lowermost sedimentary basin of the Moulouya.

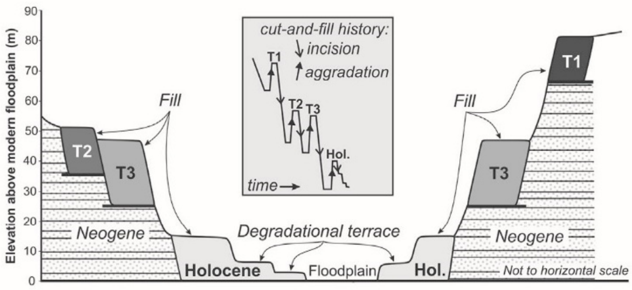

Fig. 11. Schematic sketch of the terrace staircase in the hanging wall reach, differentiating fill terraces from degradational terraces (bold black lines refer to the base of the Pleistocene terraces observed in the field). Multiple cut-and-fill events are outlined in the grey box.

Lithological contacts observed along both valley sides of the Moulouya are also slightly shifted (Fig. 2B). On the eastern valley side, the ~500 m-long offset to the south might be related to a subsidiary splay fault branching off from the main thrust (Twiss and Moores, 2007). Folding of the Neogene marine layers seems also associated to thrusting motion, as pointed out by the westward dipping of the partly solidified sand layers underneath the T2 terrace (Fig. 8C). Finally, the identification of this thrust zone in this sedimentary basin surely has implications on the local aquifer structure and water resources in the Triffa plain and Ouled Mansour plateau. This possibly implies a re-examination of several interpretations drawn by recent studies, which formerly interpreted the southern edge of the Ouled Mansour plateau as a large flexural feature (Boughriba et al., 2006; Fetouani et al., 2008).

5.3.2. *Regional implications*

The presence of this large thrust zone in the lowermost sedimentary basin of the Moulouya must also be discussed at a regional scale. First, it validates the assumption of the W–E striking main deformational front between the Rif belt and the Atlas mountains in the north-eastern part of Morocco (Barcos et al., 2014). This thrust zone is consistent with the statement that a substantial part of the N–S compressive shortening was accommodated along reverse faults located at the northern margins of the Beni Snassen massif and the Kebdana mountains (Barcos et al., 2014). A similar conclusion was previously reached by El Gout et al. (2010). Our observations clearly demonstrate that the studied thrust zone has accommodated a part of this deformation. Contrary to the claim that the marine/continental sediment cover of the Neogene-Quaternary impedes the recognition of fault patterns in the sedimentary basins of north-eastern Morocco (Chennouf et al., 2007b), we state that recent faulting activity in these basins significantly deformed the Neogene and Quaternary sediments and left clear imprints in the topography.

Second, morphometric indicators along with deformations of the drainage in the Moulouya catchment point to a general disequilibrium state (Barcos et al., 2014; Pastor et al., 2015). In particular, two major knickzones are conspicuous in the longitudinal profile (Fig. 1B). While the upstream knickzone corresponds to the deeply-incised reach into the crystalline rocks of the Palaeozoic Aouli batholith (and related metamorphic rocks), the downstream one occurs in the Mesozoic limestones of the Beni Snassen gorge. According to Pastor et al. (2015), the upstream knickzone is related to the capture of the Ksabi-Missour basin (located downstream, see Fig. 1A), which occurred at an unknown time period after the Early Pliocene (see section 5.1.). This capture induced the upstream propagation of an erosion wave which, when reaching the resistant crystalline rocks at the basin margin, resulted in the formation of a lithological knickzone. Bouazza et al. (2009) similarly suggested that the formation of the Beni Snassen gorge and the related knickzone resulted from several capture episodes at the onset of the Quaternary, although these authors provided no clear evidence for this explanation. Alternatively, it is well known that surface rupture resulting from fault motion often create knickpoints in the river channel and that these retreat at varying rates along the drainage network (e.g. Whittaker and Boulton, 2012; Cook et al., 2013; Boulton et al., 2014). Without explicitly rejecting the capture hypothesis, we suggest that the 30 km-long knickzone in the Beni Snassen gorge could also (partly) result from a transient fluvial reaction to Quaternary thrusting activity in the sedimentary basin and correlated uplift in the hanging wall block which is located >35 km downstream of the gorge outlet. In this respect, Boulton et al. (2014) showed that knickpoint formation in the Dades catchment (High Atlas) was related to increased Plio-Quaternary uplift rates as a result of fault activity along a main thrust zone (i.e. South Atlas Fault).

6. Conclusion and further research perspective

Our study confirms the usefulness of the terrace record of large rivers to investigate long-term crustal deformation. Significant thrusting activity in the lowermost sedimentary basin of the Moulouya, associated with N–S compressive shortening in this region, led to contrasting fluvial reactions and environments. On the one hand, long-lasting fluvial aggradation, materialized by 37 m-thick stacked terraces, has occurred in the footwall of the thrust. On the other hand, the hanging wall is characterized by a well-preserved terrace staircase, with (at least) three Pleistocene terrace levels. Late Cenozoic deformation and uplift induced in the hanging wall probably hindered profile regularisation of the Moulouya and might have been responsible for the knickzone observed in the Beni Snassen gorge. These interpretations agree well with independent morphometric indicators highlighting the disequilibrium state of the whole Moulouya catchment. Moreover, we showed that stratigraphies of Pleistocene terrace deposits display similar sequences in the middle and lower reaches of the river.

Assessing the rates of crustal deformation along this main thrust zone related to the ongoing collision between the African and Eurasian plates obviously constitutes the next decisive step; it therefore requires age estimations for these Pleistocene terrace deposits of the lower Moulouya. As recently stated by Rixhon et al. (2016), luminescence (OSL/IRSL) and electron spin resonance (ESR) dating techniques form one array of potentially applicable methods for the considered time span. In a northern tributary system of the Moulouya catchment, first OSL age estimates obtained on Late Pleistocene and Holocene wadi deposits highlighted the suitability of this method (Bartz et al., 2015). Likewise, the presence of quartz or quartz-bearing pebbles in the investigated profiles would allow for the application of cosmogenic nuclide dating (^{10}Be and ^{26}Al). In this case, burial dating, especially isochron dating, would be more favourable and/or suitable than surface exposure dating because of the significant thickness of silty/clayey deposits capping the terrace gravels.

Acknowledgements

This study was part of our research project C2 under the umbrella of the CRC 806 "Our Way to Europe", funded by the German Research Foundation (DFG) (ref. no. SFB 806/2). We warmly thank Aurelia Hubert-Ferrari and an anonymous reviewer; their insightful and pertinent comments greatly help improving the quality of this manuscript. We also thank the students for their enthusiastic support during the field campaign and Rolf Hollerbach (University of Cologne) for his kind assistance for the clast lithological analysis.

References

Ait Brahim, L.A., Chotin, P., Hinaj, S., Abdelouafi, A., Adraoui, A. El, 2002. Paleostress evolution in the Moroccan African margin from Triassic to present. Tectonophysics 357, 187–205.

Akoglu, A.M., Cakir, Z., Meghraoui, M., Belabbes, S., El Alami, S.O., Ergintav, S., Akyüz, H.S., 2006. The 1994–2004 Al Hoceima (Morocco) earthquake sequence: conjugate fault ruptures deduced from InSAR. Earth Planet. Sci. Lett. 252, 467–480.

Amos, C.B., Burbank, D.W., Nobes, D.C., Read, S.A.L., 2007. Geomorphic constraints on listric thrust faulting: implications for active deformation in the Mackenzie Basin, South Island, New Zealand. J. Geophys. Res. Solid Earth 112, 1–24.

Babault, J., Teixell, A., Arboleya, M.L., Charroud, M., 2008. A late Cenozoic age for long-wavelength surface uplift of the Atlas Mountains of Morocco. Terra Nov. 20, 102–107.

Barcos, L., Jabaloy, A., Azdimousa, A., Asebriy, L., Gómez-Ortiz, D., Rodríguez-Peces, M.J., Tejero, R., Pérez-Peña, J.V., 2014. Study of relief changes related to active doming in the eastern Moroccan Rif (Morocco) using geomorphological indices. J. Afr. Earth Sci. 100, 493–509.

Bartz, M., Klasen, N., Zander, A., Brill, D., Rixhon, G., Seeliger, M., Eiwanger, J., Weniger, G.-C., Mikdad, A., Brückner, H., 2015. Luminescence dating of ephemeral stream deposits around the Palaeolithic site of Ifri n'Ammar (Morocco). Quat. Geochronol. 30, 460–465.

Beck, S., Burger, D., Pfeffer, K.-H., 1993. Laborskript, Kleinere Arbeiten aus dem Geographischen Institut der Universität Tübingen, p. 11.

Bouazza, A., Ait Brahim, L., Dugué, O., Laville, E., Delcaillau, B., Cattaneo, G., Charroud, M., de Luca, P., 2009. Changements Sédimentaires dans les Bassins Néogènes de Taourirt et Guercif (Maroc Oriental): recherche de l'épisode d'érosion Messinienne. Eur. J. Sci. Res. 28, 317–327.

Boughriba, M., Melloul, A., Zarhloule, Y., Ouardi, A., 2006. Extension spatiale de la salinisation des resources en eau et modèle conceptuel des sources salées dans la plaine des Triffa (Maroc nord-oriental). Comptes Rendus Geosci. 338, 768–774.

Boulton, S.J., Stokes, M., Mather, A.E., 2014. Transient fluvial incision as an indicator of active faulting and Plio-Quaternary uplift of the Moroccan high Atlas. Tectonophysics 633, 16–33.

Candy, I., Black, S., 2009. The timing of Quaternary calcrete development in semi-arid southeast Spain: investigating the role of climate on calcrete genesis. Sediment. Geol. 220, 6–15.

Chennouf, T., Khattach, D., Milhi, A., Andrieux, P., Keating, P., 2007a. Détermination de la structure du bassin des Triffa par interprétation conjointe des données gravimétriques et sismiques : implications hydrogéologiques. Geomaghreb 4, 15–20.

Chennouf, T., Khattach, D., Milhi, A., Andrieux, P., Keating, P., 2007b. Principales lignes structurales du Maroc nord-oriental : apport de la gravimétrie. Comptes Rendus Geosci. 339, 383–395.

Cook, K.L., Turowski, J.M., Hovius, N., 2013. A demonstration of the importance of bedload transport for fluvial bedrock erosion and knickpoint propagation. Earth Surf. Process. Landforms 38, 683–695.

Cording, A., Hetzel, R., Kober, M., Kley, J., 2014. 10Be exposure dating of river terraces at the southern mountain front of the Dzungarian Alatau (SE Kazakhstan) reveals rate of thrust faulting over the past ~400ka. Quat. Res. 81, 168–178.

Demir, T., Seyrek, A., Westaway, R., Guillou, H., Scaillet, S., Beck, A., Bridgland, D.R., 2012. Late Cenozoic regional uplift and localised crustal deformation within the northern Arabian Platform in southeast Turkey: investigation of the Euphrates terrace staircase using multidisciplinary techniques. Geomorphology 165–166, 7–24.

El Gout, R., Khattach, D., Houari, M.-R., Kaufmann, O., Aqil, H., 2010. Main structural lineaments of north-eastern Morocco derived from gravity and aeromagnetic data. J. Afr. Earth Sci. 58, 255–271.

Fadil, A., Vernant, P., McClusky, S., Reilinger, R., Gomez, F., Ben Sari, D., Mourabit, T., Feigl, K., Barazangi, M., 2006. Active tectonics of the western Mediterranean: geodetic evidence for rollback of a delaminated subcontinental lithospheric slab beneath the Rif Mountains, Morocco. Geology 34, 529–532.

Faure-Muret, A., Morel, J.-L., 1994. Carte néotectonique du Maroc, Feuille 1 : Provinces du Nord, échelle : 1/1 000 000. Edition du Service Géologique du Maroc. Ministère de l'Energie et des Mines, Rabat.

Fetouani, S., Sbaa, M., Vanclooster, M., Bendra, B., 2008. Assessing ground water quality in the irrigated plain of Triffa (north-east Morocco). Agric. Water Manag. 95, 133–142.

Hollard, H., 1985. Carte géologique du Maroc (échelle 1/1 000 000). Edition du Service Géologique du Maroc. Ministère de l'Energie et des Mines, Rabat.

Ibouhouten, H., Zielhofer, C., Mahjoubi, R., Kamel, S., Linstädter, J., Mikdad, A., Bussmann, J., Werner, P., Härtling, J.W., 2010. Archives alluviales holocènes et occupation humaine en Basse Moulouya (Maroc nord-oriental). Géomorphologie Relief, Process. Environ. 1, 41–56.

Kaemmerer, M., Revel, J.C., 1991. Calcium carbonate accumulation in deep strata and calcrete in quaternary alluvial formations of Morocco. Geoderma 48, 43–57.

Khattach, D., Keating, P., Mili, E.M., Chennouf, T., Andrieux, P., Milhi, A., 2004. Apport de la gravimétrie à l'étude de la structure du bassin des Triffa (Maroc nord-oriental): implications hydrogéologiques. Comptes Rendus Geosci. 336, 1427–1432.

Khattach, D., Mraoui, H., Sbibih, D., Chennouf, T., 2006. Analyse multi-échelle par ondelettes des contacts géologiques: application à la carte gravimétrique du Maroc nord-oriental. Comptes-Rendus Geosci. 338, 521–526.

Lefèvre, D., 1984. Nouvelles données sur l'évolution plio-pléistocène du bassin de Ksabi (Moyenne Moulouya, Maroc). Comptes-Rendus Académie Sci. Paris 299, 1411–1415.

Lefèvre, D., 1989. Formations continentales pléistocenes et paléoenvironnements sédimentaires dans le bassin de Ksabi (Moyenne Moulouya, Maroc). Bull. Assoc. fr. étude Quat. 26, 101–113.

Linstädter, J., Aschrafi, M., Ibouhouten, H., Zielhofer, C., Bussmann, J., Deckers, K., Müller-Sigmund, H., Hutterer, R., 2012. Flussarchäologie der Moulouya-Hochflutebene, NO-Marokko. Madr. Mittl. 53, 1–84.

Maddy, D., Keen, D.H., Bridgland, D.R., Green, C.P., 1991. A revised model for the Pleistocene development of the River Avon, Warwickshire. J. Geol. Soc., Lond. 148, 473–484.

Margoum, D., Bouabdellah, M., Klügel, A., Banks, D.A., Castorina, F., Cuney, M., Jébrak, M., Bozkaya, G., 2015. Pangea rifting and onward pre-Central Atlantic opening as the main ore-forming processes for the genesis of the Aouli REE-rich fluorite-barite vein system, Upper Moulouya District, Morocco. J. Afr. Earth Sci. 108, 22–39.

Meghraoui, M., Morel, J.-L., Andrieux, J., Dahmani, M., 1996. Tectonique plio-quaternaire de la chaine tello-riffaine et de la mer d'Alboran. Une zone complexe de convergence continent-continent. Bull. Soc. Geol. Fr. 167, 141–157.

Monegato, G., Poli, M.E., 2015. Tectonic and climatic inferences from the terrace staircase in the Meduna valley, eastern Southern Alps, NE Italy. Quat. Res. 83, 229–242.

Nash, D.J., McLaren, S.J., 2003. Kalahari valley calcretes: their nature, origins, and environmental significance. Quat. Int. 111, 3–22.

Nash, D.J., Smith, R.F., 2003. Properties and development of channel calcretes in a mountain catchment, Tabernas Basin, southeast Spain. Geomorphology 50, 227–250.

Pastor, A., Babault, J., Owen, L.A., Teixell, A., Arboleya, M.-L., 2015. Extracting dynamic topography from river profiles and cosmogenic nuclide geochronology in the Middle Atlas and the High Plateaus of Morocco. Tectonophysics 663, 95–109.

Pazzaglia, F.J., 2013. Fluvial terraces. In: Shroder, J., Wohl, E. (Eds.), Treatise on Geomorphology, Fluvial Geomorphology, vol. 9. Academic Press, San Diego, CA, pp. 379–412.

Pissart, A., Boumeaza, T., 2010. Âge et origine de la terrasse limoneuse de la basse-Moulouya (Maroc nord-oriental). Bull. Société Géogr. Liège 54, 85–96.

Poujol, A., Ritz, J.-F., Tahayt, A., Vernant, P., Condomines, M., Blard, P.-H., Billant, J., Vacher, L., Tibari, B., Hni, L., Idrissi, A.K., 2014. Active tectonics of the Northern Rif (Morocco) from geomorphic and geochronological data. J. Geodyn. 77, 70–88.

Raynal, R., 1961. Plaines et piedmonts du bassin de la Moulouya. Etude geómorphologique. Rabat 617.

Rixhon, G., Demoulin, A., 2010. Fluvial terraces of the Amblève: a marker of the Quaternary river incision in the NE Ardennes massif (Western Europe). Z. für Geomorphol. 54, 161–180.

Rixhon, G., Briant, R.M., Cordier, S., Duval, M., Jones, A., Scholz, D., 2016. Revealing the pace of river landscape evolution during the Quaternary: recent developments in numerical dating methods. Quat. Sci. Rev. http://dx.doi.org/10.1016/j.quascirev.2016.08.016 (in press).

Rouchy, J.M., Pierre, C., Et-Touhami, M., Kerzazi, K., Caruso, A., Blanc-Valleron, M.M., 2003. Late Messinian to early Pliocene paleoenvironmental changes in the Melilla basin (NE Morocco) and their relation to Mediterranean evolution. Sediment. Geol. 163, 1–27.

Ruellan, A., 1971. Contribution à la connaissance des sols des régions méditerranénnes: les sols à profil calcaire différencié des plaines de la basse Moulouya (Maroc oriental). Mémoire Off. Rech. Sci. Tech. Outre-Mer, p. 302.

Sardinha, J., Carneiro, J.F., Zarhloule, Y., Barkaoui, A., Correia, A., Boughriba, M., Rimi, A., El Houadi, B., 2012. Structural and hydrogeological features of a Lias carbonate aquifer in the Triffa Plain, NE Morocco. J. Afr. Earth Sci. 73–74, 24–32.

Snoussi, M., Haida, S., Imassi, S., 2002. Effects of the construction of dams on the water and sediment fluxes of the Moulouya and the Sebou rivers, Morocco. Reg. Environ. Chang. 3, 5–12.

Thompson, S.C., Weldon, R.J., Berger, G.W., 2002. Late quaternary slip rates across the central Tien Shan, Kyrgyzstan, central Asia. J. Geophys. Res. 107 (B9), 2203.

Thorndycraft, V.R., Benito, G., 2006. The Holocene fluvial chronology of Spain: evidence from a newly compiled radiocarbon database. Quat. Sci. Rev. 25, 223–234.

Twiss, R.J., Moores, E.M., 2007. Structural Geology, second ed. W.H. Freeman and Company, New-York, p. 736.

Vernant, P., Fadil, A., Mourabit, T., Ouazar, D., Koulali, A., Davila, J.M., Garate, J., McClusky, S., Reilinger, R., 2010. Geodetic constraints on active tectonics of the Western Mediterranean: implications for the kinematics and dynamics of the Nubia-Eurasia plate boundary zone. J. Geodyn. 49, 123–129.

Whittaker, A.C., Boulton, S.J., 2012. Tectonic and climatic controls on knickpoint retreat rates and landscape response times. J. Geophys. Res. Earth Surf. 117, 1–19.

Zarki, H., Macaire, J.-J., Beck, C., De Luca, P., 2004. Morphosedimentary evolution of the lower Moulouya (north eastern Morocco) during the middle and upper Holocene. Seismicity Neotect. Eff. Geodin. Acta 17, 205–217.

Zielhofer, C., Bussmann, J., Ibouhouten, H., Fenech, K., 2010. Flood frequencies reveal Holocene rapid climate changes (Lower Moulouya River, northeastern Morocco). J. Quat. Sci. 25, 700–714.

Zielhofer, C., Faust, D., Linstädter, J., 2008. Late Pleistocene and Holocene alluvial archives in the Southwestern Mediterranean: changes in fluvial dynamics and past human response. Quat. Int. 181, 39–54.

Chapter 5

5 A multiple-dating approach of Quaternary fluvial terraces along the lower Moulouya River (NE Morocco)

Abstract

Our study presents the first chronological framework for Quaternary fluvial deposits of the lower Moulouya River (NE Morocco), based on a combination of ESR dating of quartz using the multiple centres (MC) approach, luminescence dating of K-feldspar (pIRIR$_{225}$, pIRIR$_{290}$) and palaeomagnetic analyses. The results indicate that the pIRIR$_{225}$ and pIRIR$_{290}$ signals of all samples are saturated, suggesting fluvial aggradation of the lower Moulouya River at least as early as the Middle Pleistocene. In accordance with the MC approach, D_e values of the Al and Ti centres generally agree within 1σ. However, a few Al centre D_e values are slightly higher than those of the Ti centre, as a possible result of slower bleaching kinetics. ESR dating results yield Early Pleistocene aggradation ages for all sampled river profiles, ranging from ~1.1 to ~1.5 Ma. Importantly, the ESR chronology is consistent with the palaeomagnetic results: the occurrence of mostly reversed polarity documented in the deposits (80 % of the samples) indicates a Matuyama age (>0.78 Ma). This consistency supports the robustness of the MC approach to date Quaternary fluvial deposits. The incision history of the lower Moulouya (0.025±0.003 mm/a) supports the assumption of Quaternary crustal shortening in the Triffa sedimentary basin, resulting from the convergence between the African and Eurasian plates.

Keywords

Quaternary, Geochronology, Fluvial sediments, ESR dating of bleached quartz, Multiple Centre approach, Palaeomagnetic analysis, Palaeoenvironment

[The results of this chapter were submitted to *Quaternary Science Reviews* (Bartz et al.)]

5.1 Introduction

The investigation of fluvial archives is of high interest for unravelling palaeoenvironmental changes linked to Quaternary climatic fluctuations (e.g., Macklin et al., 2002; Bridgland and Westaway, 2008) and/or long-term tectonic activity (e.g., Demir et al., 2012; Demoulin et al., 2017). Drained by the Moulouya River (i.e., one of the largest river systems in North Africa), the north-eastern part of Morocco is characterised by a complex geodynamic background due to its location within the convergence zone between the African and Eurasian plates (e.g., Meghraoui et al., 1996). Crustal deformation related to the main W-E striking deformational front between the Rif belt and the Atlas Mountains affected the lowermost ~65 km-long reach of the Moulouya during the Plio-Quaternary (Barcos et al., 2014; Rixhon et al., 2017b). This resulted in contrasting fluvial environments on each side of the thrust zone: thick stacked terraces in the footwall and a terrace staircase in the hanging wall (Rixhon et al., 2017b). Nevertheless, the timing of fluvial aggradation and terrace formation over the Quaternary remains as yet poorly reconstructed in the Moulouya valley and, more generally, in all river systems draining this convergence zone in NE Morocco.

Establishing chronologies for river terrace sequences and their related sediments or landforms has always been challenging. While palaeomagnetism has long proven its usefulness to yield relative chronologies of river terrace deposits (e.g., Jacobson et al., 1988; Li et al., 1997; Sancho et al., 2016), numerical dating methods have considerably evolved over the last decades, gaining both in robustness and accuracy (Rixhon et al., 2017a). Amongst the array of methods available for the Quaternary, we chose a combination of infrared stimulated luminescence (IRSL) and electron spin resonance (ESR) dating to produce numerical ages for the lower Moulouya deposits. Palaeomagetism is used to provide an additional independent age control. Though OSL of quartz is one of the most widely applied method to fluvial deposits (e.g., Wallinga, 2002; Rittenour, 2008), it suffers from the low saturation level of the quartz fast component (Wintle and Murray, 2006). In the northern catchment of the lower Moulouya River it has been shown that the OSL signal of quartz already reaches saturation at ~70 ka (Bartz et al., 2015, 2017). Alternatively, feldspar IRSL dating may serve as valuable tool in dating old Pleistocene deposits exhibiting higher dose saturation levels than conventional OSL methods (Jain, 2014). While IRSL ages may suffer from anomalous fading, leading to a loss of signal over time (e.g., Wintle, 1973; Huntley and Lamothe, 2001), elevated temperature post-infrared infrared stimulated luminescence (pIRIR) offers feldspar signals which are less or unaffected by anomalous fading (Thomsen et al., 2008; Thiel et al., 2011a). However, the investigation of anomalous fading of feldspars may also be used to predict IRSL field saturation by using an athermal detrapping model (cf. Huntley, 2006; Kars et al., 2008). The reliability of this model was tested in OSL-thermochronometry, where it successfully assessed the equilibrium state of feldspars in bedrock samples (e.g. King et al., 2016 and references therein). Its effectiveness in the context of fluvial deposits remains so far unknown and will be tested here.

ESR dating of optically bleached quartz grains potentially covers the whole Quaternary: the use of aluminium (Al) or titanium (Ti) centres allows dating Early- to Middle-Pleistocene fluvial sediments (e.g., Voinchet et al., 2010; Duval et al, 2017). As Al is the most abundant trace element in alpha quartz (Preusser et al., 2009), the Al centre is measurable in almost any quartz sample with somewhat high ESR intensities, sufficient thermal stability and high radiation saturation levels (e.g. Toyoda and Ikeya, 1991; Duval, 2012; Duval and Guilarte Moreno, 2012). Nonetheless, laboratory bleaching experiments have shown that the Al centre cannot be fully bleached (e.g. Toyoda et al., 2000; Duval et al., 2017), contrary to the Ti centre. The latter, which encompasses three sub-centres (i.e., Ti-Na, Ti-H and Ti-Li), provides faster bleaching kinetics compared to those of the Al centre and its ESR signal may be reset to zero by sunlight exposure (e.g., Tissoux et al., 2007; Duval et al., 2017). The reliability of the ESR dating method has been recently improved by the development of the multiple centres (MC) approach (Toyoda et al., 2000), where both the Al and the Ti centres are systematically measured in quartz. This method takes advantage of the different centre characteristics (i.e. bleaching kinetics, saturation level, ESR signal intensity) and checks whether both centres would provide consistent ESR results. In the fluvial context, Duval et al. (2015) have recently demonstrated the usefulness of the MC approach for dating Early Pleistocene terraces of the Alcanadre River in Spain.

Our study aims at (i) presenting the first geochronological framework for fluvial aggradation and terrace formation in the lower Moulouya valley, based on a combination of ESR dating of quartz using the MC approach, luminescence dating and palaeomagnetism applied together on four different sections along the Moulouya River; (ii) using luminescence dating techniques to study IRSL signals and field saturation and (iii) providing new insights into the long-term geomorphological evolution of this region of Morocco.

5.2 Study area

5.2.1 Geodynamic background

The NW-SE convergence between Africa and Iberia in the Straits of Gibraltar from the Miocene to the Quaternary has strongly affected the northern part of Morocco. Crustal deformation in the Western Mediterranean is most likely the result of shortening of the Betic-Rif mountain ranges and extension of the Alboran Sea (Fadil et al., 2006). Indicated by kinematic analyses of fault populations in the Rif and Tell Atlas, shortening directions and rates are characterised by an anti-clockwise block rotation of 15 to 25° (from NNE to NNW) and by movements of 1-2.3 mm/a, respectively (Meghraoui et al.,1996; Meghraoui and Pondrelli, 2012). The Rif mountain range showed NE-SW trending folds during the Quaternary manifested by left-lateral, strike-slip faults and associated overthrust structures (Meghraoui and Pondrelli, 2012). For instance, horizontal and vertical slip rates of ~0.9 and ~0.5 mm/a, respectively, have been determined for the Trougout fault in the northeastern Rif region (Poujol et al., 2014). Trend-topography surface analysis highlighted an E-W trending lithospheric dome in the eastern Rif and in the Beni Snassen massif (Barcos et al., 2014). Based on morphometric indicators, the latter is also distinguished at its northern margin by N-S shortening resulting in active deformations (Barcos et al., 2014). A disequilibrium state presented by deformations of drainage network and the presence of large knickpoints have also been detected for the Moulouya catchment (Barcos et al., 2014; Pastor et al., 2015; Rixhon et al., 2017b). There are also evidences of crustal deformation in Middle Quaternary terraces in areas eastward (Kert river) and westward (Oujda region) of the Moulouya River (Ait Brahim et al., 2002).

5.2.2 The lower Moulouya catchment

The Moulouya River, with a drainage area of ~74.000 km^2 (fig. 5.1a), represents the largest fluvial system in NE Morocco (Pastor et al., 2015). From its headwaters at the junction of the High and Middle Atlas to the outlet into the Mediterranean Sea, the ~600 km-long, SW-NE oriented main trunk flows across the Neogene Arhbalou, Ksabi-Missour and Guercif basins as well as the Zebra-Triffa plain and Ouled Mansour plateau (fig. 5.1a; Pastor et al., 2015; Rixhon et al., 2017b). Nowadays, the catchment is characterised by a semi-arid to arid Mediterranean climate. Average precipitations range from 150-200 mm in the lowlands to 600 mm in the Atlas Mountains (Kaemmerer and Revel, 1991; Ngadi, 1995). The hydrological regime of the Moulouya is characterised by extreme variations in its water discharge (Snoussi et al., 2002). The upper reaches (Arhbalou basin), encompassing the southern to southeastern foot slopes of the Middle Atlas and the northernmost flanks of the High Atlas, are composed of Palaeozoic substratum affected by the Hercynian orogeny. In the middle reaches (Ksabi-Missour and Guercif basins), the Moulouya drains the western flanks of the Moroccan High Plateaus. The lower reaches (Zebra-Triffa plain and Ouled Mansour) are mostly filled by Neogene marine sediments (Ruellan, 1971; Boughriba et al., 2006).

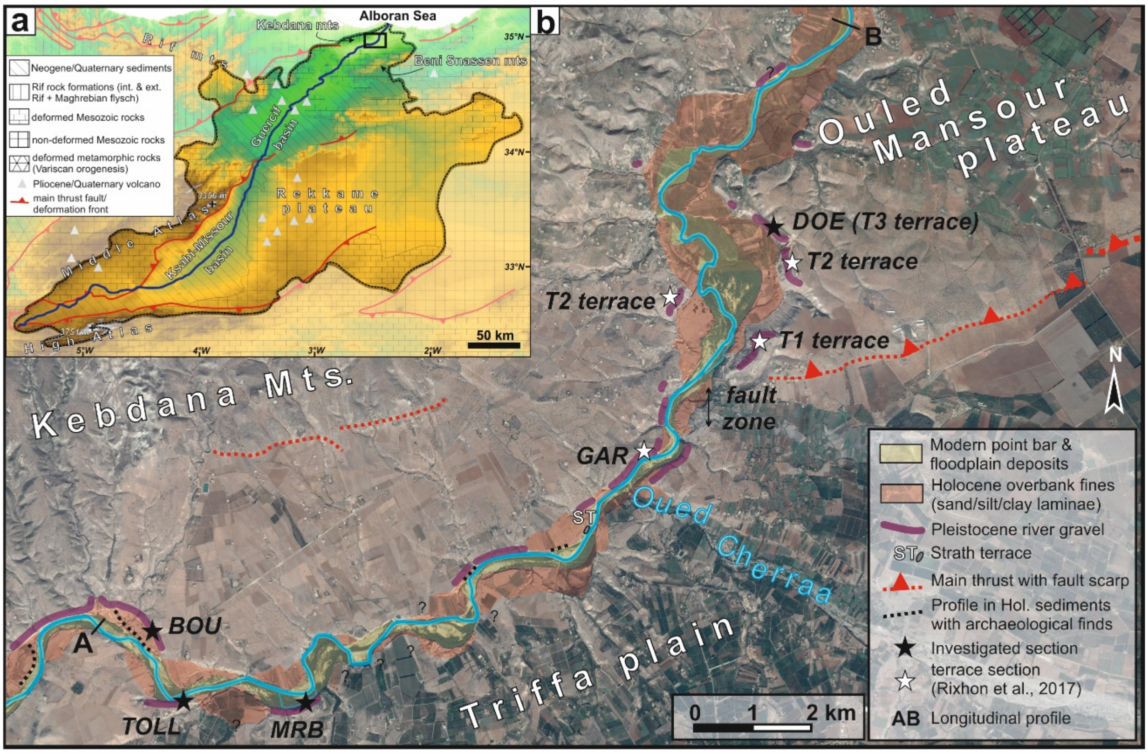

Fig. 5.1: Study area in NE Morocco (modified after Rixhon et al., 2017b). a: Relief map of the Moulouya catchment (delimited by dashed black lines) including the main geological structures (according to Barcos et al., 2014). b: The ~20 km-long studied valley reach of the lower Moulouya river with main morphological and geological features as well as profiles described in the text (BOU, TOLL, MRB and DOE; black stars). Terrace sections, decribed by Rixhon et al. (2017b) are also displayed (white stars). The longitudinal profile (see fig. 5.8) was measured from A to B (based on Google Earth) (satellite image: Google Earth CNES/Astrium 02.08.2014).

The depression is bordered by the Beni Snassen Mountains to the south and the Kebdana Mountains to the north. Both mainly consist of Mesozoic carbonate rocks, sandstone and slate formations (Ruellan, 1971; Khattach et al., 2004). Our study area encompasses the ~20 km-long river reach draining the northwestern rim of the Triffa plain and the Ouled Mansour plateau (fig. 5.1b). Rixhon et al. (2017b) have highlighted contrasting fluvial environments on both sides of a fault zone. In the hanging wall, a terrace staircase system encompasses three Pleistocene terrace levels, i.e. T1, T2 and T3, whose base lie at relative elevations of ~68, ~36 and ~26 m above the modern stream bed, respectively. Three distinct levels are also recognised in the fine-grained Holocene deposits (Pissart and Boumeazza, 2010; Rixhon et al., 2017b). In the footwall, up to 37 m-high stacked terraces characterised by two fining upward sequences bear witness to long-lasting fluvial aggradation.

5.3 Field sampling and methods

5.3.1 Sampling sites and strategy

Our fieldwork focused on four different fluvial sedimentary sequences (fig. 5.1b), located either in the footwall of the thrust zone (profiles BOU, TOLL, MRB) or in the hanging wall (DOE profile in terrace T3; see Rixhon et al., 2017b).

BOU is a ~22 m-thick section (fig. 5.2), located on the northern bank of the Moulouya River, ~9 km upstream of the fault zone (34°56’57.4’’N; 2°32’03.6’’W; 50 m a.s.l.). At our sampling location, up to 15 m-thick Holocene overbank fines hide the lower part of the section (Zielhofer et al., 2008, 2010) but coarse-grained deposits in the basal part are observable in the direct vicinity of the profile. Along the investigated uppermost ~7 m of the profile, we identify one unit: clast-supported layers show an alternation of finer and coarser gravel layers intercalated by three large sand lenses at 5.6-4.5, 1.9-1.4 and 0.9-0.2 m b.s. (below surface). The uppermost decimetres are characterised by an upward increasing calcrete development.

TOLL is a ~25 m-thick section (fig. 5.2), located on the southern bank of the Moulouya River, ~8 km upstream of the fault zone (34°56’27.2’’N; 2°31’47.5’’W; 51 m a.s.l.). The lower part of unit 1 (25-22 m b.s.) is characterised by an alternation of matrix- (sand) and clast- (cemented gravels) supported layers. The overlying (22-20 m b.s.) is characterised by a sharp boundary with a sediment change to homogeneous fine sand showing a fining-upward sequence. Taffoni-like weathering is observed in the upper part of the sand lense. The unit 2 (20-0 m b.s.) is dominated by mostly-cemented coarse-grained sediments. A transition to calcrete is observed in the uppermost metre.

MRB is a ~34 m-thick section (fig. 5.2), located on the southern bank of the Moulouya River, ~6 km upstream of the fault zone (34°56’24.4’’N; 2°30’40.2’’W; 51 m a.s.l.). The poorly sorted clast-supported unit 1 (34-25 m b.s.) encompasses rounded to subangular gravel up to 35 cm in size, where two fine laminated ~1 m-thick sand lenses are intercalated. The upper part (25-22 m b.s.) of unit 1 is composed of taffoni-like sand deposits. The unit 2 is formed by carbonate cemented clasts (22-13 m b.s.) and overlying middle to coarse sandy deposits (13-10 m b.s.). The top of unit 2 (11-10 m b.s.) is formed by a channel-like gravel layer. The upper unit 3 (10-0 m b.s.) consists of silt and clay-rich deposits, whilst the upper part is composed of a ca. 1 m-thick calcrete layer.

DOE is a ~23 m-thick section (fig. 5.2), located on the eastern bank of the Moulouya River, ~2 km downstream of the fault zone (34°59’59.2’’N; 2°26’27.3’’W; 44 m a.s.l.). A detailed stratigraphic description is provided in Rixhon et al. (2017b).

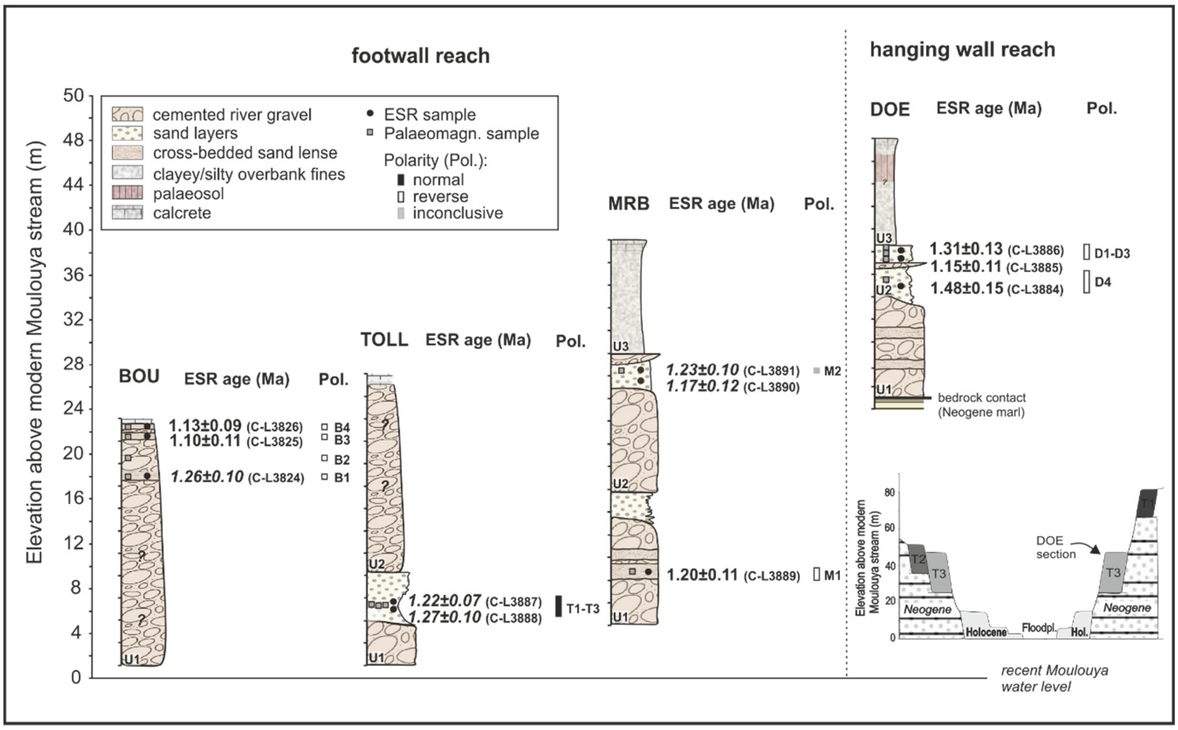

Fig. 5.2: Stratigraphy of the different investigated sections, namely the BOU, TOLL and MRB section in the footwall reach and DOE section (modified after Rixhon et al., 2017b) in the hanging wall reach of the fault zone. Sample ID's and ESR ages derived from the weighted mean D_e values of the Al and Ti centre (option D) are presented. If the Al De > Ti (option D) D_e, then the Ti (option D) ESR age is shown (italic).

For luminescence and ESR dating, we hammered steel tubes (25 cm long cylinder with a diameter of 5 cm) in the freshly cleaned vertical sections of the investigated profiles. The tubes were directly sealed from the sunlight with opaque tape and black bags. Whenever possible, sediment samples for dating analyses were collected within homogeneous layers in order to minimise the uncertainty on the external dose rate due to the absence of gamma in situ measurements. The surrounding material, in a radius of 30 cm, was additionally collected for high-resolution γ-spectrometry (HRGS), ICP-MS analyses and water content evaluations. For palaeomagnetic analysis, we sampled the same sections as for luminescence/ESR dating. A ceramic knife was used to extract hand blocks and a solution of sodium silicate was applied in order preserve the integrity of the samples. Orientation was taken in situ with a standard compass and clinometer.

Several samples were collected at each locality: At the BOU section, three samples (C-L3826-C-L3824) were extracted at depths of ~5.3, ~1.5 and ~0.5 m b.s. In addition, twelve palaeomagnetic samples were collected at depth of 7.1-7.3 (B1.1-1.3), 6.1-6.2 (B2.1-2.3), 2.3-2.6 (B3.1-3.3) and 6.5-6.8 m b.s. (B4.1-4.3). At the TOLL section, two luminescence/ESR samples (C-L3888 and C-L38887) were collected at depths of ~21.4 and ~21.6 m b.s. Three palaeomagnetic samples were extracted out of the same sand lense horizontally at depth of 21.5 m b.s. (T1.1-1.3). At the MRB section, three luminescence/ESR samples (C-L3889-3891) were collected at depths of ~30.0, ~13.8 and ~13.4 m b.s. For palaeomagnetic analyses, six samples were collected at depths of 13.4 (M1.1-1.3) and 29.5-29.9 m b.s. (M2.1-2.3). At the DOE section (unit 2), three luminescence/ESR samples (C-L3886-3884) were extracted at depths of ~3.2, ~1.9, and ~1.2 m b.s. In addition, palaeomagnetic samples were collected at 1.95-2.15 (D1.1-1.3), 2.65-2.85 (D2.1-2.3), 3.65-3.85 (D3.1-3.3) and 1.55-1.65 m b.s. (D4.1-4.2) respectively.

5.3.2 Sample preparation

Sample preparation for luminescence and ESR dating was undertaken under laboratory red light conditions. We separated the sample material of each tube in two parts to prepare OSL and ESR sample material. After wet sieving, coarse-grained (100-200 µm) sediments were treated with H_2O_2 (10 %), HCl (10 %) and sodium oxalate to remove carbonates, organic material and clay remains. Density separation with sodium polytungstate was performed to isolate quartz (ρ_1 = 2.62-2.68 g cm^{-3}) and K-feldspars (ρ_2 = <2.58 g cm^{-3}). Magnetic minerals were removed by using a strong neodymium magnet. The resulting quartz minerals were etched with HF (40 %) for 40 min plus a final HCl (10 %) wash. For luminescence dating, K-feldspars were additionally sieved to grain sizes of 100-150 µm and mounted on stainless steel discs. Each ESR quartz sample (100-200 µm) was divided into 12 aliquots. Whilst 1 aliquot was kept as a natural reference, 10 aliquots were irradiated with a calibrated Gammacell-1000 Cs-137 gamma source (dose rate = 6.8 Gy/min) to 100.0, 200.0, 394.6, 796.1, 1598.9, 3197.9, 6001.1, 10003.1, 15002.8 and 25018.1 Gy. Additionally, 1 aliquot was optically bleached in a solar simulator (Hönle SOL2) for about 1500 h. For palaeomagnetic analyses the 13 hand block samples were separated in 118 cubic specimen of ~8 cm^3.

5.3.3 ESR dosimetry

Low temperature (~90.0±0.1 K) ESR measurements were carried out at the Geochronology Facilities in the Centro Nacional de Investigación sobre la Evolución Humana (CENIEH, Burgos) with an EMXmicro 6/1 Bruker X-band ESR spectrometer coupled to a standard rectangular ER4102ST cavity and using a ER4141VT Digital Temperature control system based on liquid nitrogen cooling. Further details about the experimental setup and its stability may be found in Duval and Guilarte Moreno (2012).

Eleven samples were ESR dated with the MC approach by means of the multiple-aliquot additive-dose method (MAAD). The following experimental conditions were used for measuring (i) Al and (ii) Ti ESR intensities: (i) 5 mW microwave power, 1024 points resolution, 100 kHz modulation frequency, 1 G modulation amplitude, 40 ms conversion time and 10 ms time constant, only one scan was measured; (ii) 10 mW microwave power, 1024 points resolution, 100 kHz modulation frequency, 1 G modulation amplitude, 60 ms conversion time and 20 ms time constant, between 2 and 15 scans were used depending on ESR intensities. The given sample was placed in the exact centre of the cavity to ensure identical conditions of each aliquot. In order to take into account the angular dependence of the ESR signal each aliquot were measured three times after a ca. 120º rotation. ESR measurements were carried out on three different days to check data repeatability. Finally, we ended up with a data set consisting of nine ESR spectra for each sample for both Al and Ti centres. ESR intensities of the bleached aliquot were subtracted from ESR intensities of the natural and gamma irradiated aliquots prior to any D_e calculation (Voinchet et al., 2003).

The Al ESR intensity was measured between the top of the first peak (g = 2.018) and the bottom of the 16th peak (g = 1.993) (Toyoda and Falguères, 2003). ESR intensities of the Ti centre were extracted from three different options (Duval and Guilarte, 2015): (i) peak-to-peak amplitude measurement between g = 1.979 and the bottom of the peak at around g = 1.913 (option A, Ti); (ii) peak-to-baseline amplitude measurement around g = 1.915 (option C, pure Ti-H) and (iii) peak-to-baseline amplitude measurement around g = 1.913 (option D, Ti). It has to be noted that Ti option A and D are most likely mixtures of contributions of Ti-Li and Ti-H (Duval et al., 2017). For comparison, option E (peak at g = 1.979; Duval and Guilarte, 2015) was also explored, since this option gives the possibility to measure pure Ti-Li (Duval et al., 2017). ESR intensities of Al and Ti centres of each aliquot were then corrected by the corresponding number of scans, aliquot mass and a temperature correction factor (Duval and Guilarte Moreno, 2012).

Further details about ESR fitting procedure and D_e calculation can be found in supplementary material (Appendix A).

5.3.4 Application of luminescence dating techniques

All luminescence measurements were carried out at the Cologne Luminescence Laboratory (CLL) on automated Risø TL/OSL DA 20 readers equipped with $^{90}Sr/^{90}Y$ beta sources for irradiation and delivering dose rates of ~0.08 Gy/s. IR stimulation (880±80 nm) and signal detection through an interference filter (410 nm) were used for measuring the coarse-grained K-feldspar samples. An elevated temperature pIRIR single-aliquot regenerative-dose (SAR) protocol (Thomsen et al., 2008) was applied using a second IR stimulation temperature of either 225 (pIRIR$_{225}$; Buylaert et al., 2009) or 290 °C (pIRIR$_{290}$; Thiel et al., 2011b) after a preheat of 260 or 320 °C (both hold for 60 s), respectively. At the end of each SAR cycle an IR stimulation at 290 (pIRIR$_{225}$) or 325 °C (pIRIR$_{290}$) was used for 100 s to reduce recuperation. The response to a test dose (~30 % of expected natural D_e) was measured in the same way for both pIRIR protocols. After measurement of the natural pIRIR$_{225}$ or pIRIR$_{290}$ signal, athermal signal loss was estimated using fading tests following Auclair et al. (2003) for both the prior IR and pIRIR measurements of one sample per sediment profile (samples C-L3826, C-L3886, C-L3887 and C-L3891). Three aliquots (1 mm) per sample were measured in order to average sample specific g-values, which were normalised to a measurement delay time of 2 days after irradiation (g_{2days}; Huntley and Lamothe, 2001). Regenerative doses of 350 Gy and test doses of 125 Gy were used in the fading experiments. A prompt measurement was repeated after the longest delay measurement in order to confirm that sensitivity changes had been adequately corrected for. The model of athermal detrapping first proposed by Huntley (2006) and modified by Kars et al. (2008) was used to estimate sample specific field saturation $(n/N)_{ss}$ (Huntley and Lian, 2006), in which the natural IRSL intensity is governed only by the counterbalancing rates of signal accumulation due to environmental radiation and signal loss by anomalous fading (Kars et al., 2008). In addition to the use of the sample specific characteristic dose of saturation D_0 and the environmental dose rate, the field saturation value $(n/N)_{ss}$ is strongly dependent on the density of recombination centres ρ' which can be determined from the fading experiment data (Kars et al., 2008). We used a 15 % acceptance threshold of the environmental steady state level (Guralnik et al., 2015; King et al., 2016) in order to account for the uncertainty of interpolating a D_e value on a dose response curve close to saturation (Wintle and Murray, 2006).

5.3.5 Dose rate evaluation and age calculation

Radioelement activities (U, Th and K) were obtained by High Resolution Gamma Spectrometry (HRGS) analysis using a high-purity germanium detector. In addition, ICP-MS analysis of dry raw material was carried out via Genalysis Laboratory Services. The software DRAC v1.2 (Durcan et al., 2015) was applied for dose rate and age calculation using the conversion factors from Guérin et al. (2011) and alpha and beta attenuation factors of Bell (1980) and Guérin et al. (2012) (specifically chosen for either quartz or feldspar), respectively. The depth removed by HF etching was assumed to be 20±10 µm. Water contents (mass of water relative to the dry sample) were measured in the laboratory. The density of overburden was assumed to be 1.90±0.05 g cm^{-3}. The contribution of cosmic dose rates was assessed following the approach of Prescott and Hutton (1994) based on the altitude, latitude and longitude of the section as well as thickness and density of the overburden. For ESR dating of quartz, dose rate evaluation was done with an assumed α-efficiency k-value of 0.2±0.1 (Yokoyama et al., 1985) and an internal dose rate was assumed according to Vandenberghe et al. (2008).

5.3.6 Palaeomagnetic analysis procedures

Palaeomagnetic analyses were carried out at the Geochronology Facilities in the CENIEH. The natural remanent magnetisation (NRM) and progressive demagnetisation of each specimen was measured by using a Superconducting Rock Magnetometer (SRM) model 755-4K (2G Enterprises). A total of 52 specimens were analysed by thermal demagnetisation (TH) using an oven model TD-48SC (ASC Scientific) with progressively increasing steps between 50 and 650 °C, whilst 49 specimens were demagnetised by the alternating field method (AF) using the 3-axis degausser system built in the SRM, reaching a maximum AF field of 0.1 T. Finally, after visual inspection of the orthogonal demagnetisation diagrams (Zijderveld, 1967), the characteristic remanent magnetisation (ChRM) direction was computed for each demagnetised specimen, which is the highest stability component of the NRM by using the Virtual Paleomagnetic Directions (VPD) (Ramón and Pueyo, 2012). The corresponding virtual geomagnetic pole (VGP) position (latitude and longitude of the VGP) was computed for each ChRM direction, which were used to determine the local magnetic polarity at site level (using the software package Pmag by Tauxe, 1998).

5.3.7 Quantifying fluvial incision

DGPS (Topcon HiPer Pro) and laser distance meter (TruPulse 200 Rangefinger) were used in order estimate the relative elevations of the fluvial terrace surfaces and the modern floodplain (cf., Rixhon et al., 2017b). Fluvial incision rates were then estimated by using the age and the height of the surface of a terrace with regard to the recent position of the Moulouya stream bed (Burbank and Anderson, 2012).

5.4 Chronological data and robustness of the inferred chronologies

5.4.1 Palaeomagnetic analyses

Paleomagnetic results show that the different specimens have medium NRM intensities, with values ranging between 2.05x10^{-4} A/m to 8.11x10^{-2} A/m (fig. 5.3). Both thermal and alternating field demagnetisation procedures reveal that most samples have a secondary, viscous overprint, followed by a high temperature (or coercivity) component of magnetisation. NRM intensities and further details about the obtained data of each studied section can be found in Appendix B. VGP pole positions (Appendix B; supplementary material fig. B.1 and Table B.1) indicate reversed polarity for sections BOU, TOLL and MRB, whilst section TOLL reveals normal polarity. The presence of normal polarity in a few specimens from the BOU section can be interpreted as overprinting of the present day magnetic field (Appendix B; supplementary material Table B.1).

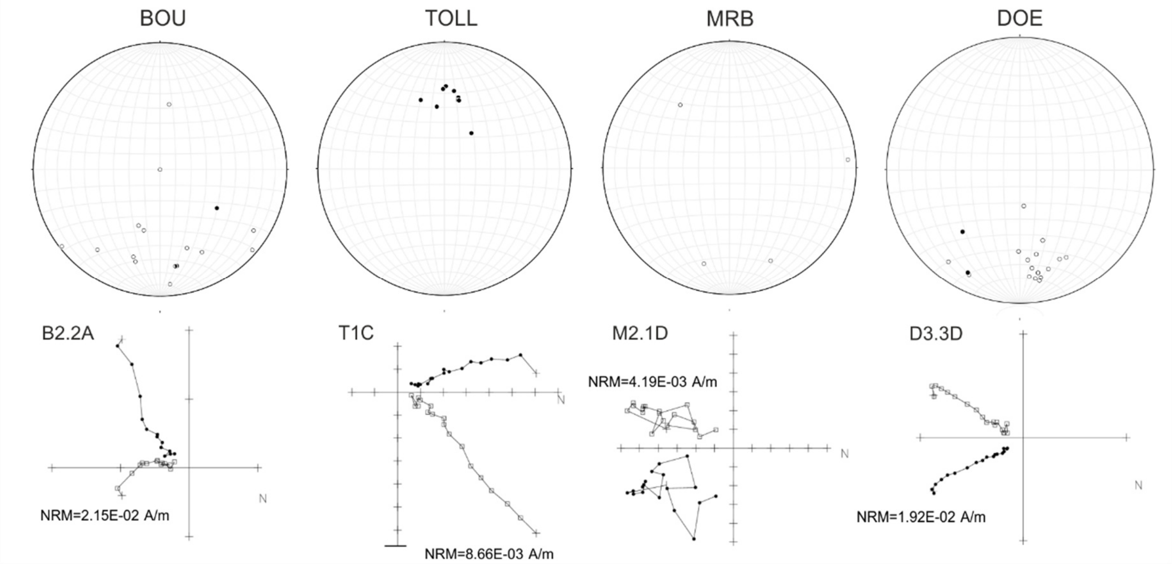

Fig. 5.3: Stereographic representation of the ChRM directions of each specimen (top); white (black) circles show upwards (downwards) inclinations, corresponding to negative and positive magnetisation directions respectively. Representative demagnetisation orthogonal plots (Zijderveld diagrams) of each sampling site (bottom); white (black) circles show vertical (horizontal) components of magnetisation.

5.4.2 ESR dating of quartz

5.4.2.1 Al centre

The Al centre (Table 5.1) of all samples shows ESR intensities with satisfactory repeatability which does not exceed 6 %. Most of the samples (7/11) present a good D_e repeatability

(<10 %), while 3 of them have a variability between 10 and 15 %. Only one sample (C-L3825) shows poor repeatability of ~23 %. Consequently, final D_e values were calculated by considering the average of nine ESR intensities. ESR intensities of the bleached aliquots range within relatively narrow range, between 47 and 57 %, suggesting thus similar bleaching conditions for all the samples.

Table 5.1: ESR data derived from the measurements of the Al centre. Fitting was performed with the EXPLIN function with weighting by the inverse of the squared ESR intensities ($1/I^2$; Appendix A). Measurement repeatability is assessed through the variability of the average ESR intensities obtained from each day of measurement. D_e repeatability is based on the variability of the D_e values obtained after each day of measurement.

Profile	**Sample ID**	**Bleaching coefficient (%)**	**ESR intensity precision (%)**	**D_e repeat. (%)**	**Al centre - EXPLIN ($1/I^2$)**		
					D_e (Gy)	**err (%)**	**r^2**
BOU	C-L3824	49 ± 6	3.3	3.6	1259 ± 144	11.5	0.9950
	C-L3825	50 ± 3	5.3	23.2	1437 ± 302	21.0	0.9809
	C-L3826	51 ± 2	2.2	14.5	1197 ± 131	10.9	0.9957
DOE	C-L3884	53 ± 3	4.0	11.1	1858 ± 261	14.0	0.9943
	C-L3885	57 ± 6	2.6	5.2	1537 ± 144	9.4	0.9971
	C-L3886	51 ± 2	1.7	9.7	1654 ± 306	18.5	0.9885
TOLL	C-L3887	54 ± 6	1.8	7.2	2008 ± 148	7.4	0.9982
	C-L3888	51 ± 2	3.7	12.5	1826 ± 170	9.3	0.9970
MRB	C-L3889	47 ± 5	4.3	2.0	1147 ± 144	12.5	0.9947
	C-L3890	56 ± 6	6.0	3.9	1747 ± 244	14.0	0.9933
	C-L3891	50 ± 2	2.4	9.5	1441 ± 92	6.4	0.9987

The DRC of the Al centre (fig. 5.4; Appendix C, supplementary material fig. C.1) of the Moulouya samples does not reach saturation at high dose points up to 25 kGy, which is consistent with previous observations (e.g. Lin et al., 2006; Duval, 2012). The EXPLIN function shows excellent goodness-of-fit with adjusted r^2 values >0.99 for the most of our samples (9/11). The only exceptions are samples C-L3825 and C-L3886 resulting both in r^2 values of ~0.98 which indicate moderate fitting results, yielding the highest relative D_e errors of 21 and 19 %, respectively. In contrast, uncertainties of the other samples are all <14 %. Finally, D_e values (Table. 5.2) range between 1537±144 and 1858±261 Gy for section DOE, 1147±144 and 1747±244 Gy for section MRB, 1826±170 and 2008±148 Gy for section TOLL as well as 1197±131 and 1437±302 Gy for section BOU.

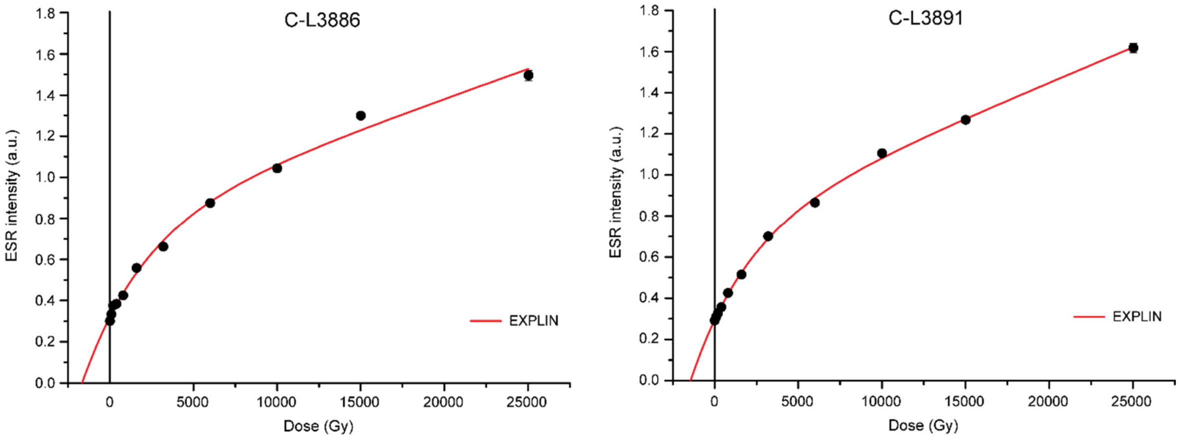

Fig. 5.4: Examples of dose response curves (DRC) of samples C-L3886 and C-L3891 obtained for the Al centre (DRC's of the Al centre of the other samples are presented in Appendix C).

5.4.2.2 Ti centres

The Ti centres measured in the Moulouya samples (fig. 5.5, see also Appendix C, supplementary material figs. C.2, C.3 and C.4) present a non-monotonic behaviour with the irradiation dose: whilst the Ti option A and D reaches a maximum ESR intensity, roughly at ~10 kGy (fig. 5.5), the Ti-H centre saturates at ~3 kGy (supplementary material fig. C.4). This behaviour is consistent with previous observations by Duval and Guilarte (2015) and Woda and Wagner (2007). Due to the lower ESR intensities, we focus on the Ti-Li centre, nevertheless further details about the Ti-H centre can be found in Appendix C (supplementary material fig. C.4, Table C.1). As expected, Ti centres reveal adequate resetting of the ESR signal after 1500 h of artificially bleaching, as no ESR signal could be observed from the bleached aliquots.

Ti options A and D (fig. 5.5) show excellent ESR intensity repeatability between 2.7 and 5.9 % as well as 3.3 and 6.8 %, respectively. This is also evident in good D_e reproducibility of the three individual measurements with relative variations <15 % for both options A and D (Table 3), except of samples C-L3887 and C-L3890 with variations up to ~20 %. In case of Ti option D, the three fitting options provide D_e values which are 1σ-consistent. For Ti option A, the SSE function reveals mostly slightly lower D_e values compared to those of the Ti-2 (EW) and Ti-2 ($1/s^2$), which are nevertheless consistent with Ti option D at 1σ. The goodness-of-fit is overall excellent with adjusted r^2 values >0.99. The only exceptions are samples C-L3884 and C-L3886 of both option A and D with an adjusted r^2 value of ~0.98. Although Ti option A and D show consistent D_e values at 2σ, option A yields systematically higher (up to 32 %) D_e values (Ti-2 $1/s^2$) compared to those of option D (fig. 5.6). Those higher D_e values may be caused by the peak at ~1.979, since option A is likely composed

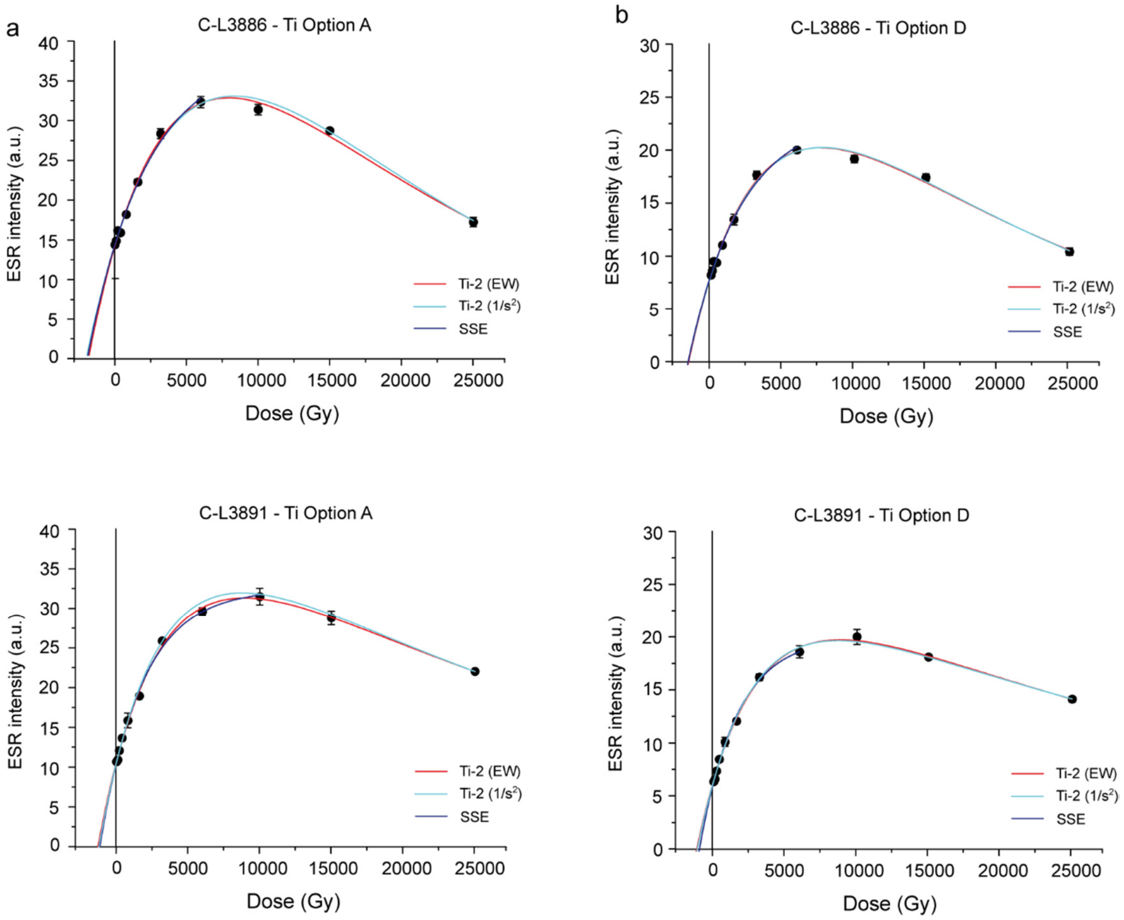

Fig. 5.5: Examples of dose response curves (DRC) of samples C-L3886 and C-L3891 obtained for a: Ti centre (option A) and b: Ti centre (option D) (DRC's of the Ti centre of the other samples are presented in Appendix C).

of a signal mixture of Ti-Li and Ti-H, which have absorption lines at very close g-values at g=1.913 and g=1.915 (Tissoux et al., 2007; Duval et al., 2016). In comparison with the isolated Ti-Li centre calculated with option E (Duval and Guilarte, 2015), D_e values are in fact higher (up to 24 %) than those from option A (Table 5.3) and even higher (up to 42 %) than those from option D. Our results are similar to observations of Beerten et al. (2006) who have investigated different ESR signals from Ti centres in comparison to OSL ages resulting in D_e overestimation based on the Ti-Li centre (option E). Additionally, Duval et al. (2017) have assumed that higher D_e values derived from option E may be the result of an influence of the Al centre, which are located near the peak at 1.979 and may thus influence the Ti-Li centre. Since it is still challenging to estimate the contribution of the Al centre to the pure Ti-Li centre (option E), it is so far questionable whether Ti option A or E give reliable D_e estimations. At the current state, it appears that both D_e data overestimate the true burial age. Since Ti option D reveal 1σ-consistency with the three fitting options, final D_e values should be derived from the Ti-2 ($1/s^2$) with excellent D_e precision. Consequently, final D_e values (Table 5.2) were calculated by considering the average ESR intensity over the three

Table 5.2: Dose rate, D_e and age data set (ESR of quartz). Summary of radionuclide activities of uranium (U), thorium (Th) and potassium (K) determined by high-resolution γ-spectrometry (HRGS) and ICP-MS analysis. Radionuclide concentrations (ppm) based on ICP-MS analyses were converted into activity values (Bq/kg). The DRAC v1.2 (Durcan et al., 2015) was used for dose rate and age calculation, with the conversion factors of Guérin et al. (2011), and alpha and beta attenuation factors of Bell (1980) and Guérin et al. (2012) for quartz. The contribution of the cosmic dose rate was assessed following the approach of Prescott and Hutton (1994). Final D_e values and ESR ages were derived from the Al (EXPLIN fitting function) and Ti option D (Ti-2 function and data weighting by $1/s^2$). Further geomorphological interpretations are based on either the weighted mean ages from the Al and Ti centre-D (if the individual ages derived from each centre are consistent), or the Ti centre-D only (if the Al age is significantly older). Key: (1) actual depth in metre below surface (m b.s.) of each section; (2) assumed water content; (3) assumed value, see main text for further details.; (4) weighted mean (wm) D_e values are calculated only when Al and Ti ages are consistent at 1σ; (5) based on the weighted mean D_e values derived from both Al and Ti centres.

Sec.	Section	BOU			DOE			TOLL		MRB		
	Sample ID	C-L3824	C-L3825	C-L3826	C-L3884	C-L3885	C-L3886	C-L3887	C-L3888	C-L3889	C-L3890	C-L3891
Unit	Grain size (µm)	100-200	100-200	100-200	100-200	100-200	100-200	100-200	100-200	100-200	100-200	100-200
	Depth (m b.s.)(1)	5.3	1.5	0.5	3.2	1.9	1.2	21.4	21.6	30.0	13.8	13.4
	Water content (%)(2)	15±5	15±5	15±5	15±5	15±5	15±5	15±5	15±5	15±5	15±5	15±5
HRGS	^{238}U (Bq/kg)	9.33±0.50	17.16±0.87	10.70±0.62	16.04±0.75	16.17±0.87	13.80±0.75	9.70±0.62	9.45±0.62	8.45±0.50	8.58±0.62	8.21±0.62
	^{232}Th (Bq/kg)	6.21±0.45	11.97±0.77	8.16±0.61	13.88±1.01	13.92±1.06	11.56±0.77	13.67±0.81	13.76±0.81	11.04±0.69	10.75±0.69	9.21±0.65
	^{40}K (%)	0.49±0.01	0.65±0.01	0.48±0.01	0.79±0.02	0.72±0.02	0.73±0.02	0.86±0.02	0.85±0.02	0.76±0.02	0.73±0.02	0.69±0.01
ICP-MS	^{238}U (Bq/kg)	9.70±0.92	20.89±1.12	11.81±0.95	19.40±1.09	13.56±0.98	15.05±1.00	10.94±0.94	9.95±0.92	9.58±0.92	8.46±0.90	9.33±0.91
	^{232}Th (Bq/kg)	8.72±0.41	12.13±0.54	9.78±0.45	14.57±0.64	11.56±0.52	14.61±0.64	14.28±0.63	13.35±0.59	11.20±0.51	10.83±0.49	10.55±0.48
	^{40}K (%)	0.52±0.01	0.68±0.02	0.47±0.01	0.78±0.02	0.56±0.02	0.77±0.02	0.85±0.02	0.79±0.02	0.74±0.02	0.62±0.02	0.67±0.18
Dose rate	Internal (Gy/ka)(3)	0.05±0.03	0.05±0.03	0.05±0.03	0.05±0.03	0.05±0.03	0.05±0.03	0.05±0.03	0.05±0.03	0.05±0.03	0.05±0.03	0.05±0.03
	External alpha (Gy/ka)	0.01±0.01	0.03±0.02	0.02±0.02	0.03±0.03	0.03±0.02	0.02±0.02	0.02±0.02	0.02±0.02	0.02±0.02	0.02±0.01	0.02±0.01
	External beta (Gy/ka)	0.41±0.02	0.60±0.04	0.42±0.03	0.69±0.04	0.64±0.04	0.62±0.04	0.68±0.04	0.67±0.04	0.60±0.04	0.58±0.04	0.54±0.03
	External gamma (Gy/ka)	0.24±0.01	0.39±0.02	0.27±0.02	0.43±0.03	0.42±0.02	0.38±0.02	0.40±0.02	0.39±0.02	0.33±0.02	0.33±0.02	0.30±0.02
	Cosmic (Gy/ka)	0.11±0.01	0.17±0.02	0.21±0.02	0.14±0.01	0.16±0.02	0.18±0.02	0.03±0.003	0.03±0.003	0.02±0.002	0.05±0.005	0.05±0.005
	Total (Gy/ka)	0.82±0.04	1.24±0.06	0.97±0.05	1.34±0.06	1.31±0.06	1.25±0.06	1.18±0.06	1.17±0.06	1.02±0.05	1.02±0.05	0.96±0.05
Dose	Al centre (Gy)	1259±144	1437±302	1197±131	1858±261	1537±144	1654±306	2008±148	1826±170	1147±144	1747±244	1441±92
	Ti centre-D (Gy)	1038±57	1361±111	1086±44	2040±172	1469±132	1643±134	1441±42	1479±85	1246±72	1200±105	1182±72
	wm Al and Ti-D (Gy)(4)	-	1370±125	1097±69	1985±175	1500±123	1645±148	-	-	1226±89	-	-
Age	Al centre (Ma)	1.53±0.19	1.16±0.25	1.24±0.15	1.39±0.21	1.18±0.12	1.32±0.25	1.70±0.15	1.57±0.17	1.12±0.15	1.70±0.25	1.50±0.12
	Ti centre-D (Ma)	**1.26±0.10**	1.10±0.10	1.12±0.07	1.53±0.15	1.13±0.12	1.31±0.12	**1.22±0.07**	**1.27±0.10**	1.22±0.10	**1.17±0.12**	**1.23±0.10**
	Combined Al-Ti age (Ma)(5)	-	**1.10±0.11**	**1.13±0.09**	**1.48±0.15**	**1.15±0.11**	**1.31±0.13**	-	-	**1.20±0.11**	-	-

Table 5.3: ESR data derived from the measurements of the different Ti centres. Fitting was performed with the Ti-2 function with weighting by the inverse of the squared errors ($1/s^2$) and the SSE function with weighting by the inverse of the squared ESR intensities ($1/I^2$). Measurement repeatability is assessed through the variability of the average ESR intensities obtained from each day of measurement. D_e repeatability is based on the variability of the D_e values obtained after each day of measurement.

Option	**A**		**D**								**E**	
Centre	**Mixture of Ti-Li and Ti-H**		**Mixture of Ti-Li and Ti-H**								**Pure Ti-Li**	
Function	**SSE**		**Ti-2**				**Ti-2**		**SSE**		**SSE**	
Weighting	**$1/I^2$**		**$1/s^2$**				**EW**		**$1/I^2$**		**$1/I^2$**	
Sample	Adj. r^2	D_e (Gy)	Meas. re-peat. (%)	D_e repeat. (%)	Adj. r^2	D_e (Gy)	Adj. r^2	D_e (Gy)	Adj. r^2	D_e (Gy)	Adj. r^2	D_e (Gy)
C-L3824	0.9941	1091±88	4.1	2.4	0.9960	1038±57	0.9964	1067±78	0.9968	1027±61	0.9883	1439±193
C-L3825	0.9975	1302±70	4.1	7.2	0.9922	1361±111	0.9955	1440±117	0.9947	1282±99	0.9985	1333±55
C-L3826	0.9967	1007±60	3.5	5.2	0.9982	1086±44	0.9973	1068±69	0.9968	939±58	0.9952	1277±106
C-L3884	0.9802	2158±336	6.8	14.6	0.9929	2040±172	0.9947	2017±150	0.9891	1803±203	0.9474	2915±796
C-L3885	0.9952	1511±125	3.3	6.0	0.9955	1469±132	0.9922	1433±120	0.99465	1433±124	0.9918	1653±182
C-L3886	0.9841	1879±270	3.5	4.9	0.9931	1643±134	0.9907	1609±145	0.9857	1642±239	0.9776	2248±449
C-L3887	0.9967	1602±99	4.6	18.1	0.9977	1441±42	0.9946	1654±119	0.9987	1314±52	0.9632	2352±606
C-L3888	0.9910	1397±141	4.9	7.3	0.9964	1479±85	0.9907	1435±119	0.9939	1462±137	0.9702	1490±305
C-L3889	0.9975	1269±67	4.2	3.9	0.9996	1246±72	0.9966	1551±88	0.9974	1223±67	0.9976	1599±97
C-L3890	0.9972	1373±78	3.9	22.1	0.9937	1200±105	0.9841	1653±210	0.9923	1131±108	0.9859	1969±258
C-L3891	0.9938	1162±96	3.8	2.8	0.9973	1182±72	0.9958	1221±92	0.9951	1041±78	0.9858	1400±177

repeated measurement of each aliquot of a given sample. D_e values for Ti option D range between 1469±132 and 2040±172 Gy for section DOE, 1182±72 and 1246±72 Gy for section MRB, 1441±42 and 1479±85 Gy for section TOLL as well as 1038±57 and 1361±111 Gy for section BOU.

5.4.2.3 D_e comparison between the different centres

An overview of the most reliable D_e values derived from Al (EXPLIN) and Ti option D (Ti-2 1/s²) is displayed on fig. 5.6: the results are mostly 1σ-consistent (6/11). Five samples (C-L3824, C-L3887, C-L3888, C-L3890 and C-L3891) are 2σ-consistent, showing clearly lower Ti (option D) D_e values compared to those of the Al centre (Table 5.2). Given the different bleaching kinetics of the different centres, with the Al, Ti-Li and Ti-H centres being the least, intermediate and most light sensitive centres, respectively, little higher D_e values derived from the Al centre may be the result of incomplete bleaching (Duval et al., 2016). Therefore, based on the principle of the MC approach all centres from samples C-L3825, C-L3826, C-L3884, C-L3885, C-L3886 and C-L3889 may be considered as completely bleached during

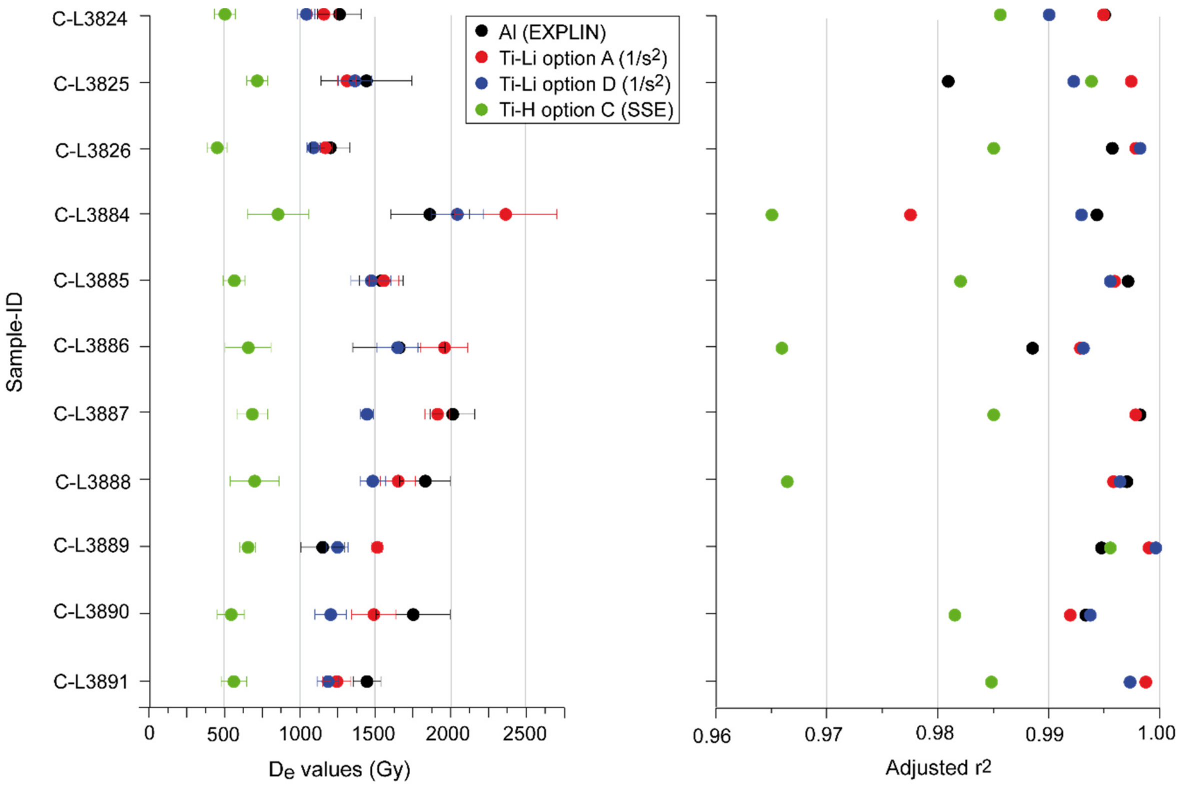

Fig. 5.6: Summary of the final fitting results of the different centres including D_e values and adjusted r² values.

fluvial transport (Toyoda et al., 2000; Duval et al., 2015). Due to stable ESR signals, adequate bleaching kinetics and 1σ-consistency of the Al and Ti (option D) of the latter six samples, we consider D_e values derived from both centres as reliable for calculating final ESR ages. Therefore, weighted mean D_e values were used to estimate combined Al-Ti ESR ages (Table 5.2). In case of the five samples resulting in higher Al D_e values, we consider the Ti (option D) D_e value as most suitable for further geomorphological interpretation (Table 5.2).

5.4.3 pIRIR dating of K-feldspar

Due to quartz OSL signal saturation, K-feldspars were used for further luminescence analyses. Sensitivity changes could be adequately corrected for and recuperation was <5 % of the sensitivity-corrected natural signal for both pIRIR protocols. We used laboratory fading tests in order to measure sample specific g-values from the IRSL 50 °C and the two pIR temperatures (Table 5.4) which range from g_{2days} of 3.56±0.60 to 6.05±0.79 %/decade ($IRSL_{50,225}$) and from 1.66±0.31 to 2.66±0.46 %/decade (pIR_{225}) as well as from 2.04±1.34 to 4.56±0.64 %/decade ($IRSL_{50,290}$) and from 0.80±1.17 to 2.35±0.43 %/decade (pIR_{290}). Such high g-values cannot be interpreted as laboratory artefacts and should be considered as athermal signal loss over geological time scales (Thiel et al., 2011b).

Table 5.4: Results of the fading experiments following the procedures of Auclair et al. (2003). Three aliquots (1 mm) per sample were measured in order to average sample specific g-values and normalised to a measurement delay time of 2 days after irradiation (g_{2days}; Huntley and Lamothe, 2001).

Profile	Sample ID	Fading rates g-value (%/decade)			
		$IRSL_{50,225}$	**pIR_{225}**	**$IRSL_{50,290}$**	**pIR_{290}**
BOU	C-L3824	6.05±0.79	2.66±0.46	-	-
BOU	C-L3826	-	-	4.56±0.64	2.26±0.34
DOE	C-L3886	3.56±0.60	1.66 ±0.31	2.04±1.34	0.80±1.17
TOLL	C-L3887	5.25±0.26	2.26 ±0.30	3.07±0.75	2.35±0.43
MRB	C-L3891	5.61±0.36	2.06 ±0.36	2.07±1.08	1.25±0.74

The athermal detrapping model of Huntley (2006) as implemented by Kars et al. (2008) was used in order to investigate whether our feldspar samples (C-L3826, C-L3891, C-L3887 and

C-L3886) are either in steady-state (i.e. field saturation; Huntley and Lian, 2006) or in disequilibrium which would give further chronometric information. Our observations show $(n/N)_{ss}$ and (n/N) values for the $pIRIR_{225}$- and $pIRIR_{290}$-protocols, using both the $IRSL_{50}$ and pIR signals, which are approximately equivalent, indicating that our samples are either in, or close to, field saturation (fig. 5.7).

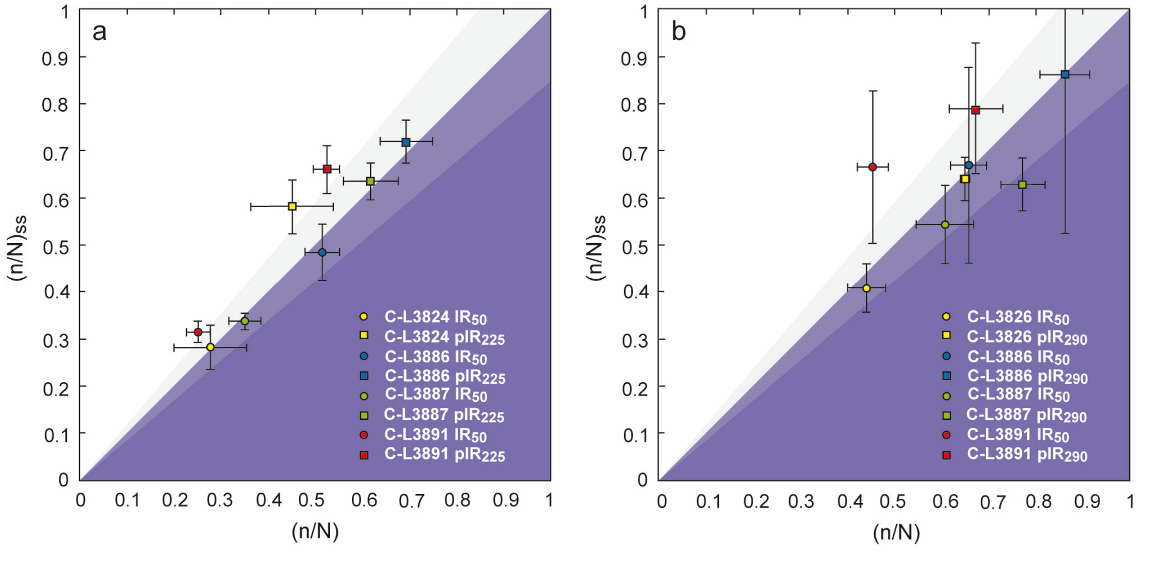

Fig. 5.7*:* Measured trap filling (n/N) vs. predicted field saturation $(n/N)_{ss}$. Plots for samples C-L3824, C-L3826, C-L3886, C-L3887 and C-L3891 assessing sample specific field saturation (Huntley, 2006; Kars et al., 2008). Error bars reflect 1σ-uncertainty. a) $pIRIR_{225}$ protocol and b) $pIRIR_{290}$ protocol. The large uncertainties in the $IR_{50,290}$ and pIR_{290} of the $(n/N)_{ss}$ values originated from the high standard deviations of the sample specific g-values, which are rather imprecise for the $pIRIR_{290}$-protocol.

5.4.4 Dose rate evaluation

Radionuclide activity values were determined by HRGS and ICP-MS analysis (Table 5.2). Both techniques provide consistent results at 1σ for 70 % of the samples (24/33), whilst the seven other samples are consistent at 2σ. Only two activity values vary slightly higher for samples C-L3885 and C-L3886, which might be simply due to sediment heterogeneity, as ICP-MS analyses are carried out on 5 g of material, vs. >400 g for HRGS measurements. No significant radioactive disequilibrium in the uranium decay chain was observed. Generally, when using either HRGS or ICP-MS activity values for calculating total dose rates, all ESR ages remain within an 1σ-error range (Appendix D, supplementary material fig. D.1). Therefore, total dose rates were calculated based on HRGS (Table 5.2). The thickness of overburden varies between 0.5 and 30 m b.s giving a contribution of the cosmic dose rate to the total dose rate between ~2 and ~21 %, respectively. The contribution of the beta and gamma dose rates to the total dose rate varies between 43 and 58 % as well as 27 and 33 %, respectively.

5.4.5 ESR age estimations and chronostratigraphical framework

Screening the IRSL signals for field saturation (Huntley, 2006; Kars et al., 2008; fig. 5.7), shows that all feldspar samples are saturated, suggesting fluvial aggradation of the lower Moulouya River at least as early as the Middle Pleistocene. Following the principles of the MC approach (Duval et al. 2017), final ESR ages were calculated using either a weighted mean of the Al and Ti (option D) D_e, if both D_e values are consistent, or the Ti (option D) D_e only, if the Al D_e is significantly higher than the Ti (option D) D_e (Table 5.2). Measured water contents varied between 2 and 15 %. Since sampling was carried out during a dry spring/summer season, the measured water contents probably underestimate the true water contents. Therefore, we assume a water content of 15±5 % for calculating the final ESR ages as a reasonable estimate. Nevertheless, a large associated error (30 % relative uncertainty) was assumed to encompass short- and long-term variations in the water content. If considering 25 % of water content instead, the resulting age estimates increase by ~10 % in average, but nevertheless remains within 1 sigma error (Appendix D, supplementary material fig. D.2).

ESR ages are stratigraphically 2σ-consistent within each terrace section (fig. 5.2). In combination with the palaeomagnetic analyses, these new data provide the first chronological framework for the evolution of the Moulouya terraces during Early Pleistocene times.

Regarding the uppermost part of the BOU section (fig. 5.2), ESR ages are stratigraphically consistent: the two samples from the upper part and stratigraphically distant by about 1 m provide two close ages of 1.10±0.11 and 1.13±0.09 Ma, while the third sample collected about 4 m below yields a somewhat older age of 1.26±0.10 Ma. These results clearly indicate an Early Pleistocene chronology for the deposits which is consistent with the reversed magnetic polarities identified at this section.

Similarly, the MRB section (fig. 5.2) reveals a deposition age of 1.20±0.11 Ma in its lowermost unit 1, which is in good agreement with the reverse polarity given by palaeomagnetic results, and indicating thus a Matuyama age (>0.78 Ma; Ogg, 2012). In contrast, palaeomagnetic analyses of the upper part of unit 2 in the MRB section did not provide conclusive results, but highly consistent burial ESR ages of 1.17±0.12 and 1.23±0.10 Ma indicate that aggradation took place during similar time periods.

In comparison, the unit 2 of the DOE section dates back to 1.48±0.15, 1.15±0.11 and 1.31±0.11 Ma, from the lower to the upper sample, respectively. The slight scatter of those ESR ages (12.7 %) may be partially explained by the heterogeneity of the depositional context which is displayed in gravel-dominated deposits (unit 2: channel-like structure at 11.5 m b.s.; fig. 5.2). In the absence of in situ gamma measurements, it is possible that the gamma dose rate derived from laboratory measurements might not fully reflect the actual sediment structure of unit 2 in the DOE section for some of the samples, inducing thus some age scatter. However, the three ESR samples unambiguously indicate chronologies >1 Ma, i.e. in excellent agreement with the reversed polarities identified within the unit 2. Similarly to the BOU and MRB sections, the DOE section indicates fluvial aggradation during the Matuyama chron as well.

In comparison, section TOLL (fig. 5.2) presents somewhat more contrasted results. Two consistent burial ESR ages of 1.27±0.10 and 1.22±0.07 Ma were obtained, indicating thus a similar chronology to the other sections. However, the corresponding palaeomagnetic study provide a normal polarity for those deposits. Given the excellent consistency between ESR and palaeomagnetic results obtained for the other sections, the possibility of a Brunhes chronology for those deposits may be reasonably discarded. Taking into account the ESR age errors, it seems instead that the deposits are more likely correlated to a normal polarity subchron like Jaramillo (1.05-1.00 Ma) or Cobb Mountain (1.22-1.19 Ma) (Singer, 2014) within the Matuyama chron, with some preferences for the former as it is very close to the ESR age results.

Finally, the excellent consistency between the ESR chronology obtained in this work and the palaeomagnetic results is remarkable, which give us a good confidence in the reliability and robustness of the chronological framework that has been established for the lower fluvial terraces of the Moulouya River.

5.5 Quaternary evolution of the lower Moulouya and geomorphological implications

5.5.1 Early Pleistocene fluvial deposition vs. absence of Middle and Late Pleistocene sediments

In addition to the remarkable concordance between the results of ESR dating and palaeomagnetism, the most striking result of this study is that all ESR ages point to massive fluvial deposition during the end of the Early Pleistocene. While ~1.5 Ma represents the oldest age found in the DOE section, a large majority of ages cluster around 1.1-1.3 Ma and there is no numerical age younger than 1 Ma (fig. 5.2). Although we cannot definitively preclude that fluvial deposition might also have occurred during the Middle Pleistocene, we observed and dated no fluvial sediment belonging to this time period in the 20 km-long studied river reach on both sides of the thrust. Given the massive aggradation recorded in the footwall reach (Rixhon et al., 2017b), Middle and Late Pleistocene sediments, if any, should be found in the uppermost part of the fluvial sequences. This assertion contradicts our ESR ages of 1.10±0.11-1.26±0.10 Ma in the BOU profile (all three in the very upper part of the sequence and all confirmed by a reverse polarity) and of 1.17±0.12-1.23±0.10 Ma in the MRB profile (the two upper ones). We thus assume that the complete hypothetical removal of the Middle and Late Pleistocene deposits over an unknown timespan appears unlikely and that the latter are absent in this river reach. In the hanging wall reach, no cemented terrace sediments are observed between the Early Pleistocene T3, i.e. the lowermost Pleistocene level in the terrace staircase, and the present-day valley bottom characterised by a Holocene infill (Rixhon et al., 2017b and this study). This also points to the absence of terrace formation during the Middle and Late Pleistocene.

In large river systems, cyclic fluvial aggradation and entrenchment episodes were largely interpreted as a response to Quaternary climatic fluctuations, especially since the Mid-Pleistocene revolution (e.g. Bridgland and Westaway, 2008). This cyclic pattern was also largely recognised in river networks draining the western Mediterranean basin, for instance in SE Spain (Macklin et al., 2002; Schulte et al., 2008). In contrast, the seemingly exclusive Early Pleistocene fluvial record in the lowermost sedimentary basin of the Moulouya strongly points to a highly discontinuous and acyclic sedimentation pattern over the second half of the Quaternary. We therefore suggest that the postulated absence of Middle and Late Pleistocene deposits from our sedimentary record seems ruling out climate as the main driver for long-term fluvial evolution of the lower Moulouya.

5.5.2 Fluvial incision in the lower reaches

Fadil et al. (2006) have assumed that shortening of the Betic-Rif mountain ranges and the extension of the Alboran Sea most likely caused crustal deformations in the Western Mediterranean. Observations in this study reveal that recent faulting activity considerably deformed the Neogene and Quaternary sediments, significantly changing the landscape pattern (Rixhon et al, 2017b).

The lowermost (TOLL and MRB) and the uppermost units (BOU) of the ~24-40 m-high fill terraces in the footwall reach show long-term, fast aggradation between ~1.3 and ~1.1 Ma. Similar to observations by Rixhon et al. (2017b), the bedrock could not be observed in the footwall reach. A strath terrace carved into cemented river gravels is evident ~2 km upstream of the fault zone (Rixhon et al., 2017b; fig. 5.1b), suggesting incision of ~3-4 m since the Mid Holocene attested by radiocarbon ages around ~7.8 ka from an archaeological site in the overlying overbank fines (Linstädter et al., 2012b). Strath terraces from the older river deposits are not evident in the investigated sections. Estimating incision rates remains therefore challenging due to the unknown duration of aggradation of the terraces (Rixhon et al., 2011; Burbank and Anderson, 2012; Demoulin et al., 2017).

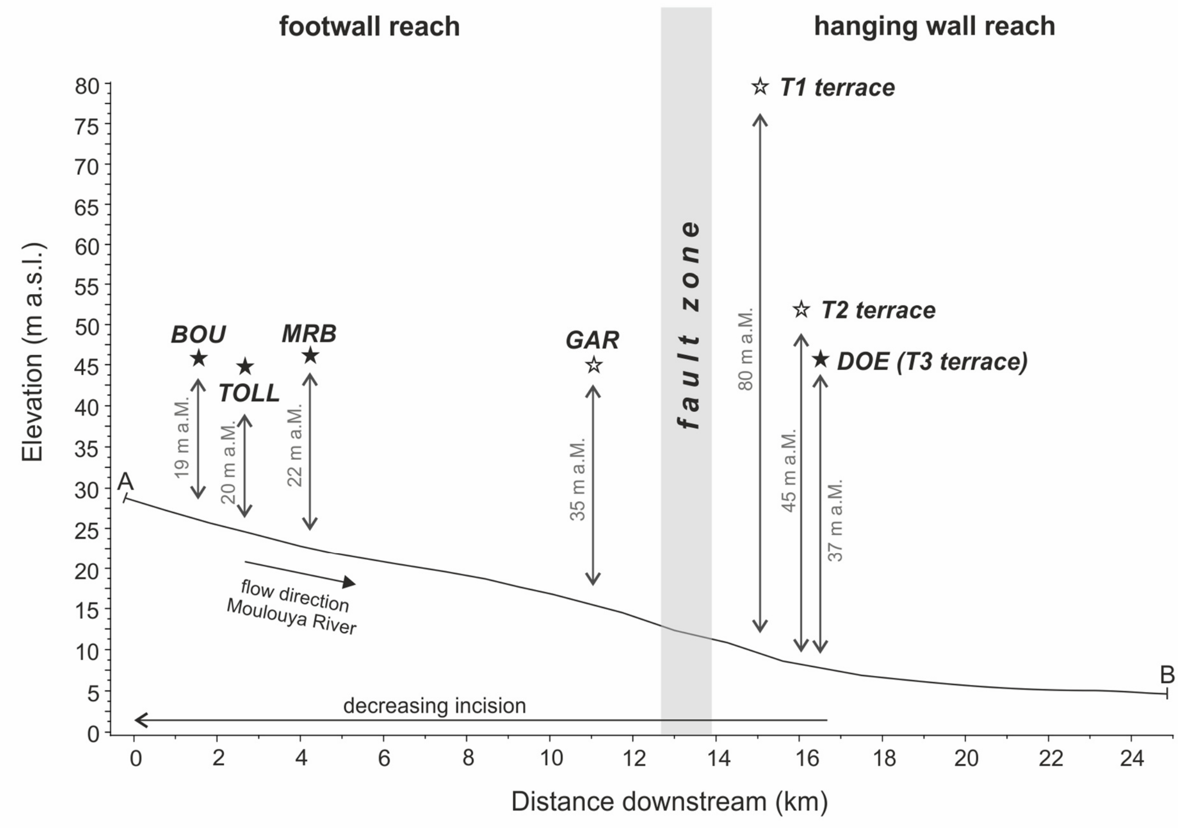

Fig. 5.8: Longitudinal profile of the 20 km-long studied Moulouya reach in the lower basin (see fig. 5.1b). Both river sections, investigated in this study (black stars) and reported by Rixhon et al. (2017b) (white stars), are presented. Section locations are shown with the actual height of the top of river gravels (metre above Moulouya; m a.M.), indicating a decreasing trend of incision in the upstream direction.

The well-preserved terrace flight in the hanging wall reach, characterised by the T1, the T2 and the T3 terrace (DOE section), from the highest to the lowest, respectively (Rixhon et al., 2017b) gains further knowledge about the fluvial incision history in the lower Moulouya basin. The DOE section is dated to between ~1.5 and ~1.3 Ma, which allow estimations of incision rates of 0.025±0.003 mm/a after 1.3 Ma. Similarly, the Oued Amekrane in the northern Rif Mountains yields minimum long-term incision rates of 0.035 mm/a (Barcos et al., 2014). In contrast, in the middle Moulouya reaches, tributary streams of the Moulouya River incised with rates of ~0.3 mm/a since the Mid Pleistocene, which has been calculated on the basis of terrestrial cosmogenic nuclide dating (Pastor et al., 2015). This is most likely due to different tectonic signals coming from the Middle Atlas Mountains caused by mantle-driven and thrust-related uplift (Pastor et al., 2015). Uplifting is also evident in the hanging wall reach, since the basement of Neogene bedrock of the T1, T2 and T3 terrace have clearly been raised (Rixhon et al., 2017b).

It appears that incision clearly reveals a diminishing trend in the upstream direction (fig. 5.8). Given the height of the top of river gravels in each investigated Moulouya section, the DOE, GAR (Rixhon et al., 2017b), MRB, TOLL and BOU sections reveal decreasing incision with heights above the present-day Moulouya stream of 35, 30, 22, 20 and 19 m, respectively (fig. 5.8). Also, a steepening of the stream slope can be identified. Barcos et al. (2014) have reported that stream length-gradient analysis yields maximum SLk values (e.g. Pérez-Peña et al., 2009) in the Beni Snassen gorge, ~40 km upstream of the investigated river sections (fig. 5.1). Based on morphometric indicators, the Moulouya drainage network is not at equilibrium state, but it is rather subject to active tectonics associated to lithospheric uplift (Barcos et al., 2014; Pastor et al., 2015). In this respect, in Holocene fluvial deposits, deformations have been observed suggesting ongoing neotectonics in this part of the region (Zarki et al., 2004; fig. 1.3).

Crustal shortening of the Rif Mountains, extension of the Alboran Sea, and active lithospheric doming in the Rif and Beni Snassen Massif (Fadil et al., 2006; Barcos et al., 2014) leads to tectonic impulses to the studied river reach. Therefore, it might be assumed that since the Early Pleistocene, the Moulouya most likely reacts on ongoing tectonics in its lower reach in order to reach an equilibrium state.

5.6 Conclusion

The Moulouya River (NE Morocco) is somewhat affected by long-term tectonic activity disrupting the whole sedimentary basin due to the convergence between the African and Eurasian plates. Recently, Rixhon et al. (2017b) have identified and reported for the first time a description of the Pleistocene fluvial terraces on the lower 65 km-long reach of the Moulouya River, which reflect crustal deformations due to a SW-NE striking fault zone (fig. 5.1). In the absence of numerical ages, the timing of these processes was nevertheless quite unknown. This study fills this gap by providing the first numerical ESR ages obtained for the fluvial terraces of the lower Moulouya River.

Due to the expected Early- to Middle Pleistocene age of the Moulouya terraces, establishing luminescence chronologies has been challenging. Therefore, ESR dating presents an alternative, reliable way to gain further chronological information on the ancient Pleistocene fluvial deposits. The results provide for the first time a chronological framework for the evolution of the Moulouya terraces during Early Pleistocene times. The ESR chronology is consistent with palaeomagnetic results. By presenting the first numerical age estimates of the Moulouya fluvial terraces, this study shows the high potential of the multiple centres (MC) approach in ESR dating. In the near future, further age control will tentatively be achieved by using single-grain TT-OSL dating and isochron burial dating (^{26}Al/^{10}Be) on the same fluvial deposits.

These geochronological and geomorphological analyses help to further understand the environmental evolution of the lower Moulouya fluvial terraces (see also Rixhon et al., 2017b) in a tectonically active area related to the convergence between the African and Eurasian plates. This study reveals crustal deformations during Early Pleistocene times associated to a main fault zone resulting in incision rates of 0.025±0.003 mm/a. Observations in this study validates the assumption of the W-E striking main deformational front and N-S compressive shortening encompassed along faults between the Rif and Atlas Mountains. However, further investigations should be carried out in the future in order to study the onset of fluvial deposition in the lower Moulouya basin (e.g., at the outlet of the Beni Snassen gorge) to improve the Quaternary stratigraphy of the Moulouya River in NE Morocco.

Chapter 6

6 Discussion

This research deals with fluvial environments in NE Morocco in the direct vicinity of a prehistoric site, the rock shelter of Ifri n'Ammar. Detailed investigations were conducted in order to establish a precise geochronological framework of two fluvial systems of different spatial scales. Furthermore, analyses were carried out in order to study past landscape changes. At last, a linkage between the onsite archive (Ifri n'Ammar) and the offsite archives (Wadi Selloum, lower Moulouya River) was made to discuss the influence of the AMH on natural conditions in this area.

6.1 Fluvial geomorphology in NE Morocco

Hypothesis 1 – Both small and large fluvial systems provide valuable insights into the geomorphic evolution of the study area

Given the different fluvial patterns and spatial dimensions of the Wadi Selloum and the lower Moulouya River, impulses (e.g. climatic, tectonic) that affect the geomorphological evolution are discussed.

Objective a: Investigating ephemeral stream deposits of Wadi Selloum

The Mediterranean region is characterised by a high sensitivity with regard to environmental parameters (e.g., climate, hydrology, vegetation; cf., Brückner, 1994). In Mediterranean North Africa, the semi-arid climate is directly reflected by the hydrological regime, characterised by episodic and highly energetic flash flood events with rapid flow velocities and high sediment discharge (e.g., Abdalla et al., 2014). Therefore, ephemeral streams are ubiquitous in semi-arid landscapes (Shaw and Cooper, 2008). However, these fluvial systems tend to be in an unstable state and discontinuous, since floods occur when and where sufficient surface runoff is generated, which is highly sensitive to short-term environmental changes (e.g., increase in precipitation, soil properties, land use) (Bull, 1997; Hook and Mant, 2002; López-Bermúdez et al., 2002).

The Wadi Selloum (Chapters 2 and 3), which drains the foot slopes of the rock shelter of Ifri n'Ammar (fig. 1.7), is one of those fluvial systems. While sediment properties of the Wadi

Selloum deposits are primarily determined by the carbonate- and limestone-rich source material (Benjelloun et al., 1971), their composition also reflects the sedimentary evolution including, e.g., transport processes and chemical modifications (Weltje and von Eynatten, 2004). Due to high contents of allochthonous material (quartz, K-feldspar, plagioclase), it seems that the fine-grained sediments observed in the different profiles (Chapters 2 and 3) form a mixture of fluvial (authochthonous) and aeolian (allochthonous) sediments.

Observations in this study have shown that the rather small catchment (290 km², fig. 3.1) of Wadi Selloum is characterised by a high morphodynamic variability with deposition on the valley floor and incision of the main trunk (Chapter 3; fig. 3.2). Whilst the former is likely the result of the larger accommodation space downstream and upstream of the rock shelter of Ifri n'Ammar, vertical erosion directly in front of the archaeological site is probably enhanced by the narrow local valley relief (e.g., Rock Selloum). Also, at least two larger rock falls narrow the accommodation space in front of Rock Selloum (fig. 3.2). It is noteworthy that bedrock was never reached during field work, indicating Wadi Selloum's incision into its own sediments. Therefore, given the two modes of operation, either aggradation or degradation (Bull, 1997), disequilibrium in Wadi Selloum's main stream is promoted by sediment deposition or channel downcutting. That causes either the fall or the rise of the local base level (Chapter 3).

As a northern first-order tributary stream of the Moulouya River, Wadi Selloum is located in the convergence zone of the Eurasian and African Plates implying a disequilibrium state of the whole Moulouya catchment (Barcos et al., 2014). Morphometric indicators show that the catchment of Wadi Selloum is also affected by this long-term tectonic activity. Two larger knickpoints downstream and upstream of the studied reach (Chapter 3; fig. 3.2) might point to tectonic influence in the study area. However, the time scale considered by Barcos et al. (2014) clearly differs with the last ~100 ka considered in this study (Chapters 2 and 3). Thus, recent tectonics may be neglected in Wadi Selloum's catchment area and in particular as a potential trigger of fluvial incision. Furthermore, the knickpoints are related to thick calcrete layers at the surface (fig. 3.2), which lead to an open question whether climate variability increased regressive erosion instead of tectonics in the studied reach.

Direct or indirect climatic forcing in form of precipitation or vegetation are crucial triggers on fluvial system dynamics (Vandenberghe, 2003). Both are of particular importance for Wadi Selloum's geomorphological evolution. The Moroccan landscape has been characterised by evergreen oaks and riparian forests during the early Holocene (Zapata et al., 2013; Zielhofer et al., 2017). Nowadays, however, scarce vegetation is obvious in the direct vicinity of Ifri n'Ammar, representing strong human influence due to intensive land use, e.g. by former deforestation and recent overgrazing (e.g., goats) and tillage. Consequently, enhanced soil erosion delivers abundant sediment supply from the hillslopes (Chapter 3; e.g., Brückner et al., 1986).

Thus, the ecologically unstable Wadi Selloum catchment is sensitive to human impact as well as short-term climatic changes, leading to a high discontinuity of aggradation and degradation phases (Chapter 3). This is reflected by the high erosional power during flash floods, which lead to large hiatuses in Wadi Selloum's sediment record.

In comparison with other palaeoclimate studies at a regional scale (e.g. Pérez-Folgado et al., 2004; Tjallingii et al., 2008; Ehrmann et al., 2013), this study shows considerable potential to give insights into palaeoenvironmental conditions based on the geomorphic and sedimentary fluvial features of an ephemeral stream system (Chapter 3).

Objective b: Studying fluvial terrace systems along the lower Moulouya River

After the Nile River, the perennial Moulouya River has the second largest catchment (~74,000 km²) in North Africa debouching into the Mediterranean Sea (Pastor et al., 2015). This study focuses on the lowermost reach of the Moulouya (Chapters 4 and 5), draining the Zebra-Triffa plain and the Ouled Mansour plateau (fig. 4.1). The investigated Moulouya reach is located >20 km upstream of the estuary in the Alboran Sea (fig. 1.4). Therefore, base level changes associated with eustatic variations cannot be excluded for terrace formation (Boumeazza und Pissart, 2010), but this factor alone is unable to explain the complex terrace pattern observed in this valley reach. Therefore, it remains the question whether tectonic activity and/or climate change is responsible for the shape of the lower Moulouya landscape (e.g., Bridgland et al., 2017).

Field observations and measurements highlight (Chapter 4) that the fluvial terrace record has been considerably affected by tectonic processes related to the collision between the African and Eurasian plates (Barcos et al., 2014). The newly identified W-E striking fault zone disrupted the sedimentary basin, associated with N-S compressive shortening in this region. While long-lasting aggradation formed up to 37 m-thick composite fill terraces in the footwall reach (Triffa plain), a terrace staircase with at least three distinct terrace levels (T1-T3; fig. 4.9) characterises the hanging wall reach (Ouled Mansour plateau).

The fluvial terraces are composed of coarse-grained deposits intercalated by sandy lenses (Chapters 4 and 5). Channel-like structures in, e.g., the T3 terrace (DOE section; fig. 6.1) in the hanging wall reach point to the development of multi-thread channels separated by channel bars (Eaton et al., 2010). Decimetre-large boulders (fig. 4.10), observed at the foot slopes of this profile (Chapter 4), indicate high stream power and transport capacities, similar to Pleistocene river deposits in SE Spain (Schulte, 2002). Thus, the sedimentary facies likely represent a former braided-river system defined by the presence of horizontal- and cross-bedded gravel and sand lenses as well as frequent boulders.

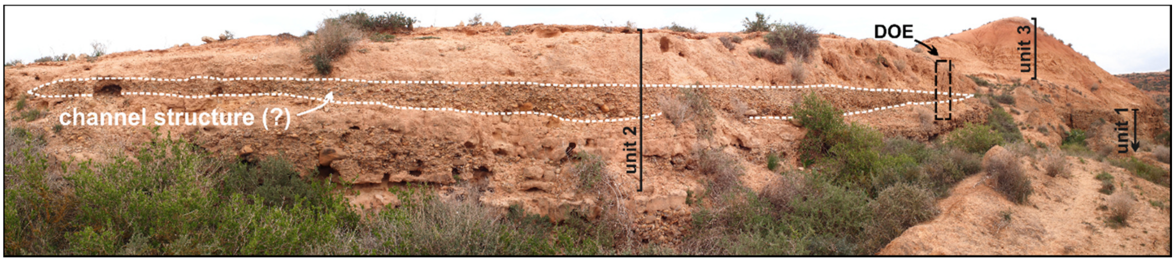

Fig. 6.1: Panoramic view of the DOE profile, showing the main units described in Chapter 4 (see also fig. 4.10). A channel-like structure is evident in unit 2 of the DOE profile.

In contrast, the Moulouya River pattern is nowadays sinuous to meandering, whilst its main trunk has changed during the last century due to the construction of several dams along the river. For instance, prior to the construction of the dam Mohammed V in the year 1967 (fig. 1.7), the Moulouya transported a mean sediment flux of ~$12x10^6$ t/a, which is nowadays reduced by ~93 % (Snoussi et al., 2002). During Holocene times, up to 15 m-thick fine-grained sediments have been deposited as overbank fines in the lower Moulouya reach (e.g., Zielhofer et al., 2008, 2010). In contrast to the braided-river deposits of the fluvial terraces, it might be assumed that the Moulouya stream pattern was similar to the modern meandering system during Holocene times when the vegetation cover was fully evolved (e.g., Zapata et al., 2013).

The development of these two fluvial systems, either meandering or braided, might have been affected by catchment-scale climatic pulses. While today the Moulouya catchment is not glaciated, former glacial and periglacial features have been observed around the highest peaks of the Middle and High Atlas Mountains (Awad, 1963; Hughes et al., 2011; fig. 1.5 and 1.6). Given the distance of at least 200 km to the upstream-located mountainous areas, the question remains, to which extent sediments were produced due to these climatic impulses and were subsequently accumulated in the investigated lower reaches of the Moulouya. Furthermore, due to the fact that those glacial/periglacial features have so far never been dated, it is still difficult to define the climatic cyclicity in the area.

Thus, it remains challenging to quantify the climate influence on the development of the fluvial terraces in the lower reaches of the Moulouya River. It is, however, certain that active tectonics played a crucial role in Moulouya's long-term fluvial evolution.

Given the Early Pleistocene age of the lower Moulouya fluvial terraces (Chapter 5), human impact on the development of the fluvial terraces may be neglected. In contrast, during Holocene times, human influence is an important factor in the study area (Linstädter et al., in press). For instance, on the left river bank ~2 km upstream of the fault zone, strath surfaces point to a 3-4 m higher base level during Holocene times (Chapter 4; fig. 4.6). However, it remains rather challenging to determine the human impact on this downcutting events alongside tectonic or climate factors during Holocene times.

6.2 Quaternary landscape evolution in the Moulouya catchment

Hypothesis 2 – Deposits of ephemeral streams and perennial rivers serve as suitable geo-archives for reconstructing past landscape changes

Fluvial response to a complex interplay between tectonics, climate and human impact is obvious in the study area. Alongside identifying and quantifying the geomorphic processes (Chapter 6.1) that affect the Wadi Selloum and the lower Moulouya River landscape, detailed investigations were carried out in order to check whether both systems give valuable insights into the Quaternary landscape evolution in NE Morocco.

Objective c: Dating fluvial deposits of different natures

Different luminescence (OSL, pIRIR and TL) and ESR dating techniques in combination with palaeomagnetic analyses were used to establish local chronologies of (i) the Wadi Selloum and (ii) the lower Moulouya fluvial terraces (Chapters 2, 3 and 5; fig. 6.2).

(i) Optical dating of ephemeral stream deposits is generally challenging (e.g., Klasen et al., 2013). Firstly, fluvial transport within the 290 km²-wide catchment area of the Wadi Selloum is characterised by short mobilisation distances during high-energetic flash flood events, which lead to an incomplete resetting of the luminescence signals of quartz and K-feldspar. This was proven by measuring the residual dose of a modern analogue sample (Chapter 2). It has been shown that aliquot size and the choice of the age model for calculating the true burial age are crucial points to obtain reliable OSL results (e.g. Klasen et al., 2013). In this respect, single-grain dating in combination with the minimum age model (Galbraith et al., 1999) could be used to remove partially bleached quartz grains from age calculation.

Secondly, due to the fact that soil forming processes occurred in the ephemeral stream deposits, demonstrated by micromorphological analysis (Chapter 3), sediment mixing may result in erroneous burial ages (e.g., Bateman et al., 2007). Some studies applied the finite mixture model (Galbraith, 2005) in order to receive different grain populations (e.g. Duller, 2008; Lomax et al., 2012). This approach could not be used in this study, since equivalent doses showed a rather symmetrical pattern (fig. 3.10). Therefore, the central age model (Galbraith et al., 1999) has been used on the single grain base, since laboratory analyses show reliable results. Nevertheless, it should be noted that the OSL age of sample C-L3828 (IAM 29; fig. 3.5), influenced by post-depositional processes, should be considered as a minimum age: it is not clear whether single- or multiple-grain aliquots underestimate or overestimate the true burial age, respectively (Chapter 3).

Thirdly, quartz OSL dating is limited due to the low saturation level of the fast component (Wintle and Murray, 2006). The upper dating range of quartz in the investigated ephemeral stream deposits is around 70 ka, which limits its application to older sediments (Chapter 2). As a consequence, high-elevated temperature IRSL measurements ($pIRIR_{290}$) were used to circumvent OSL saturation issues. In order to compare OSL and $pIRIR_{290}$ dating of the ephemeral stream sediments, two samples were dated by both luminescence techniques (profile IAM 6; Chapter 3) and yielded consistent ages within 1σ. Thus, $pIRIR_{290}$ dating has proven its reliability and could be used for dating Late Pleistocene ephemeral stream deposits.

Radiocarbon dating has often been used as independent age control in order to check the reliability of the luminescence ages in fluvial records (e.g., Klasen et al., 2013). In this study, the application of the radiocarbon technique was hampered due to the lack of well-preserved organic material. Also, shells of terrestrial gastropods found in the sediment sections (a) have the problem of the hard water effect, and (b) are known to be prone to reworking (Rixhon et al., 2017a); thus they should not be used for ^{14}C dating. Although independent age control was not possible, inter-method comparisons with TL dating of one pottery shard (Chapter 2) and OSL/pIRIR dating of two sediment samples of the same stratum (Chapter 3), allowed to establish robust chronologies of the ephemeral stream deposits. Ages range between 102±8 and 1.3±0.2 ka, highlighting discontinuous fluvial deposition between MIS 5c and the Holocene (Chapter 3).

(ii) Establishing chronostratrigraphies of the Moulouya fluvial terraces is equally challenging (Chapter 5). The low saturation level of the quartz fast component (Wintle and Murray, 2006) hampered the use of OSL dating. Alternatively, pIRIR dating techniques on K-feldspar were tested in order to avoid quartz saturation, but athermal detrapping modelling (cf. Huntley, 2006; Kars et al., 2008) also predicted sample-specific field saturation even of high-temperature pIRIR signals ($pIRIR_{225}$ and $pIRIR_{290}$; fig. 5.7).

In order to extend the dating range beyond the saturation level of the different luminescence signals, ESR dating of quartz was applied as an alternative dating procedure. Using the MC approach with ESR dating in fluvial environments (Duval et al., 2015), the Al and Ti centres were measured in order to check whether both paramagnetic centres would provide consistent results. An issue of the Al centre is that a light-sensitive “bleachable” and insensitive “unbleachable” component exist (Toyoda, 2015), which was also observed in the Moulouya samples (residual signals of ~50 % of the natural ESR intensity). However, using the method of Voinchet et al. (2003) (subtracting the Al residual dose from the D_e prior to any age calculation) resulted in overall agreement between the different paramagnetic centres, which proves that all centres were adequately bleached prior to deposition (e.g., Duval et al., 2016).

The dating results provide a chronological framework for the lower Moulouya terrace deposits of the Early Pleistocene (fig. 6.2). ESR ages between 1.27±0.10 and 1.13±0.09 Ma in the footwall of the fault zone show sediment aggradation approx. between MIS 37 and MIS 33, whilst the formation of the lowermost terrace (DOE profile) in the hanging wall dates between 1.48±0.15 and 1.31±0.13 Ma, indicating even older fluvial deposition (fig. 5.2).

First numerical age estimates of the Pleistocene fluvial terraces of the lower Moulouya River can be compared to relative age information inferred from palaeomagnetic analyses. The occurrence of mostly reversed polarity may be interpreted as deposition during the Matuyama chron (>0.78 Ma; Ogg, 2012). The lowermost part of the TOLL section shows normal polarity, most likely belongs to the Jaramillo (1.05-1.00 Ma) or the Cobb Mountains subchron (1.22-1.19 Ma) (Singer, 2014). In addition, saturated feldspar pIRIR signals indicate fluvial aggradation of the lower Moulouya River at least as early as the Middle Pleistocene.

Bearing in mind that chronostratigraphies of the ephemeral stream deposits and Moulouya fluvial terraces have not yet existed, the application of different trapped charge dating techniques served as valuable tools to get chronological information about deposition in the different fluvial systems. Whilst luminescence dating has been widely applied to fluvial sediments (e.g. Wallinga, 2002; Rittenour et al., 2008), ESR dating presents an innovative way to gain further chronological information of ancient Pleistocene fluvial environments.

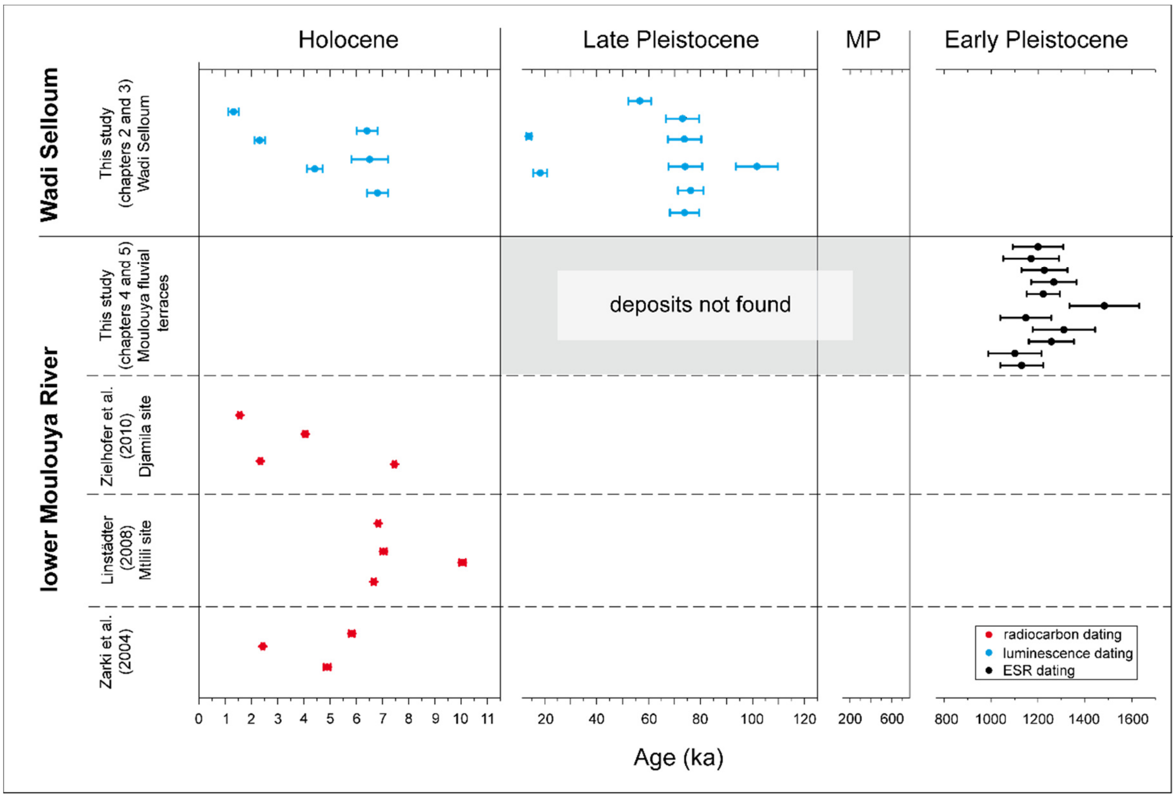

Fig. 6.2: Chronological constraints for fluvial records of the ephemeral stream Wadi Selloum and the perennial lower Moulouya River. Alongside luminescence and ESR dating (Chapters 2, 3 and 5) on both sites, radiocarbon ages from Zarki et al. (2004), Linstädter (2008) and Zielhofer et al. (2010) are presented. Here, only data from charcoal in fluvial layers and archaeological sites were retained. 1σ-standard deviations were used for ^{14}C-dating by these authors. Similarly, luminescence and ESR ages presented in this study show 1σ-confidence interval.

Objective d: Differentiating between phases of fluvial morphodynamic activity and stability

The Wadi Selloum and the Moulouya River are ephemeral and perennial fluvial systems, respectively, and record fluvial morphodynamics on different spatial and temporal scales (fig. 6.2). Fluvial terraces of the lower Moulouya River were formed during the Early Pleistocene between ~1.5 and ~1.1 Ma (Chapter 5). In contrast, Wadi Selloum mostly deposited fine-grained sediments in periods at ~100, ~75, ~55 ka, after the LGM and during short-term environmental changes in Holocene times (Chapters 2 and 3).

However, these time periods may have been interrupted by phases of decreased flooding and lower aggradation rates related to morphodynamically stable conditions, likely characterised by vegetation-rich land surfaces leading to soil formation and weathering processes (e.g, Zielhofer et al., 2009). Both fluvial systems show age-related soil forming processes typical for Mediterranean semi-arid environments (e.g., Badía et al., 2009; Candy and Black, 2009). In the lower Moulouya River, relictual features of pedogenetic processes have been observed in form of *per descendum* calcrete formations in the upper metres of the investigated Moulouya sections (Chapter 4; fig. 6.3). At the current state, it might be assumed that soil formation inferred from stable morphodynamic conditions occurred after 1.31±0.13 Ma in the hanging wall reach (DOE profile, T3 terrace). Similarly in the footwall reach, the uppermost ESR datings of the MRB and BOU profiles suggest soil forming processes post-dating 1.23±0.10 and 1.13±0.09 Ma, respectively (fig. 6.3), although it remains unknown when soil forming processes occurred. In the Wadi Selloum catchment, the development of three well-preserved soils were observed during the MIS 3 (palaeosol; Calcisol), the early- to mid-Holocene (recent Calcisol) and the late Holocene (recent Fluvisol) (Chapter 3). Pedogenic features in the Wadi Selloum deposits might be used as local palaeoenvironmental markers. The weak development of a Fluvisol in the Holocene section of the Wadi Selloum (Chapter 3), characterised by A horizon features, are similar to soil horizons in the lower Moulouya River, which date back to between ~7.3 and ~6.6 ka (Zielhofer et al., 2010). In the Wadi Selloum sediment sections a Calcisol has likely been developed during the same time (Chapter 3).

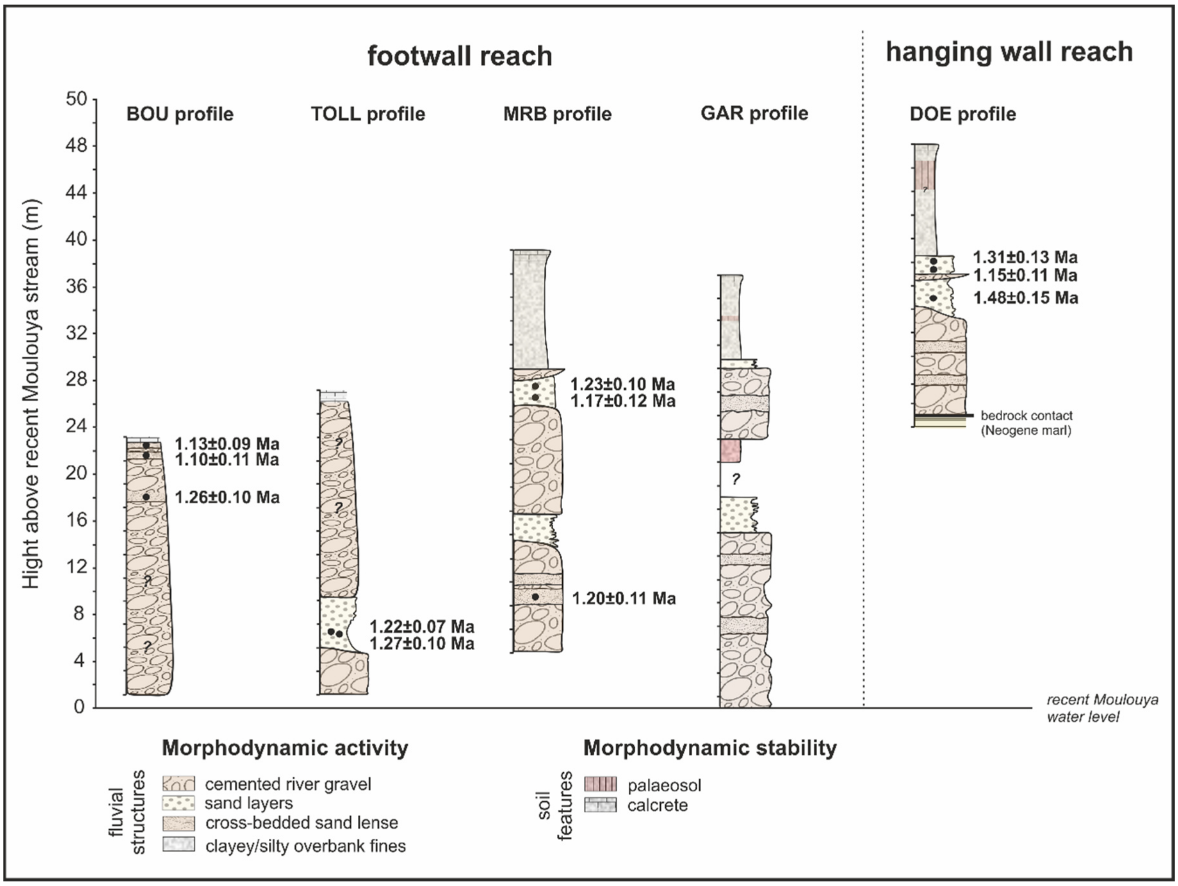

Fig. 6.3. Correlation of the investigated sediment profiles in the lower Moulouya reach. ESR ages (1σ) are presented for the different sections (see Chapter 5). Sediment properties (fluvial structures, pedogenetic features) are illustrated, which are characteristic of morphodynamic phases of activity and stability.

Our observations in Wadi Selloum (Chapter 3) show that overbank fines have mostly been deposited during more humid periods (e.g., Ehrmann et al., 2013). It might be assumed that these morphodynamic phases are characterised by enhanced flooding, likely due to peak precipitation. Taking into account the different fluvial pattern in the Moulouya deposits, either characterised by a braided-river or meandering system, it might be suggested that different climate signals are evident. In this respect, coarse-grained terrace sediments materialised by a braided-river system are a typical river pattern in glacial times, whilst fine-grained fluvial sediments deposited as overbank fines in a meandering river system are characteristic for interglacials (e.g., Schulte, 2002; Vandenberghe, 2002). In comparison to the Wadi Selloum record, it might be suggested that the fine-grained deposits on top of the Moulouya fluvial profiles (fig. 6.3) have been deposited in more humid periods, whilst the coarse-grained sediments are related to more arid times.

According to Zielhofer et al. (2010), Holocene cooling is reflected by higher sedimentation rates and increased flooding. However, the uncertainty of the radiocarbon ages and issues related to dating organic material deposited in flood plains (Rixhon et al., 2017a) should be taken into account. Therefore, assumptions about climatic forcings should be considered with caution, in particular in the semi-arid, highly sensitive Mediterranean region (Brückner, 1994).

Objective e: Unravelling long-term tectonic activity in the convergence zone of NE Morocco

Based on geodynamic and geomorphic studies, recent tectonic activity has been reported in North Morocco (Morel and Meghraoui, 1996; Gomez et al., 2000; Fadil et al., 2006; Barcos et al., 2014). Given its location in this tectonically active area (e.g., Fadil et al., 2006; Barcos et al., 2014), the Moulouya River presents a drainage network which is likely affected by long-term tectonic activity (Chapter 4 and 5).

Pastor et al. (2014) have shown that the upper and middle Moulouya reaches (e.g., High and Middle Atlas, High Plateaus; fig. 1.4) are not at steady state represented by large knickpoints along the main trunk and its tributaries (e.g., Za River; fig. 1.4). Here, the fluvial drainage system is likely affected by surface uplift which led to a considerable knickpoint development (Delcaillau et al., 2008; Pastor et al., 2014). Whilst knickpoints have not been observed in the lower Moulouya reach, only ~40 km upstream, the Beni Snassen gorge is characterised by maximum SLk values (e.g., Pérez-Peña et al., 2009) indicating active lithospheric uplift by knickzone development (Barcos et al., 2014).

The lower Moulouya River flows across a newly identified fault zone (Chapter 4). As a consequence, constrasting fluvial environments have been developed on both sides of the thrust (i.e., stacked terraces in the footwall reach and a terrace staircase in the hanging wall reach; Chapter 4). Similar observation have been observed by Poujol et al. (2014) in the northern Rif, who have reported that the El-Hadid River crosses the Trougout fault and formed a 20 m-deep canyon in the footwall, whilst the hanging wall block is characterised by at least three fill terraces.

Previous studies have reported that the Ouled Mansour plateau (hanging wall reach; fig. 4.1) might represent a Miocene horst leading to the assumption that normal faults are present at its borders (Khattach et al., 2004; Chennouf et al., 2007). Due to observations in this study (e.g., contrasting fluvial environments, recrystallization processes in the fluvial deposits) faulting seems to be adequate in the investigated Moulouya reach, although fault motion have not been indicated.

Therefore, uplifting in the hanging wall reach (Ouled Mansour plateau; fig. 4.1) has determined the position of the Moulouya base level. ESR dating of the lowermost terrace (T3 terrace; DOE) in the hanging wall reach suggests a minimum time-averaged incision rate of 0.025±0.003 mm/a over the last 1.3 Ma. This indicates rather low incision since Early Pleistocene times, but fluvial studies in the northern Rif show that incision rates are in the same order of magnitude after ~6 Ma (Barcos et al., 2014). The lower Moulouya, in its current direction, is most likely apparent since the onset of the Quaternary due to opening of the endorheic Guercif basin (Bouazza et al., 2009; fig. 1.4). Assuming the T1 terrace as the oldest fluvial formation in the hanging wall reach, according to Bouazza et al. (2009), the T1 terrace cannot be older than ~2.6 Ma. Therefore, it might be assumed that active tectonics played a crucial role in developing the terrace staircase during at least three cut-and-fill events between ~2.6 and ~1.3 Ma (T1 to T3, respectively; Chapters 4 and 5). Furthermore, it might be assumed that the knickzone in the Beni Snassen gorge (fig. 1.7; Barcos et al., 2014) could be caused by a transient fluvial reaction to Quaternary thrusting activity in the sedimentary basin and correlated uplift in the hanging wall block.

The Moulouya River has developed long-lasting aggradation sequences in the footwall reach between ~1.4 and ~1.1 Ma (fig. 6.3). The bedrock could not be found in the footwall block, hence it can be assumed that it likely lies below the present-day Moulouya stream. Therefore, bedrock incision is not apparent in the footwall reach, since the Moulouya is characterised by composite fill terraces (e.g. Pazzaglia, 2013) and has incised in its own sediments since the Early Pleistocene (Chapter 5). Since the duration of aggradation is unknown in this stacked terrace system, the estimation of incision rates remains challenging (Burbank and Anderson, 2012; Demoulin et al., 2017).

In contrast to the hanging wall block, direct uplift is not obvious in the footwall block. However, due to a decreasing incision trend, from downstream (DOE section) to upstream (BOU section) in this Moulouya reach and a steepening of the stream gradient, it might be assumed that the whole lower Moulouya River has been affected by tectonic activity since the Early Pleistocene. Observations in this study validates the assumption of the W-E striking main deformational front and N-S compressive shortening (Fadil et al., 2006) encompassed along faults between the Rif and Atlas Mountains. Ongoing neotectonics have also been observed in Holocene fluvial deposits (Zarki et al., 2004; fig. 1.3). Therefore, recent faulting activity considerably deformed the Neogene and Quaternary sediments and changed the landscape pattern of the lower Moulouya River.

Objective f: Linking the Wadi Selloum and the lower Moulouya River

The ephemeral stream Wadi Selloum represents a first-order tributary stream of the perennial Moulouya River, giving thus first local insights into fluvial morphodynamics in its northern catchment. The Wadi Selloum record does not provide insights from the onset of fluvial deposition due to the non-apparent bedrock contact at the base. However, taking into account the local relief in the vicinity of Ifri n'Ammar (fig. 3.2), valley filling is probably not much older than the lowermost part of profile IAM 2 (102±8 ka; fig. 3.3).

Whilst Wadi Selloum displays morphodynamic activity during Late Pleistocene times, though discontinuously, in the lower Moulouya reaches, deposits dating back to this time period have not been observed (fig. 6.2).

Given the different ages of the two fluvial systems (Chapter 3 and 5), it might either be the case that both fluvial systems have not been active synchronously during the Pleistocene or that Middle to Late Pleistocene Moulouya deposits have been eroded during the last millennia. Apparently, this is not the case in Holocene times, since mid- to late Holocene overbank fines are formed in both fluvial records. Previous studies have precisely documented the Holocene fluvial evolution in the lower Moulouya reaches without a focus on older deposits (fig. 6.2; Zarki et al., 2004; Ibouhouten et al., 2010; Pissart and Boumeaza, 2010; Zielhofer et al., 2008, 2010). In the Wadi Selloum, at least one investigated sediment section covers fluvial sediments between ~6.8 and ~1.3 ka (IAM 6; fig. 2.2).

Obviously, Middle to Late-Pleistocene fluvial deposits have not been found in the area (fig. 6.2). This leads to the following scenarios:

(i) The drainage network of the lower Moulouya River has significantly changed during the Quaternary. This may suggest that stream capture from newly developed tributaries might have led to higher erosional power. Thus, former Middle to Late Pleistocene fluvial deposits might have been eroded and these sediments were re-deposited further downstream or directly transported into the Alboran Sea (fig. 1.4).

(ii) The connection between the middle Moulouya reaches (Guercif basin; fig. 1.4) and the lower Moulouya were discontinuous during the Quaternary. In this respect, the tectonically active Beni Snassen massif (Barcos et al., 2014) might have been characterised by phases with enhanced uplift. During these periods, the Moulouya River might not have been connected to the Alboran Sea. Thus, deposits dating back to the Middle and Late Pleistocene might have not been available.

(iii) Channel relocation of the main stream led to the absence of deposits between the Early Pleistocene and the Holocene in the study area. Due to the lack of research in the lower Moulouya catchment dealing with Pleistocene time scales, it remains open whether it is possible to find fluvial deposits at other locations in that area.

6.3 Relationship between human occupation and natural conditions

Hypothesis 3 – Palaeoenvironmental information can be linked to the occupation phases of settlement history of Ifri n’Ammar

Environmental changes due to climatic shifts and tectonic activity have been observed for the Wadi Selloum and the lower Moulouya River (Chapter 6.2). Discontinuous occupation phases since the last ~200 ka are documented for NE Morocco (e.g., Nami and Moser, 2010). Therefore, the interplay between human activity and the landscape evolution have to be considered.

Objective g: Determining palaeoenvironmental archives that provide information about the human impact

Fluvial records may provide valuable insights into evidences of prehistoric hominid occupation, e.g., lithic traditions or immigration pulses (Bridgland et al., 2006; Mishra et al., 2007). In order to get information about human behaviour in the direct vicinity of fluvial systems, archaeological findings should be preserved within the sediment sections. As stated by Bridgland et al. (2006), Middle Palaeolithic sites are mostly in caves or rock shelters, whilst artefacts are rather rare in fluvial records at the Iberian Peninsula. Similarly, in NE Morocco, Middle Palaeolithic evidence is mainly preserved in caves such as Ifri n’Ammar (Nami and Moser, 2010) or Rhafas (Dörschner et al., 2016). Archaeological findings of the Middle and

Late Palaeolithic period (if any) have not been preserved in the investigated fluvial sequences of the lower Moulouya River or the Wadi Selloum.

In contrast, Neolithic pottery have frequently been found in the apron of Ifri n'Ammar (pers. comm. J. Eiwanger, 2014). A single pottery shard has been collected in profile IAM 6 in the foot slope of the rock shelter, dating back to 7.4±0.6 ka by TL and yielding Early Neolithic settling in the area (IAM 6, Chapter 2). Open-air sites such as Mtlili or Taoungat at the lower Moulouya banks (Linstädter et al., 2012a; fig. 1.7) have not been found.

Mediterranean ecosystems are known to have been impacted by human activity during the last millennia (e.g., Brückner, 1986; van Andel et al., 1986; Hooke, 2006; Mercuri et al., 2011; Chedaddi et al., 2015). The Moroccan landscape has been characterised by evergreen oaks and riparian forests during the early Holocene (Zapata et al., 2013; Zielhofer et al., 2017), whilst it has remarkably changed at the onset of the Neolithic due to intensive land use (Zapata et al., 2013). According to Linstädter et al. (in press), Neolithic innovations (e.g., pottery, domestic plants) began at ~7.6 ka in NE Morocco. Plant cultivation is clearly reported for cereals and pulses (Linstädter et al., in press). Wainwright and Thornes (2004) have demonstrated that enhanced land use during the last ~6 ka has affected fluvial systems in form of changes in the hydrological cycle or increased rates of erosion. Nowadays, in the Wadi Selloum valley, scarce vegetation is obvious in the direct vicinity of Ifri n'Ammar, representing strong human influence due to intensive land use (e.g., former deforestation, tillage), which led to enhanced soil erosion (Chapter 3).

However, based on pollen analyses from Morocco, Cheddadi et al. (2015) have reported that human impact (e.g., grazing, expansion of cultivated land, deforestation) clearly affects the landscape only since the last 2 ka. Prior to this period, past human disturbance on the environment had been minimal, since hunting and food gathering yielded barely effects on the environment (Baartman et al., 2007; Cheddadi et al., 2015).

Obviously, the sedimentation ended after ~1.3 ka in the Wadi Selloum when incision dominated aggradation (Chapter 3; fig. 3.4). Based on pollen analyses and radiocarbon dating, Wainwright and Thornes (2004) have shown peak anthropogenic disturbances around 1.3 ka in the Mediterranean region. Similar observations have been reported from the alluvial deposits of the lower Moulouya River (Zielhofer et al., 2010) and terrace sequences of the Kert River (El Amrani et al., 2008).

According to Faust et al. (2004), it remains challenging to estimate human influence on geomorphic processes, since anthropogenic land use or environmental/climatic changes may induce different and similar geomorphic effects, respectively. For instance, in northern Tunisia, Faust et al. (2004) came to the conclusion that climate variations are the main impulse on fluvial systems, whilst human impact only accentuated (intensified or weakened) geomorphologic processes. Similarly, river terraces in SE Spain show evidence of climate and human impact, while the latter likely played a subordinate role (Schulte, 2002). Thus, it remains open to which extent human impact has affected fluvial geomorphic processes in the Wadi Selloum and the lower Moulouya River.

It is, however, important to point out that human impact on nature resulting in, e.g., badlands or enormous sediment accumulation in the valleys, is most likely linked to the ecologically unstable environment of the Mediterranean region (Brückner, 1986).

Objective h: Correlation between human occupation phases and palaeoenvironmental changes

Human occupation in the rock shelter of Ifri n'Ammar and its vicinity is reported to have been discontinuous during the last ~170 ka, i.e., from the Middle Palaeolithic to the Neolithic cultures (Nami and Moser, 2010; Richter et al., 2010). In the framework of this thesis, the considered time span of the archaeological site is only captured in the Wadi Selloum record (Chapters 2 and 3), whilst the lower Moulouya terraces (Chapters 4 and 5) pre-date the time of modern humans in NE Morocco. Aggradation sediments in the Wadi Selloum have been dated to periods at ~100, ~75, ~55 ka, after the LGM and during the Holocene (fig. 3.12). Therefore, only the ephemeral stream deposits reveal first insights into palaeoenvironmental features in the time of human occupation (Chapters 2 and 3).

Middle Palaeolithic (~300-30 ka)

Archaeological finds of the Aterian techno-complex in the rock shelter of Ifri n'Ammar prove intensive human occupation between 171±12 and 83±6 ka, though discontinuously (Richter et al., 2010). According to Nami and Moser (2010), at least one phase of climate conditions appropriate for human occupation occurred during MIS 5a. This is in agreement with the Wadi Selloum record, which reveals overbank deposition during MIS 5c and MIS 5a. In North Africa, more humid climate conditions have been detected during these periods, based on marine palaeoenvironmental records (Pérez-Folgado et al., 2004; Tjallingii et al., 2008; Ehrmann et al., 2013; Larrasoaña et al., 2013). Furthermore, increased sea surface temperatures in the Alboran Sea indicating warmer climate conditions have been detected for MIS 5a (Pérez-Folgado et al., 2004).

Deposits from MIS 4 (~71-57 ka) have not been preserved within the rock shelter of Ifri n'Ammar (Nami and Moser, 2010), similar to the Rhafas cave near Oujda in NE Morocco

(Dörschner et al., 2016). According to Blome et al. (2012), MIS 4 is known to be a drier climate period in North Africa. Considering the confidence interval of the luminescence age in profile IAM 2 (fig. 3.3), the offsite archive Wadi Selloum has recorded sediments dating back to the end of MIS 4 and the beginning of MIS 3. The profile IAM 6 in the Wadi Selloum presents a high-energy accumulation sequence characterised by gravel-bearing layers after ~76 ka (Chapter 3). Thorp et al. (2002) assumed that such coarse-grained deposits in a fluvial system on the southern margin of the Anti-Atlas in Morocco relates to drier climate conditions. These findings would thus support the hypothesis of Nami and Moser (2010) that the absence of archaeological artefacts dating to MIS 4 is the result of unfavourable climate conditions.

Bearing in mind the uncertainties of the radiocarbon ages, humans occupied the rock shelter at 51.5±1.5 and 39.8±1.2 ka BP during the Middle Palaeolithic in MIS 3 (Moser, 2003; Linstädter et al., 2012a). This is in agreement with the Aterian data set of the Maghreb (Linstädter et al., 2012a; Dörschner et al., 2016). One palaosol has been observed in the Wadi Selloum record, post-dating 74±6 ka (fig. 3.5), which might have been developed during MIS 3 when humid and warmer climate conditions prevailed in North Africa (Pérez-Folgado et al., 2004; Tjallingii et al., 2008). Thus, it might be suggested that humans settled in Ifri n'Ammar in times of increased stabilisation of the land surface during MIS 3.

Upper Palaeolithic (~30-11 ka)

The archaeological sequence is, however, characterised by a large chronological hiatus of at least 25 ka between the Middle and the Upper Palaeolithic. The Iberomaurusian culture begins in the archaeological stratigraphy of the rock shelter of Ifri n'Ammar at 16.3±0.1 ka cal BP (Moser et al., 2003; Linstädter et al., 2012a; fig. 1.8). Observations presented in Chapter 3 show an increased aeolian input during MIS 2, indicating more arid climate conditions during and after the LGM. The Western Mediterranean climate is known to be characterised by drier and colder climate conditions (Pérez-Folgado et al., 2004; Tjallingii et al., 2008).

The Iberomaurusian culture is also present in the Bølling-Allerød interstadial (Nami and Moser, 2010) which has been characterised by intensive consumption of terrestrial gastropods indicating a warmer and more humid stage (Zielhofer, 2007; Hutterer et al., 2014). The Wadi Selloum was also active during this time (fig. 3.4).

Epipalaeolithic (~11-7.6 ka)

One potential cause for the settlement hiatus in Ifri n'Ammar during the Epipalaolithic may be related to inappropriate environmental conditions for human occupation. In the Wadi Selloum, the Younger Dryas is possibly revealed by morphodynamic features from coarse-grained deposits evident in profile IAM 6 (fig. 3.4). Based on marine palaeoenvironmental records from the Alboran Sea, drier and colder climate conditions prevailed during the Younger Dryas (Cacho et al., 2001; Fletcher and Sánchez Goñi, 2008). According to Barathon et al. (2000) and El Amrani et al. (2008), the cold stage of the Younger Dryas is reflected in the coarser sediments of the Kert River.

Neolithic (7.6-4 ka)

The development of the recent Calcisol (fig. 3.5), most likely in Early Holocene times, indicates warmer and humid climate conditions; they were also reported for North Africa (Pérez-Folgado et al., 2004; Tjallingii et al., 2008; Ehrmann et al., 2013). Up to now, the Neolithic has not been excavated within the rock shelter of Ifri n'Ammar, but was found in the direct vicinity of the archaeological site (pers. comm. J. Eiwanger, 2014). In the Wadi Selloum, one dated pottery shard (TL age of 7.4±0.6 ka; Chapter 2) proves the presence of the Neolithic culture in this area. Fluvial activity has changed during the Holocene, presented by a weakly-developed Fluvisol (fig. 3.4). This pedogenesis might point to short-term environmental changes during the Holocene, since it appears that Wadi Selloum's morphodynamics had not been stable long enough for the formation of Calcisol (Chapter 3).

Thus, with respect to the Wadi Selloum data, it may be assumed that peak precipitation due to wetter and warmer climate conditions occurred in North Morocco, which, in turn, led to enhanced flash flood activity in Wadi Selloum. Due to the observations in the fluvial archives, it may be suggested that humans occupied this area during periods with warmer and wetter climate conditions. Water is the basic precondition for human settling number one (Petraglia et al., 2010). The location of the rock shelter of Ifri n'Ammar, in the catchment of the Moulouya River (fig. 1.3), may have secured the hydrologic water supply for housing (Nami and Moser, 2010). However, it is not realistic that Wadi Selloum served as an adequate water source, since its water discharge has been too discontinuous. Nevertheless, the location in the catchment area of the Moulouya River and a rough distance of ~20 km to the main stream, seem to have allowed AMH settlement at least during wetter conditions. In particular, it seems that stable land surfaces characterised by enhanced vegetation cover and nutritious soils induced by more humid climate conditions favoured human settling in this area (Chapter 3). Plus, and this argument especially holds true for the earlier phases of human occupation, Ifri n'Ammar was an excellent site for hunting: its natural setting is comparable to a bottle neck, flanked on both sides by steep rocks and additionally narrowed by a rockfall. Any potential prey had to pass through this narrow gate and could, therefore, be easily hunted.

Chapter 7

7 Conclusion and Outlook

This geomorphological and geochronological research gives new insights into the environmental evolution of fluvial systems in NE Morocco. Up to now, Pleistocene landscape dynamics have only been poorly reconstructed, which is mainly due to missing geochronological data. Particularly, trapped charge dating methods and palaeomagnetic analyses have never been used in order to provide a better geochronological constraint of an ephemeral stream system and ancient Pleistocene river terraces in this part of Morocco.

This study shows that establishing chronologies of fluvial systems in the study area is somewhat challenging (Chapters 2, 3, and 5), but the application of different luminescence dating techniques (OSL, pIRIR, TL), the multiple centres approach in ESR dating, and palaeomagnetic analyses serve as suitable tools to produce robust chronologies for the investigated fluvial deposits. By presenting the first numerical ages, further knowledge about the Quaternary palaeolandscape could be gained.

The Wadi Selloum (Chapters 2 and 3) could be dated to between 102±8 and 1.3±0.2 ka. This reliable geochronological framework covers different morphodynamically stable and active phases in the time of Middle and Late Palaeolithic occupation in the rock shelter of Ifri n’Ammar. Periods of enhanced aggradation occurred around ~100 ka, ~75 ka, ~55 ka, after the LGM, and during the Holocene, whilst sedimentation ended after ~1.3 ka. The Wadi Selloum might be characterised by enhanced flooding during humid phases. Pedogenesis may be used as environmental indicator for more humid climate conditions during MIS 3 (palaeo-Calcisol), the early Holocene (Calcisol) and the late Holocene (Fluvisol).

However, these first implications about the palaeoclimate and environmental changes should be taken with caution, since the highly sensitive ecosystem of the Mediterranean region clearly affects the fluvial landscape of the Wadi Selloum. Short-term climatic shifts or human influence for example can lead to an extremely discontinuous and heterogeneous sediment record. For instance, a single high-energy flash flood event can cause a significant hiatus in the sediment archive. Therefore, it remains challenging to deduce climatic conditions that favoured or impeded occupation of the rock shelter of Ifri n’Ammar on the basis of the fluvial sediments in its vicinity. However, at the current state it seems that more humid and warmer climate phases favoured human settling in the area.

In order to support this first insights into the Quaternary landscape evolution and to gain further knowledge about environmental changes, the comparison with other geo-archives (e.g., lake sediments or speleothems) is still required. Caves are ubiquitous in the carbonate-rich Rif and Middle Atlas Mountains. Since speleothem growth requires humid and sufficiently warm climate, speleothems may serve as a suitable continental palaeoclimate record (e.g. Stoll, 2013). In collaboration with Prof. Dr. Denis Scholz (Johannes Gutenberg Universität Mainz/Germany), preliminary speleothem studies on cave archives in the Beni Snassen Massif (fig. 1.4) have been carried out in the second phase of the CRC 806. Stalagmite and flowstone samples from the cave "Grotte Jalida" (34°51'49"N 2°21'39"W, ~500 m a.s.l., ~80 km east of Ifri n'Ammar) were analysed to get first age information on the basis of U/Th MC-ICP-MS data. First results reveal U/Th ages of ~70 ka, ~75 ka, and ~123 ka (fig. 7.1), indicating more humid climate conditions during the MIS 5e and 5a that favoured speleothem growth. These preliminary U/Th data considerably support the conclusions from the Wadi Selloum record (Chapter 3) that morphodynamic activity has mainly been dominated during humid climate phases. In order to establish a high resolution palaeoclimate record, detailed investigations of speleothems from the surroundings of Ifri n'Ammar should be under focus in the near future.

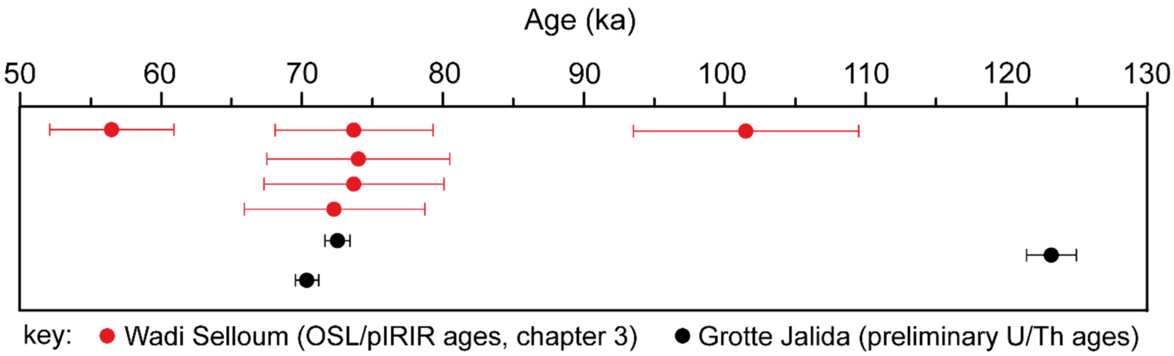

Fig. 7.1: Preliminary U/Th results in comparison with a selection of OSL/pIRIR ages from the Wadi Selloum record (see Chapter 3). Uncertainties of both luminescence and U/Th age results are presented with 1σ-confidence interval.

In contrast to the ephemeral stream Wadi Selloum, the lower Moulouya terraces date back to Early Pleistocene times (Chapter 5). The ESR chronology is consistent with the palaeomagnetic results, as the occurrence of mostly reversed polarity among the deposits indicates a Matuyama age (>0.78 Ma). So far, this study presents the first numerical age estimates of the lower Moulouya terraces and presents the high potential of the MC approach in ESR dating, especially beyond the dating range of luminescence dating. However, further independent age control is still required to evaluate the reliability of the geochronological framework; this shall be achieved in the near future by using single grain TT-OSL (cf., Arnold et al., 2016) and isochron burial dating ($^{26}Al/^{10}Be$; cf., Rixhon et al., 2017a) of the same deposits.

Based on this geochronological framework and geomorphological analyses (Chapters 4 and 5) it might be assumed that tectonic activity is the main trigger of fluvial development in the lower Moulouya reaches. This is in agreement with previous studies (e.g., Barcos et al., 2014; Pastor et al., 2015) which show that the whole Moulouya catchment is in disequilibrium state. A newly identified fault zone related to the collision of the African and Eurasian plates supports the assumption of a W-E striking deformational front between the Rif and Middle Atlas Mountains. Furthermore, observations in this study reveal that crustal shortening of the Betic-Rif Cordillera might also be assumed (Chapters 4 and 5).

At the current state, it appears that the lower Moulouya fluvial deposition has been discontinuous during the Quaternary: (i) there is still an open question about the onset of fluvial deposition in the lower Moulouya reaches. According to Bouazza et al. (2009), it might be assumed that the present-day lower Moulouya River has not been drained into the Alboran Sea prior to the Quaternary due to the endorheic conditions of the Guercif basin (fig. 1.4). So far, the two older terraces T1 and T2 could not be dated, but give tentatively information about the palaeolandscape from the beginning of the Quaternary; (ii) fluvial deposits from the Middle and Late Pleistocene were not observed in the investigated river reach, leading to the assumption that fluvial deposits have not existed or have been eroded since the Early Pleistocene (Chapter 5).

In order to investigate the fluvial environment in this area over timescales of the whole Quaternary and to understand the tectonic activity during this time period, further studies on the Moulouya deposits should be carried out at the outlet of the Beni Snassen Massif (fig. 1.7). Here, well-preserved alluvial fan deposits have been detected in the year 2016. These fluvial deposits may correspond to the oldest fluvial sediments of the lower Moulouya River and may potentially give new insights into the Quaternary palaeolandscape, which could then be linked to the studied reach further downstream (fig. 7.2).

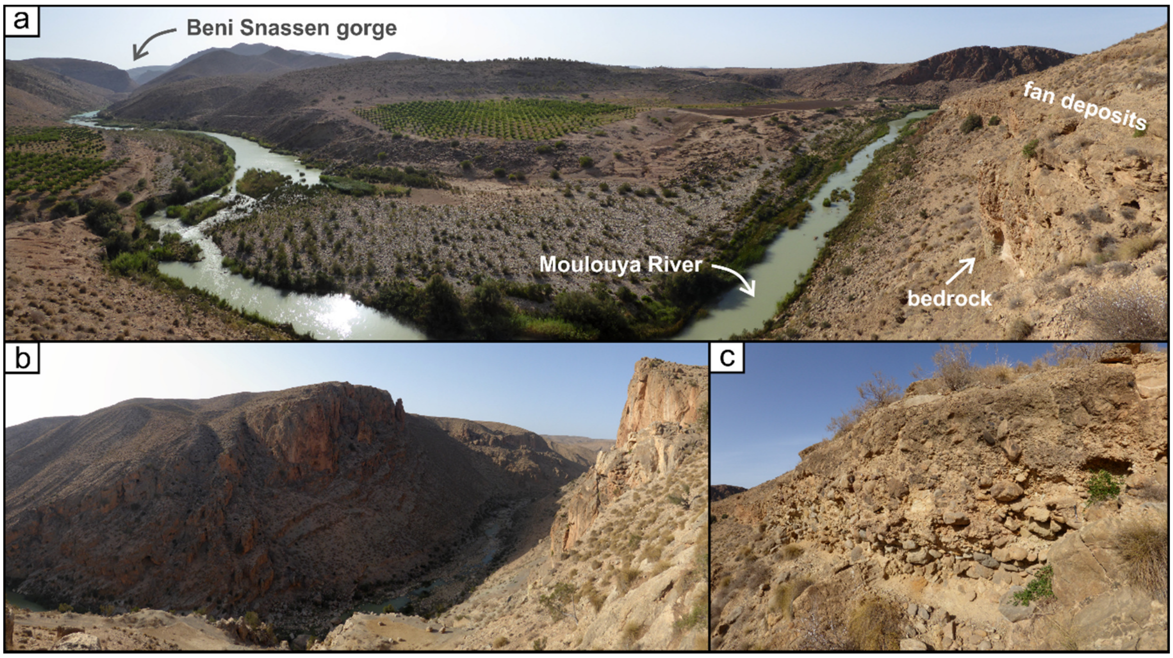

Fig. 7.2: The Moulouya River at the outlet of the Beni Snassen Massif. a) Panoramic view towards northwest; b) the Beni Snassen gorge near the Hammadi dam, ~50 km upstream of the investigated Moulouya sections; c) zoom in of the fan deposits.

Environmental changes due to climatic shifts and tectonic activity have been observed for the Wadi Selloum and the lower Moulouya River. With respect to the archaeological sequence of Ifri n'Ammar, which documents discontinuous occupation phases during the last ~170 ka, also an interplay between human activity and the landscape evolution can be considered for this region. However, it may be assumed that the Middle and Late Palaeolithic culture have not much affected the landscape, since people, who settled the area, were mainly represented by a hunter-gatherer community. This has considerably changed since the Early Holocene onwards, at the transition from the Epipalaeolithic to the Neolithic culture. Subsequent plant cultivation and animal domestication affects the landscape in the Mediterranean environment and represents another trigger for fluvial activity. During this time, human impact can be described in terms of land use (e.g., overgrazing by goats, tillage, and deforestation), while later colonisation periods – e.g., the French colonial era – are rather unknown in NE Morocco with regard to human influence on the environment.

In conclusion, this study presents new insights into palaeoenvironmental changes in NE Morocco based on two fluvial systems of different spatial and temporal scales. In particular, it has been shown that an interplay between climate, tectonics and/or human activity form the fluvial landscapes in this high sensitive Mediterranean region. Further work in the future will potentially fill the gap of Quaternary palaeoenvironmental research in NE Morocco.

Chapter 8

8 References

Abdalla, F., El Shamy, I., Bamousa, A.O., Mansour, A., Mohamed, A., Tahoon, M., 2014. Flash Floods and Groundwater Recharge Potentials in Arid Land Alluvial Basins, Southern Red Sea Coast, Egypt. International Journal of Geosciences 5, 971-982.

AG Boden, 2005. Bodenkundliche Kartieranleitung, Schweizerbartsche Verlagsbuchhandlung, Hannover.[5]

Ait Brahim, L., Chotin, P., Hinaj, S., Abdelouafi, A., El Adraoui, A., Nakcha, C., Dhont, D., Charroud, M., Sossey Alaoui, F., Amrhar, M., Bouaza, A., Tabyaoui, H., Chaouni, A., 2002. Paleostress evolution in the Moroccan African margin from Triassic to Present. Tectonophysics 357 (1-4), 187-205.

Aitken, M.J., 1985. Thermoluminescence Dating. Studies in archaeological science. Academic Press, London.

Aitken, M.J., 1992. Optical dating. Quaternary Science Reviews 11, 127-131.

Antón, L., Rodés, A., De Vicente, G., Pallàs, R., Garcia-Castellanos, D., Stuart, F.M., Braucher, R., Bourlès, D., 2012. Quatnification of fluvial incision in the Duero Basin (NW Iberia) from longitudinal profile analysis and terrestrial cosmogenic nuclide concentrations. Geomorphology 165-166, 50-61.

Arboleya, M.L., Teixell, A., Charroud, M., Julivert, M., 2004. A structural transect through the High and Middle Atlas of Morocco. Journal of African Earth Sciences 39 (3-5), 319-327.

Auclair, M., Lamothe, M., Huot, S., 2003. Measurement of anomalous fading for feldspar IRSL using SAR. Radiation Measurements 37, 487-492.

Awad, H., 1963. Some aspects of the geomorphology of Morocco related to the quaternary climate. The Geographical Journal 129 (2), 129-139.

Baartman, J.E.M., van Lynden, G.W.J., Reed, M.S., Ritsema, C.J., Hessel, R., 2007. Desertification and land degradation: origins, processes and solutions. A literature review. Desire Report Series ISRIC, Netherlands 4, 1-100.

Babault, J., Teixell, A., Arboleya, M.L., Charroud, M., 2008. A Late Cenozoic age for long-wavelength surface uplift of the Atlas Mountains of Morocco. Terra nova 20 (2), 102-107.

Badía, D., Martí, C., Palacio, E., Sancho, C., Poch, R.P., 2009. Soil evolution over the Quaternary period in a semiarid climate (Segre river terraces, northeast Spain). Catena 77, 165-174.

Bahain, J.-J., Falguères, C., Laurent, M., Voinchet, P., Dolo, J.-M., Antoine, P., Tuffreau, A., 2007. ESR chronology of the Somme River Terrace system and first human settlements in Northern France. Quaternary Geochronology 2, 356-362.

Barathon, J.-J., El Abassi, H., Lechevalier, C., Malek, F., Jolly-Saad, M.-C., 2000. Mise au point sur les formations holocènes dans le Rif oriental (Maroc)/A chronology of Holocene deposits in the eastern Rif Mountains (Morocco). Géomorphologie: relief, processus, environnement. Octobre-décembre 6 (4), 221-238.

Barcos, L., Jabaloy, A., Azdimousa, A., Asebriy, L., Gómez-Ortiz, D., Rodríguez-Peces, M.J., Tejero, R., Pérez-Peña, J.V., 2014. Study of relief changes related to active doming in the eastern Moroccan Rif (Morocco) using geomorphological indices. J. African Earth Sci. 100, 493–509.

Bartz, M., Klasen, N., Zander, A., Brill, D., Rixhon, G., Seeliger, M., Eiwanger, J., Weniger, G.-C., Mikdad, A., Brückner, H., 2015. Luminescence dating of ephemeral stream deposits around the Palaeolithic site of Ifri n'Ammar (Morocco). Quaternary Geochronology 30, 460-465.

Bartz, M., Rixhon, G., Kehl, M., El Ouhabi, M., Klasen, N., Brill, D., Weniger, G.-C., Mikdad, A., Brückner, H., 2017. Unravelling fluvial deposition and pedogenesis in ephemeral stream deposits in the vicinity of the prehistoric rock shelter of Ifri n’Ammar (NE Morocco) during the last 100 ka. Catena 152, 115-134.

Bateman, M.D., Frederick, C.D., Jaiswal, M.K., Singhvi, A.K., 2003. Investigations into the potential effects of pedoturbation on luminescence dating. Quaternary Science Reviews, 22, 1169-1176.

Bateman, M.D., Boulter, C.H., Carr, A.S., Frederick, C.D., Peter, D., Wilder, M., 2007. Detecting post-depositional sediment disturbance in sandy deposits using optical luminescence. Quaternary Geochronology 2, 57-64.

Beckmann, T., 1997. Präparation bodenkundlicher Dünnschliffe für mikromorphologische Untersuchungen. Hohenheimer Bodenkundliche Hefte 40, 89–103.

Beerten, K., Lomax, J., Clémer, K., Stesmans, A., Radtke, U., 2006. On the use of Ti centres for estimating burial ages of Pleistocene sedimentary quartz: Multiple-grain data from Australia. Quaternary Geochronology 1, 151-158.

Bell, W.T., 1980. Alpha dose attenuation in quartz grains for thermoluminescence dating. Ancient TL 12, 4-8.

Benjelloun, S.E., Douïeb, M., Saadi, M., Ennadifi, Y., 1971. Carte Géologique du Maroc. 167, 1:100000, Tistoutine.

Bertrams, M., Protze, J., Löhrer, R., Schyle, D., Richter, J., Hilgers, A., Klasen, N., Schmidt, C., Lehmkuhl, F., 2012. Multiple environmental change at the time of the Modern Human passage through the Middle East – First results from geoarchaeological investigations on Upper Pleistocene sediments in the Wadi Sabra (Jordan). Quaternary International 274, 55-72.

Bertrams, M., Protze, J., Eckmeier, E., Lehmkuhl, F., 2014. A geochemical approach on reconstructing Upper Pleistocene environmental conditions from wadi deposits – an example from the Wadi Sabra (Jordan). Zeitschrift für Geomorphologie 58, 51-80.

Blome, M.W., Cohen, A.S., Tryon, C.A., Brooks, A.S., Russell, J., 2012. The environmental context for the origins of modern human diversity: A synthesis of regional variability in African climate 150.000-30.000 years ago. Journal of Human Evolution 62 (5), 563-592.

Blott, S.J., Pye, K., 2001. GRADISTAT: a grain size distribution and statistics package for the analysis of unconsolidated sediments. Earth Surface Processes and Landforms 26, 1237-1248.

Bouabdli, A., Saidi, N., M'Rabet, S., Escarre, J., Leblanc, M., 2005. Oued Moulouya: vecteur de transport des métaux lourds (Maroc). Revue des sciences de l'eau 18 (2), 199-213.

Bouazza, A., Ait Brahim, l., Dugué, O., Cattaneo, G., Laville, E., Delcaillau, B., Charroud, M., de Luca, P., 2009. Changements Sédimentaires dans les Bassins Nèogènes de Taourirt et Guercif (Maroc Oriental): Recherche de L'épisode D'érosion Messinienne. European Journal of Scientific Research 28 (3), 317-327.

Boughriba, M., Melloul, A., Zarhloule, Y., Ouardi, A., 2006. Extension spatiale de la salinisation des ressources en eau et modèle conceptuel des sources salées dans la plaine des Triffa (Maroc nord-oriental). Comptes Rendus Geosci. 338, 768–774.

Bridgland, D.R., Antoine, P., Limondin-Lozouet, N., Santisteban, J.I., Westaway, R., White, M.J., 2006. The Palaeolithic occupation of Europe as revealed by evidence from the rivers: data from IGCP 449. Journal of Quaternary Science 21 (5), 437-455.

Bridgland, D.R., Westaway, R., 2008. Climatically controlled river terrace staircase: A worldwide Quaternary phenomenon. Geomorphology 98, 285-315.

Bridgland, D.R., Demir, T., Seyrek, A., Daoud, M., Abou Romieh, M., Westaway, R., 2017. River terrace development in the NE Mediterranean region (Syria and Turkey): Patterns in relation to crustal type. Quaternary Science Reviews 166, 307-323.

Brückner, H. 1986. Man's impact on the Evolution of the Physical Environment in the Mediterranean Region in Historical Times. GeoJournal 13 (1), 7-17.

Brückner, H., 1994. Das Mittelmeergebiet als Naturraum. In: Martin, J. (ed.). Das alte Rom. Gütersloh, München, 13-29.

Bull, W.B., 1997. Discontinuous ephemeral streams. Geomorphology 19, 227-276.

Burbank, D.W., Anderson, R.S., 2012. Tectonic Geomorphology. Wiley-Blackwell, Oxford, 2nd ed.

Butler, R.F., 1992. Paleomagnetism: Magnetic Domains to Geologic Terranes. Blackwell Scientific Publications.

Buylaert, J.P., Murray, A.S., Thomsen, K.J., Jain, M., 2009. Testing the potential of an elevated temperature IRSL signal from K-feldspar. Radiation measurements 44, 560-565.

Cacho, I., Grimalt, J.O., Canals, M., Sbaffi, L., Shackleton, N.J., Schönfeld, J., Zahn, R., 2001. Variability of the western Mediterranean Sea surface temperature during the last 25.000 years and its connection with the Northern Hemisphere climatic changes. Paleoceanography 16 (1), 40-52.

Camps, G., 1974. Les civilisation prehistoriques de l'Afrique du Nord et du Sahara. Paris.

Candy, I., Black, S., 2009. The timing of Quaternary calcrete development in semi-arid southeast Spain: Investigating the role of climate on calcrete genesis. Sedimentary Geology 218 (1-4), 6-15.

Cann, R.L., Stoneking, M., Wilson, A.C., 1987. Mitochondrial DNA and human evolution. Nature 325, 31-36.

Chalouan, A., Michard, A., El Kadiri, K., Negro, F., Frizon de Lamotte, D., Soto, J.I., Saddiqi, O., 2008. The Rif Belt. In: Michard, A., Saddiqi, O., Chalouan, A., Frizon de Lamotte, D. (eds.). Continental Evolution: The Geology of Morocco. Structure, Stratigraphy, and Tectonics of the Africa-Atlantic-Mediterranean Triple-Junction. Springer Verlag, Berlin Heidelberg, 203-301.

Cheddadi, R., Nourelbait, M., Bouaissa, O., Tabel, J., Rhoujjati, A., López-Sáez, J.A., Alba-Sánchez, F., Khater, C., Ballouche, A., Dezileau, L., Lamb, H., 2015. A history of human impact on Moroccan mountain landscapes. African Archaeological Review 32 (2), 233-248.

Day, J.W., Pont, D., Hensel, P.F., Ibañez, C., 1995. Impacts of sea-level rise on deltas in the Gulf of Mexico and the Mediterranean: The importance of pulsing events to sustainability. Estuaries 18 (4), 636-647.

Delcaillau, B., Laville, E., Carozza, J.-M., Dugué, O., Charroud, M., Amrhar, M., 2008. Morphotectonic evolution of the Jebel Bou Naceur in the South Middle Atlas Fault Zone (Morocco). Comptes Rendus Geoscience 339, 553-561.

Demir, T., Seyrek, A., Westaway, R., Guillou, H., Scaillet, S., Beck, A., Bridgland, D.R., 2012. Late Cenozoic regional uplift and localised crustal deformation within the northern Arabian Platform in southeast Turkey: Investigation of the Euphrates terrace staircase using multidisciplinary techniques. Geomorphology 165-166, 7-24.

Demoulin, A., Mather, A., Whittaker, A., 2017. Fluvial archives, a valuable record of vertical crustal deformation. Quaternary Science Reviews 166, 10-37.

Dörschner, N., Fitzsimmons, K.E., Ditchfield, P., McLaren, S.J., Steele, T.E., Zielhofer, C., McPherron, S.P., Bouzouggar, A., Hublin, J.-J., 2016. A new chronology for Rhafas, Northeast Morocco, spanning the North African Middle Stone Age through to the Neolithic. PLOS One 11 (9), 1-34.

Driouech, F., Déqué, M., Mokssit, A., 2009. Numerical simulation of the probability distribution function of precipitation over Morocco. Climate Dynamics 32, 1055-1063.

Duller, G.A.T., 2008. Luminescence Dating: guidelines on using luminescence dating in archaeology. Swindon: English Heritage, London.

Durcan, J.A., King, G.E., Duller, G.A.T., 2015. DRAC: Dose rate and age calculator for trapped charge dating. Quaternary Geochronology, 28, 54-61.

Duval, 2012. Dose response curve of the ESR signal of the Aluminium centre in quartz grains extracted from sediment. Ancient TL 30 (2), 41-49.

Duval, M., 2016. Electron spin resonance (ESR) in archaeological context. In: Gilbert, A.S. (ed.). Encyclopedia of Geoarchaeology. Springer, 224-233.

Duval, M., Guilarte Moreno, V., 2012. Assessing the influence of the cavity temperature on the ESR signal of the Aluminium centre in quartz grains extracted from sediment. Ancient TL 30 (2), 51-56.

Duval, M., Guilarte, V., 2015. ESR dosimetry of optically bleached quartz grains extracted from Plio-Quaternary sediment: Evaluating some key aspects of the ESR signals associated to the Ti-centres. Radiation Measurements 78, 28-41.

Duval, M., Sancho, C., Calle, M., Guilarte, V., Penna-Monné, J.L., 2015. On the interest of using the multiple centre approach in ESR dating of optically bleached quartz grains: Some examples from the Early Pleistocene terraces of the Alcanadre River (Ebro basin, Spain). Quaternary Geochronology 29, 58-69.

Duval, M., Arnold, L.J., Guilarte, V., Demuro, M., Santonja, M., Pérez-Ganzález, A., 2017. Electron spin resonance dating of optically bleached quartz grains from the Middle Palaeolithic site of Cuesta de la Bajada (Spain) using the multiple centres approach. Quaternary Geochronology 37, 82-96.

Eaton, B.C., Millar, R.G., Davidson, S., 2010. Channel patterns: Braided, anabranching, and single-thread. Geomorphology 120 (3-4), 353-364.

Ehrmann, W., Seidel, M., Schmiedl, G., 2013. Dynamics of Late Quaternary North African humid periods documented in the clay mineral record of central Aegean Sea sediments. Global and Planetary Change 107, 186-195.

El Amrani, M., Macaire, J.-J., Zarki, H., Bréhéret, J.-G., Fontugne, M., 2008. Contrasted morphosedimentary activity of the lower Kert River (northeastern Morocco) during the Late Pleistocene and the Holocene. Possible impact of bioclimatic variations and human action. C. R. Geoscience 340, 533-542.

Fadil, A., Vernant, P., McClusky, S., Reilinger, R., Gomez, F., Sari, D. Ben, Mourabit, T., Feigl, K., Barazangi, M., 2006. Active tectonics of the western Mediterranean: Geodetic evidence for rollback of a delaminated subcontinental lithospheric slab beneath the Rif Mountains, Morocco. Geology 34, 529–532.

Faust, D., Zielhofer, C., Baena Escudero, R., Diaz del Olmo, F., 2004. High-resolution fluvial record of late Holocene geomorphic change in northern Tunisia: climatic or human impact? Quaternary Science Reviews 23, 1757-1775.

Finlayson, C., 2005. Biogeography and evolution of the genus *Homo*. Trends in Ecology and Evolution 20 (8), 457-462.

Fletcher, W.J., Sánchez Goñi, M.F., 2008. Orbital- and sub-orbital-scale climate impacts on vegetation of the western Mediterranean basin over the last 48.000 yr. Quaternary Research 70 (3), 451-464.

Foley, R.A., Lahr, M.M., 1992. Current events. Beyond “out of Africa”: reassessing the origins of *Homo sapiens*. Journal of Human Evolution 22, 523-529.

Folk, R.L., Ward, W.C., 1957. Brazos River bar: a study in the significance of grain size parameters. Journal of Sedimentary Petrology 27, 3-26.

Frizon de Lamotte, D., Zizi, M., Missenard, Y., Hafid, M., El Azzouzi, M., Maury, R.C., Charrière, Taki, Z., Benammi, M., Michard, A., 2008. The Atlas System. In: Michard, A., Saddiqi, O., Chalouan, A., Frizon de Lamotte, D. (eds.). Continental Evolution: The Geology of Morocco. Structure, Stratigraphy, and Tectonics of the Africa-Atlantic-Mediterranean Triple-Junction. Springer. Berlin, Heidelberg.

Fuller, I.C., Macklin, M.G., Lewin, J., Passmore, D.G., Wintle, A.G., 1998. River response to high-frequency climate oscillations in southern Europe over the past 200 k.y. Geology 26 (3), 275-278.

Galbraith, R.F., 2005. Statistics for Fission Track Analysis, Chapman & Hall/CRC, Boca Raton.

Galbraith, R.F., Roberts, R.G., Laslett, G.M., Yoshida, H., Olley, J.M., 1999. Optical dating of single and multiple grains of quartz from Jinmium rock shelter, northern Australia: Part I, experimental design and statistical models. Archaeometry 41 (2), 339-364.

Garcea, E.A.A.. 2004. Crossing deserts and avoiding seas: Aterian north-African-European relations. Journal of Anthropological Research 60, 27-53.

Gomez, F., Beauchamp, W., Barazangi, M., 2000. Role of the Atlas Mountains (northwest Africa) within the African-Eurasian plate-boundary zone. Geology 28 (9), 775-778.

Groucutt, H.S., Petraglia, M.D., Bailey, G., Scerri, E.M., Parton, A., Clark-Balzan, L., Jennings, R.P., Lewis, L., Blinkhorn, J., Drake, N.A., Breeze, P.S., Inglis, R.H., Devès, M.H., Meredith-Williams, M., Boivin, N., Thomas, M.G., Scally, A., 2015. Rethinking the Dispersal of *Homo sapiens* out of Africa. Evolutionary Anthropology 24, 149-164.

Grün, R., 1989. Die ESR-Altersbestimmungsmethode. Springer. Berlin, Heidelberg.

Grün, R., 2001. Trapped charge dating (ESR, TL, OSL). In: Brothwell, D.R., Pollard, A.M. (eds.). Handbook of Archaeological Sciences. John Wiley & Sons Inc, West Sussex, 47-62.

Guérin, G., Mercier, N., Adamiec, G., 2011. Dose-rate conversion factors: update. Ancient TL, 29, 5-8.

Guérin, G., Mercier, N., Nathan, R., Adamiec, G., Lefrais, Y., 2012. On the use of the infinite matrix assumption and associated concepts: A critical review. Radiation Measurements, 47, 778-785.

Guralnik, B., Jain, M., Herman, F., Ankjægaard, C., Murray, A.S., Valla, P.G., Preusser, F., King, G.E., Chen, R., Lowick, S.E., Kook, M., Rhodes, E.J., 2015. OSL-thermochronometry of feldspar from the KTB Borehole. Germany. Earth Planetary Science Letters 423, 232-243.

Harvey, A.M., Wells, S.M., 1987. Response of Quaternary fluvial systems to differential epeirogenic uplift: Aguas and Feos river systems, southeast Spain. Geology 15, 689-693.

Hook, J., Mant, J., 2002. Morpho-dynamics of ephemeral streams. In: Bull, L.J., Kirkby, M.J. (eds.). Dryland rivers: hydrology and geomorphology of semi-arid channels. Wiley, Chichester, 173-204.

Hooke, J.M., 2006. Human impacts on fluvial systems in the Mediterranean region. Geomorphology 79, 311-335.

Howell, F.C., 1999. Paleo-demes, species clades, and extinctions in the Pleistocene hominin record. Journal of Anthropology Research 55, 191-243.

Hughes, P. D., Gibbard, P.L., Woodward, J.C. 2004. Quaternary glaciation in the Atlas Mountains of North Africa. In: Ehlers, J., Gibbard, P.L (eds.). Quaternary Glaciation – Extent and Chronology. Volume 3: Asia, Latin America, Africa, Australia, Antarctica. Elsevier, Amsterdam, 255-260.

Hughes, P.D., Fenton, C.R., Gibbard, P.L. 2011. Quaternary glaciations of the Atlas Mountains, North Africa. In: Ehlers, J., Gibbard, P.L., Hughes, P.D. (eds.). Quaternary Glaciations - Extent and Chronology, Part IV - A Closer Look. *Elsevier,* Amsterdam, 1065-1074.

Huntley, 2006. An explanation of the power-law decay of luminescence. Journal of Physics: Condensed Matter 18, 1359-1365.

Huntley, D.J., Godfrey-Smith, D.I., Thewalt, M.L.W., 1985. Optical dating of sediments. Nature 313, 105-107.

Huntley, D.J., Lamothe, M., 2001. Ubiquity of anomalous fading in K-feldspars and the measurement and correction for it in optical dating. Canadian Journal of Earth Sciences 38, 1093-1106.

Huntley, D.J., Lian, O.B., 2006. Some observations on tunnelling of trapped electrons in feldspars and their implications for optical dating. Quaternary Science Reviews 25 (19-20), 2503-2512.

Hutterer, R., Linstädter, J., Eiwanger, J., Mikdad, A., 2014. Human manipulation of terrestrial gastropods in Neolithic culture groups of NE Morocco. Quaternary International 320, 83-91.

Ibouhouten, H., Zielhofer, C., Mahjoubi, R., Kamel, S., Linstädter, J., Mikdad, A., Bussmann, J., Werner, P., Härtling, J.W., Fenech, K., 2010. Archives alluvialles holocène et occupation humaine en Basse Moulouya (Maroc nord-oriental). Géomorphologie: relief, processus, environnement 1, 41-56.

Ikeya, M., 1993. New applications of electron spin resonance: dating, dosimetry and microscopy. World Scientific Publishing, Singapore.

Jacobson R.B., Elston D.P. and Heaton J.W., 1988. Stratigraphy and magnetic polarity of the high terrace remnants in the upper Ohio and Monongahela rivers in West Virginia, Pennsylvania and Ohio, Quaternary Reasearch 29, 216–232.

Jain, M., 2014. Feldspar, Infrared-Stimulated Luminescence. In: Encyclopedia of Scientific Dating Methods.

Jébrak, M., Marcoux, É., Nasloubi, M., Zaharaoui, M., 1998. From sandstone- to carbonate-hosted stratabound deposits: an isotope study of galena in the Upper-Moulouya District (Morocco). Mineralium Deposita 33, 406-415.

Kaemmerer, M., Revel, J.C., 1991. Calcium carbonate accumulation in deep strata and calcrete in Quaternary alluvial formations of Morocco. Geoderma 48, 43–57.

Kars, R.H., Wallinga, J., Cohen, K.M., 2008. A new approach towards anomalous fading correction for feldspar IRSL dating – tests on samples in field saturation. Radiation Measurements 43, 786-790.

Khattach, D., Keating, P., Mili, E.M., Chennouf, T., Andrieux, P., Milhi, A., 2004. Apport de la gravimétrie à l'étude de la structure du bassin des Triffa (Maroc nord-oriental) : implications hydrogéologiques. Comptes Rendus Geosci. 336, 1427–1432.

King, G.E., Herman, F., Guralnik, B., 2016. Northward migration of the eastern Himalayan syntaxis revealed by OSL thermochronometry. Science 353 (6301), 800-804.

Klasen, N., Hilgers, A., Schmidt, C., Bertrams, M., Schyle, D., Lehmkuhl, F., Richter, J., Radtke, U., 2013. Optical dating of sediments in Wadi Sabra (SW Jordan). Quaternary Geochronology 18, 9-16.

Krijgsman, W., Hilgen, F.J., Raffi, I., Sierro, F.J., Wilson, D.S., 1999. Chronology, causes and progression oft he Messinian salinity crisis. Nature 400, 652-655.

Larrasoaña, J.C., Roberts, A.P., Rohling, E.J., 2013. Dynamics of Green Sahara Periods and their role in hominin evolution. PLOS one 8 (10), 1-12.

Lefèvre, D., 1989. Formations continentales pléistocenes et paléoenvironnements sédimentaires dans le bassin de Ksabi (Moyenne Moulouya, Maroc). Bull. Assoc. française pour l'étude du Quat. 26, 101–113.

Li, J.-J., Fang, X.-M., Van der Voo, R., Zhu, J.-J., Niocaill, C.M., Ono, Y., Pan, B.-T., Zhong, W., Wang, J.-L., Sasaki, T., Zhang, Y.-T., Cao, J.-X., Kang, S.-C., Wang, J.-M., 1997. Magnetostratigraphic dating of river terraces: Rapid and intermittent incision by the Yellow River of the northeastern margin of the Tibetan Plateau during the Quaternary. Journal of Geophysical Research 102 (B5), 10121-10132.

Lin, M., Yin, G., Ding, Y., Cui, Y., Chen, K., Wu, C., Xu, L., 2006. Reliability study on ESR dating of the aluminium center in quartz. Radiation measurements 41, 1045-1049.

Linstädter, J., 2008. The Epipalaeolithic-Neolithic-Transition in the Mediterranean region of Northwest Africa. Quartär 55, 41-62.

Linstädter, J., 2013. Raues Land – Feine Funde. Archäologie im Norden Marokkos. Heinrich Barth Kurier 01/2013. Köln.

Linstädter, J., Eiwanger, J., Mikdad, A., Weniger, G-C., 2012a. Human occupation of Northwest Africa: A review of Middle Palaeolithic to Epipalaeolithic sites in Morocco. Quaternary International 274, 158-174.

Linstädter, J., Aschrafi, M., Ibouhouten, H., Zielhofer, C., Bussmann, J., Deckers, K., Müller-Sigmund, H., Hutterer, R., 2012b. Flussarchäologie der Moulouya-Hochflutebene, NO-Marokko. Madrider Mitteilungen 53, 1-84.

Linstädter, J., Fili, A., Amarir, A., Mikdad, A., 2012c. Bouchih, un site aloravide sur la rive oust de Moulouya (Rif oriental). Bulletin de l'Archéologie Marocain XXII, 343-361.

Linstädter, J., Broich, M., Weninger, B. Defining the early Neolithic of the Eastern Rif, Morocco – Spatial distribution, chronological framework and impact of environmental changes. Quaternary International. http://dx.doi.org/10.1016/j.quaint.2016.07.042 (in press).

Lonergan, L., White, N., 1997. Origin of the Betic-Rif Mountain belt. Tectonics 16 (3), 504-522.

López-Bermúdez, F., Conesa-Garcia, C., Alonso-Sarria, F., 2002. Floods: Magnitude and Frequency in ephemeral streams of the Spanish Mediterranean Region. In: Bull, L.J., Kirkby, M.J. (eds.). Dryland rivers: hydrology and geomorphology of semi-arid channels. Wiley, Chichester, 173-204.

Lubell, D., Hassan, F.A., Gautier, A., Ballais, J.-L., 1976. The Caspian Escargotières. Science 5 191 (4230), 910-920.

Macklin, M.G., Lewin, J., Woodward, J.C., 1995. Quaternary fluvial systems in the Mediterranean basin. In: Lewin, J., Macklin, M.G., Woodward, J.C. (eds.). Mediterranean Quaternary River Environments. Balkema, Rotterdam, 1-25.

Macklin, M.G., Fuller, I.C., Lewin, J., Maas, G.S., Passmore, D.G., Rose, J., Woodward, J.C., Black, S., Hamlin, R.H.B., Rowan, J.S., 2002. Correlation of fluvial sequences in the Mediterranean basin over the last 200 ka and their relationship to climate change. Quaternary Science Reviews 21 (14-15), 1633-1641.

Maher, E., Harvey, A.M., 2008. Fluvial system response to tectonically induced base-level change during the late-Quaternary : The Rio Alias southeast Spain. Geomorphology 100 (1-2), 180-192.

McBrearty, S., Brooks, A.S., 2000. The revolution that wasn't : a new interpretation of the origin of modern human behavior. Journal of Human Evolution 39 (5), 453-563.

Meghraoui, M., Morel, J.-L., Andrieux, J., Dahmani, M., 1996. Tectonique plio-quaternaire de la chaine tello-riffaine et de la mer d'alboran. Une zone compexe de convergence continent-continent. Bull.Soc.Geol.Fr. 167, 141–157.

Meghraoui, M., Pondrelli, S., 2012. Active faulting and transpression tectonics along the plate boundary in North Africa. Annals of Geophysics 55 (5), 955-967.

Mensching, H., 1960. Bericht und Gedanken zur Tagung der Kommission für Periglazial forschung in der IGU in Marokko vom 19. Bis 31. Oktober 1959. Zeitschrift für Geomorphologie N.F. 4, 159-170.

Mercuri, A.M., Sadori, L., Uzquiano Ollero, P., 2011. Mediterranean and north-African cultural adaptations to mid-Holocene environmental and climatic changes. The Holocene 21 (1), 189-206.

Messerli, B. 1967. Die eiszeitliche und die gegenwärtige Vergletscherung im Mittelemeerraum. Geographica Helvetica 22, 105-228.

Michard, A., Frizon de Lamotte, D., Saddiqi, O., Chalouan, A., 2008. An outline of the Geology of Morocco. In: Michard, A., Saddiqi, O., Chalouan, A., Frizon de Lamotte, D. (eds.). Continental Evolution: The Geology of Morocco. Structure, Stratigraphy, and Tectonics of the Africa-Atlantic-Mediterranean Triple-Junction. Springer. Berlin, Heidelberg.

Mikdad, A., Moser, J., Ben-Neer, A., 2002. Recherche préhistoriques dans le gisement d'Ifri n'Ammar au Rif Oriental (Maroc). Premiers résultats. Beiträge zur Allgemeinen und Vergleichenden Archäologie 22, 1-20.

Mishra, S., White, M.J., Beaumont, P., Antoine, P., Bridgland, D.R., Limondin-Lozouet, N., Santisteban, J.I., Schreve, D.C., Shaw, A.D., Wenban-Smith, F.F., Westaway, R.W.C., White, T.S., 2007. Fluvial deposits as an archive of early human activity. Quaternary Science Reviews 26 (22-24), 2996-3016.

Morel, J.L., Meghraoui, M., 1996. Goringe-Alboran-Tell tectonic zone: A transpression system along the African-Eurasia plate boundary. Geology 24 (8), 755-758.

Moreno, D., Falguères, C., Pérez-González, A., Duval, M., Voinchet, P., Benito-Calvo, A., Ortega, A.I., Bahain, J.-J., Sala, R., Carbonell, E., Bermúdez de Castro, J.M., Arsuaga, J.L., 2012. ESR chronology of alluvial deposits in the Arlanzón valley (Atapuerca, Spain): Contemporaneity with Atapuerca Gran Dolina site. Quaternary Geochronology 10, 418-423.

Moser, J., 2003. La grotte d'Ifri n'Ammar. Tome 1. L'Ibéromaurusien. AVA-Forschungen Band 8. Kommission für Allgemeine und Vergleichende Archäologie des Deutschen Archäologischen Instituts. Köln.

Murray, A.S., Roberts, R.G., 1997. Determining the burial time of single grains of quartz using optically stimulated luminescence. Earth and Planetary Science Letters 152, 163-180.

Nami, M., 2008. Les techno complexes ibéromaurusiens d´Ifri El Baroud (Rif Oriental, maroc). Beiträge zur Allgemeinen und Vergleichenden Archäologie 27.

Nami, M., Moser, J., 2010. La grotte d'Ifri n'Ammar. Le Paléolithique moyen. Forschungen zur Archäologie Außereuropäischer Kulturen, 9: 325-337. Reichert Verlag, Wiesbaden.

Nathan, R.P., Thomas, P.J., Jain, M., Murray, A.S., Rhodes, E.J., 2003. Environmental dose-rate heterogeneity of beta irradiation and its implications of luminescence dating: Monte Carlo modelling and experimental validation. Radiation Measurements 37, 305-313.

Ngadi, M., 1995. Précipitations et ecoulement dans le basin versant de la Moulouya (Maroc). Thèse de doctorat de l'Université Paul Valery, Montpellier III, 333 pp.

Ogg, J.G., 2012. Geomagnetic Polarity Time Scale. In: Gradstein, F.M., Ogg, J.G., Schmitz, M.D., Ogg, G.M., (eds.) 2012. The geological time scale. Amsterdam, Elsevier.

Olley, J.M., Caitcheon, G.G., Roberts, R.G., 1999. The origin of dose distributions in fluvial sediments, and the prospect of dating single grains from fluvial deposits using optically stimulated luminescence. Radiation Measurements 30, 207-217.

Osmaston, H.A., Harrison, S.P., 2005. The Late Quaternary glaciation of Africa: A regional synthesis. Quaternary International 138-139, 32-54.

Pastor, A., Babault, J., Owen, L.A., Teixell, A., Arboleya, M.-L., 2015. Extracting dynamic topography from river profiles and cosmogenic nuclide geochronology in the Middle Atlas and the High Plateaus of Morocco. Tectonophysics 663, 95–109.

Pazzaglia, F.J., 2013. Fluvial terraces. In: Shroder, J. (Editor in Chief), Wohl, E. (Ed.), Treatise on Geomorphology. Academic Press, San Diego, CA, vol. 9, Fluvial Geomorphology, 379–412.

Pérez-Folgado, M., Sierro, F.J., Flores, J.A., Grimalt, J.O., Zahn, R., 2004. Palaeoclimatic variations in foraminifer assemblages from the Alboran Sea (Western Mediterranean) during the last 150 ka in ODP site 977. Marine Geology 212, 113-131.

Pérez-Peña, J.V., Azañón, J.M., Delgado, J., González-Lodeiro, F. 2009. Spatial analysis of stream power using GIS: SLk anomaly maps. Earth Surface Processes and Landforms 34 (1), 16-25.

Petraglia, M.D., Haslam, M., Fuller, D.Q., Boivin, N., Clarkson, C., 2010. Out of Africa: new hypotheses and evidence for the dispersal of Homo sapiens along the Indian Ocean rim. Annals of Human Biology 37 (3), 288-311.

Pissart, A., Boumeaza, T., 2010. Âge et origine de la terrasse limoneuse de la basse Moulouya (Maroc Nord-Oriental). Bulletin de la Société Géographique de Liège 54, 85-96.

Piqué, A., 2001. Geology of Northwest Africa. In: Bender, F., Jacobshagen, V., Lüttig, G. (eds.). Beiträge zur regionalen Geologie der Erde Band 29. Gebrüder Borntraeger, Berlin, Stuttgart.

Piqué, A., Soulaimani, A., Hoepffner, C., Bouabdelli, M., Laville, E., Amrhar, M., Chalouan, A., 2007. Geologie du Maroc. Collection Terre et Patrimoine Séries Manuels. Marrakech.

Poujol, A., Ritz, J.-F., Tahayt, A., Vernant, P., Condomines, M., Blard, P.-H., Billant, J., Vacher, L., Tibari, B., Hni, L., Idrissi, A.K., 2014. Active tectonics of the Northern Rif (Morocco) from geomorphic and geochronological data. J. Geodyn. 77, 70–88.

Prescott, J.R., Hutton, J.T., 1988. Cosmic ray and gamma ray dosimetry for TL and ESR. Nuclear Tracks Radiation Measurements 14 (1/2), 223-227.

Prescott, J.R., Hutton, J.T., 1994. Cosmic ray contributions to dose rates for luminescence and ESR dating: Large depths and long-term time variations. Radiation Measurements, 23, 497-500.

Preusser, F., Degering, D., Fuchs, M., Hilgers, A., Kadereit, A., Klasen, N., Krbetschek, M., Richter, D., Spence, J.Q.G., 2008. Luminescence dating: basics, methods and applications. Eiszeitalter und Gegenwart. Quaternary Science Journal 57 (1-2), 95-149.

Preusser, F., Chithambo, M.L., Götte, T., Martini, M., Ramseyer, K., Sendezera, E.J., Susino, G.J., Wintle, A.G., 2009. Quartz as a natural luminescence dosimeter. Erath-Science Reviews 97 (1-4), 184-214.

Ramón, M. J., and Pueyo, E. L., 2012. Automatic calculation of demagnetization intervals; a new approach based on the virtual directions method and comparison with the linearity spectrum análisis. Geotemas, 13, 1080–1083.

Raynal, R., 1961. Plaines et piedmonts du basin de la Moulouya (Maroc oriental). Rabat.

Raynal, R., Dresch, J., Joly, F., 1953. Deux exemples régionaux de glaciation quaternaire au Maroc: Haut Atlas Oriental, Moyen Atlas Septentrional. IV Congrès INQUA, Rome-Pisa, p.65.

Reed, F. A., Tishkoff, S.A., 2006. African human diversity, origins and migrations. Current Opinion in Genetics & Development 16, 597-605.

Richter, D., Moser, J., Nami, M., Eiwanger, J., Mikdad, A., 2010. New chronometric data from Ifri n'Ammar (Morocco) and the chronostratigraphy of the Middle Palaeolithic in the Western Maghreb. Journal of Human Evolution 59 (6), 672-679.

Richter, J., Hauck, T., Vogelsang, R., Widlok, T., Le Tensorer, J.-M., Schmid, P., 2012. „Contextual areas" of early *Homo sapiens* and their significance for human dispersal from Africa into Eurasia between 200 ka and 70 ka. Quaternary International 274, 5-24.

Rittenour, T.M., 2008. Luminescence dating of fluvial deposits: applications to geomorphic, palaeoseismic and archaeological research. Boreas 37, 613-635.

Rixhon, G., Braucher, R., Bourlès, D., Siame, L., Bovy, B., Demoulin, A., 2011. Quaternary river incision in NE Ardennes (Belgium) – Insights from ^{10}Be/^{26}Al dating of river terraces. Quaternary Geochronology 6, 273-284.

Rixhon, G., Briant, R.M., Cordier, S., Duval, M., Jones, A., Scholz, D., 2017a. Revealing the pace of river landscape evolution during the Quaternary: recent developments in numerical dating methods, Quaternary Science Reviews 166, 91-113.

Rixhon, G., Bartz, M., El Ouahabi, M., Szemkus, N., Brückner, H., 2017b. Contrasting terrace systems of the lower Moulouya river as indicator of crustal deformation in NE Morocco. Journal of African Earth Sciences 126, 45-57.

Rose, J., Meng, X. 1999. River activity in small catchments over the last 140 ka, northeast Mallorca, Spain. In: Brown, A.G., Quine, T.A., (eds.). Fluvial Processes and Environmental Change, Wiley, Chichester, 91-102.

Ruellan, A., 1971. Contribution à la connaissance des sols des régions méditerranénnes: les sols à profil calcaire différencié des plaines de la basse Moulouya (Maroc oriental). Mémoire Off. la Rech. Sci. Tech. d'Outre-Mer, 302 p.

Sancho, C., Calle, M., Peña-Monné, J.L., Duval, M., Oliva-Urcia, B., Pueyo, E.L., Benito, G., Moreno, A., 2016. Dating the Earliest Pleistocene alluvial terrace of the Alcanadre River (Ebro Basin, NE Spain): Insights into the landscape evolution and involved processes. Quaternary International 407, 86-95.

Santisteban, J.I., Schulte, L., 2007. Fluvial networks oft he Iberian Peninsula: a chronological framework. Quaternary Science Reviews 26, 2738-2757.

Schulte, L., 2002. Climatic and human influence on river systems and glacier fluctuations in southeast Spain since the Last Glacial Maximum. Quaternary International 93-94, 85-100.

Schulte, L., Julià, R., Burjachs, F., Hilgers, A., 2008. Middle Pleistocene to Holocene geochronology of the River Aguas terrace sequence (Iberian Peninsula): Fluvial response to Mediterranean environmental change. Geomorphology 98, 13-33.

Shaw, J.R., Cooper, D.J., 2008. Linkages among watersheds, stream reaches, and riparian vegetation in dryland ephemeral stream networks. Journal of Hydrology 350, 68-82.

Singer, B.S., 2014. A Quaternary geomagnetic instability time scale. Quaternary Geochronology 21, 29-52.

Snoussi, M., Haida, S., Imassi, S., 2002. Effects of the construction of dams on the water and sediment fluxes of the Moulouya and the Sebou Rivers, Morocco. Regional Environmental Change 3, 5-12.

Stokes, M., Cunha, P.P., Martins, A.A., 2012. Techniques for analysing Late Cenozoic river terrace sequences. Geomorphology 165-166, 1-6.

Stoll, H.M., Moreono, A., Mendez-Vicente, A., Gonzales-Lemos, S., Jimenez-Sanchez, M., Dominguez-Cuesta, M.J., Edwards, R.L., Cheng, H., 2013. Paleoclimate and growth rates of speleothems in the northwestern Iberian Peninsula over the last two glacial cycles. Quaternary Research 80 (2), 284-290.

Stoops, 2003. Guidelines for Analysis and Description of Soil and regolith Thin Sections. Soil Science Society of America, Inc. Madison, Wisconsin.

Straus, 2001. Africa and Iberia in the Pleistocene. Quaternary International 75, 91-102.

Stringer, C.B., 2002. Modern human origins: progress and prospects. Philosophical Transactions of the Royal Society 357, 563-579.

Tauxe, L., 1998. Paleomagnetic Principles and Practice, Springer, New York, 299 pp.

Tauxe, L, Banerjee, S.K., Butler, R.F., van der Voo R., 2016. Essentials of Paleomagnetism. 4th Web Edition.

Thiel, C., Buylaert, J.P., Murray, A.S., Tsukamoto, S., 2011a. On the applicability of post-IR IRSL dating to Japanese loess. Geochronometria 38, 369-378.

Thiel, C., Buylaert, J.-P, Murray, A., Terhorst, B., Hofer, I., Tsukamoto, S., Frechen, M., 2011b. Luminescence dating of the Stratzing loess profile (Austria) - Testing the potential of an elevated temperature post-IR IRSL protocol. Quaternary International 234, 23-31.

Thomsen, K.J., Murray, A.S., Jain, M., Bøtter-Jensen, L., 2008. Laboratory fading rates of various luminescence signals from feldspar-rich sediment extracts. Radiation Measurements 43, 1474-1486.

Thorndycraft, V.R., Benito, G., 2006. The Holocene fluvial chronology of Spain: evidence from a newly compiled radiocarbon database. Quaternary Science Reviews 25, 223-234.

Thorp, M., Glanville, P., Stokes, S., Bailey, R., 2002. Preliminary optical and radiocarbon age determinations for Upper Pleistocene alluvial sediments in the southern Anti Atlas Mountains, Morocco. Comptes Rendus Geoscience 334 (12), 903-908.

Tissoux, H., Falguères, C., Voinchet, P., Toyoda, S., Bahain, J.J., Despriée, J., 2007. Potential use of Ti-centre in ESR dating of fluvial sediment. Quaternary Geochronology 2, 367-372.

Tjallingii, R., Claussen, M., Stuut, J.-B. W., Fohlmeister, J., Jahn, A., Bickert, T., Lamy, F., Röhl, U., 2008. Coherent high- and low-latitude control of the northwest African hydrological balance. Nature Geoscience 1, 670-675.

Toyoda, S., 2015. Paramagnetic lattice defects in quartz for applications to ESR dating. Quaternary Geochronology 30, 498-505.

Toyoda, S., Ikeya, M., 1991. ESR dating of quartz and plagioclase from volcanic ashes using $E`_{1,}$ Al and Ti centers. Nuclear Tracks Radiation Measurements 18 (1/2), 179-184.

Toyoda, S., Voinchet, P., Falguères, C., Dolo, J.M., Laurent, M., 2000. Bleaching of ESR signals by the sunlight: a laboratory experiment for establishing the ESR dating of sediments. Applied Radiations and Isotopes 52, 1357-1362.

Toyoda, S., Falguères, C., 2003. The method to represent the ESR signal intensity of the aluminium hole centre in quartz for the purpose of dating. Advanced ESR applications 20, 7-10.

van Andel, T.H., Runnels, C.N., Pope, K.O., 1986. Five thousand years of land use and abuse in the Southern Argolid, Greece.

van Andel, T.H., Zangger, E., Demitrack, A., 1990. Land use and soil erosion in prehistoric and historical Greece. Journal of Field Archaeology 17 (4), 379-396.

Vandenberghe, D., 2002. The relation between climate and river processes, landforms and deposits during the Quaternary. Quaternary International 91 (1), 17-23.

Vandenberghe, D., 2003. Climate forcing of fluvial system development: an evolution of ideas. Quaternary Science Reviews 22 (20), 2053-2060.

Vandenberghe, D., De Corte, F., Buylaert, J.-P., Kučera, J., Van den haute, P., 2008. On the internal radioactivity in quartz. Radiation Measurements 43, 771-775.

Vita-Finzi, C.,1969. The Mediterranean Valleys: Geological Changes in Historical Times. Cambridge: Cambridge University Press.

Vita-Finzi, C., 1976. Diachronism in old World alluvial sequences. Nature 263, 218-219.

Voinchet, P., Falguères, C., Laurent, M., Toyoda, S., Bahain, J.J., Dolo, J.M., 2003. Artificial optical bleaching of the Aluminium center in quartz implications to ESR dating of sediments. Quaternary Science Reviews 22, 1335-1338.

Voinchet, P., Despirée, J., Tissoux, H., Falguères, C., Bahain, J.-J., Gageonnet, R., Dépont, J., Dolo, J.-M., 2010. ESR chronology of alluvial deposits and first human settlements of the Middle Loire Basin (Region Centre, France). Quaternary Geochronology 5, 381-384.

Voinchet, P., Toyoda, S., Falguères, C., Hernandez, M., Tissoux, H., Moreno, D., Bahain, J.-J., 2015. Evaluation of ESR residual dose in quartz modern samples, an investigation on environmental dependence. Quaternary Geochronology 30, 506-512.

von Suchodoletz, H., Menz, M., Kühn, P., Sukhishvili, L., Faust, D., 2015. Fluvial sediments of the Algeti River in southeastern Georgia – An archive of Late Quaternary landscape activity and stability in the Transcaucasian region. Catena 130, 95-107.

Wagstaff, J.M., 1981. Buried assumptions: some problems in the interpretation of the "Younger fill" raised by recent data from Greece. Journal of Archaeological Science 8, 247-264.

Wainwright, J., Thornes, J.B., 2004. Environmental Issues in the Mediterranean. Processes and perspectives from the past and present. Routledge, London, New York.

Wallinga, J., 2002. Optically stimulated luminescence dating of fluvial deposits: a review. Boreas 31, 303-322.

Weltje, G.J., von Eynatten, H., 2004. Quantitative provenance analysis of sediments: review and outlook. Sedimentary Geology 171, 1-11.

Wintle, A., 1973. Anomalous fading of thermoluminescence in mineral samples. Nature 245, 143-144.

Wintle, A.G., Murray, A., 2006. A review of quartz optically stimulated luminescence characteristics and their relevance in single-aliquot regeneration dating protocols. Radiation Measurements 41, 369-391.

Woda, C., Wagner, G.A., 2007. Non-monotonic dose dependence of the Ge- and Ti-centres in quartz. Radiation Measurements 42, 1441-1452.

Wolf, D., Seim, A., Faust, D., 2014. Fluvial system response to external forcing and human impact – Late Pleistocene and Holocene fluvial dynamics of the lower Guadalete River in western Andalucía (Spain). Boreas 43, 422-429.

Wolf, D., Faust, D., 2015. Western Mediterranean environmental changes: Evidences from fluvial archives. Quaternary Science Reviews 122, 30-50.

Yokoyama, Y., Falguères, C., Quaegebeur, J.P., 1985. ESR dating of quartz from Quaternary sediments: first attempt. Nucl. Tracks 10 (4-6), 921-928.

Zapata, L., López-Sáez, J.A., Ruiz-Alonso, M., Linstädter, J., Pérez-Jordà G., Morales, J., Kehl, M., Peña-Chocarro, L., 2013. Holocene environmental change and human impact in NE Morocco: Palaeobotanical evidence from Ifri Oudadane. The Holocene 23 (9), 1286-1296.

Zarki, H., Macaire, J.-J., Beck, C., De Luca, P., 2004. Morpho-sedimentary evolution of the lower Moulouya (North Eastern Morocco) during middle and upper Holocene. Seismicity and neotectonic effects. Geodinamica Acta 17 (3), 205-217.

Zielhofer, C., 2007. Climate change and landscape-ecological effects in the Western Mediterranean – future, present and learning from the past. Europa Regional 15 (2), 110-118.

Zielhofer, C., Faust, D., Linstädter, J., 2008. Late Pleistocene and Holocene alluvial archives in the southwestern Mediterranean: Changes in fluvial dynamics and past human response. Quaternary International 181, 39-54.

Zielhofer, C., Recio Espejo, J.M., Núnez Granados, M.A., Faust, D., 2009. Durations of soil formation and soil development indices in a Holocene floodplain. Quaternary International 209 (1-2), 44-65.

Zielhofer, C., Bussmann, J., Ibouhouten, H., Fenech, K., 2010. Flood frequencies reveal Holocene rapid climate changes (Lower Moulouya River, northeastern Morocco). Journal of Quaternary Science 25 (5), 700-714.

Zielhofer, C., Fletcher, W.J., Mischke, S., De Batist, M., Campbell, J.F.E., Joannin, S., Tjallingii, R., El Hamouti, N., Junginger, A., Stele, A., 2017. Atlantic forcing of Western Mediterranean winter rain minima during the last 12000 years. Quaternary Science Reviews 157, 29-51.

Zijderveld, J.D.A., 1967. A.C. Demagnetization of Rocks: Analysis of Results. In: Collinson, D.W., Creer, K.M., Runcorn, S.K. (eds.). Methods in Palaeomagnetism. Elsevier, Amsterdam, New York, 254-286.

Appendix A

ESR Fitting procedure and D_e calculation

Fitting procedure and D_e calculation were performed with Microcal OriginPro 8.5 software using a Levenberg-Marquardt algorithm by chi-square minimisation. Al ESR intensities were fitted by using the exponential+linear (EXPLIN) function following Duval (2012). Data points were weighted by the inverse of the squared ESR intensity ($1/I^2$) to reduce the leverage of high dose points (Hayes et al., 1988). Ti ESR intensities were fitted with the Ti-2 function (Woda and Wagner, 2007; Duval and Guilarte, 2015), which describes the decreasing behaviour of the ESR intensity at high doses. Data points were either not weighted (EW) or weighted by the inverse of the squared errors ($1/s^2$) to reduce the influence of dose points with large experimental errors. In order to get information about the behaviour of the low irradiation dose points, the Ti ESR intensities were additionally fitted with the SSE function ($1/I^2$) until the maximum ESR intensity (I_{max}), whilst the Ti-2 function was fitted over the full dose range. Fitting equations can be found in supplementary Table A.1. The goodness-of-fit is assessed through the adjusted r-square (r^2) value, which accounts for the degree of freedom of the system. We adopted the fitting criteria by Duval et al. (2013) in order to assess the fitting reliability of each dose response curve (DRC) and followed the quality control procedures recommended by Duval and Guilarte (2015).

Table A.1. List of the fitting functions: single saturation exponential (SSE), exponential + linear (EXPLIN) and Ti-2 function. D is the absorbed dose (Gy), I is the ESR intensity (arbitrary units). Fitted parameters are the equivalent dose (D_e), the saturation ESR intensity (I_{sat}), the characteristic saturation dose (D_0), m may be considered as an estimation of the radiation sensitivity of the second component of the EXPLIN function. Further information can be found in Duval (2012) and Duval and Guilarte (2015).

Function	**Equation**	**Fitted parameter**
SSE	$I(D) = I_{sat}*(1 - e^{-(D+De)/D0})$	D_e, I_{sat}, D_0
EXPLIN	$I(D) = I_{sat}*(1 - e^{-(D+De)/D0}) + m(D + D_e)$	D_e, I_{sat}, D_0, m
Ti-2	$I(D) = a*(e^{-(D+De)/D1} - e^{-(D+De)/D2})$	a, D1, D2, D_e

References

Duval, 2012. Dose response curve of the ESR signal of the Aluminium centre in quartz grains extracted from sediment. Ancient TL 30 (2), 41-49.

Duval, M., Guilarte Moreno, V., Grün, R., 2013. ESR dosimetry of fossil enamel: some comments about the measurement precision, long-term signal fading and dose-response curve fitting. Radiation Protection Dosimetry 157 (4), 463-476.

Duval, M., Guilarte, V., 2015. ESR dosimetry of optically bleached quartz grains extracted from Plio-Quaternary sediment: Evaluating some key aspects of the ESR signals associated to the Ti-centres. Radiation Measurements 78, 28-41.

Hayes, R.B., Haskell, E.H., Kenner, G.H., 1998. An assessment of the Levenberg-Marquardt fitting algorithm on saturating exponential data sets. Anc. TL 16 (2), 57-62.

Woda, C., Wagner, G.A., 2007. Non-monotonic dose dependence of the Ge- and Ti-centres in quartz. Radiation Measurements 42, 1441-1452.

Appendix B

Palaeomagnetic results

For the BOU section, NRM intensities range between 2.71x10^{-3} A/m to 8.11x10^{-2} A/m. 16 of 32 specimens have been demagnetised by TH, whilst the other 16 specimens have been processed by AF. The results show a dominance of southeast and negative directions (fig. 5.3). A total of 10 specimens have been processed from the TOLL section, with a range of NRM intensities between 8.66x10^{-3} A/m and 1.40x10^{-2} A/m. 5 of those subsamples have been demagnetised by TH and the other 5 by AF. In contrast to the other sections, TOLL display to the north to northeast and with downwards directions. Many specimens from the MRB section were either unstable upon demagnetisation or too weak after the initial demagnetisation steps. As a consequence, only sample M2 (18 specimens) have produced reproducible and interpretable results. NRM intensities range between 1.75x10^{-3} A/m and 6.52x10^{-3} A/m. Whilst 7 of those subsamples have been analysed by TH demagnetisation, AF demagnetisation was used to analyse the other 11 specimens. The results show a south west direction and a negative inclination. NRM intensities from 39 specimens of the DOE section range between 2.05x10^{-4} A/m and 1.09x10^{-3} A/m. 23 specimens have been demagnetised by TH and the remaining by AF. The ChRM directions in this site, similar to the BOU section, are southeast, and upwards (Table B.1).

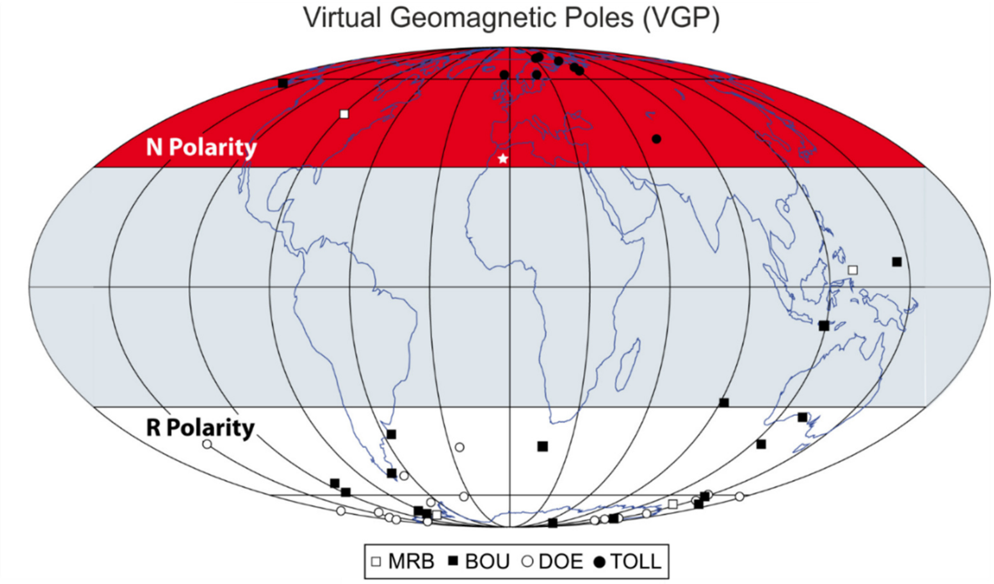

Fig. B.1: Virtual Geomagnetic Poles (VGP) of the four different locations at the lower Moulouya River, namely the MRB, BOU, DOE and TOLL section. VGP pole positions indicate reversed polarity for sections BOU, TOLL and MRB, whilst section TOLL reveals normal polarity. Star denotes study area. The presence of normal polarity in a few specimens from the BOU section can be interpreted as overprinting of the actual magnetic field.

Table B.1: Characteristic remanent magnetisation (ChRM) direction of the palaeomagnetic samples. We used the Fisherian mean of the ChRM directions to calculate the corresponding virtual geomagnetic pole (VGP) position for each sample site.

Section	**Sample ID**	**Declination**	**Inclination**	**VGPLat**	**VGPLon**
BOU	B1.2A	218	-21	-51	290
	B1.3A	83	-45	-9	118
	B1.3C	8	-47	58	200
	B1.3D	131	-4	-41	125
	B2.1A	175	-10	-84	156
	B2.1C	153	-28	-61	151
	B2.2A	232	-2	-38	304
	B2.2B	195	-26	-71	265
	B2.2D	170	24	-43	15,3
	B2.3A	195	-49	-59	241
	B4.1C	171	-24	-77	174
	B4.2A	123	-13	87	131
	B4.2C	124	45	-33	92
	B4.3B	161	-35	87	168
	B4.3C	197	-29	-29	265
	B4.3D	201	-51	87	246
DOE	D1.1C	162	-44	-61	178
	D1.2C	223	37	-42	335
	D1.3A	206	-14	-64	293
	D2.1A	207	15	-61	325
	D2.2A	174	-68	-41	210
	D2.2D	156	-28	-63	154
	D2.3A	175	-33	-74	197
	D3.1A	170	-23	-76	169
	D3.1C	170	-17	-78	157
	D3.1D	169	-19	-77	159
	D3.2A	181	-39	-70	217
	D3.2B	164	-24	-71	158
	D3.2C	173	-27	-76	185
	D3.2D	175	-21	-80	184
	D3.3A	169	-36	-69	184
	D3.3B	170	-23	-76	169
	D3.3C	172	-19	-79	168
	D3.3D	152	-27	-60	149
	D4.1A	218	-14	-52	296
TOLL	T1.C	341	42	62	356
	T1.A	1	35	73	38
	T2.A	359	37	72	32
	T2.B	11	42	66	60
	T2.C	7	38	70	54
	T3.A	11	44	64	58
	T3.B	353	49	62	22
	T3.C	37	61	38	70
	T3.D	12	44	64	60
MRB	M2.1A	86	-7	4	129
	M2.1D	156	-21	-65	145
	M2.2C	322	-37	46	271
	M2.3D	195	-23	-72	272

Appendix C

Al centre

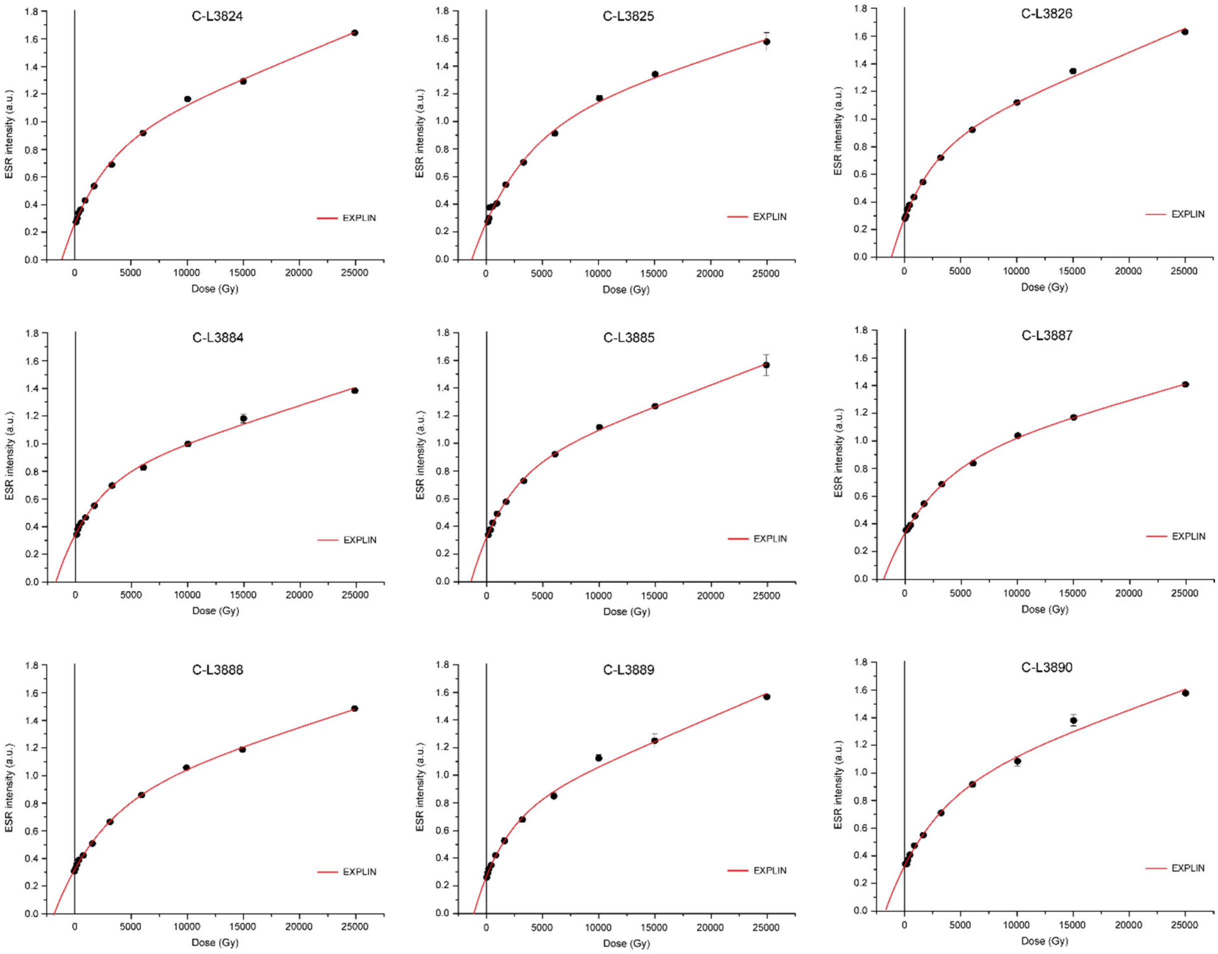

Fig. C.1: Dose response curves (DRC) of the Al centre of the different samples.

Ti centre (option A)

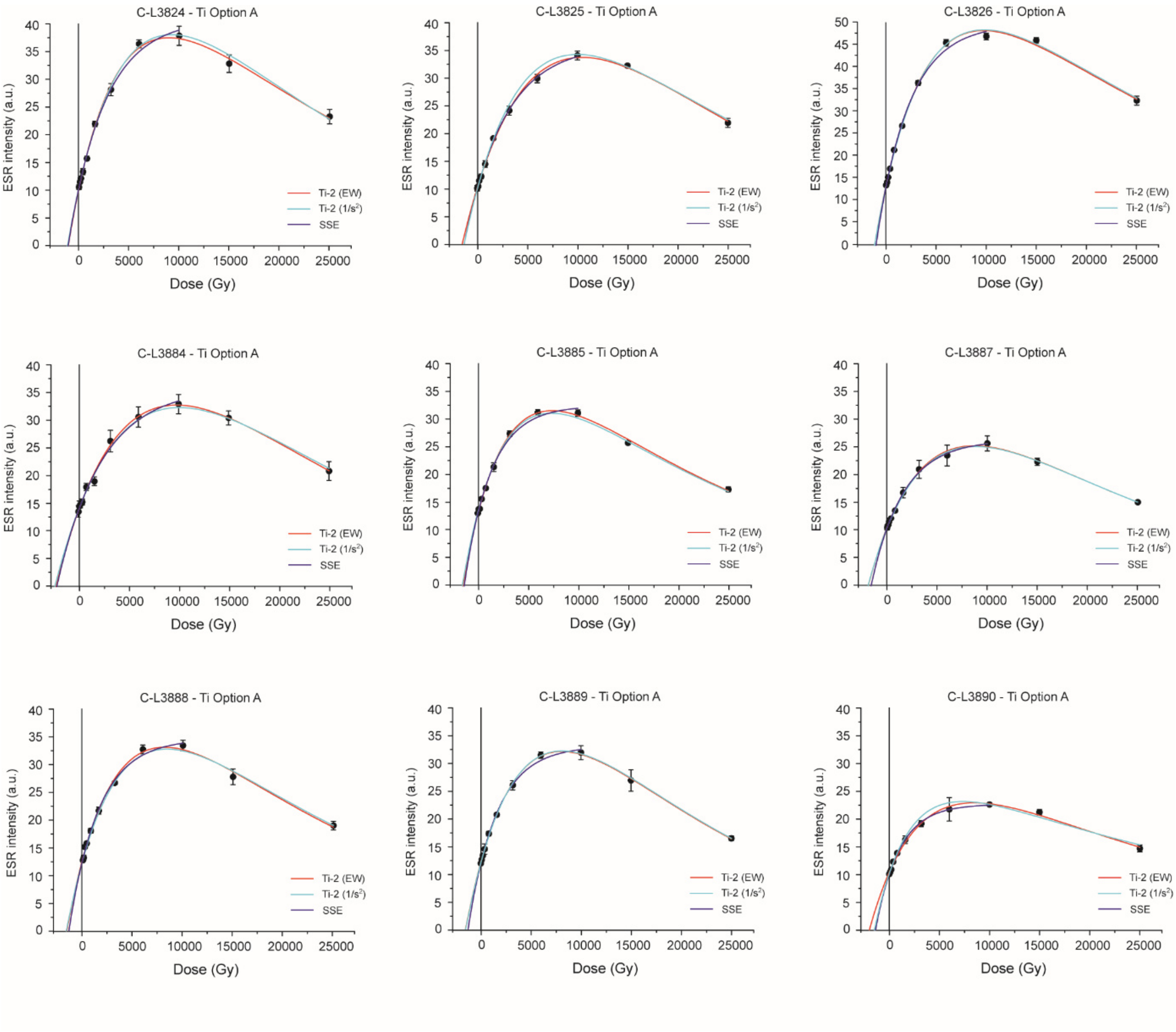

Fig. C.2: Dose response curves (DRC) of the Ti centre (option A) of the different samples.

Ti centre (option D)

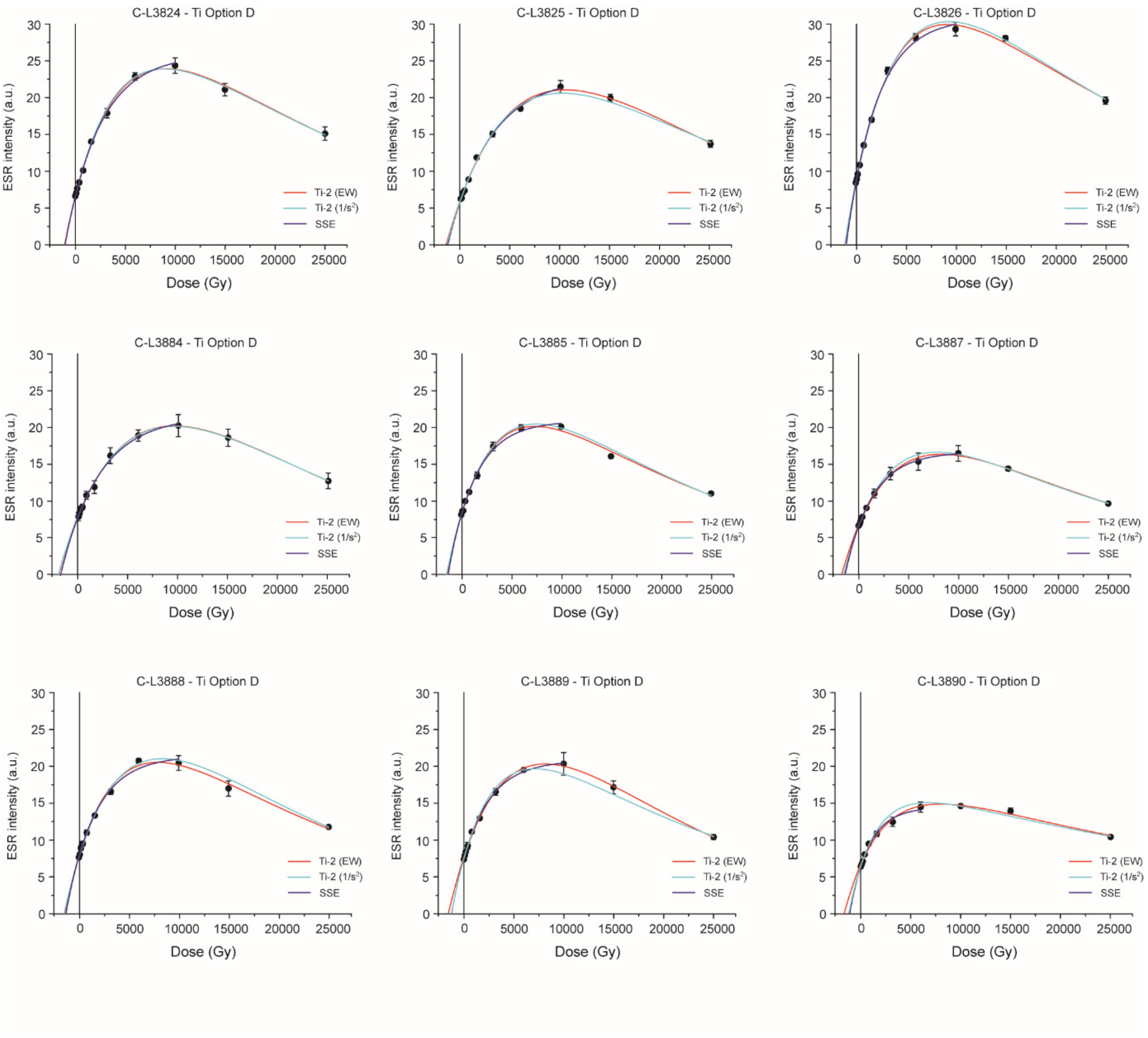

Fig. C.3: Dose response curves (DRC) of the Ti centre (option D) of the different samples.

Evaluation of the Ti-H centre

The Ti-H centre (option C; Table C.1) yield on average much lower ESR intensities compared to those measured with Ti option A (38±7 %) and D (43±9 %). Those values are similar to those measured by Duval and Guilarte (2015) on a wider range of samples, suggesting that the amount of Ti-H centres in the quartz from the Moulouya River falls within the standards. The measurement repeatability is somewhat higher to that achieved for the Al centre, ranging between 9.1 and 16.1 %. As a direct consequence, D_e repeatability over three different days varies largely between 7.3 and 42.2 % (mean = 23 %). Final D_e values were calculated by considering the average of nine ESR intensities. The three fitting configurations yield mostly very poor fitting results with adjusted r^2 values <0.98. The SSE function fitted on the lower dose range (fig. C.4) yields more satisfactory goodness-of-fit (r^2 values >0.98) as fitted with the Ti-2 function. The only exceptions are samples C-L3884, C-L3886 and C-L3888 with adjusted r^2-values <0.97 indicating insufficient fitting. Although fitting was not excellent, the three different fitting configurations yielded D_e values which are 1σ-consistent. Due to the poor goodness-of-fit of the Ti-2 function and the large errors derived from unsatisfied fitting, we assume the SSE D_e values as the most suitable calculation results. D_e values range between 561±73 and 851±202 Gy for section DOE, 540±90 and 651±53 Gy for section MRB, 680±102 and 696±162 Gy for section TOLL as well as 447±66 and 712±70 Gy for section BOU. The Ti-H centre (option C) yielded throughout the lowest D_e values of the eleven samples as well as a fitting which is not as good as for the Al or Ti option D (fig. 5.6). Similarly, Duval et al. (2015) have shown systematically lower D_e values of the Ti-H centre compared to those of the Ti centre (option D). This may be explained by the lower saturation level of the Ti-H centre (Duval et al., 2015), which might also be an explanation for our samples characterised by D_e values <850 Gy derived from the Ti-H centre. Likewise, Beerten et al. (2006) have suggested that the Ti-H centre is not enough stable in Middle Pleistocene or older samples. Therefore, we assume that the Ti-H centre in the fluvial samples of the Moulouya River has reached saturation and cannot be used for further dating procedures.

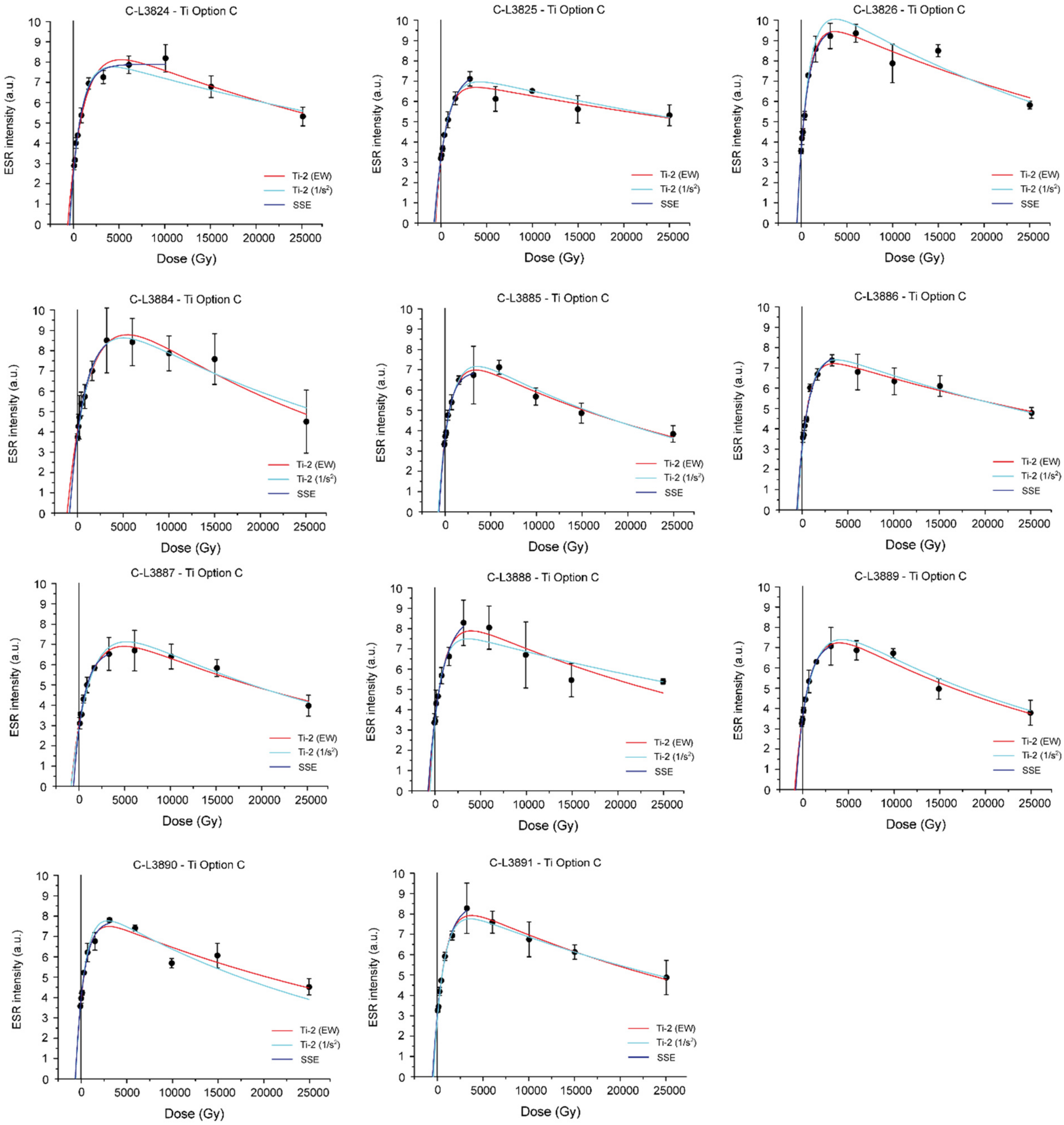

Fig. C.4: Dose response curves (DRC) of the Ti-H centre (option C) of the different samples.

Table C.1: ESR data derived from the measurements of the Ti-H centre (option C). Fitting was performed with both the SSE and Ti-2 functions with equal weights (EW), weighting by the inverse of the squared ESR intensities ($1/I^2$) and weighting by the inverse of the squared errors ($1/s^2$). Measurement repeatability is assessed through the variability of the average ESR intensities obtained from each day of measurement. D_e reproducibility is based on the variability of the D_e values (using the Ti-2 function) obtained after each day of measurement.

Profile	**Sample ID**	**ESR intensity repeatability (%)**	**D_e reproduc. (%)**	**Ti-H centre - Option C**								
				SSE ($1/I^2$)			**Ti-2 (EW)**			**Ti-2 ($1/s^2$)**		
				D_e (Gy)	**err (%)**	**r^2**	**D_e (Gy)**	**err (%)**	**r^2**	**D_e (Gy)**	**err (%)**	**r^2**
BOU	C-L3824	10.3	23.1	499 ± 69	13.8	0.9856	703 ± 164	23.3	0.9567	474 ± 63	13.3	0.9788
	C-L3825	13.3	20.4	712 ± 70	9.9	0.9938	560 ± 138	24.7	0.9511	638 ± 60	9.5	0.9933
	C-L3826	12.8	17.4	447 ± 66	14.8	0.9850	436 ± 111	25.5	0.9528	428 ± 54	12.6	0.9731
DOE	C-L3884	16.1	42.2	851 ± 202	23.8	0.9650	1143 ± 241	21.1	0.9504	895 ± 105	11.8	0.9779
	C-L3885	14.0	29.8	561 ± 73	13.0	0.9882	675 ± 126	18.7	0.9644	684 ± 72	10.5	0.9838
	C-L3886	11.8	10.0	653 ± 150	22.9	0.9659	555 ± 99	17.8	0.9706	577 ± 98	17	0.9654
TOLL	C-L3887	11.0	39.0	680 ± 102	15.0	0.9850	962 ± 151	15.7	0.9738	943 ± 159	16.9	0.9721
	C-L3888	14.2	18.9	696 ± 162	23.3	0.9664	622 ± 187	30.1	0.9202	486 ± 79	16.3	0.9668
MRB	C-L3889	13.2	19.5	651 ± 53	8.2	0.9955	783 ± 126	16.2	0.9728	838 ± 79	9.4	0.9909
	C-L3890	9.1	7.3	540 ± 90	16.7	0.9815	540 ± 155	28.8	0.9229	532 ± 66	12.4	0.9821
	C-L3891	11.2	22.9	558 ± 85	15.2	0.9848	525 ± 72	13.7	0.9892	466 ± 50	10.7	0.9808

References

Beerten, K., Lomax, J., Clémer, K., Stesmans, A., Radtke, U., 2006. On the use of Ti centres for estimating burial ages of Pleistocene sedimentary quartz: Multiple-grain data from Australia. Quaternary Geochronology 1, 151-158.

Duval, M., Guilarte, V., 2015. ESR dosimetry of optically bleached quartz grains extracted from Plio-Quaternary sediment: Evaluating some key aspects of the ESR signals associated to the Ti-centres. Radiation Measurements 78, 28-41.

Duval, M., Sancho, C., Calle, M., Guilarte, V., Penna-Monné, J.L., 2015. On the interest of using the multiple centre approach in ESR dating of optically bleached quartz grains: Some examples from the Early Pleistocene terraces of the Alcanadre River (Ebro basin, Spain). Quaternary Geochronology 29, 58-69.

Appendix D

Comparison between HRGS and ICP-MS values

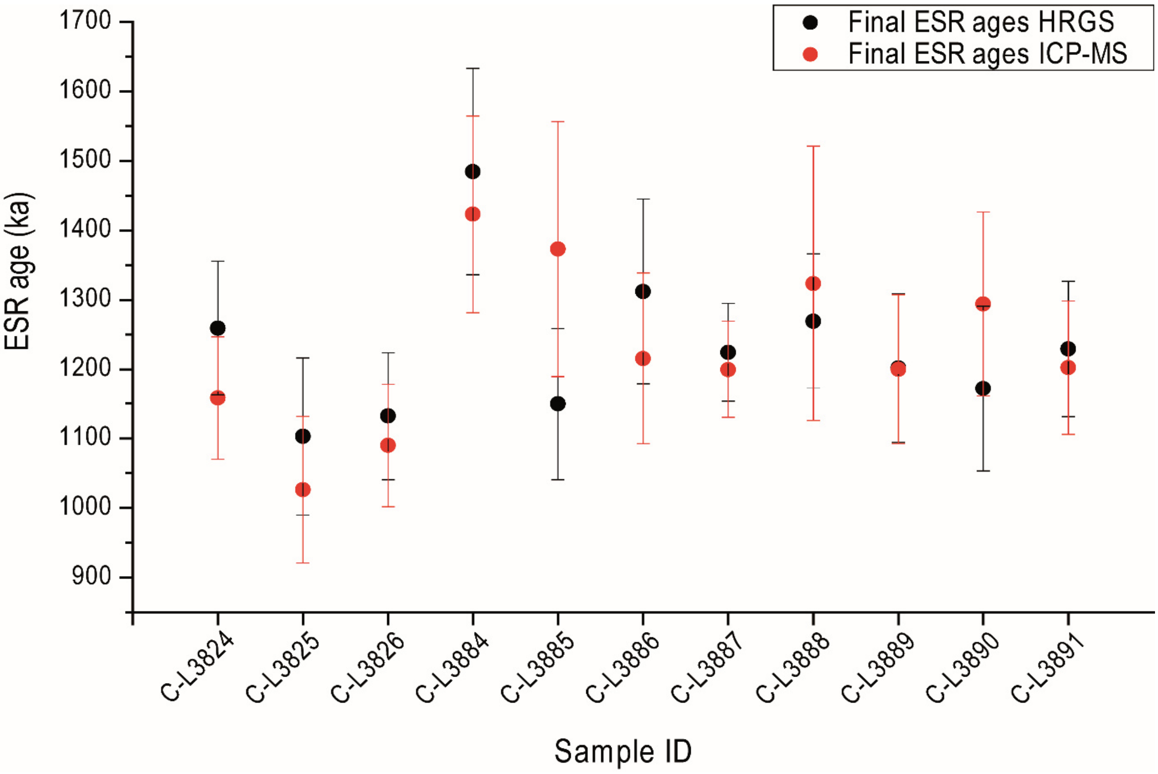

Fig. D.1: Comparison between ESR age calculations based on HRGS and ICP-MS activity values.

Testing the influence of water content on the final ESR age

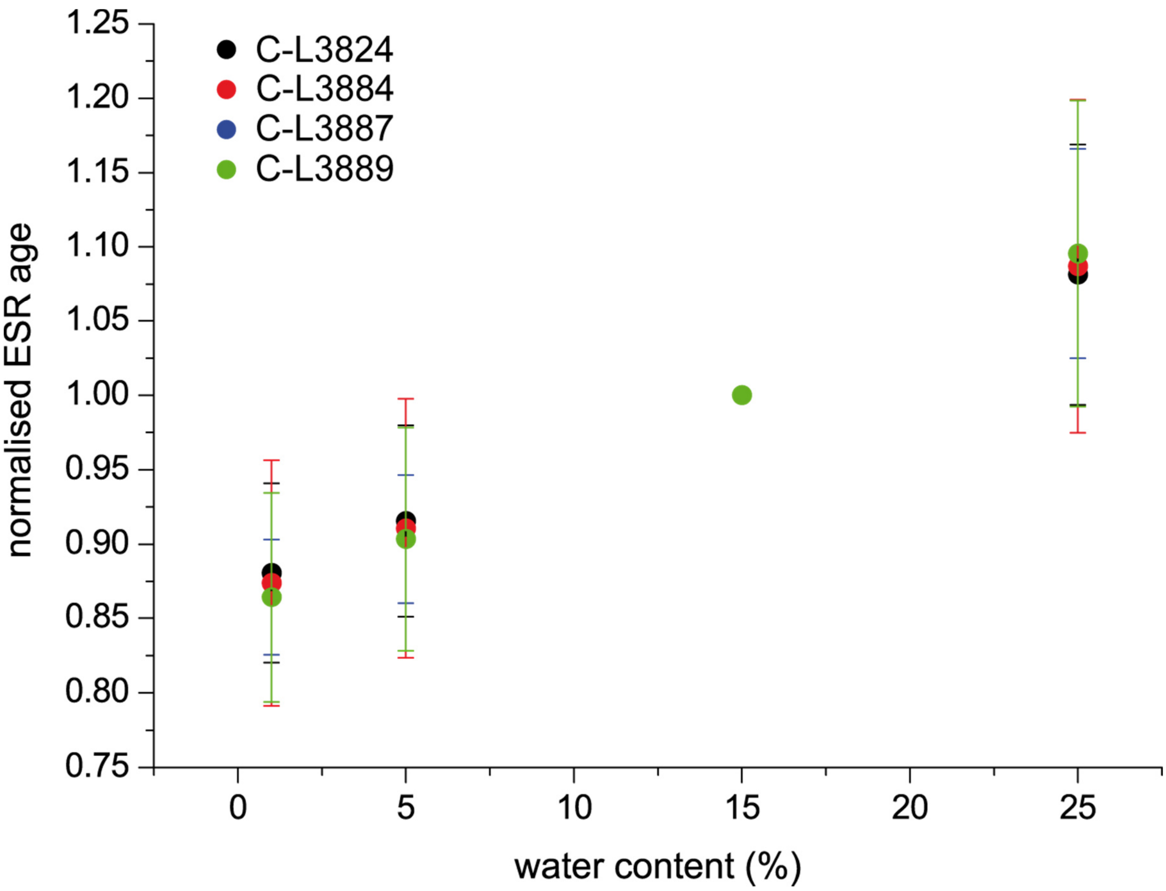

Fig. D.2: Assumed water contents between 1 and 25 % vs. ESR ages. The resulting ESR ages were normalised to an assumed water content of 15±5 %.

Paper contribution

1. **Bartz, M.,** Klasen, N., Zander, A., Brill, D., Rixhon, G., Seeliger, M., Eiwanger, J., Weniger, G.-C., Mikdad, A., Brückner, H., 2015. Luminescence dating of ephemeral stream deposits around the Palaeolithic site of Ifri n‘Ammar (Morocco). *Quaternary Geochronology* 30, 460-465. **[Contribution: 80 %]**

   Geländearbeit: 80 %

   Erhebung der Daten im Labor: 90 %

   Auswertung und Interpretation: 80 %

   Verfassen der Publikation: 70 %

2. **Bartz, M.**, Rixhon, G., Kehl, M., El Ouahabi, M., Klasen, N., Brill, D., Weniger, G.-C., Mikdad, A., Brückner, H., 2017. Unravelling fluvial deposition and pedogenesis in ephemeral stream deposits in the vicinity of the prehistoric rock shelter of Ifri n'Ammar (NE Morocco) during the last 100 ka *Catena* 152, 115-134. **[Contribution: 75 %]**

   Geländearbeit: 80 %

   Erhebung der Daten im Labor: 80 %

   Auswertung und Interpretation: 70 %

   Verfassen der Publikation: 65 %

3. Rixhon, G., **Bartz, M.,** El Ouahabi, M., Szemkus, N., Brückner, H., 2017. Contrasting terrace systems of the lower Moulouya river as indicator of crustal deformation in NE Morocco. *Journal of African Earth Sciences* 126, 45-57. **[Contribution: 45 %]**

   Geländearbeit: 80 %

   Erhebung der Daten im Labor: 20 %

   Auswertung und Interpretation: 35 %

   Verfassen der Publikation: 40 %

Erklärung

"Ich versichere, dass ich die von mir vorgelegte Dissertation selbständig angefertigt, die benutzten Quellen und Hilfsmittel vollständig angegeben und die Stellen der Arbeit − einschließlich Tabellen, Karten und Abbildungen −, die anderen Werken im Wortlaut oder dem Sinn nach entnommen sind, in jedem Einzelfall als Entlehnung kenntlich gemacht habe; dass diese Dissertation noch keiner anderen Fakultät oder Universität zur Prüfung vorgelegen hat; dass sie − abgesehen von unten angegebenen Teilpublikationen − noch nicht veröffentlicht worden ist, sowie, dass ich eine solche Veröffentlichung vor Abschluss des Promotionsverfahrens nicht vornehmen werde. Die Bestimmungen der Promotionsordnung sind mir bekannt. Die von mir vorgelegte Dissertation ist von Prof. Dr. H. Brückner betreut worden."

Nachfolgend genannte Teilpublikationen liegen vor:

1. **Bartz, M.,** Klasen, N., Zander, A., Brill, D., Rixhon, G., Seeliger, M., Eiwanger, J., Weniger, G.-C., Mikdad, A., Brückner, H., 2015. Luminescence dating of ephemeral stream deposits around the Palaeolithic site of Ifri n'Ammar (Morocco). *Quaternary Geochronology* 30, 460-465.
2. **Bartz, M.**, Rixhon, G., Kehl, M., El Ouahabi, M., Klasen, N., Brill, D., Weniger, G.-C., Mikdad, A., Brückner, H., 2017. Unravelling fluvial deposition and pedogenesis in ephemeral stream deposits in the vicinity of the prehistoric rock shelter of Ifri n'Ammar (NE Morocco) during the last 100 ka *Catena* 152, 115-134.
3. Rixhon, G., **Bartz, M.,** El Ouahabi, M., Szemkus, N., Brückner, H., 2017. Contrasting terrace systems of the lower Moulouya river as indicator of crustal deformation in NE Morocco. *Journal of African Earth Sciences* 126, 45-57.

Köln, den 18.01.2018

(Melanie Bartz)